



AVERTISSEMENT

Ce document est le fruit d'un long travail approuvé par le jury de soutenance et mis à disposition de l'ensemble de la communauté universitaire élargie.

Il est soumis à la propriété intellectuelle de l'auteur. Ceci implique une obligation de citation et de référencement lors de l'utilisation de ce document.

D'autre part, toute contrefaçon, plagiat, reproduction illicite encourt une poursuite pénale.

Contact : ddoc-theses-contact@univ-lorraine.fr

LIENS

Code de la Propriété Intellectuelle. articles L 122. 4

Code de la Propriété Intellectuelle. articles L 335.2- L 335.10

http://www.cfcopies.com/V2/leg/leg_droi.php

<http://www.culture.gouv.fr/culture/infos-pratiques/droits/protection.htm>

**THESE**

Présentée et soutenue publiquement le 3 juin 2021

Pour l'obtention du titre de :

DOCTEUR DE L'UNIVERSITE DE LORRAINE

Mention : Chimie-Chimie des Matériaux

par : **Mélanie DE VOS**

Electrodeposition of low dimensional thermoelectric materials: the case of SnSe

Directeur de thèse :	Dr Nicolas STEIN	Maitre de conférence HDR, IJL, Université de Lorraine, FRANCE
Président du jury :	Pr Clotilde BOULANGER	Professeur, IJL, Université de Lorraine, FRANCE
Rapporteuse :	Pr Marie-Christine RECORD	Professeur, IN2MP, Université d'Aix-Marseille, FRANCE
Rapporteur :	Pr Phillip DALE	Professeur, Laboratory for Photovoltaics, University of Luxembourg, LUXEMBOURG
Examineur :	Dr László PETER	Directeur de recherche, Institute for Solid State Physics and Optics, Budapest, HONGRIE
Examineur :	Pr David LACROIX	Professeur, LEMTA, Université de Lorraine, FRANCE

According to the requirements of the CM2P doctoral school, this thesis being written in English, the summary, the general introduction, as well as the introduction and conclusion of each chapter were also written in French.

Conformément aux exigences de l'école doctorale CM2P, cette thèse étant rédigée en anglais, le résumé, l'introduction générale, ainsi que l'introduction et la conclusion de chaque chapitre ont également été rédigés en français.

« Tout obstacle renforce la détermination. Celui qui s'est fixé un but n'en change pas. »

Léonard De Vinci

« La connaissance s'acquiert par l'expérience, tout le reste n'est que de l'information. »

Albert Einstein

A mon parrain, « tonton Picsou » qui sera à jamais présent dans mon cœur.

This work was carried out within the Institut Jean Lamour, specifically the team n°208, devoted to the chemistry and electrochemistry of materials. I want to thank Dr. Nicolas STEIN, Associate Professor and my PhD director for allowing me to evolve in such favorable scientific framework. I am grateful to him for sharing his knowledge and advice. I thank him for supporting me and for giving me the opportunity to share my knowledge.

I want to thank Prof. Marie-Christine RECORD and Prof. Phillip DALE for accepting to report this work and for being part of my thesis committee. I thank them for the time and interest in reading my manuscript.

I want to address my sincere acknowledgements to Dr. László PÉTER, Prof. Clotilde BOULANGER and Prof. David LACROIX for agreeing to review this work and for being members of my thesis committee. I would like to thank Dr. László PÉTER who let me work in his laboratory and for his help and his kindness. I also thank his colleagues, Attila CSÍK, Kálmán VAD and the others who welcomed me. Special thanks to Prof. Clotilde BOULANGER and Prof. David LACROIX who followed my PhD from near or far and for their support.

I want to express my sincere considerations to Dr. Abdelaadim DANINE, who initiated me in the beginning of my PhD and for his advice and listening. I thank Dr. José BARBOSA, Karen AL HOKAYEM for accompanying me during this PhD. I thank them for their kindness and consider them as friends.

This work was also carried out by several trainees I want to congratulate for their patience and perseverance against difficulties: Chloé CEYRAT, Milan TOLEDO, Lorena RAMIREZ and Katarzyna SKIBINSKA (PhD student who came thanks to Erasmus). Milan, my friend who was a sunshine ray during these few months and never lost her smile, you can be proud of yourself.

I also thank all team members: Dr. Sébastien DILIBERTO, Dr. Nathalie LECLERC, Dr. Sophie LEGEAI, Dr. Eric MEUX, Dr. Stéphanie MICHEL, and Dr. Alexandre ZIMMER for their kindness and for evolving in such pleasant conditions. Thank you very much to Dr. Sébastien DILIBERTO specifically for the Mössbauer and XRD analyses. I thank also Dr. Stéphanie MICHEL for ICP measurements.

I am grateful to the Institut Jean Lamour where I could carry out my experiences. I am also grateful to the Université de Lorraine and the opportunity to teach to students in Bachelor degree. It was really pleasant.

I want to thank Dr. Sylvie MIGOT for the preparation of FIB lamellas, as well as Dr. Jaafar GHANBAJA and Dr. Hiba KABBARA for TEM analyzes. I also thank Dr. Alexandre ZIMMER and Dr Laurent BROCH for ellipsometric characterizations. I am also grateful to Prof. Aotmane EN NACIRI who followed the progress of my PhD and for his support.

For welcoming me into their laboratory, I want to thank Prof. Marisol MARTÍN-GONZÁLEZ and Dr. Olga CABALLERO-CALERO. I will never forget these trips as well as the Lego exhibition. I want to thank the other members who were really nice with me, Alex, Lili and Pedro.

Le travail de thèse est un fruit de plusieurs années et de durs labeurs dont le soutien ne saurait manquer. C'est pourquoi je tiens à remercier la première personne à m'avoir soutenue dans cette démarche et sans qui je ne serais là : ma mère. Je lui suis reconnaissante de m'avoir épaulée durant ces trois dernières années et de m'avoir écoutée tous les soirs sans jamais faiblir. Je remercie ma sœur Pascaline de m'avoir soutenue. Merci à mon tonton Jacky pour sa confiance et son soutien. Merci à mon Bébou d'avoir été présent durant les derniers moments de ma thèse. Merci à Anne ma meilleure amie de m'avoir fait rire quand j'en avais besoin, de m'avoir écouté me plaindre et pour toutes nos conversations inutiles sur Facebook. En garde, prêt, allez ! Merci à mes amis Marthe, Ivan, Amandine, Julie, Clémence, mais également celles que j'ai rencontrées à Metz dans le cadre de stage, Pauline et Sophie.

Je remercie Angela DELL'ANNUNZIATA pour nos discussions et sa gentillesse.

Enfin je remercie toutes les personnes que je n'aurais pas citées mais qui ont contribué de près ou de loin à cette thèse.

Table of contents

Table of contents	12
List of abbreviations	17
Nomenclature.....	19
Introduction (English).....	22
Introduction (Français)	24
Chapter 1. Fundamental concepts and state of the art	26
Introduction	27
I. What is thermoelectricity?	27
a. Explanation of the phenomena	27
b. Why thermoelectricity?	29
c. How a thermoelectric material is characterized?	29
d. Currently and recently studied materials.....	31
II. Description of SnSe	33
a. Phase diagram	33
b. Crystal structure	34
c. Electronic configuration	34
d. Thermoelectric properties.....	36
III. Different ways of SnSe films synthesis	38
a. Dry deposition methods	38
b. Wet synthesis methods	44
IV. Electrodeposition of SnSe	46
a. Electrodeposition of Sn	46
b. Electrodeposition of Se	51
c. Electrodeposition of SnSe	57
1. Synthesis in absence of additives.....	57
2. Synthesis with additives	60
3. TE properties of SnSe films.....	63
4. Doping of SnSe films	65
Conclusion	68
Chapter 2. Materials and methods	69
Introduction	70
I. The electrolyte solution.....	70

a.	Thermodynamic stability of the electrolyte solution	70
b.	Definition and preparation of the electrolyte solution	74
c.	Time evolution of the bath.....	78
II.	Electrochemical experiments	79
a.	Electrochemical setup	79
b.	Linear Sweep voltammetries (LSV) and cyclic voltammetries (CV)	80
c.	Electrodeposition methods	81
III.	Microstructural characterizations	82
a.	Sample preparation for analysis.....	82
b.	X-ray Diffraction (XRD)	83
c.	Scanning Electron Microscopy (SEM)	84
d.	Energy Dispersive X-ray Spectroscopy (EDS).....	85
e.	Transmission Electron Microscopy (TEM)	86
f.	Focused Ion Beam (FIB)	87
IV.	Other chemical characterization techniques	88
a.	Inductively Coupled Plasma-Optical Emission Spectroscopy (ICP-OES).....	88
b.	Conversion Electron Mössbauer Spectrometry (CEMS)	89
c.	Raman spectrometry	90
d.	Secondary Ion and Neutral Mass Spectrometry (SIMS and SNMS)	91
e.	X-ray photoelectron spectroscopy	93
f.	Ellipsometry	93
	Conclusion	95
Chapter 3. Continuous electrodeposition of SnSe films		96
	Introduction	97
I.	Study of the electrochemical systems.....	97
a.	Electrochemical stability window	97
b.	Study of Sn electrochemical system.....	100
c.	Study of Se electrochemical system.....	104
d.	Study of SnSe electrochemical system	108
II.	Electrodeposition of SnSe films	111
a.	Study of the chronoamperometric curves	111
b.	SEM characterizations	113
c.	TEM characterizations	117
d.	XRD characterizations	119
e.	CEMS characterizations	121

f.	Raman characterizations	123
g.	SIMS/SNMS characterizations	126
	Conclusion	128
Chapter 4. Pulse electrodeposition of SnSe films		130
	Introduction	131
I.	Choice of the pulse mode	132
II.	First set of results: pulse depositions with $t_{OFF} = 1$ s	133
a.	Effect on the double layer charging	133
b.	Study of the chronoamperograms	134
c.	HRSEM and SEM characterizations	135
d.	TEM characterizations	137
e.	XRD characterizations	141
III.	Second set of results: pulse deposition with reduced relaxation time	144
a.	Optimization of the replenishment time	144
b.	Study of the chronoamperograms	146
c.	HRSEM and SEM characterizations	147
d.	TEM characterizations	148
e.	XRD characterizations	151
f.	XPS characterizations	152
g.	Raman characterizations	154
h.	Ellipsometric characterizations	155
IV.	Towards doping of SnSe films	158
a.	Choice of the dopant	158
b.	Chemical compatibility of Co(II)	158
c.	Chemical compatibility of Ni(II)	160
d.	Chemical compatibility of Cu(II)	161
e.	Electrochemical study of the system Cu(II)-Sn(II)-Se(IV)/SnSeCu	164
f.	Pulse electrodeposition of $\text{Cu}_x\text{Sn}_{1-x}\text{Se}$	166
g.	SEM characterizations	167
h.	XRD characterizations	168
	Conclusion	170
Chapter 5. Towards electrodeposition of SnSe nanowires		172
	Introduction	173
I.	Electrodeposition of Sn nanowires	174
a.	Studies in ionic liquid	174

b.	Growth mechanism in alumina templates in aqueous and organic media.....	175
II.	Electrodeposition of Se nanostructures.....	178
III.	Study of SnSe nanostructures	180
a.	Theoretical properties: first principles calculations	180
b.	Synthesis and properties	183
IV.	Electrodeposition of SnSe nanostructures in alumina templates.....	187
a.	Preliminary study of the alumina templates.....	187
1.	Geometric characteristics.....	187
2.	Determination of the exposed and real surfaces.....	189
b.	Study of the electrochemical system	192
c.	Electrodeposition of SnSe nanostructures	194
1.	Typical chronoamperograms during template electrodeposition	195
2.	Influence of the counter-electrode.....	196
3.	Influence of the applied potential.....	197
4.	Filling time, steady state current and filling charge quantity.....	198
d.	Microstructural characterization.....	199
1.	XRD characterizations	199
2.	HRSEM characterizations	201
3.	TEM characterizations.....	203
4.	Raman characterizations	205
	Conclusion.....	208
	General conclusion and prospects.....	210
	Conclusion générale et perspectives	213
	Appendices	217
	References	227
	Summary.....	239
	Résumé.....	240

List of abbreviations

ALD: Atomic Layer Deposition

AAO: Anodic Aluminum Oxide

BSE: Back Scattered Electrons

CV: Cyclic Voltammogram

CBD: Chemical Bath Deposition

CVD: Chemical Vapor Deposition

DFT: Density Functional Theory

EDS (or EDX or EDXS): Energy Dispersive X-ray Spectroscopy

EDTA: Ethylenediaminetetraacetic Acid

FIB: Focused Ion Beam

FWHM: Full Width at Half-Maximum

GC: Glassy Carbon

(HR)SEM: (High Resolution) Scanning Electron Microscopy

(HR)TEM: (High Resolution) Transmission Electron Microscopy

ICP-OES: Inductively Coupled Plasma Optical Emission Spectroscopy

LSV: Linear Sweep Voltammetry

OCP: Open Circuit Potential

PLD: Pulsed Laser Deposition

PVD: Physical Vapor Deposition

RT: Room Temperature

SCE: Saturated Calomel Electrode

SIMS: Secondary Ion Mass Spectrometry

SNMS: Secondary Neutral Mass Spectrometry

SPS: Spark Plasma Sintering

STM: Scanning Tunneling Microscope

TE: Thermoelectric

UPD: Under Potential Deposition

UV-Vis-NIR: UltraViolet-Visible-Near InfraRed

XPS: X-ray Photoelectron Spectroscopy

XRD: X-Ray Diffraction

Nomenclature

A: Amperes (intensity unit)

A.cm⁻²: Amperes per square centimeter (current density unit)

A: Deposition area

AgCl/Ag: Silver chloride-silver reference electrode

C: Coulombs (charge quantity unit)

cm: Centimeter (length unit)

C.mol⁻¹: Coulombs per moles (Faraday constant unit)

D: Diffusion coefficient

E_g: Band gap

F: Faraday constant

g.cm⁻³: Grams per cube centimeter (density unit)

g.mol⁻¹: Grams per mole (molar mass unit)

h: Thickness

I: Current

i_A : Average current

i_p : Peak current

K: Kelvin (temperature unit)

mM: mmol.L⁻¹ (millimole per liter, concentration unit)

n: Number of exchanged electrons

M_{SnSe} : Molar mass of SnSe

Na₂C₂O₄: Sodium oxalate

Q_{th} : Theoretical charge quantity

s: Second (time unit)

S : Seebeck coefficient

$S.cm^{-1}$: Siemens per centimeter (electrical conductivity unit)

SnSe: Tin selenide

T : Temperature

V : Volts (voltage unit)

W : Watt (power or heat flux unit)

t_{ON} : Pulse time

t_{OFF} : Relaxation time

ZT : Dimensionless figure of merit

κ : Thermal conductivity

ρ : Electrical resistivity

ρ_{SnSe} : density of SnSe

σ : Electrical conductivity

$\mu V.K^{-1}$: Microvolt per Kelvin (Seebeck coefficient unit)

$^{\circ}C$: Celsius degrees (temperature unit)

$\Omega.cm$: Ohm centimeter (resistivity unit)

Introduction (English)

Facing the depletion of fossil fuels and the greenhouse gas emission, the interest focuses on new promising alternatives such as thermoelectricity. It is an eco-friendly production mode thanks to its direct conversion of heat into electricity, without gas emission. Although the phenomenon was discovered during the 19th century, thermoelectricity created an enthusiasm since the 90's. A material is rapidly distinguished, Bi_2Te_3 and finds its major application in Peltier modules, also utilized for refrigeration. Nevertheless, a major inconvenience subsists: the conversion yield. In order to optimize this yield, several approaches are available. Among them, an approach consists in improving its performances by nanostructuration. Another option is to work on new materials in order to try to get better properties than the reference material.

My thesis is in the framework of the ANR 3DThermoNano project whose finality is the conception of a tridimensional nanostructured material, for an autonomous sensor application. The major interest of such object is the combination of the mechanical stability, generated by the 3D structure with the decrease of the thermal conductivity, related to the nanostructuration. Its general objective consists in synthesizing thermoelectric films, active elements of Peltier micro-generator, enabling the transformation of waste heat into electricity.

Commonly synthesized in bulk shapes, more and more thermoelectric materials are thus studied in 0D, 1D or 2D shape. Indeed, theoretical and experimental studies demonstrate a considerable decrease of the thermal conductivity with the material dimensionality. Although various physical and chemical methods can be employed, electrodeposition seems to be a particularly adapted method due to its ease of implementation, low cost and moderate growth rates (typically in the order of 10 $\mu\text{m/h}$). This method also enables the control of the deposits morphology and composition.

Among the thermoelectric materials of interest, SnSe is a p-type semiconductor containing abundant and eco-friendly chemical elements. Mainly studied in bulk shape, several studies present it as an excellent candidate for applications in thermoelectricity. Indeed, it exhibits a high Seebeck coefficient and a low thermal conductivity, conferring to it a figure of merit hardly equaled by other materials of 2.6 at 923 K. However, it was poorly elaborated by electrodeposition and essentially studied for photovoltaic applications.

This thesis manuscript is divided into five chapters :

The first chapter exposes on the first hand, in a succinct way, the fundamental principles of thermoelectricity. The physical and chemical properties of SnSe as well as the main synthesis methods

are also described. A state of the art concerning electrodeposition of tin, selenium and SnSe establishes the current progress and the envisaged issues. An electrolyte solution is thus defined.

The second chapter defines the electrochemical bath preparation before tackling the electrodeposition conditions. All the methods of microstructural characterization are described. Systematic analyzes are performed at the defined conditions in this chapter. In order to complete our results, additional characterization methods are used. The operating principle and conditions are specified in this chapter.

The third chapter deals with the electrodeposition of SnSe films in continuous mode. After studying the different electrochemical systems, a deposition potential window can be defined. The influence of the potential on the film morphology and composition is investigated. The influence of the counter-electrode as well as of the electrodeposition time is briefly studied.

In order to improve the morphology and the crystallinity of the SnSe films, we study the impact of pulse electrodeposition in the fourth chapter. The electrodeposition conditions are defined. The pulse parameters are progressively optimized. The influence of the pulse duration on the morphology and composition of the films is investigated. Values of band gaps are determined and compared to those of the literature. An introduction to doping by copper is discussed in the end of the chapter.

The fifth and last chapter represents a prospect to these works. The electrodeposition of SnSe nanotubes and/or nanowires having never been reported, a state of the art concerning the electrodeposition of tin and selenium nanostructures is given. A review concerning the synthesis methods and properties of SnSe nanostructures provides supplementary information. The electrodeposition of the nanostructures is studied in continuous mode. The influence of the potential on the crystallinity, composition and morphology is established.

Introduction (Français)

Face à l'épuisement des énergies fossiles et l'émission de gaz à effet de serre, l'intérêt se porte sur de nouvelles alternatives prometteuses telles que la thermoélectricité. C'est un mode de production respectueux de l'environnement de par sa conversion directe de la chaleur en électricité, sans émission de gaz. Bien que le phénomène soit découvert au cours du XIX^{ème} siècle, la thermoélectricité connaît un engouement depuis les années 1990. Un matériau s'illustre très rapidement, Bi_2Te_3 et trouve son application majeure dans les modules Peltier, entre autres utilisé pour la réfrigération. Néanmoins, il subsiste un inconvénient majeur : le rendement de conversion. Pour optimiser ce rendement, plusieurs approches sont abordées. Parmi elles une approche consiste en l'amélioration de leurs performances en les nanostructurant. Une autre option est de travailler sur de nouveaux matériaux afin de tenter d'obtenir de meilleures propriétés que le matériau de référence.

Ma thèse s'inscrit dans le cadre du projet ANR 3DThermoNano dont la finalité est la conception d'un matériau tridimensionnel nanostructuré, pour une application de capteur autonome. L'intérêt majeur d'un tel objet est la combinaison de la stabilité mécanique, engendrée par la structure 3D avec la diminution de la conductivité thermique, liée à la nanostructuration. Son objectif général consiste en la synthèse de films thermoélectriques, éléments actifs de micro-générateur Peltier, permettant de transformer de la chaleur perdue en électricité.

Communément synthétisés sous formes massives, de plus en plus de matériaux thermoélectriques sont ainsi étudiés sous forme 0D, 1D ou 2D. En effet, des études théoriques et expérimentales démontrent une diminution considérable de la conductivité thermique avec la dimensionnalité du matériau. Bien que diverses méthodes physiques et chimiques puissent être employées, l'électrodéposition semble être une méthode particulièrement adaptée de par sa facilité de mise en œuvre, son faible coût et les vitesses de croissance modérées (typiquement de l'ordre de $10\text{ }\mu\text{m/h}$). Cette méthode permet également de contrôler la morphologie et la composition des dépôts.

Parmi les matériaux thermoélectriques d'intérêt, SnSe est un semiconducteur de type p possédant des éléments chimiques abondants et respectueux de l'environnement. Principalement étudié sous forme massive, plusieurs études le présentent comme un excellent candidat pour des applications en thermoélectricité. En effet, il affiche un coefficient Seebeck élevé et une faible conductivité thermique, lui conférant un facteur de mérite difficilement égalé par d'autres matériaux de 2,6 à 923 K. En revanche, il n'a été que très peu élaboré par électrodéposition et essentiellement étudié pour des applications photovoltaïques.

Ce mémoire de thèse se divise en cinq chapitres :

Le premier chapitre expose d'une part, de manière succincte, les principes fondamentaux de la thermoélectricité. Les propriétés physiques et chimiques de SnSe ainsi que les principales méthodes de synthèse sont également décrites. Un état de l'art concernant l'électrodéposition de l'étain, du sélénium et de SnSe établit les avancées actuelles et les problématiques envisagées. Une solution électrolytique est ainsi définie.

Le second chapitre définit la préparation du bain électrochimique avant d'aborder les conditions d'électrodéposition. L'ensemble des méthodes de caractérisation microstructurale sont décrites. Des analyses systématiques sont effectuées aux conditions définies dans ce chapitre. Afin de compléter nos résultats, des méthodes de caractérisation supplémentaires sont utilisées. Leur principe de fonctionnement et les conditions opératoires sont précisés dans ce chapitre.

Le troisième chapitre traite de l'électrodéposition des films de SnSe en mode continu. Après l'étude des différents systèmes électrochimiques, une fenêtre de potentiels de déposition peut être définie. L'influence du potentiel sur la morphologie et la composition des films est investiguée. L'influence de la contre-électrode ainsi que celle du temps d'électrodéposition est brièvement étudiée.

Dans un souci d'amélioration de la morphologie et de la cristallinité des films de SnSe, nous étudions l'impact de l'électrodéposition en mode impulsif dans le quatrième chapitre. Les conditions d'électrodéposition sont définies. Les paramètres impulsifs sont progressivement optimisés. L'influence du temps d'impulsion sur la morphologie et la composition des films est investiguée. Des valeurs de largeur de bandes interdites sont déterminées et comparées à celles de la littérature. Une introduction au dopage par le cuivre est également abordée en fin de chapitre.

Le cinquième et dernier chapitre représente une perspective à ces travaux. L'électrodéposition de nanotubes et/ou nanofils de SnSe n'ayant jamais été reportée, un état de l'art concernant l'électrodéposition de nanostructures d'étain et de sélénium est établi. Un panorama concernant les méthodes de synthèses et propriétés des nanostructures de SnSe apporte des informations complémentaires. L'électrodéposition des nanostructures est étudiée en mode continu. L'influence du potentiel sur la cristallinité, la composition et la morphologie est établie.

Chapter 1.

Fundamental concepts
and state of the art

Introduction

This chapter briefly exposes, in the first part, the principles of thermoelectricity, its interests, its applications as well as the characteristic physical parameters of the thermoelectric (TE) materials. Then, all families of the current TE materials are presented before focusing on the compound of interest of this work: SnSe. Thus, the second part deals with its crystal structure, as well as some of its TE properties, which are the origin of the interest in this material. A non-exhaustive review of the SnSe film synthesis techniques is also exposed. Finally, the third and last part concerns the presentation of the work from the literature dealing with electrodepositions of tin, selenium and tin selenide films and enables to establish the objectives and the challenges of the thesis.

Ce chapitre expose brièvement, en première partie, les principes de la thermoélectricité, ses intérêts, ses domaines d'applications ainsi que les paramètres physiques caractéristiques des matériaux thermoélectriques (TE). L'ensemble des familles des matériaux TE actuels est ensuite présenté avant de se focaliser sur le composé d'intérêt de ce travail: SnSe. Ainsi, la deuxième partie porte sur sa structure cristalline, de même que certaines de ses propriétés TE, qui sont à l'origine de l'intérêt pour ce matériau. Une revue non exhaustive des techniques de synthèse de films de SnSe est également exposée. Enfin, la troisième et dernière partie, concerne la présentation de travaux de la littérature portant sur l'électrodépositions de films d'étain, de sélénium et de sélénure d'étain et permet d'établir les objectifs et challenges de cette thèse.

I. What is thermoelectricity?

a. Explanation of the phenomena

Thermoelectricity is related to the direct conversion of electricity in a thermal flux and vice versa. We can distinguish three TE effects. The first one, discovered in 1821, called Seebeck effect is the most famous effect. During his experiment, Thomas Johann Seebeck showed that, by applying a temperature gradient between two different conductors linked to a compass, the needle is deviated from its initial position. This experiment let the scientist think about a magnetic effect, which was contradicted later. Indeed, when applying a thermal gradient dT (in K) between two opposite junctions of a material, a potential difference dV appears (in μV), whose value is proportional to the Seebeck coefficient S (in $\mu V.K^{-1}$), according to [equation 1.1](#). This effect is currently used for thermocouples.

$$dV = -S dT \quad 1.1$$

The second TE effect was discovered by Jean Charles Peltier, in 1834. He made the reverse experiment of Seebeck: applying an electrical current I (in A) has the consequence to generate or absorb a heat flux, called Q (in W), depending on the current direction, at the junction of two conductors (Figure 1.1). These physical quantities are proportional and lead to the Peltier coefficient, namely π (in V) (equation 1.2). The Peltier effect finds application for cooling.



Figure 1.1: Schematic representation of Peltier experiment

$$\pi = \frac{Q}{I} \quad 1.2$$

Finally, the third and last TE effect was studied by William Thomson. He showed that the two previous effects can be combined. If a material is submitted to an electrical field and to a temperature gradient, it exchanges heat with the external environment and vice versa (Figure 1.2).

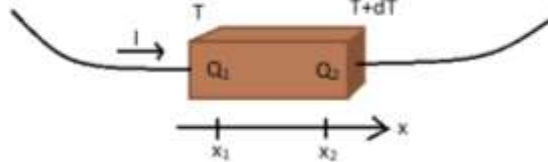


Figure 1.2: Representation of the Thomson effect

The thermal flux gradient is then given by the relation 1.3:

$$\frac{dQ}{dx} = -I \tau \frac{dT}{dx} \quad 1.3$$

Where x and τ are respectively the spatial coordinate (in m) and the Thomson coefficient (in V.K⁻¹).

Finally, the Seebeck, Peltier and Thomson coefficients are linked together according to the Kelvin equations 1.4 and 1.5:

$$\pi = S T \quad 1.4$$

$$\tau = T \frac{dS}{dT} \quad 1.5$$

b. Why thermoelectricity?

Thermoelectricity is a production mode of a green, sustainable and renewable energy. It has other advantages such as long lifetime and non-requirement of moving parts, which enables fabrication of small devices. A TE module, such as Peltier module is composed of pillars of two TE materials, one p-type and one n-type, which are electrically connected in series but thermally in derivation (Figure 1.3). When applying a current, a thermal gradient is generated according to the Peltier effect (Figure 1.1). It is thus interesting for cooling application, common application of the Peltier modules. But other devices are used in the electricity generation mode. The power of the TE device ranges from several μW to hundreds of μW for micro TE generators, to several W or dozens of W for modules. Radio-isotopic TE generators supplying space probe delivers power from tens of W to hundreds of W ^[1]. Thus, the TE generators are beneficial to recover the waste heat and convert it into electricity, which would reduce the energy consumption. Another example is the project envisaged by Renault Trucks to include TE modules in their vehicles in order to convert the heat flux at the exhaust of the reactor ^[2]. This project is still relevant, but not only for Renault, as mentioned in Liu's paper ^[3]. Current TE films are mostly used for micro TE generators or for wearable devices, including autonomous sensors ^[4].

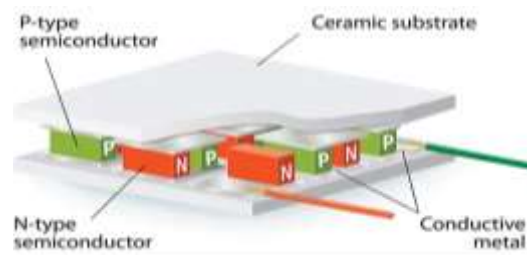


Figure 1.3: Schematic representation of a Peltier module ^[5]

c. How a thermoelectric material is characterized?

The performances of a TE material is defined by the figure of merit ZT ^[6]. This figure of merit depends on three variables according to the relation 1.6 :

$$ZT = \frac{S^2 T}{\rho \kappa} \quad 1.6$$

Where S , T , ρ and κ are the Seebeck coefficient (in V.K^{-1}), the temperature (in K), the electrical resistivity (in $\Omega.\text{m}$) and the thermal conductivity (in $\text{W.m}^{-1}.\text{K}^{-1}$) respectively. The Power Factor (PF) can be defined according to $S^2\sigma$, where σ is the electrical conductivity (in S.m^{-1}).

The sign of S is given by the type of the majority carriers in the material. Thus, for n-type semiconductor, electrons diffuse from the hottest side to the coldest (Figure 1.4). So S is negative. In the case the holes are the majority carriers, they move in the same direction of the temperature gradient, hence S is positive.



Figure 1.4: Direction of the electrons and temperature ^[7]

κ has two contributions: the first one is the electronic thermal conductivity, κ_e (equation 1.7) and the second one depends on the lattice structure (the phonon contribution), κ_l (equation 1.8).

$$\kappa_e = L \sigma T \quad 1.7$$

$$\kappa_l = \frac{1}{3} C v l \quad 1.8$$

where L is the Lorenz number, C , v and l are the specific heat, the speed of sound and the mean free path of the phonons.

According to relation 1.7, σ also influences the thermal conductivity. An increase in σ is impossible without increasing the electronic part of κ .

The conversion yield of a TE generator, depending on the dimensional Z value, is defined by the following relation 1.9:

$$\eta_{max} = \frac{T_H - T_C}{T_H} \times \frac{\sqrt{1 + Z\bar{T}} - 1}{\sqrt{1 + Z\bar{T}} + \frac{T_C}{T_H}} \quad 1.9$$

Where η_{max} , T_H , T_C \bar{T} and are respectively the maximum conversion yield, the temperature of the hot side, the temperature of the cold side and the average temperature.

The better the figure of merit is, the better the thermoelectric properties and the yield are. For Bi_2Te_3 and a ZT value of 1, the conversion yield is close to 10 %^[8]. With respect to [relation 1.6](#), a good TE compound should have a high S , a low ρ (or a high σ) and a weak κ . Thus, an insulator would not be a good thermoelectric material because of its high ρ . Moreover, a metal has a high κ so it could not be a good candidate. An ideal case would be to have a material with the electrical resistivity of a metal and the thermal conductivity of glass, as proposed by Slack with the so-called phonon glass electron single crystals concept^[9]. To optimize the value of ZT and so, the related power factor PF, it was shown that the best TE materials are doped semiconductors or semimetals ([Figure 1.5](#)) : maximum of ZT and PF is estimated at a charge carrier concentration of the order of 10^{19} to 10^{20} cm^{-3} .

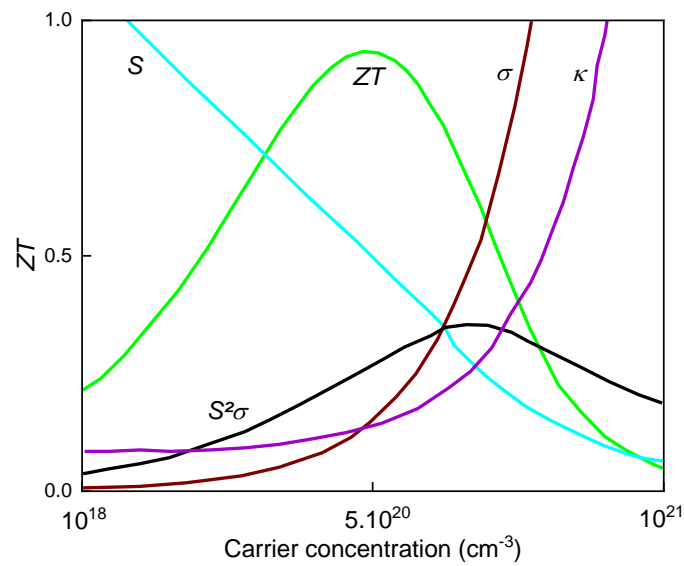


Figure 1.5: Variation of the TE parameters with the carrier concentration (adapted from ^[10])

d. Currently and recently studied materials

The reference material in thermoelectricity is Bi_2Te_3 for applications at room temperature. For a long time, researchers thought that it had the best value of the figure of merit at 300 K, around 1. This material, as well as its analogs (Sb_2Te_3 and Bi_2Se_3), are still commercialized both in n and p-type for RT applications. But for temperatures up to 450 K, other materials are needed. That is the reason why PbTe was used from temperature between 450 to 800 K. Then, SiGe replaced it, to increase the utilization temperature near 1300 K^[11].

The problems with several of these materials, specifically those containing Sb, Pb or Te, are their toxicity and their price^[12]. That is the reason why several research teams work on new TE materials which contain cheap, abundant and eco-friendlier elements in order to allow mass

production. Moreover, an objective for the thermoelectricity community would be to have a value of the figure of merit close to 3, allowing to have a competitive efficiency with current cooling technology [6]. Thus, different families of materials emerged such as skutterudites, clathrates, half-Heusler or silicides (Figure 1.6). Most of them are used at moderate temperature (400-800 K) and reveal better properties in p-type. Currently, the highest reported value is about 2.6 around 850 K for chalcogenides [13]. The family of the IV-VI semiconductors seems to show good properties [14,15], in particular metal chalcogenides are good candidates for photovoltaic, optoelectronic and thermoelectric applications. Among them, SnSe is a narrow gap p-type semiconductor, with constituting elements more abundant and less toxic than Te, Sb and Pb. Thanks to its crystal structure, SnSe benefits from a low κ and a high S is expected [16]. This material, relatively non-toxic and abundant in comparison with Bi_2Te_3 is thus interesting for TE applications. That is the reason why we decided to study SnSe.

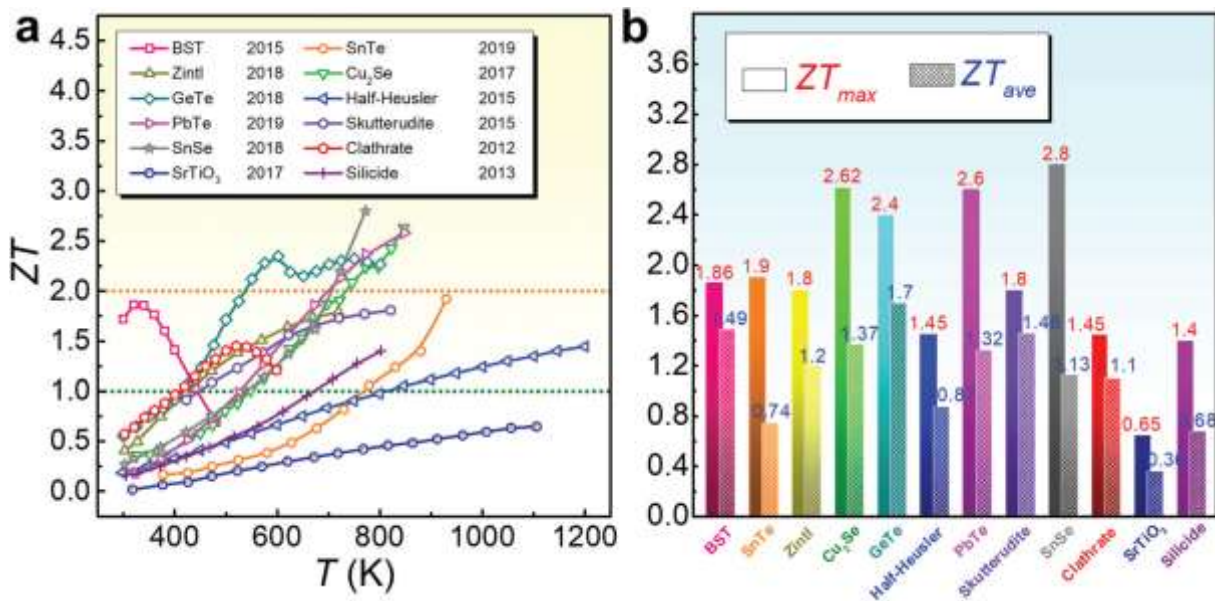


Figure 1.6: (a) Temperature dependence of ZT values for several representative families of TE materials and (b) maximum (ZT_{max}) and average (ZT_{ave}) ZT values [17]

- ✓ Thermoelectricity is a green source of electricity produced from waste heat.
- ✓ The figure of merit characterizes the TE materials thanks to S , σ and κ .
- ✓ The best TE material should have high S and σ but low κ .
- ✓ A compromise is the use of semimetals or degenerate semiconductors.
- ✓ Current materials are expensive and toxic for applications at RT. Thus SnSe appears as an alternative and promising material.

II. Description of SnSe

a. Phase diagram

To understand the thermodynamics and assure good sample preparation, it is important to study the binary Sn-Se phase diagram (Figure 1.7). SnSe has a high melting point (874 °C) and exists in two phases, namely α and β , both crystallizing in an orthorhombic structure. More stable performances are obtained with the α phase [18]. In the Sn-SnSe region, a liquid miscibility gap as well as an eutectic reaction can be found (reaction 1.10).

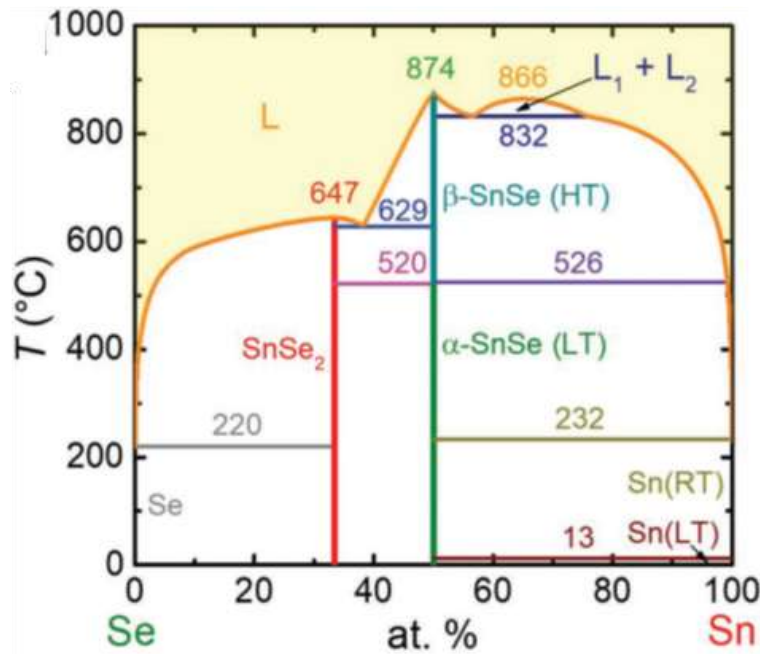
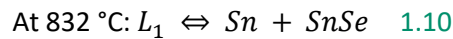
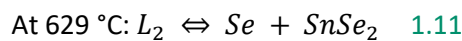


Figure 1.7: Phase diagram of Sn-Se [18]



Since the eutectic point is close to pure Sn, it is not surprising to find Sn as secondary phase when Sn excess was used to prepare the sample. The phase diagram shows the presence of another phase which is SnSe₂, made under Se excess. As mentioned by the authors, another eutectic point can be found in the SnSe₂-Se region, which can lead to Se as secondary phase since close to pure Se (reaction 1.11):



b. Crystal structure

SnSe is known to crystallize in an orthorhombic, derived from a 3D distortion of the rock-salt structure type ($Pnma$ space group). A cubic structure has also been reported in nanocrystalline samples and thin films ^[19]. The calculated lattice parameters are $a = 11.570 \text{ \AA}$ $b = 4.190 \text{ \AA}$ $c = 4.460 \text{ \AA}$ ^[20]. A transition to a distorted orthorhombic structure can be observed at around 800 K ^[21]. The distorted structure would be due to the 5s electrons of tin. The unit cell is composed of 8 atoms with two adjacent layers which are orthogonal to the longest axis (Figure 1.8). The 5s electron pair of tin, influences the structure of the double layer, resulting in an influence on the phonons and consequently on the thermoelectric properties ^[14].

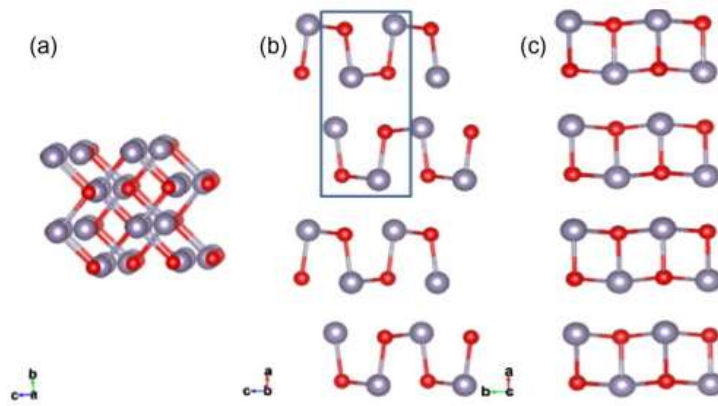


Figure 1.8: Crystal structure of SnSe, respectively along the a , b and c axis ^[20]

c. Electronic configuration

The growing interest in chalcogenides as candidates for TE applications is first related to their predicted narrow band gap. Indeed, semiconductors have a band gap between 1 and 2 eV and metal chalcogenides are well known by their applications in photovoltaic cells.

SnSe is a p-type semiconductor, for which different and opposite trends are observed in the literature data. Films were reported to have a direct band gap, generally ranging from 0.81 to 1.36 eV, according to UV-visible spectroscopy determinations ^[22–27], whereas indirect band gaps were also determined, with experimental values varying from 0.85 to 1.20 eV ^[24,25,28]. Engelken *et al.* demonstrated an increase of the bandgap with the annealing ^[24], confirmed by El-Menawy *et al.* who obtained very high values from 2.24 et 2.77 eV ^[27]. They also obtained high indirect bandgaps varying from 1.36 et 1.70 eV. This phenomenon is both related to an increase of the crystallinity and partial transformation into SnSe₂. However another work showed high values of 1.95 eV and 1.11 eV for the

direct and indirect bandgaps respectively ^[29]. According to Shikha *et al.* and Ananthi *et al.*, the bandgap is also influenced by the grain size. Thus a decrease of E_g was observed with an increase of the grain size ^[30,31].

Theoretical calculations using DFT were also made and revealed direct and indirect gaps respectively around 0.914 and 0.85 eV ^[6,32]. These values are in agreement with the lowest experimental ones. The gaps can differ, depending on the dimensionality of the samples (Table 1.1). Thus, we can expect an evolution of the gaps with the thickness of the films, which can explain the wide range of values found in the literature. According to the table, decreasing the dimensionality tends to increase the gaps.

	Single layer	Double layer	Bulk	Nanowires	Nanosheets	Nanoflowers	Nanocrystals	Nanoplates
Direct gap (eV)	1.66 0.92	1.62	1.3	1.03	1.10	1.05	1.71	1.74
Indirect gap (eV)	1.63 0.77	1.47	0.9	0.92	0.86	0.95	X	0.93
Reference	[33,34]	[33]	[35]	[36]	[37]	[37]	[38]	[39]

Table 1.1: Reported band gaps for different dimensionalities (the blue values were obtained using DFT calculations)

Sn and Se having respectively as electronic configurations $[\text{Kr}] 4d^{10} 5s^2 5p^2$ and $[\text{Ar}] 3d^{10} 4s^2 4p^4$, the total density of state of SnSe reveals a strong influence of the 5p orbitals of Sn and 4p orbitals of Se Figure 1.9 a. Because S and σ are related to the band structure, the latter was calculated by the DFT method. SnSe was found to have both direct and indirect band gaps as shown in the band structure represented in Figure 1.9 b. Indeed, the valence band maximum (VBM) is observed along the $\Gamma - Y$ whereas the conduction band minimum (CBM) is observed along the $\Gamma - X$ direction. We can also observe the presence of flat bands in the valence band, near the Γ lines which are opposed to dispersive CBM. This feature is interesting for TE applications because it leads to a weak distribution of the energies on the flat band and an important speed of the carriers on the dispersive band. These properties are in favor with high Seebeck coefficient and high electrical conductivity.

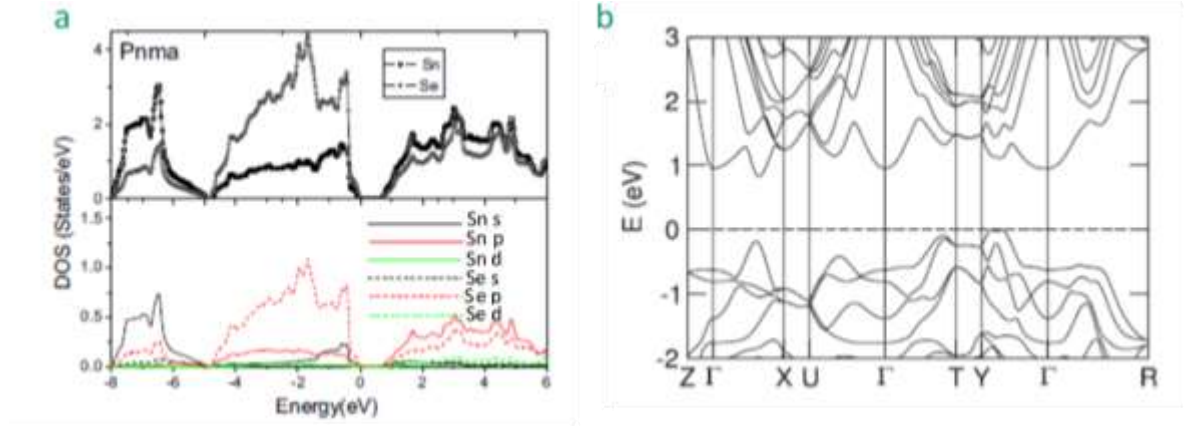


Figure 1.9: (a) Density of states ^[40] and (b) band structure of SnSe ^[41]

d. Thermoelectric properties

As previously mentioned, SnSe exhibits interesting TE properties due to low κ and high S . Moreover, as mentioned by Zhao *et al.*, SnSe is composed of $5s^2$ lone pair of tin which induces distorted rock salt structure type and thus anisotropic TE properties ^[16]. That is the reason why ρ , S and κ were measured along the three crystallographic axes (Figure 1.10). In particular, the TE properties differ along the a axis compared to b and c axes.

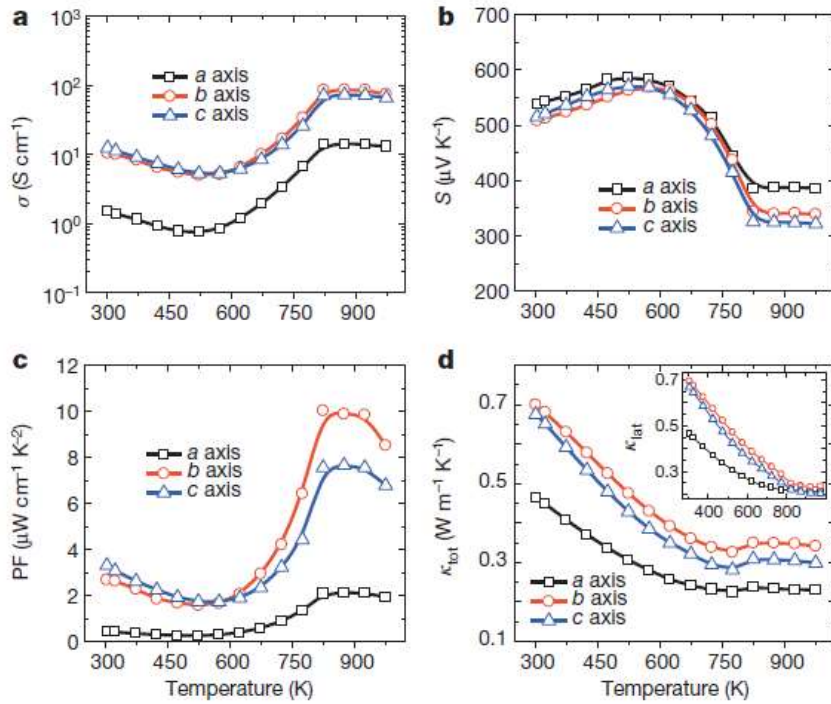


Figure 1.10: Thermoelectric properties of SnSe single crystal: (a) electrical conductivity, (b) Seebeck coefficient, (c) Power Factor and (d) total thermal conductivity ^[16]

The values of S along the three axes are close and positive, that means SnSe is a p-type semiconductor (Figure 1.10 b). Moreover, this coefficient is high, with a minimum of $320 \mu\text{V.K}^{-1}$ near 900 K. It increases from RT to 525 K, which makes it very interesting for room temperature (RT) applications. Then the slope change is due to the activation of another carrier pocket (multiple disk-shaped constant energy surface ^[42]). A plateau is observed from the phase transition at 800 K.

The power factor slightly evolves along the a axis with the temperature whereas it evolves from 3 to $10 \mu\text{W.cm}^{-1}.\text{K}^{-1}$ along the other axes (Figure 1.10 c). This low power factor is strongly influenced by the low electrical conductivity and can be increased by doping SnSe.

Globally, the main interest in SnSe concerns its unexpected low thermal conductivity. κ decreases until 800 K and is weak even from RT (Figure 1.10 d). At RT κ is about $0.5 \text{ W.m}^{-1}.\text{K}^{-1}$ for the a axis against $0.7 \text{ W.m}^{-1}.\text{K}^{-1}$ for b and c axes. Thanks to the whole results, we can expect a value of the figure of merit of about 0.15 at RT, along the b and c axes. Sassi *et al.* obtained a similar trend, with κ decreasing until $0.5 \text{ W.m}^{-1}.\text{K}^{-1}$ from 500 K ^[21]. They noticed that lower values are obtained for single crystals. It is unexpected since polycrystalline samples contain grains boundaries which thus induce more phonon scattering. Whatever the crystallinity, κ is lower than that of Bi_2Te_3 , which confirms our interest in this compound.

For a single crystal, the electrical conductivity decreases from 300 to 525 K, which means that, in this range of temperature, SnSe has a metallic behavior (Figure 1.10 a). Then, σ increases, until the plateau at 800 K, which means that SnSe has a semiconductor behavior from 525 to 800 K. The change of slope at 525 K is due to the thermal excitation of carriers and the change at 800 K is due to a phase transition (from $P n m a$ to $C m c m$). Different behaviors on the electrical conductivity have been observed in the literature according to the microstructure. Indeed, it has been established that the semiconducting behavior depends on the nature of the studied sample (bulk, polycrystalline or single crystal). Polycrystalline bulks show a semiconducting behavior from RT to around 400 K and a small decrease of σ at about 500 K, which quickly increases afterwards ^[21,43–45].

Finally, Lv *et al.* have studied the influence of the stoichiometry on the thermoelectric properties ^[43]: the electrical conductivity is higher for a Se enrichment. A deviation from the stoichiometry seems to always benefit for the electrical conductivity compared to the stoichiometric polycrystalline SnSe. Moreover, the Seebeck coefficient is stabilized at about $250 \mu\text{V.K}^{-1}$ for an overstoichiometry in Se. An understoichiometry in Se decreases the Seebeck coefficient, leading to a n-type semiconductor. An increase in the understoichiometry of Se tends to increase the thermal conductivity.

- ✓ SnSe is expected to crystallize in a orthorhombic structure ($P n m a$ space group)
- ✓ SnSe is known to have an indirect and a direct gap of 0.9 and 1.3 eV for bulk
- ✓ SnSe has anisotropic properties:
 - Maximum S is close to $500 \mu\text{V.K}^{-1}$ at RT
 - κ is low (between 0.45 and $0.7 \text{ W.m}^{-1}.\text{K}^{-1}$ at RT)
 - σ is low and its behavior depends on the crystallinity (film or bulk, poly or single crystal)

Thanks to theoretical ^[46] and experimental findings ^[47], it is well known in the community that decreasing the dimensionality contributes to a decrease of the thermal conductivity by increasing the scattering of phonon. That is the reason why SnSe films are promising. Moreover, recently, Al-Alam *et al.* predicted a decrease of κ for film thicknesses lower than $1 \mu\text{m}$ ^[48]. It was confirmed by Burton *et al.* who experimentally obtained κ lower than $0.1 \text{ W.m}^{-1}.\text{K}^{-1}$ ^[49]. Another interest in fabricating SnSe films is the waste heat recovery in microsystems and thermal regulation. Thus, this thesis focused on the synthesis and characterization of SnSe films for that application.

III. Different ways of SnSe films synthesis

The main works devoted to SnSe concern bulk samples for their TE and photovoltaic properties. On the contrary, few studies focus on films. Among the films synthesis techniques, the most frequently used are Chemical Vapor Deposition (CVD), Physical Vapor Deposition (PVD), thermal evaporation and Atomic Layer Deposition (ALD). The choice of a technique is very important because the properties are highly dependent on the growth process ^[50].

a. Dry deposition methods

A first physical technique is the Pulsed Laser Deposition (PLD). Suen *et al.* investigated the influence of the temperature and deposition angle on silicon substrates ^[51]. Using normal angle, they obtained 730 nm thick films crystallized in the orthorhombic structure with preferred growth directions along the a axis. The samples made with a glancing angle do not show preferential growth and have a thickness of 300 nm. At normal angle, the films are compact and smooth whereas those

synthesized at a glancing angle are composed of nanopillars and non-compact. The grain size also changes with the configuration from 730 nm for the large grains to 120 nm for the nanopillars. However, S and σ were found to be higher for the films made at a glancing angle with maximum values of $498.5 \mu\text{V.K}^{-1}$ at 426 K and about 275 S.cm^{-1} at 575 K. These results are surprisingly higher than those obtained on bulk. Moreover, it is surprising to get a better σ for non-compact films than bulk SnSe. They measured a κ value of $0.189 \text{ W.m}^{-1}.\text{K}^{-1}$ at 340 K.

A similar study was made by Saini *et al.* ^[52], who performed PLD on sapphire substrates with different crystallographic orientations, namely r -, a - and c - of the rhombohedral crystal structure. On $r\text{-Al}_2\text{O}_3$ and $a\text{-Al}_2\text{O}_3$, the films exhibit orthorhombic structures close to single crystal whereas those made on $c\text{-Al}_2\text{O}_3$ substrate are polycrystalline. All films were found to have a thickness of 400 nm. On the $r\text{-Al}_2\text{O}_3$ substrate, the grains are smaller, 200 nm large and highly connected, whereas on $a\text{-Al}_2\text{O}_3$, they are randomly connected. Films grown on the $c\text{-Al}_2\text{O}_3$ substrate revealed grain size of 300 nm. XPS analyses of the films confirmed the presence of Sn(II) and Se(-II), with atomic ratio of 1.1:0.9. The TE properties were generally better for the films grown on the $r\text{-Al}_2\text{O}_3$. Indeed, the maximum S and σ obtained were of $264 \mu\text{V.K}^{-1}$ and 28.3 S.cm^{-1} at 800 K, whereas κ at RT was of $0.35 \text{ W.m}^{-1}.\text{K}^{-1}$. The ZT at 800 K was determined to be equal to 0.45.

Teghil *et al.* performed laser ablation on SnSe pellets ^[53]. SrTiO_3 , MgO and glass substrates were either heated at 293 K or at 423 K to manage the epitaxial growth of SnSe films. The XRD showed that the films made at 423 K on SrTiO_3 and MgO were preferentially grown with the (100) plane and crystallized in the orthorhombic structure. The films made at RT exhibit the (011) preferential orientation. The films made on glass substrates were not crystalline, indicating the close dependence between the substrate crystallinity and the resulting SnSe film crystallinity for this growth mode. The crystalline films have a smooth morphology and a Sn:Se ratio close to 1:1.

ALD was used by Drozd *et al.* for the synthesis of SnSe films ^[54]. The authors tested the influence the deposition temperature. The morphology was found to become rougher by increasing the temperature but spherical particles with diameter of 200 nm were found. A band gap of 1.15 eV was obtained.

SnSe films were grown by Molecular Beam Epitaxy (MBE) on Bi_2Se_3 films, previously grown on SrTiO_3 substrates at 300 °C ^[55]. The XRD showed an additional peak after the deposition of SnSe related to the (111) plane in the orthorhombic structure. HRTEM and STM showed flat interface between SnSe and Bi_2Se_3 in agreement with successful epitaxial growth. Using Angle-Resolved PhotoEmission Spectroscopy (ARPES), they found that SnSe was electron-doped, because of Se vacancies as often observed for selenides.

Singh and Bedi made SnSe films thanks to the Hot Wall Epitaxy Technique (HWE) at different temperatures ^[56]. The XRD analyses exhibit polycrystalline deposits, indexed into the orthorhombic structure and with the (111) preferential plane. The SEM images show long grains whose size increases with the substrates temperature, from 0.5 to 3.8 μm . The authors noticed that films peeled off when the temperature exceeded 568 K. The films resistivity was found to decrease with their thickness. Moreover, the mobility and carrier concentration increase with the temperature. Finally, they measured a direct bandgap of 1.2 eV.

PVD was used from SnSe powder to obtain SnSe nanoplates ^[57]. The plates exhibit side lengths of about 10 μm and thicknesses close to 20 nm. They were found to crystallize in the well-known orthorhombic structure of SnSe, with preferential growth normal to the (100) plane. Gao *et al.* made similar experiments with “Narrow Gap PVD”, using SiO_2/Si as substrate and applied a temperature of 800 °C but they also studied the substitution of Se by S at different atomic ratios ^[58]. In their work, the powder was put on a SiO_2/Si substrate and covered by another one, which enables the immediate sublimation of the powder. The samples lengths varied from 5 to 80 μm and were found to crystallized in the previously mentioned crystal structure, with preferential growth normal to the (100) plane. Their photocurrent measurements also confirm the anisotropic properties of such compounds.

Another used physical route is reactive evaporation, in which tin and selenium were simultaneously evaporated at 523 K and deposited on glass substrate ^[59]. The XRD analysis confirmed the polycrystallinity of the deposits and from the Debye-Scherrer equation, a crystallite size of 52 nm was determined. John *et al.*, who made films using the same technique showed a preferential growth, perpendicular to the (100) direction for a temperature of 553 K and higher ^[60]. The deposits exhibit a thickness close to 180 nm. Both analyses suggest a pure SnSe deposit. Moreover, the composition determined from XPS was found to be close to 1:1. UV-Vis-NIR spectrophotometry was used to determine a direct bandgap of 1.2 eV, very close to that of John *et al.*. The authors also determined the TE properties. Using Hall effect they obtained a hole concentration of $8.7 \times 10^{16} \text{ cm}^{-3}$ and a hole mobility of $10.8 \text{ cm}^2 \cdot \text{V}^{-1} \cdot \text{s}^{-1}$ at RT. σ was found to be $0.15 \text{ S} \cdot \text{cm}^{-1}$. The increase of σ with the temperature confirmed the semiconducting behavior of SnSe. Furthermore, the first heating-cooling cycle was found to modify the electrical properties, due to the removal of initial defects generated from the evaporation process and so acts as an annealing effect. At RT, S and κ were about $231 \mu\text{V} \cdot \text{K}^{-1}$ and $0.045 \text{ W} \cdot \text{m}^{-1} \cdot \text{K}^{-1}$ respectively. This low thermal conductivity is surprising and one of the lowest values obtained for SnSe. Finally, their work indicates that this material has a photoconducting nature and is thus interesting for photovoltaic applications.

Similarly, flash evaporation was employed from SnSe ingots^[61]. The deposition was carried out on glass substrates at different temperatures from 303 to 513 K. At temperatures lower than 513 K, the films exhibit Se excess as well as SnSe preferentially oriented along the (111) plane. The presence of SnSe₂ as a secondary phase was observed, which decreases by increasing the temperature. At 513 K, SnSe is preferentially oriented along the (100) plane and SnSe₂ totally disappeared. The deposits show needle-like grains with size increasing with the deposition temperature from 250 to 350 nm and the thickness varied from 150 to 300 nm. Optical measurements made on the sample synthesized at 513 K show a direct bandgap of 1.26 eV. For this range of deposition temperature, the deposits exhibit resistivity from 0.006 to 0.12 S.cm⁻¹. On samples made with thicknesses from 150 to 300 nm, σ varied from 0.033 to 0.12 S.cm⁻¹.

Recently, Burton *et al.* took advantage of thermal evaporation technique^[49]. The obtained films had orthorhombic crystal structure with preferred orientations along the (111) plane and also the (011). The authors suggest this preferred orientation is promoted by energetic interactions with the SiO₂ substrate. The SEM analysis shows that the films are “a network of porous nanosheets” in which we can recognize needle-like grains. Their thickness is around 75 nm. The EDS revealed the presence of oxygen which can either be explained by the presence of secondary phases such as SnO₂ or Sn(SeO₃)₂ or the glass substrate. The Si substrate was detected by EDS as a consequence of the limited thickness of the layer. XPS analysis do not show the presence of Sn(IV) or Se(IV). Thus, SnO₂ and Sn(SeO₃)₂ phases were excluded. A Sn:Se atomic ratio of 1.7:1 was determined by XPS. Furthermore, the thermoelectric properties were measured. At RT, S is higher than 600 $\mu\text{V.K}^{-1}$ and one of the highest obtained value for SnSe films. σ was found to be lower than other polycrystalline SnSe but κ was found to be close to 0.1 W.m⁻¹.K⁻¹ at RT. Finally, post annealing treatment at 611 K was found to decrease S and increase σ .

Sabli *et al.* studied the effect of Argon Gas Condensation (AGC) to thermal evaporation^[62]. The films exhibit polycrystallinity in the orthorhombic structure with preferred orientation along the (111) plane. According to Debye-Scherrer equation, they determined bigger crystallite size using AGC. Thicker 20.8 nm flakes were obtained with AGC in comparison with 18.4 nm flakes without AGC. The effect of the AGC was also observed on the optical properties since the value of the direct bandgap decreases from 1.26 eV without AGC to 1.19 eV with AGC.

Fernandes *et al.* performed selenization of Sn layers deposited by DC-magnetron sputtering on soda lime glass and studied the influence of the selenization temperature^[63]. For temperatures set from 300 to 470 °C, the samples contain almost twice Se than Sn whereas for 530 and 570 °C, the Sn:Se ratio is close to 1:1. The XRD analyses showed the presence of SnSe₂ crystallized in an hexagonal

structure ($P\bar{3}m1$ space group) for the first series and only the presence of SnSe for the two last temperatures, crystallized in the orthorhombic structure. A preferred orientation along the (100) plane was found. For these temperatures, the deposits exhibit compact, smooth morphology with large grains which is suitable for the electrical properties. Finally, they determined an indirect bandgap of 0.95 eV and a direct one of 1.15 eV.

Electron Beam Evaporation was used to deposit SnSe amorphous films on silver coated glass substrates and at RT ^[64]. The authors specifically showed the interest in SnSe for switching memory application.

CVD was used for the deposition of SnSe and SnSe₂ ^[65]. The authors studied the deposition on bottom and top glass substrates heated at different temperatures from 400 to 650 °C. On the bottom substrates, black-silver films could be deposited at a temperature above 550 °C whereas on the top substrates, depositions could be possible from 350 °C. The films made on the top substrates contain plate-like grains, with composition close to SnSe₂ for temperatures in the range from 400 to 550 °C. For the films made at 400 °C, the composition was close to SnSe_{1.5}. The XRD analyses confirmed the presence of the SnSe₂ phase with a preferred orientation along the (001) axis. On the bottom substrates, the same plate-like grains with a Se excess was found. The samples made at 650 °C exhibit the stoichiometry corresponding to SnSe. This, in agreement with their XRD and Raman analyses, highlighted the coformation of SnSe and SnSe₂. Indeed, XRD showed SnSe₂ with preferred orientation along the (001) axis for all the temperatures deposition except at 650 °C, whose films were indexed in SnSe structure. Raman spectroscopy only showed SnSe₂ phase, except at 650 °C which showed both phases. XPS analyses confirmed the signature of SnSe but not SnSe₂.

The main properties of SnSe films elaborated by dry deposition methods are summarized in [Table 1.2](#).

Chapter 1. Fundamental concepts and state of the art

Synthesis method	Preferential growth direction	Secondary phase	Grains typical morphology	Grain size (μm)	σ_{max}/σ_{RT} (S.cm^{-1})	S_{max}/S_{RT} ($\mu\text{V.K}^{-1}$)	κ_{min}/κ_{RT} ($\text{W.m}^{-1}.\text{K}^{-1}$)	E_g (eV)	Reference
PLD	<i>a</i> axis	No	Compact + smooth	0.73	$\sim 148/\sim 0$	193.7/x	$\sim 0.137/\sim 0.159$	No	[51] [52]
	No	No	Nanopillars	0.12	$\sim 275/\sim 25$	498.5/x	$\sim 0.123/\sim 0.162$	No	
	<i>a</i> axis	No	Plate/sphere	0.2-0.3	28.3/2.54	264/4.1	x/0.35	No	
Laser ablation	$\perp (100) + (011)$	No	Smooth	?	No	No	No	No	[53]
ALD	No	No	Spherical	0.2	No	No	No	1.15	[54]
MBE	$\perp (111)$	No	« islands »	No	No	No	No	No	[55]
HWE	$\perp (111)$	No	Needles?	0.5-3.8	?	No	No	1.2	[56]
PVD	$\perp (100)$	No	Nanoplates	10	No	No	No	No	[57][66][58]
	No	No	Nanoflakes	8	No	No	No	No	
	$\perp (100)$	No	Nanosheets	5-80	No	No	No	No	
Reactive Evaporation	$\perp (100)$	No	No	0.052	x/0.15	7863/231	0.023/0.045	1.2	[59][60]
		No	No	No	No	No	No	1.21	
Flash evaporation	$\perp (111) + (100)$	SnSe ₂ + No (T dependent)	Needles	0.25-0.35	0.006/0.12	No	No	1.26	[61]
Thermal evaporation	$\perp (111) + (011)$	No	Needles	0.075	0.05/4.9	630/700	0.05/0.08	No	[49]
Thermal evaporation (+AGC)	$\perp (111)$	No	Nanoflakes	0.0184-0.0208	No	No	No	1.19-1.26	[62]
DC magnetron sputtering + selenization	Major SnSe ₂ Or SnSe (100) (T dependent)	SnSe ₂	Disk-like to compact	No	No	No	No	0.95 (indirect) 1.15 (direct)	[63]
Electron Beam Evaporation	?	?	?	?	No	No	No	No	[64]
CVD	Major SnSe ₂ or SnSe (100)	SnSe ₂	Plate-like	10-80	No	No	No	No	[65]

Table 1.2: Summary of the main properties of deposited SnSe films by dry deposition methods

- ✓ SnSe commonly crystallizes in a orthorhombic structure ($Pnm2_1$ space group) with (100) preferential plane for PVD/PLD techniques instead of (111) for evaporation techniques and (100) at higher temperature
- ✓ SnSe₂ is occasionally co-synthesized (evaporation and CVD)
- ✓ Wide variety of thicknesses and grain sizes are obtained but they might be lower for evaporation, generally until hundreds of nm
- ✓ Indirect gaps are observed ranging from 1.15 to 1.26 eV
- ✓ The stoichiometry is close to 1:1 but Se excess is generally obtained using evaporation instead of Sn excess for PVD, PLD...
- ✓ Variable TE properties are measured : S values are between 230 and 600 $\mu\text{V.K}^{-1}$ at RT and κ between 0.045 and 0.35 $\text{W.m}^{-1}.\text{K}^{-1}$ at RT. Very low σ values are obtained at RT, between 0.033 and 25 S.cm^{-1} .

b. Wet synthesis methods

SnSe films have also been synthesized by spray pyrolysis as a minority phase, at different temperatures [67,68]. Indeed, it was shown that under a temperature of 200 °C, there were several unidentified phases and over 200 °C, the majority phase was SnSe₂, in presence of SnSe and SeO₂. Above 375 °C, the films exhibit low crystallinity due to volatility of Se. The grain size increases with the temperature from 14.96 to 19.48 nm. On the contrary, the thickness decreases from 7.5 to 3.6 μm .

SnSe nanosheets were made from a colloidal route [37] from SnCl₄, SeO₂, oleylamine (C₁₈H₃₅NH₂, reductant and capping agent) and phenanthroline (morphology control agent). The nanosheets were obtained with lateral size close to 300 nm and thickness close to 1 nm. HRTEM revealed the single crystallinity of the nanosheets with the (011) plane orientation of the orthorhombic structure. EDS analyses showed a Sn:Se ratio close to 1:1. The authors studied the influence of the addition of phenanthroline. The formation of nanoflowers is obtained from nanosheets when no phenanthroline is added. The nanoflowers with diameter about 1.2 μm , are (100) single crystalline oriented.

Pejova *et al.* used Chemical Bath Deposition (CBD) from SnCl₂ and SeSO₃²⁻, in presence of EthyleneDiamineTetraacetic Acid (EDTA) to prevent the hydrolysis of tin [28]. According to the XRD analyses, they obtained SnSe pure deposits, crystallized in the orthorhombic structure. Annealing was performed at 150 °C during 1 hour and has the consequence to increase the lattice parameters and the crystallite size from 14.8 to 23.3 nm. Finally, they determined the indirect and direct bandgaps of

as-deposited and annealed films, using UV-Vis-NIR spectroscopy. Shifts occurred from 1.20 eV and 1.74 eV for the as-deposited films to 1.10 eV and 1.65 eV for annealed films.

Finally, it should be noticed that a similar technique to electrodeposition was employed by Subramanian *et al.*, called the brush plating technique, also defined as Dalic process ^[69]. For that, an electrolyte solution was composed of SnCl_2 and SeO_2 , acidified at a pH of 1.5. Tin oxide coated substrates were considered as cathode. The anode was a stylus, consisting in carbon rod wrapped in cotton wool. The depositions were carried out at RT, 50 and 60 °C and voltages were applied between 2 and 8 V. The authors kept a SnCl_2 concentration of 5 mM but modified that of SeO_2 , from 1 mM to 2 mM then to 3 mM. The film color changed from pale red to steel gray and then red, but no explanation was given. They found that the optimum applied voltage was 5 V for concentrations leading to the steel gray color. At higher voltage, the deposits exhibit gray color, corresponding to tin rich films, and peel off. For a plating voltage of 5 V, a temperature of 50 °C and a deposition time of 4 minutes, the deposits exhibit polycrystalline structure into the orthorhombic structure with the (111) preferential orientation. The temperature of 50 °C enables the formation of smooth and uniform deposits whereas at higher temperatures, the deposits show selenium particles. On the best deposits, a thickness of 1.2 μm was calculated and closely packed grains were observed by SEM, with size around 0.3 μm . An indirect gap of 1.0 eV was measured.

- ✓ According to the chemical route, SnSe crystallizes in a orthorhombic structure ($P n m a$ space group) with (011), (100) or (111) preferential orientation
- ✓ Secondary phases are possible, such as SnSe_2 but the stoichiometry is close to 1:1
- ✓ Variable thicknesses and grain sizes are obtained depending on the experimental setup.
- ✓ Indirect gaps are measured with a large range of values: 1.20 eV for CBD and 1.0 eV for brush plating
- ✓ Few chemical synthesis were made with no TE characterizations
- ✓ By comparing with physical methods, smaller grains size and higher thicknesses are generally obtained using chemical methods

IV. Electrodeposition of SnSe

As reviewed in the previous section, the conventional methods to synthesize SnSe films are thermal evaporation ^[59], CBD ^[28], PLD ^[51] and spray pyrolysis ^[67]. In an objective to combine low cost, simple processing, moderate growth rate and good crystallinity, the method of electrodeposition was chosen as an alternative. This technique enables synthesis in various media, aqueous or organic solvent as well as from RT to higher temperature. The morphology, the thickness and the composition of the films can be controlled by adjusting the deposition parameters. This method has already been applied to synthesize semiconductors, specifically TE materials ^[70]. Furthermore, this technique is interesting since both shape and thickness can be adapted to the final application, such as wearable energy harvesting ^[4]. In order to have a better understanding, we have firstly studied the individual electrochemical systems of tin and selenium, before reviewing the studies of electrodeposition of SnSe films.

a. Electrodeposition of Sn

The tin Pourbaix diagram (Figure 1.11) shows a large stability zone along a wide range of pH for Sn(0). It can be oxidized into Sn²⁺ and Sn⁴⁺ but the latter is less stable ($\Delta G^0 = +2.72 \text{ kJ.mol}^{-1}$) than Sn(II) ($\Delta G^0 = -26.27 \text{ kJ.mol}^{-1}$). Another information is that tin hydroxides are less stable than tin oxides, that is the reason why they are not represented in this diagram. Moreover, Sn can be oxidized at a pH between 2 and 12, into SnO₂, which is the predominant phase ^[71]. Furthermore, SnO₂ was shown to be hardly dissolvable, except in presence of HCl and under heating ^[72]. SnO₂ is completely dissolvable in a solution containing 10 % of HCl at 90°C during 15 min ^[73]. The tin deposition is below the stability domain of hydrogen so the formation of H₂ can be observed. House *et al.* have shown that the formation of SnCl₄²⁻ and SnCl₆²⁻ leads to a decrease of the predominance zone of SnO₂ and unfortunately of Sn(0). The increase of the temperature tends to increase the redox potential of Sn(IV)/Sn(II).

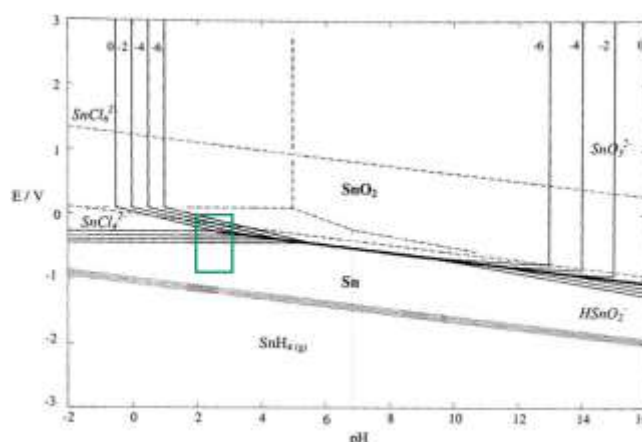


Figure 1.11: Pourbaix diagram of tin in chloride medium. The green rectangle corresponds to the pH area of this work [72]

Conventional electrochemical baths from Sn(IV) (stannic) salts are alkaline. From tin-lead plating, they can also be composed of fluoroborate or methanesulfonic acid (MSA) [74,75]. To the best of our knowledge, few articles reported the electrodeposition of pure tin films from a bath containing Na_2SnO_3 in NaOH medium. Sorbitol ($\text{C}_6\text{H}_{14}\text{O}_6$) can eventually be present as additive to improve the quality of the deposit, while the bath is stable without additives [76,77]. Compact and smooth deposits, crystallized in the tetragonal structure (β phase) were obtained in pulse mode. The porosity increases with the applied current density (Figure 1.12). The absolute current densities compared to those observed in Sn(II) (stannous) acidic media are weaker [78]. Moreover, the reduction of Sn(IV) into Sn(0) is a 4 electron reaction whereas the reduction of Sn(II) into Sn(0) is 2 electron reaction. Thus the electrodeposition of Sn from Sn(IV) requires a stronger energetic consumption. This might be the reason why tin electrodeposition is generally carried out from stannous baths.

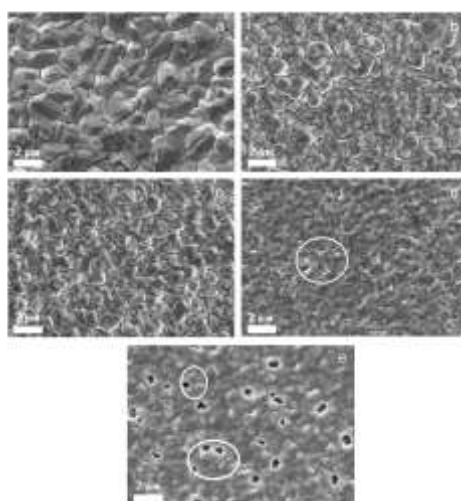
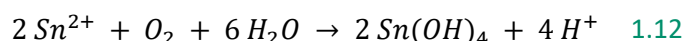
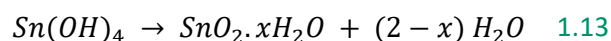


Figure 1.12: SEM images of pulse electrodeposited tin films from an electrolyte solution containing 0.34 M of Na_2SnO_3 and 0.38 M of NaOH at : (a) 0.1, (b) 0.2, (c) 0.3, (d) 0.4 and (e) 0.5 $\text{A}\cdot\text{cm}^{-2}$ [76]

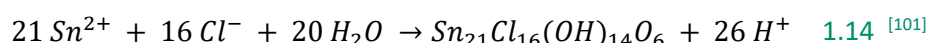
According to the literature, stannous electrolyte solutions are commonly based from SnSO_4 and H_2SO_4 [75,79–91]. Other electrolyte solutions contain SnCl_2 , H_3BO_3 and sodium gluconate ($\text{C}_6\text{H}_{11}\text{O}_7\text{Na}$) [92,93]. Alternatively they can be based from $\text{CH}_3\text{SO}_3\text{H}$ and $(\text{CH}_3\text{SO}_3)_2\text{Sn}$ [89,94,95] reagents. Several exceptions can be found, such as those derived from H_2SO_4 and MSA baths [96–99] or deep eutectic solvent [100]. For most of the electrolyte solutions, the higher the current density, the shorter the deposition time. However, the use of additives is required since Sn(II) is not stable in aqueous media in presence of dioxygen [78]. The tin cations are irreversibly oxidized following the [reaction 1.12](#):



When the film is dehydrated, the stability of Sn(OH)_4 is lowered and is turned into SnO_2 as indicated by the Pourbaix diagram ([reaction 1.13](#)) :



Another possible hydrolysis reaction is possible in chloride media ([reaction 1.14](#)):



In MSA baths, electrodepositions were performed at different potentials [78]. For a deposition potential between -0.45 to -0.65 V vs Ag/AgCl, matt and non-dendritic deposits were obtained ([Figure 1.13](#)), whereas for more and more negative potentials, the deposits have needle-like dendrites, influenced by the co-reduction of hydrogen.

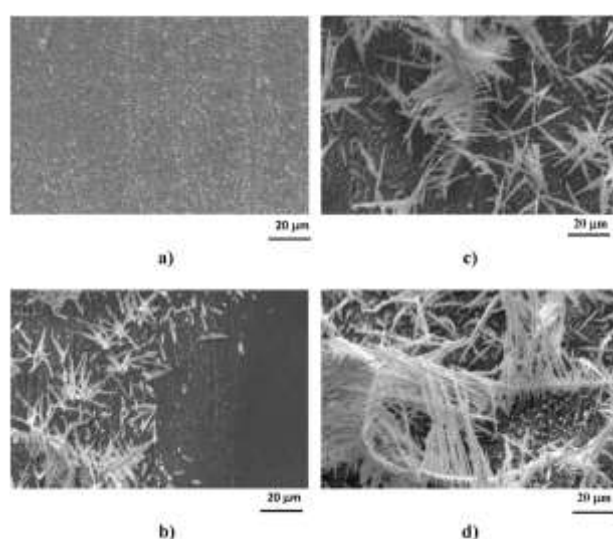


Figure 1.13: SEM scans of tin deposits made from a bath containing 0.014 mol.L⁻¹ of SnSO_4 and 12.5% vol. of $\text{CH}_3\text{SO}_3\text{H}$ at (a) -0.65 V, (b) -0.75 V, (c) -0.85 V and (d) -0.95 V vs Ag/AgCl [78]

From SnSO_4 based baths, deposits crystallize in the tetragonal structure but they are rougher and less compact deposits than stannic bath. Porosity is still observed, depending on the additives involved in the bath (Figure 1.14).

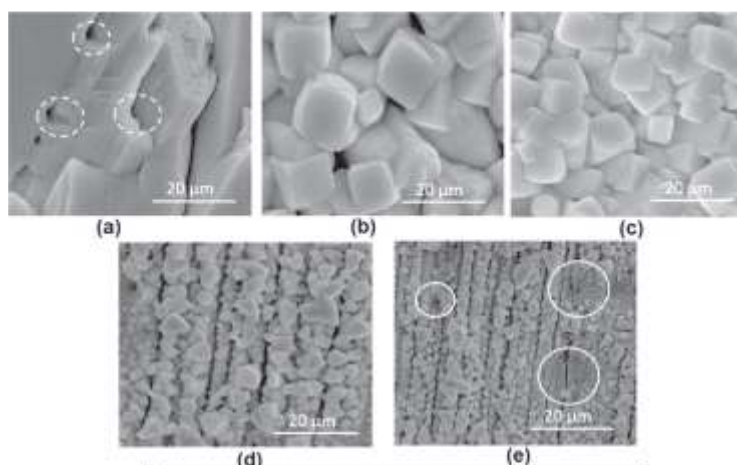


Figure 1.14: SEM scans of pulse deposited tin films from a bath containing SnSO_4 0.19 mol.L^{-1} and citric acid ($\text{C}_6\text{H}_8\text{O}_7$) 0.62 mol.L^{-1} at (a) 10, (b) 20, (c) 30, (d) 40 and (e) 50 mA.cm^{-2} [102]

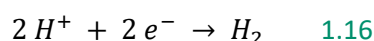
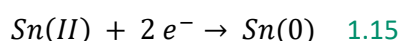
Since without additives the deposits from Sn(II) baths are porous with whiskers, surfactants can be employed to reduce the surface tension and help the reaction near the working electrode. The choice of the additive(s) is important. The presence of additives usually shifts the deposition potential to more negative potentials. Oxidation inhibitors will reduce the formation of Sn(IV) . Moreover, grain refiners avoid the formation of dendrites. Brighteners help to obtain bright surface. Low and Walsh have shown that the addition of an reducer like hydroquinone enables to drastically decrease the oxidation into Sn(IV) but also the deposition current density, probably due to an adsorption of the antioxidant on the electrode surface [98]. A similar effect with surfactant like a perfluorinated cationic one was reported, where its adsorption hindered the hydrogen evolution reaction [97].

Among the commonly used additives for the electrodeposition of tin from Sn(II) baths, we can find aromatic carbonyl compounds, amines, aromatic heterocyclic aldehydes or aromatic ketones. Depositions from baths containing formaldehyde, propionaldehyde and benzaldehyde lead to significant overpotentials [82]. When combined in the electrolyte solution, polypropylene glycol was found to improve the absorption of polyethylene glycol on the electrode and phenolphthalein improved the smooth and matt surface of the as-deposited films [94]. Their adsorption lead to minimize the reduction into dihydrogen, the grain size and roughness. Syntanol, formalin and benzyl alcohol help to reduce the double layer capacitance and the lustrous aspect of the films [80]. The polarization of the electrode can be increased by adding octylphenol ethoxylate. Finally, benzalacetone,

benzophenone and amines are respectively used as leveller, grain refiner and agent for uniform deposits ^[86].

Thus, the presence of additives plays a role on the deposition temperature and as well as on the aspect of the deposit (mat or bright). The electrolyte solutions used for mat deposits are less sensitive to high temperature.

As conventional complexing agents for stannous baths, hydroxycarbonic acids (gluconic, citric or tartaric) or diphosphates are commonly used ^[74]. Thus, Rudnik and Wloch investigated the electrochemical behavior of Sn(II) from tin chloride and gluconate as a complexing agent ^[93] on a glassy carbon (GC) disk electrode (Figure 1.15). This study is the closest to our work and we expect similar results concerning Sn(II) electrochemical system. In the cathodic part, three peaks can be observed. The C1* and C1 peaks were respectively associated to the dissociation of Sn(II) complexes and the reduction of Sn(II) into Sn(0) (equation 1.15). The C2 peak might be related to hydrogen evolution (equation 1.16).



In the anodic part, two peaks are visible, both linked to the dissolution of bulk tin. The authors noticed an increase of the peak potential and current density with the tin concentration, indicating the metal deposition is improved. Thus, the peak A2 around -0.45 V was only observed for Sn(II) concentrations of 5 and 10 mM. A first cross-over, represented by E_n , was related to the nucleation potential. Another one, E_c , might be related to the equilibrium potential. The last cross-over E^* , suggest the nucleation of a new phase of tin.

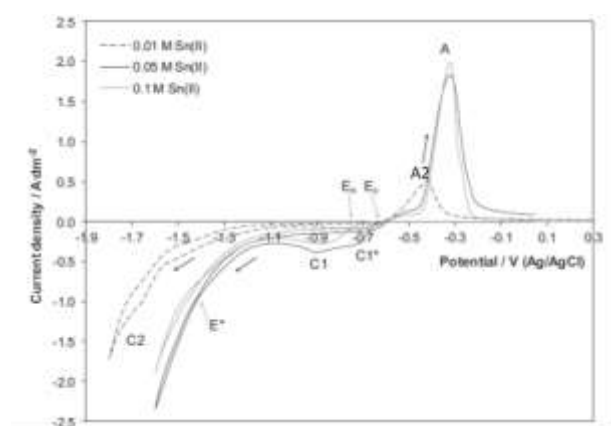


Figure 1.15: Cyclic voltammograms (CV) on GC of a tin chloride gluconate based electrolyte solution at different tin concentrations (adapted from ^[93])

Chapter 1. Fundamental concepts and state of the art

From this electrolyte solution, the deposits obtained at -1.1 V vs AgCl/Ag and for tin concentrations of 50 mM and 100 mM both exhibit a polycrystallinity in the tetragonal structure with low compacity and a general trend to form dendritic grains (Figure 1.16).

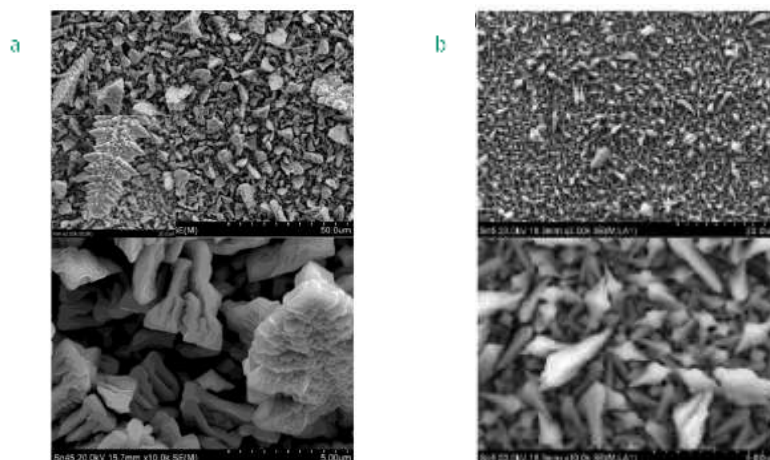


Figure 1.16: SEM scans of deposits made at -1.1 V vs AgCl/Ag and for a tin concentration of (a) 50 mM and (b) 100 mM ^[93]

From the state of the art of the tin electrodeposition we can conclude that:

	Stannic baths	Stannous baths
Stability	Stable	Require additive
Chemical media	Mostly alkaline	Acidic
Absolute cathodic current density	Weak (long deposition)	High (short deposition)
Deposits quality	Smooth and compact	Mat, porous, dendritic

Table 1.3: Comparison with stannic and stannous baths

To limit the energetic consumption and to avoid the corrosion effect of alkaline media, stannous bath is to be kept in mind.

b. Electrodeposition of Se

Se(0) has a wide stability zone along the pH (Figure 1.17). Selenium (0) and selenious (+IV) compounds are stable in water without adding any oxidizing or reducing agent as opposed to selenides

(-II). Moreover, in most cases, selenides, selenites (+IV) and selenates (+VI) have limited solubility in water ^[103]. Selenium can be oxidized into Se(IV) into H_2SeO_3 , HSeO_3^- and SeO_3^{2-} from acidic to alkaline medium. Oxidation into Se(VI) into HSeO_4^- and SeO_4^{2-} from a pH of 2 are observed. Se(0) can be reduced in Se(-II), either in the form of H_2Se (toxic gas) in acidic medium or HSe^- in less acidic bath (above a pH around 5). To the best of our knowledge, no Pourbaix diagram of selenium in aqueous chloride electrolyte solution is available in the literature. In presence of chloride ions, Se(0) can be oxidized into Se_2Cl_2 with a standard potential of 1.1 V vs SHE, considering (reaction 1.17) :

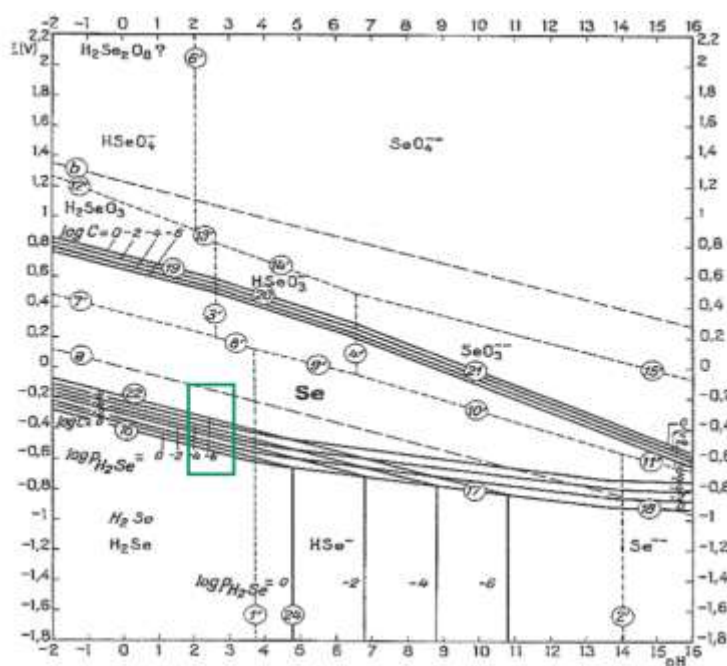
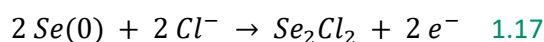


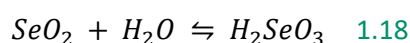
Figure 1.17: Pourbaix diagram of selenium in water. The green rectangle corresponds to the pH area of this work ^[103]

Selenium(0) exhibits different allotropic phases ^[104,105]. The first one is the vitreous insulating phase and not well distinguished from the three amorphous phases. There are also a rhombohedral phase, three monoclinic insulating phases (α , β , γ) and a hexagonal (grey and most stable) semiconductor phase. In the amorphous forms, we can distinguish the black, which is an assembly of large polymeric rings with more than 1000 atoms per ring and the red one, which has a distorted chain structure and can be transformed into the hexagonal phase by heat treatment. The monoclinic phase is metastable and spontaneously converted into the hexagonal phase under high temperature. The hexagonal phase is semiconductor thanks to the ordered selenium chains which help the electronic conduction.

The electrodeposition of selenium films is not carried out from Se(VI) salts, since these species are not electroactive ^[106]. The most common electrolytic baths were made from the dissolution of SeO₂ in sulfuric acid ^[107–111] or perchlorate acid ^[112–116]. Alternative electrolyte solutions have been developed from H₂SeO₃ or Na₂SeO₃ as selenium precursors ^[117–122]. It should be noticed that research groups performed electrochemical studies in ionic liquids ^[105,123–127].

The electrodeposition of selenium is difficult, specifically because of the possible underpotential deposition (UPD), leading to the formation of selenium alloys with several electrode materials. The formation of H₂Se is problematic and must be avoided due to its toxicity ^[123]. Moreover, it is also difficult to avoid the deposition of an amorphous phase. Thus, in order to ensure the formation of a metallic grey deposit, several conditions need to be respected.

According to A. Von Hippel *et al.* ^[110], acidic solutions with SeO₂ as Se(IV) precursor, which in acidic medium leads to H₂SeO₃ (equation 1.18), are more inclined to form a metallic deposit (hexagonal phase), by electrodeposition, in presence of an acid such as HCl, H₂SO₄ or HNO₃ ^[110].



The optimal acid concentration was found to be at about 20 in normality for a high concentrated (even saturated) SeO₂ solution at 100 °C (Figure 1.18).

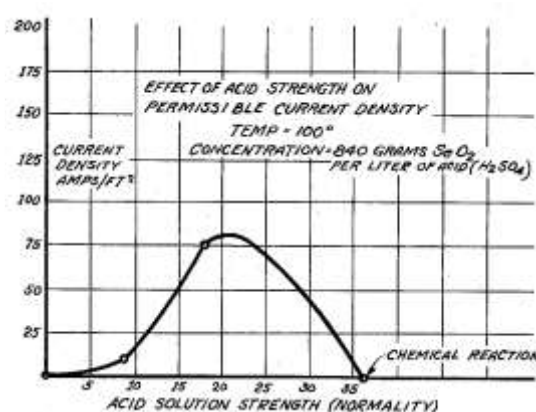


Figure 1.18: Effect of the acid concentration on the density of current ^[110]

Moreover, this study also shows that without large acid concentration, the electrodeposition needs a minimum temperature of 100 °C, leading to a faster deposition and uniform metallic films (Figure 1.19). If the temperature is lower than 100 °C, the deposit turns into the red amorphous phase (insulator). Increasing the temperature and the acid concentration increases the efficiency to form a metallic film of Se. However, such experimental setup (high temperature, high acid solution strength) is highly corrosive for the electrodes and cannot be transposed to practical use.

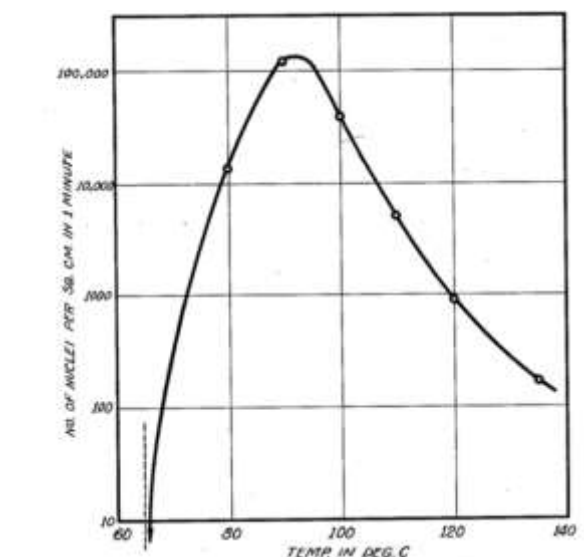


Figure 1.19: Influence of the temperature on the nucleation rate ^[110]

At RT, the potential should be applied in agreement with the reduction of the quadrivalent selenium cations. In these conditions, the faradaic yield is improved and the hydrogen evolution is limited (or avoided). Otherwise, for higher voltages, an amorphous red deposit can be synthesized. The decrease in the applied current density is in favor of the generation of a metallic selenium deposit. But, if the current is too cathodic, the hydrogen evolution is too important which causes the formation of the red deposit. It can be transformed into the metallic phase since the phase transition of red selenium to grey selenium takes place at about 100°C ^[128].

Dilmi and Benaicha studied the electrochemical behavior of Se(IV) from SeO₂ in a citrate aqueous medium acidified by HCl ^[129] (Figure 1.20).

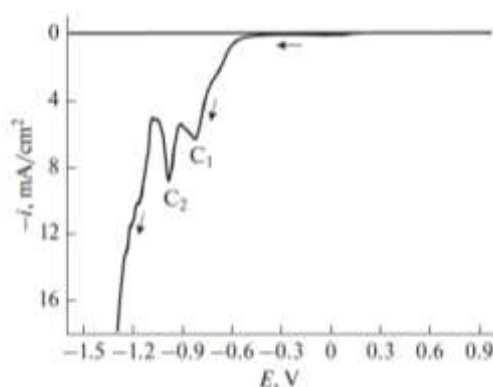
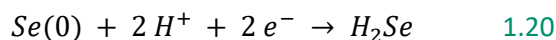
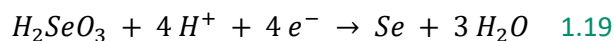
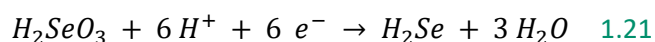


Figure 1.20: CV on platinum of SeO₂ in presence of citrate ^[129]

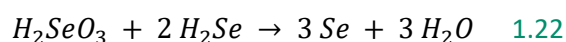
Two cathodic peaks are observed, respectively related to the reduction of Se(IV) into Se(0) and H₂Se from the reactions 1.19 and 1.20.



Several studies on noble electrodes such as gold or silver suggest a six-electron process associated to one peak ^[107,108,114–117,119], which occurs at more negative potentials (reaction 1.21):

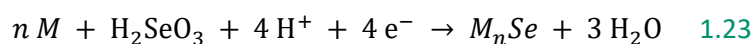


If the H_2SeO_3 concentration is higher than $400 \mu\text{g.mL}^{-1}$, that is to say 3.10 mmol.L^{-1} , a disproportionation (dismutaton) reaction occurs between the formed H_2Se and H_2SeO_3 leading to the formation of amorphous selenium (reaction 1.22):



The reaction rate increases with the decrease of the pH.

Moreover, on noble metal electrodes, anodic stripping of $Se(0)$, whose first layers were generated following reaction 1.23 ^[106] was observed. On the contrary, anodic stripping peaks were not observed on glassy carbon ^[112] and polycrystalline gold electrodes ^[130].



In their study, Coelho *et al.* pointed out the effect of illumination. Indeed, they show that at under illumination at 20 and 40 °C, red amorphous deposits are obtained, whereas at 60 and 80°C, grey crystallized films cover homogenously the substrate with hexagonal microrods (Figure 1.21) ^[131]. Without illumination, the deposits contain spherical grains, corresponding to amorphous selenium. A theory concerning this phenomenon is that the growth of the microrods is governed by a photoelectrocorrosion mechanism. In the semiconductor phase, electron/hole pairs are generated. Holes can oxidize amorphous selenium, having the effect to maintain the current to a steady-state value. Without illumination, amorphous particles are not oxidized and are accumulated on the electrode surface, to form a film.

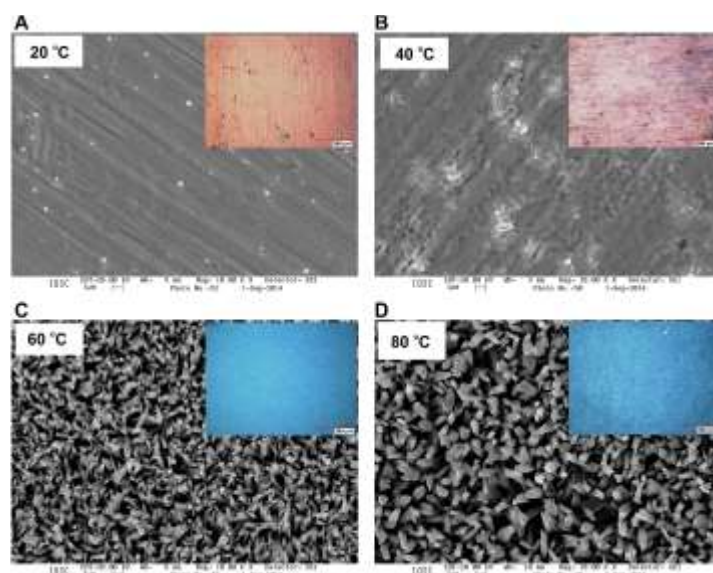


Figure 1.21: SEM and insert optical images of Se deposit from SeO_2 in acidic medium and under illumination and magnetic stirring, at -0.45 V vs SCE [131]

This mechanism was confirmed by Fan *et al.* [118]. They revealed that the illumination enhances the reduction of Se(IV) into Se(0) and of Se(IV) into Se(-II) via generated photo-electrons and holes. They obtained coarser deposits under illumination.

From the state of the art of selenium electrodeposition we can conclude that:

- ✓ Se(0) electrodeposition is carried out from Se(IV) baths
- ✓ Several allotropic forms exist but the hexagonal phase is promoted from acidic media
- ✓ A temperature lower than 100°C leads to amorphous Se
- ✓ Hydrogen evolution and acid medium lead to disproportionation
- ✓ The amorphous selenium can be annealed at 100°C to generate the hexagonal structure
- ✓ Alloys with the working electrode generally occur
- ✓ Illumination leads to the formation of metallic films

Amorphous selenium is generally obtained and can be avoided using a temperature of 100°C . It requires the use of non-aqueous solvents (organic, ionic liquids...) which are more complex and expensive. Another idea is to use acidic media, as investigated, and to anneal the films at a minimum temperature of 100°C .

c. Electrodeposition of SnSe

Geoffroy and Demopoulos superimposed the Pourbaix diagrams of Sn and Se and deduced the predominance zones of SnSe (Figure 1.22) [101]. SnSe can be generated whatever the pH but the secondary phases obviously depend on the pH and the potential used for the electrodeposition. Taking into account our electrodeposition conditions (green rectangle), it is possible that our films have a homogeneity zone between the $\text{SnSe}_2+\text{SnO}_2$, $\text{SnSe}+\text{SnO}_2$ and $\text{SnSe}+\text{Sn}$ domains. If the potential is more cathodic, the domain of $\text{H}_2\text{Se}+\text{Sn}$ can be reached.

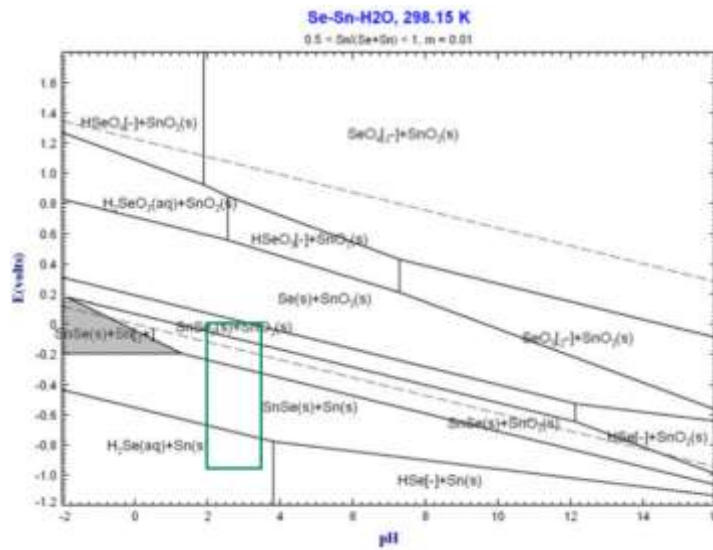
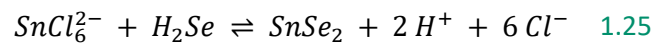
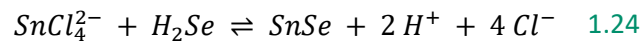


Figure 1.22: Calculated potential-pH diagram of SnSe in water at RT. The green rectangle corresponds to the pH area of this work [101]

We suggest, the precipitation of SnSe and SnSe_2 following the reactions 1.24 and 1.25, according to the same mechanisms of SnS and SnS_2 [132]:

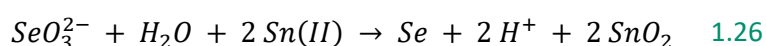


1. Synthesis in absence of additives

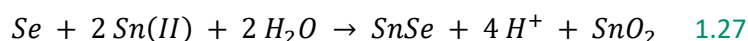
To the best of our knowledge, few studies, all realized by the Murali's research group, performed the electrodeposition of SnSe films from stannic baths [30,133–135]. The films were deposited at RT, using pulse deposition from a bath containing SnCl_4 and SeO_2 on ITO substrates. Polycrystalline films indexed in the orthorhombic structure were obtained, with preferred orientation along the (111)

plane. Crystallite sizes, increasing from 37 to 78 nm, were calculated from the Debye-Scherrer equation, as the duty cycle increases from 6 to 50 %. These values are in agreement with the grain size measured by Atomic Force Microscopy, varying from 40 to 80 nm. A slight excess of Se is always found, although for a 50 % duty cycle the composition is nearly stoichiometric. A bandgap was determined, evolving from 1.26 to 1.50 eV, when the duty cycle decreases.

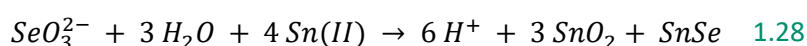
All other studies related to the synthesis of SnSe films by electrodeposition were realized from stannous acidic baths. Surprisingly, several of them performed the deposition without additives [15,24,136–141]. Generally, SnCl_2 was used in presence of H_2SeO_3 , except for Lukinkas *et al.* using SnSO_4 and H_2SeO_3 [136]. The electrolyte solution was highlighted to be unstable by Engelken *et al.*, who suggested an immediate reduction of Se(IV) in presence of Sn(II). Indeed, the Sn(IV)/Sn(II) couple has a standard redox potential of 0.15 V vs SHE (Figure 1.11), lower than that of the Se(IV)/Se(0) couple, of 0.74 V vs SHE (Figure 1.17). The difference between the two standard potentials is sufficient to allow a spontaneous reaction. This phenomenon was also reported by Geoffroy and Demopoulous, who confirmed the formation of amorphous selenium according to the reaction 1.26 [101]:



Increasing the tin concentration modifies the color of the precipitate into yellow or beige. Moreover, the spontaneous formation of SnSe is not excluded (reaction 1.27) [101]:



Both reactions can lead to the overall reaction 1.28 [101]:



Engelken *et al.*, in their case, observed yellow-brown precipitates, assigned to Sn_xSe compounds, when increasing the selenium concentration [24]. Looking at the reaction 1.27, increasing the Se concentration forces the reaction into the right. Thus the yellow-brown color may be due to a reddish color of SnSe and white SnO_2 . They noticed that the SnSe films appeared reddish-brown when thin, yellow-brown when thicker and gray for the thickest. Slightly adherent gray powder was also observed and may be due to the disproportionation of selenium (reaction 1.22). The SnSe films were found to be polycrystalline, indexed into the orthorhombic structure with a preferred orientation along the (111) plane. The overall stoichiometry was close to 1:1. The annealing at 300 °C created a selenium excess, decreased the thickness of the films and made them more transparent and orange. Indirect bandgaps were obtained from 0.85 to 0.95 eV for as-deposited films and 1.3 eV for annealed films.

Subramanian *et al.* deposited their films with the electrolyte solution temperature of 55 °C ^[15]. The same orthorhombic structure was identified and the films exhibit a closely-packed granular morphology and is almost stoichiometric. An annealing at 200 °C was found to keep the value of the indirect bandgap, close to 1.05 eV. Mathews obtained orthorhombic polycrystalline nanoporous films at 45 °C along the same preferred direction ^[138] (Figure 1.23). However they determined a direct bandgap of 1.1 eV. Similarly, using the same temperature and deposition potential, Zatirostami obtained films with the same morphology but the direct bandgap was estimated to 1.38 eV ^[140].

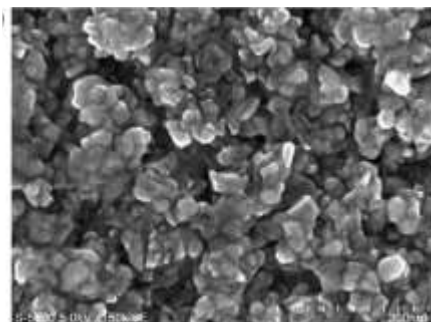
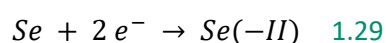


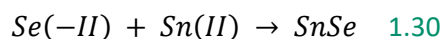
Figure 1.23: SEM image of a SnSe films synthesized at -0.75 V vs Hg₂Cl₂/Hg from a bath containing H₂SeO₃ 1.5 mM and SnCl₂ 2.2 mM ^[138]

Since the electrolyte solution with Se(IV) and Sn(II) is not stable, Lukinskas *et al.* decided to use an alternative approach by preparing separate solutions ^[136]. After 12 hours, a tin solution is still stable. This is not the case when adding Se(IV). Indeed, after 12 hours, Sn(II) is no more detectable, since it was oxidized into Sn(IV) species, which are not electroactive. Moreover, the authors mentioned that the use of EDTA does not improve the stability. Hence, tin was first deposited from SnSO₄ and then selenium, from H₂SeO₃. They obtained gray deposits, and a cathodic current peak related to the generation of Se(-II) was detected (analogous to reaction 1.20). SnSe was found, as well as Sn(0) and Se(0) residual phases. This result suggests a reaction between Sn(0) and Se(0) leading to the formation of SnSe. At more cathodic selenium deposition potential, SnSe₂ was identified.

Alternatively, Ham *et al.* synthesized SnSe films by photoelectrochemical deposition ^[137]. Formerly, selenium was electrodeposited on gold substrates from dissolved SeO₂. As previously mentioned in the literature, Se(0) is reduced into Se(-II) under illumination thanks to generated photoelectrons (reaction 1.29) ^[118,131]:



Thus, in presence of Sn(II) cations, SnSe may result from a precipitation reaction (reaction 1.30):



The films were polycrystalline, indexed in the orthorhombic structure and had a Sn:Se ratio of 1:1.

2. Synthesis with additives

Other studies were performed in presence of additive to avoid tin hydrolysis ^[23,142–147]. In presence of EDTA, Zainal *et al.* investigated the influence of the SnCl_2 and Na_2SeO_3 concentrations on the films ^[142]. They showed that a bath with equal molar ratio between SnCl_2 and Na_2SeO_3 or higher Na_2SeO_3 concentration produces orthorhombic SnSe films. Moreover, the morphology also changes with the concentration and the grain size decreases when the Na_2SeO_3 concentration increases (Figure 1.24).

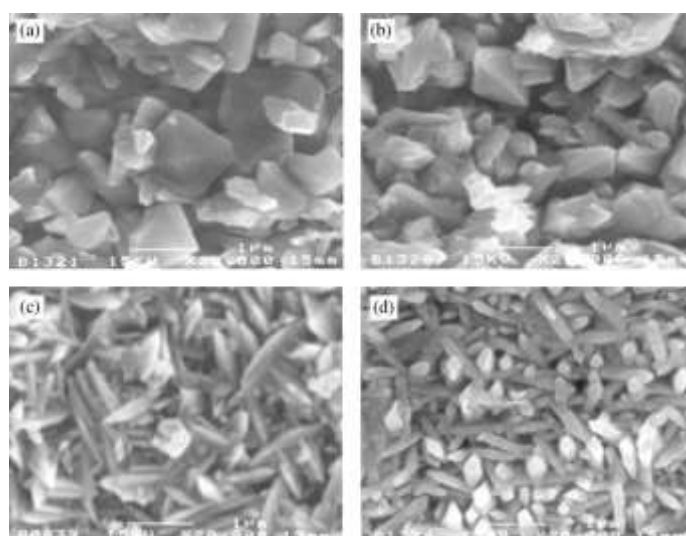


Figure 1.24: SEM images of SnSe films deposited at 0.01 M of SnCl_2 and Na_2SeO_3 concentration of (a) 0.005 M, (b) 0.01 M, (c) 0.015 M and (d) 0.02 M ^[142]

Biçer and Sisman decided to focus firstly on the influence of the deposition potential ^[23]. They obtained orthorhombic polycrystalline films, with a preferential orientation along the (111) plane. Furthermore, the grains evolved from spherical-shaped to platelet-like as the deposition potential was more and more cathodic. Moreover, the films were found to contain more and more tin. The morphology changed also from spherical to platelet-like by increasing the deposition time. The thickness was found to increase with the deposition time. A direct bandgap of 1.3 eV was finally evaluated for the thickest films.

Shinde *et al.* used tartaric acid as complexing agent for Sn(II) to avoid the precipitation of selenium ^[144]. SnSe films were obtained with spherical-shaped grains in both potentiostatic and galvanostatic modes. The composition was found to be close to the stoichiometry, with a slight selenium excess, except for the films deposited at -0.9 V vs AgCl/Ag, which were tin rich. A direct bandgap of 1.2 eV was finally determined.

Lu *et al.* preliminary investigated the electrochemical behavior of their electrolyte solution containing SnCl₂, SeO₂ and K₄P₂O₇ as a complexing agent of Sn(II) (Figure 1.25) before making the electrodeposition of SnSe films ^[146]. A cathodic peak was observed and assigned to the deposition of SnSe according to reaction 1.31 as well as an anodic peak, related to the anodic dissolution of SnSe.

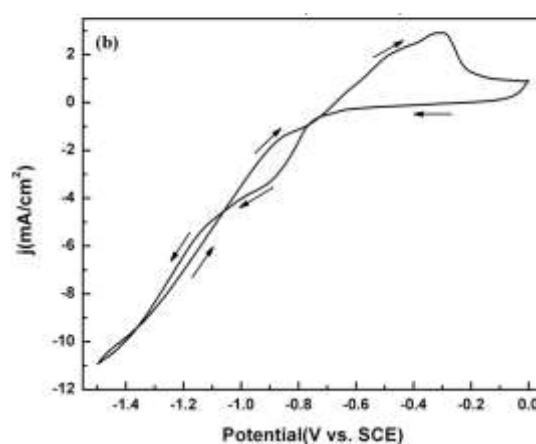
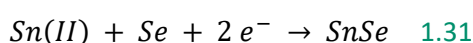


Figure 1.25: CV on ITO on an electrolyte solution containing SnCl₂, SeO₂ and K₄P₂O₇ ^[146]



Although the films exhibit a Se excess, suggesting the additional reduction of SeO₃²⁻ into Se(0), XPS analyses showed only the presence of Se(-II), in agreement with the presence of SnSe. The XRD revealed the orthorhombic structure, as commonly observed, with a preferential growth along the (111) plane. SEM shows an irregular flake-like structure. Finally, direct and indirect gaps of 1.29 and 0.89 eV were respectively measured.

The main conditions of synthesis and properties of electrodeposited SnSe films are summarized in Table 1.4.

Chapter 1. Fundamental concepts and state of the art

Precursors	Conditions	Additives	Bath temperature (°C)	Preferential growth	Morphology	E _g (eV)	Reference
SnCl ₄ and SeO ₂	-0.90 V vs SCE, 6-50 % duty cycle	No	RT	⊥ (111)	Spherical?	1.26-1.50	[30,133–135]
SnCl ₂ and SeO ₂	-0.56 V vs SHE	No	55	⊥ (210) and (402)	granular	1.05	[15]
SnCl ₂ and SeO ₂	-0.35 to -0.4 V vs SCE?	No	20-90 and 110-130	⊥ (111)	?	0.85-0.95 +1.30 (annealed)	[24]
SnSO ₄ and H ₂ SeO ₃	-0.50 V/-0.85 V vs SHE	No	20	Sn	Spherical to needle-like?	No	[136]
SnCl ₂ and SeO ₂	-0.30 V vs AgCl/Ag?	No	RT?	⊥ (111)	?	No	[137]
SnCl ₂ and H ₂ SeO ₃	-0.75 V vs SCE	No	45	⊥ (111)	Spherical (nanoporous)	1.1	[138]
SnCl ₂ and SeO ₂	-0.55 to -0.85 V vs SCE	No	40-80	Cubic SnSe	Nanorods	1.10-1.17	[139]
SnCl ₂ and H ₂ SeO ₃	-0.75 V vs SCE	No	45	⊥ (111) ?	Spherical	1.38	[140]
SnCl ₂ and Na ₂ SeO ₃	-1.1 V vs SCE	No	80	⊥ (210)	Ball-shaped	1.44	[141]
SnCl ₂ and Na ₂ SeO ₃	-0.85 vs AgCl/Ag	EDTA	RT?	SnSe/Sn	Various	No	[142]
SnCl ₂ and Na ₂ SeO ₃	-0.2 to -0.6 V vs AgCl/Ag	EDTA	RT	⊥ (111)	Spherical to platelet-like	1.3	[23]
SnCl ₂ and SeO ₂	-0.70/-0.80 V vs AgCl/Ag + 2 mA/cm ²	Tartaric acid	RT?	⊥ (111) ?	Spherical	1.2	[144]
SnSO ₄ and SeO ₂	-0.60 V vs AgCl/Ag	EDTA	RT	⊥ (111) ?	Spherical	No	[145]
SnCl ₂ and Na ₂ SeO ₃	-1.0 V vs SCE	K ₄ P ₂ O ₇	30	⊥ (111) ?	Flake-like	1.29 (direct) + 0.89 (indirect)	[146]
SnCl ₂ and Na ₂ SeO ₃	-0.50 vs SCE	EDTA	RT	⊥ (111) ?	Needle-like	No	[147]

Table 1.4: Conditions and properties of electrodeposited SnSe films

3. TE properties of SnSe films

Mandal *et al.* deposited SnSe films on FTO substrates at RT, at an applied potential of -0.6 V vs AgCl/Ag ^[145]. If they obtained SnSe in the orthorhombic structure, the films surprisingly exhibit a Sn excess (67 %) according to the EDS analyses. Porous films were obtained, with a grain size of 130 nm. The TE properties were measured, by keeping the film on the substrate which results in aberrations. Thus they found a negative S , about $-80 \mu\text{V.K}^{-1}$ at RT, influenced by the n-type behavior of the FTO substrate. They found a lower κ than the reference material and a satisfactory σ (1260 S.cm^{-1} at RT), leading to a ZT of 0.3 at RT. These results are doubtful since the electrical properties are influenced by the electronic properties of the substrate ^[148]. Moreover, the electrical conductivity is not supported by the porous film.

Very recently, Burton *et al.* successfully obtained, for the first time, the complete TE properties of SnSe films electrodeposited from a bath containing SnCl_2 , Na_2SeO_3 and EDTA ^[147]. A preliminary CV was performed, where a cathodic signal was assigned to the hydrogen evolution (Figure 1.26). In the anodic part, two peaks, called A and B, were respectively related to the stripping of Sn and Se. From the CV, the authors defined a deposition potential window and specifically operated at -0.5 V vs SCE.

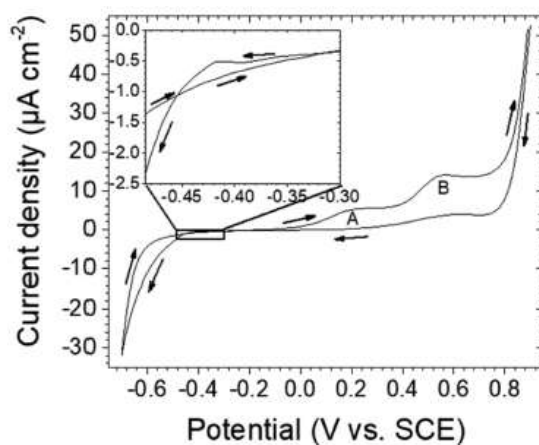


Figure 1.26: CV performed on Au-coated Si wafer from an electrolyte solution containing SnCl_2 , Na_2SeO_3 and EDTA ^[147]

A slight Se excess (51.8 %) was detected by EDS and signals in agreement with the SnSe phase were found by XPS. This phase was confirmed by XRD analysis, the pattern being indexed according to the orthorhombic structure. According to SEM analyses, the as-deposited films are porous, with needle-like grains (Figure 1.27 a), whose morphology is maintained after annealing at 473 K (Figure 1.27 b and c). However, the porosity is strongly decreased after annealing.

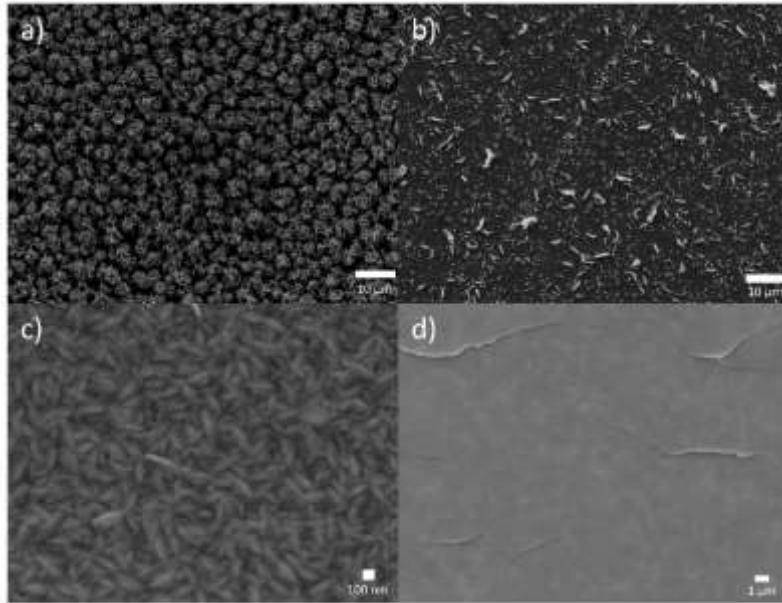


Figure 1.27: SEM images of SnSe films deposited at -0.5 V vs SCE: (a) as-deposited, (b) annealed, (c) annealed (HR), (d) after delamination ^[147]

σ was measured from 310 to 680 K (Figure 1.28 a). The as-deposited film exhibits the lowest σ which is explained by the high disorder level and porosity. It strongly increases at 450 K thanks to an annealing effect, which densifies and increases the crystallinity of the film. The annealing treatment at 523 K improves σ , specifically in temperatures ranging from 450 to 570 K but the resulting values of σ were generally lower than those of single crystal. It is noticed that the low σ can be explained either by the porosity or by cracks generated from the delamination process (Figure 1.27 d). The Seebeck coefficient S of the as-deposited sample was generally higher than that of the annealed film, with a value at room temperature about $450 \mu\text{V.K}^{-1}$, which is in the same range of single crystal (Figure 1.28 b). As a result, the PF was found to be improved for the annealed film in comparison with the as-deposited one. However, it remains lower than that reported for the single crystal (Figure 1.28 c). The thermal conductivity of the as-deposited films was also measured and was found to increase with the temperature whereas that of single crystal decreases. This behavior is typical of disorder and boundaries created in the film. Nevertheless, the values remain interesting, since lower than the reference material (Figure 1.28 d). Finally their TE measurements lead to a limited value of ZT below 0.4.

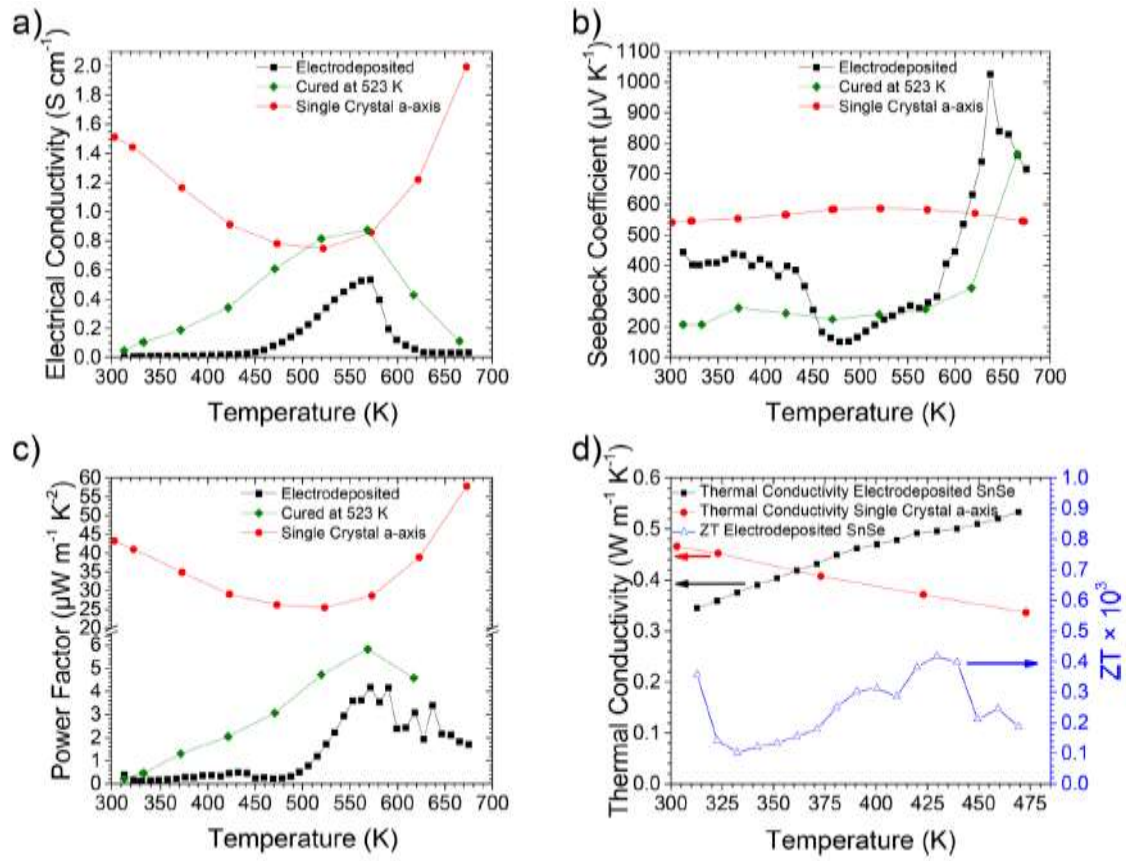


Figure 1.28: TE properties of electrodeposited SnSe films: (a) σ , (b) S , (c) PF and (d) κ ^[147]

4. Doping of SnSe films

To improve the electrical properties, a possibility is to add a ternary element into the SnSe films in order to tune the electronic structure. This approach has been widely used for bulk or film but remains limited by electrodeposition. Jamali-Sheini *et al.* investigated the changes involved by the incorporation of Zn and Pb ^[141]. The depositions were carried out at 80 °C and at -1.1 V vs SCE. The XRD revealed the same orthorhombic structure but shifts in the diffraction peak positions occurred respectively to higher and lower d-spacing for Pb and Zn-doped films. These results are correlated to higher and lower ionic radius of Pb and Zn respectively. Moreover, the addition of dopants increases the intensity of the (210) diffraction peak. The un-doped films exhibit ball-shaped morphology whereas Pb- and Zn-doped respectively exhibit rods and wires in presence of other particles. Finally, the optical properties also changed with the doping: bandgaps of 1.44, 1.36 and 1.51 eV were respectively obtained for un-, Pb- and Zn-doped SnSe films. Pb and Zn contribute to increase the carrier concentration, modifying the band structure.

Dhanasekaran *et al.* studied the effect of adding Cd into SnSe^[143]. The $\text{Cd}_x\text{Sn}_{1-x}\text{Se}$ films exhibit crystallinity evolving with the incorporation of Cd. Indeed, for x between 0 and 1, three peaks could be indexed in the orthorhombic structure of SnSe and one in the cubic structure of CdSe. The SEM analyses were in agreement with the XRD since the morphology changed progressively from spherical grains for CdSe to nano-rod grains for SnSe, with a decrease of the grain size. Thus the direct bandgap was found to vary from 1.83 eV for CdSe to 1.02 eV for SnSe. In another study, they added S into SnSe by varying the deposition potential^[149]. The films were deposited onto ITO, from -700 to -1000 mV vs SCE. More cathodic potentials were found to peel off the films. The XRD analyses revealed the formation of the $\text{SnS}_x\text{Se}_{1-x}$ orthorhombic phase, for which peak intensities increase with the deposition potential. The crystallite size was found to increase with the deposition potential. However, the films at -700 mV vs SCE exhibit lower grain size with hillocks and voids. The $\text{SnS}_x\text{Se}_{1-x}$ deposits obtained at -900 mV vs SCE were nearly stoichiometric films, with x estimated at 0.42 and composed of spherical grains. The roughness was found to increase with the deposition potential. Finally the bandgap varied from 1.08 to 1.25 eV as the deposition potential decreased. The authors suggest that the evolution of the bandgap is due to stress reduction since the films have linearly oriented surface. However, an evolution with the S content is also observed.

The electrodeposition of SnSe doped by In was investigated by Jalalian-Larki *et al.*^[150]. In their study, the influence of the concentration of InCl_2 salt in the bath was highlighted. The depositions were cathodically performed at 60 °C from a bath containing 2 mM of SnCl_2 and 2 mM of Na_2SeO_3 . The InCl_2 concentration was varied from 0 to 0.023 mM. For each sample, the XRD analyzes confirmed the presence of SnSe indexed into the orthorhombic structure. By increasing the In concentration until 0.015 mM, shifts of the diffraction peaks to lower angles are observed. This feature is in agreement with the fact that In atoms replace Sn atoms and have lower radii. However, at 0.023 mM, the peaks are shifted to higher angles. The authors explain this phenomenon by the difference of the radii of Sn and In. Several In atoms can be inserted in interstitial positions which leads to irregularities in the SnSe structure. Thus the distances between planes are increased. The intensity of the patterns was found to increase with the In concentration. Moreover, the crystallite size decreases when the In concentration increases. The films exhibit spherical nanoparticles, whatever the In percentage. The band gap was found to slightly decrease from 1.43 eV to 1.39 eV as the In percentage increases.

From the state of the art of tin selenide films electrodeposition we can conclude that:

- ✓ SnSe electrodeposition is generally carried out from Sn(II) acidic baths
- ✓ There is a reactivity between Se(IV) and Sn(II) leading to Se(0) and SnO₂
- ✓ The Sn and Se concentrations influence the morphology
- ✓ Different values of the bandgaps were obtained, depending on the thickness and purity of the deposits
- ✓ Few teams performed doping but only one successfully measured all the TE properties of undoped films

A stability problem emerging from a spontaneous reaction between Sn(II) and Se(IV) is demonstrated. To avoid it, the replacement of Sn(II) by Sn(IV) is possible but highly energy-consuming. Sn(II) hydrolysis can be prevented using another solvent such organic or ionic liquids. A last possibility is the use of additives, this approach was chosen in this work. As reported in the literature, EDTA was commonly used as chelating reagent of Sn(II) but this chemical species is expensive, non-biodegradable and was not found to improve the bath stability. Thus, a new class of additives is envisaged. We decided to investigate the effect of oxalate.

Conclusion

This first chapter explains the fundamental principles of thermoelectricity, as well as the interest in SnSe films within this field. The objective is to reach the highest possible Seebeck coefficient and electrical conductivity, as well as a low thermal conductivity. Since SnSe is known to have a high Seebeck coefficient and a low thermal conductivity, an extensive but not exhaustive review of the different films synthesis techniques, up to now, has been described. The obtained physical or thermoelectric properties were reported. An in-depth state of the art concerning electrodeposition of tin, selenium and tin selenide films was also reported. As a result, the use of tin(IV) salt would be more appropriate since it avoids the tin(II) hydrolysis but would consume more energy. Moreover, the selenium electrochemical system being complex, supplementary reactions are strongly possible (disproportionation, reduction in presence of tin(II)). Nevertheless, in order to limit the tin(II) hydrolysis and with the intention to not use organic solvent or ionic liquid medium, we chose to study the electrodeposition in an aqueous medium, in presence of a complexing and reducing agent ^[151,152] : sodium oxalate. It also has the advantage to be more biodegradable, eco-friendlier and cost-effective than EDTA ^[153,154].

Ce premier chapitre explique les principes fondamentaux de la thermoélectricité, ainsi que l'intérêt des films de SnSe au sein de cette thématique. L'objectif est d'atteindre le coefficient Seebeck et la conductivité électrique les plus élevés possible, ainsi qu'une faible conductivité thermique. SnSe étant connu pour avoir un coefficient Seebeck élevé et une faible conductivité thermique, une revue étendue mais non exhaustive des différentes techniques de synthèse de films, jusqu'à ce jour, a été décrite. Les propriétés physiques ou thermoélectriques obtenues ont été reportées. Un état de l'art approfondi concernant l'électrodéposition de films d'étain, de sélénium et de sélénure d'étain a également été reporté. Il en résulte que l'utilisation d'un sel d'étain(IV) serait plus approprié car évite l'hydrolyse de l'étain(II) mais consommerait plus d'énergie. Par ailleurs, le système électrochimique du sélénium étant complexe, des réactions additionnelles sont fortement probables (disproportionation, réduction en présence d'étain(II)). Néanmoins, afin de limiter l'hydrolyse de l'étain(II) et avec la volonté de ne pas utiliser de solvant organique ou de liquide ionique, nous avons choisi d'étudier l'électrodéposition en milieu aqueux, en présence d'un agent complexant et réducteur ^[151,152] : l'oxalate de sodium. Celui-ci a également pour avantage d'être biodégradable, plus respectueux de l'environnement et moins onéreux que l'EDTA ^[153,154].

Chapter 2.

Materials and methods

Introduction

In this chapter, we will explain how the electrochemical bath was optimized in order to limit the stability problems. The material needed for the electrodeposition of SnSe films will briefly be presented. The electrodeposition conditions will be evoked both in continuous and pulse mode. Finally, the used techniques to characterize these deposits will also be described on the operating principle and in terms of use. They will concern the microstructural characterizations, systematically employed, but also additional techniques occasionally used in order to obtain information, either on the chemical composition, or the oxidation degree of the constituting elements, and also physical properties such as the gap.

Dans ce chapitre, nous expliquerons comment le bain électrochimique a été optimisé tout en cherchant à limiter les problèmes de stabilité. Le matériel nécessaire à l'électrodéposition des films de SnSe sera brièvement présenté. Les conditions d'électrodéposition seront évoquées que ce soit en mode continu ou en mode impulsionnel. Enfin, les techniques utilisées pour caractériser ces dépôts seront également décrites tant sur le principe de fonctionnement que leurs conditions d'utilisation. Elles concerneront les caractérisations microstructurales, systématiquement employées, mais également des techniques complémentaires utilisées occasionnellement dans le but d'obtenir des informations, soit sur la composition chimique, soit sur le degré d'oxydation des éléments présents ou encore, des propriétés physiques telles que la largeur de bande interdite.

I. The electrolyte solution

a. Thermodynamic stability of the electrolyte solution

The Pourbaix diagram of tin was calculated using the Spana[®] ¹ software taking into account our electrolyte solution conditions as below (Figure 2.1). The chemical bath composition will be justified in the next subsection:

-0.2 M KCl

-0.2 M Na₂C₂O₄

-20 mM SnCl₂

¹ Found on <https://www.amphos21.com/producto/chimera-4-2/>

-5 mM Na_2SeO_3

-pH 2.5

The specific diagram is different from the one made without oxalate (Figure 1.11). Surprisingly, no tin oxalate complex is visible on the diagram. However, its existence is known^[155] and the chelating behavior of oxalate with tin was also reported by Ju *et al.*^[156]. Moreover, it seems that there is a small pH-potential zone where Sn(II) exists in our conditions. That can explain its trend to hydrolyze. A wide existence zone of SnO_2 is visible, as well as Sn(0). From our pH and potential used during electrodeposition, these two phases should be encountered (orange rectangle). Moreover, due to bath instability and since the pH is not adjusted in the last step (close to 2 in the end of the preparation), we do not exclude the formation of $\text{Sn}_{21}\text{Cl}_{16}(\text{OH})_{14}\text{O}_6$ from its thermodynamic stability, as previously reported by Geoffroy and Demopoulos^[101] (reaction 1.14). Nevertheless, the kinetic conditions have to be taken into account for its formation. At a pH of 2.5, the redox potential of the couple SnO_2/Sn seems to be -0.23 V vs SHE, that is to say -0.45 V vs AgCl/Ag. This value is close to that obtained for Sn(II)/Sn without oxalate (-0.52 V vs AgCl/Ag) (Figure 1.11). This might be different in our experimental conditions since the temperature will not be room temperature and the concentrations can slightly differ. Moreover, the majority species in the electrolyte solution might be SnCl_2 and is complexed, thus its reduction potential is more negative.

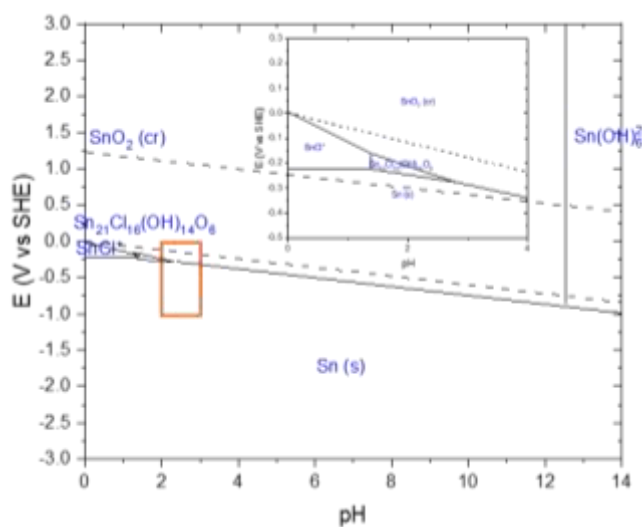


Figure 2.1: Calculated Pourbaix diagram according to our electrolyte solution conditions: 0.2 M Cl^- , 0.2 M $\text{Na}_2\text{C}_2\text{O}_4$ and 20 mM SnCl_2 . The orange rectangle corresponds to the pH area of this work.

It should be underlined that, under our electrolyte conditions, the predominance diagram (Figure 2.2), as well as the Pourbaix diagram indicate SnO_2 as majority species. However, the Spana[®] software does not take into account SnC_2O_4 as an existing solid compound. No K_s value was found in

the literature. Since the chelating behavior is confirmed by the literature ^[156], we can suggest the presence of SnC_2O_4 and of SnO_2 at $\text{pH}=2.5$. The existence zones of SnCl_2 , SnCl^+ and Sn^{2+} are very close to each other.

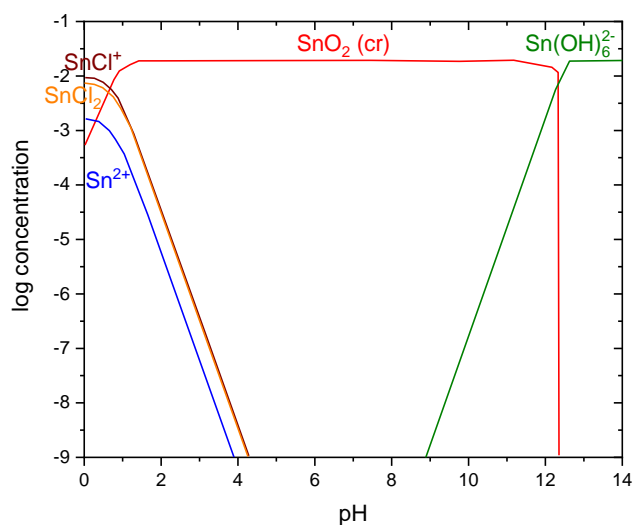


Figure 2.2: Tin species predominance diagram with 0.2 M Cl^- , 0.2 M $\text{Na}_2\text{C}_2\text{O}_4$ and 20 mM SnCl_2

In comparison with the previous diagram, the calculated pH-potential diagram of selenium, taking into account the used concentrations and the presence of oxalate is very similar to the previous one in Figure 1.17, since we assumed that there is no complex between Se and oxalate. This observation was also expected from Ju *et al.* ^[156] and to the best of our knowledge, no complex between Se and oxalate was reported. Se(IV) can be reduced into Se(0), which can be reduced into H_2Se or HSe^- at more cathodic potentials (Figure 2.3). Thus, in our conditions of electrodeposition, the species that should be encountered are Se(0) and H_2Se (orange rectangle).

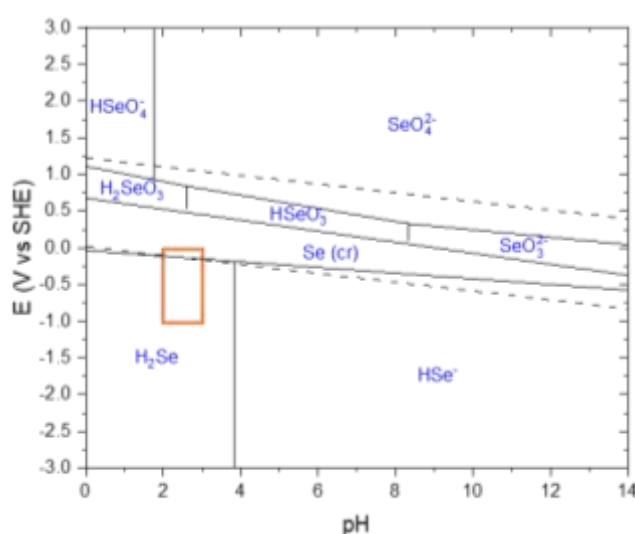


Figure 2.3: Calculated Pourbaix diagram according to our electrolyte solution conditions: 0.2 M Cl^- , 0.2 M $\text{Na}_2\text{C}_2\text{O}_4$ and 5 mM Na_2SeO_3

It should be noted that, according to the species dominance diagram made on selenium species and taking into account our electrolyte solution composition, the majority species at a pH of 2.5 might be H_2SeO_3 , although very close to HSeO_3^- (Figure 2.4). Moreover, at the end of the electrolyte solution preparation, the pH is lower than 2, thus we can assume that H_2SeO_3 are the majority selenium species. According to the diagram, at a pH of 2.5, the redox potential of the couple $\text{H}_2\text{SeO}_3/\text{Se}$ is 0.49 V vs SHE, equal to 0.27 V vs AgCl/Ag. This value remains quite close to that obtained without oxalate in Figure 1.17 (0.38 V vs AgCl/Ag). Furthermore, it confirms the ability to generate a spontaneous reaction with tin since its redox potential is higher than that of Sn(IV)/Sn(II) .

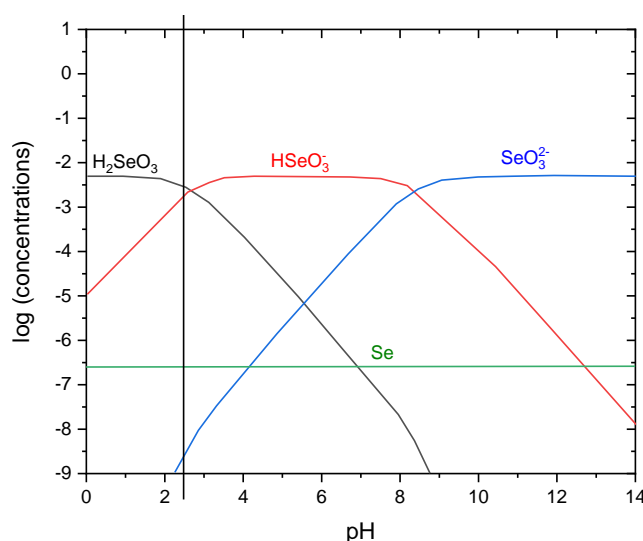


Figure 2.4: Selenium species predominance diagram with 0.2 M Cl^- , 0.2 M $\text{Na}_2\text{C}_2\text{O}_4$ and 5 mM Na_2SeO_3

As Geoffroy and Demopoulos^[101], we made a superposition of the calculated diagrams obtained for tin and selenium systems (Figure 2.5). It is a bit different from the one published in Figure 1.22. The main differences are due to a wider existence zone of SnO_2 and quasi inexistence of SnCl^+ zone. Taking into account the pH and potential range of the deposition (orange rectangle), the films composition should be between three homogeneity zones: SnO_2+Se , $\text{SnO}_2+\text{H}_2\text{Se}$ and $\text{Sn}+\text{H}_2\text{Se}$. The second calculated zone “ $\text{SnO}_2+\text{H}_2\text{Se}$ ” is inconsistent with the published diagram. By analogy with the diagram calculated by Geoffroy and Demopoulos, we suggest that SnO_2 in presence of H_2Se tends to generate SnSe_2 since there is no “ $\text{SnO}_2+\text{H}_2\text{Se}$ ” zone but “ $\text{SnO}_2+\text{SnSe}_2$ ” and “ $\text{SnO}_2+\text{HSe}^-$ ” zones. In other words, Sn(IV) and Se(-II) may generate SnSe_2 . Taking into account the reactions 1.26 and 1.27 which lead to 1.28, SnSe precipitation occur with SnO_2 and Se precipitation with Sn excess. Thus we can correlate this zone from our diagram with $\text{SnSe}+\text{SnO}_2$. In the following equations, the notation Sn(II) means that the cation is complexed and is not a under a non-complex form Sn^{2+} .

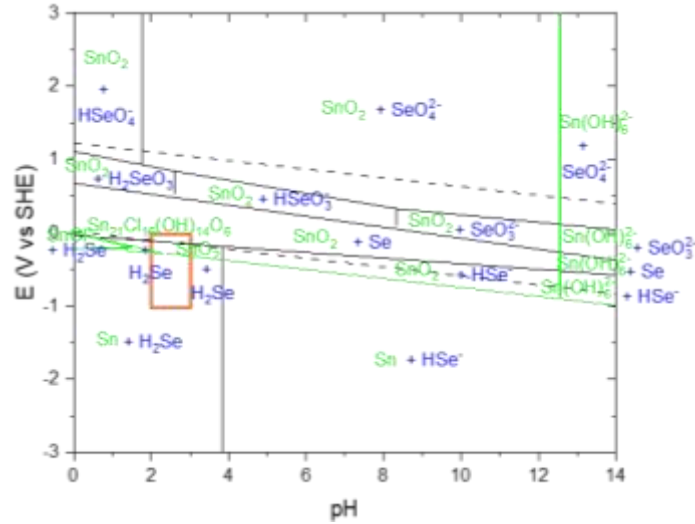
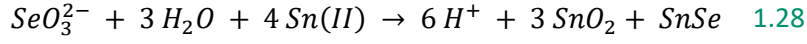
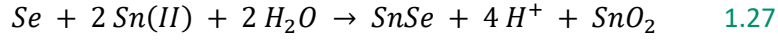
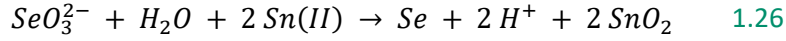


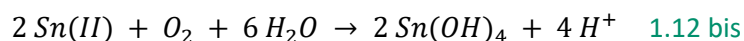
Figure 2.5: Calculated Pourbaix diagram according to our electrolyte solution conditions: 0.2 M Cl⁻, 0.2 M Na₂C₂O₄, 20 mM SnCl₂ and 5 mM Na₂SeO₃. The green rectangle corresponds to the pH area of this work.

b. Definition and preparation of the electrolyte solution

The section describes the formulation of the electrolytic bath. First of all, in order to perform the depositions under diffusion control and minimize migration mass transport, 0.2 M KCl (>99%, VWR) is used as supporting electrolyte. According to the state of the art exposed in the first chapter, we decided to work in an aqueous acidic medium based on a stannous salt (SnCl₂, ≥98%). To limit its hydrolysis, the use of a complexing agent is required. We suggest sodium oxalate (Na₂C₂O₄, >99.5%, Alfa Aesar) as a bath stabilizing reagent instead of EDTA. It is well-known for its reducing behavior ($E_{\text{CO}_2/\text{H}_2\text{C}_2\text{O}_4}^0 = -0.48 \text{ V vs NHE}$)^[151] and to be a ligand for cations^[152]. Recently, Ju *et al.* benefited for the chelating behavior of oxalate with Sn(II) to elaborate SnSe/Se composites^[157]. An advantage of sodium oxalate is its biodegradability, eco-friendlier properties and cost-efficiency compared with EDTA^[153,154].

Chapter 2. Materials and methods

The pH is adjusted at 2.5 by HCl ($\geq 37\%$, Fluka), before adding tin cation, to prevent the formation of tin hydroxides, not soluble in aqueous media ^[78] (adapted from reaction 1.12 and Figure 2.6 green and yellow).



Indeed, ICP analyses showed an important decrease of both Sn and Se quantities. After a 3 day storage at a pH of 4, the remaining concentration percentages are respectively of 63.32 % and 59.96 % (Figure 2.7 red). On the contrary, the remaining concentration percentages of Sn and Se reaches 97.98 % and 97.82 % for a 15 day storage at a pH of 2.5 (Figure 2.7 green). That is the reason why the acidification to a pH of 2.5 was retained (Figure 2.6 green and yellow).

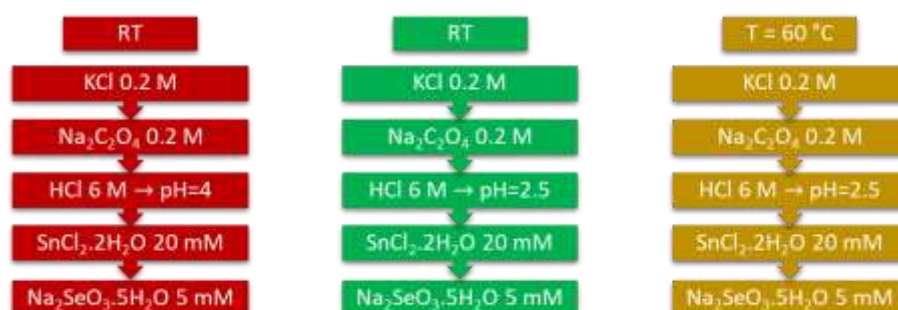
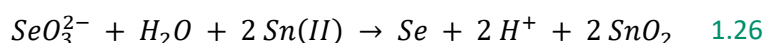


Figure 2.6: Preparation steps of the electrolyte solution by three methods: pH=4, RT (red), pH=2.5, RT (green) and pH=2.5, T=60 °C (yellow)

Sn				Se			
Relative quantity (%)	100	100	100	Relative quantity (%)	100	100	100
t = 0 days	94.97	110.10	101.54	t = 0 days	100.2	103.96	82.99
t = 1 day	x	106.06	100.51	t = 1 day	x	100.20	80.93
t = 15 days	63.32 (3 days)	97.98	82.56	t = 15 days	59.96 (3 days)	97.82	69.16
	pH=4	pH=2.5	60 °C		pH=4	pH=2.5	60 °C

Figure 2.7: Influence of the pH and of the temperature solution on the composition of the electrolyte solution (ICP analyzes)

Se(IV) ions, coming from Na₂SeO₃ ($\geq 99\%$, Fluka), were gradually introduced inside the bath to limit the precipitation of Se(0), observable by an orange precipitate (reaction 1.26). This precipitation was also reported by Engelken *et al.* ^[24]. While this precipitation is mostly avoided, a small quantity can be recovered, as proved by XRD analyses at 60 °C (Figure 2.8 orange).



Thanks to ICP analyses, we could set the good preparation and storage temperature. Indeed, it seems that at 60 °C, the Sn and Se quantities drastically decrease after 15 days. The remaining concentration percentages are of 82.56 % and 69.16 % respectively (Figure 2.7 yellow) whereas they were of 97.98 % and 97.82 % for Sn and Se respectively, at room temperature (Figure 2.7 green). Thus a high temperature favors the precipitation of Se (reaction 1.26). This precipitation was also observed after a 2 day storage at 60 °C. A black supernatant appeared and was found to be Se(0) crystallized in the hexagonal structure (Figure 2.8 black). That is the reason why the electrolyte solution must be prepared and stored at a moderate bath temperature (30 °C).

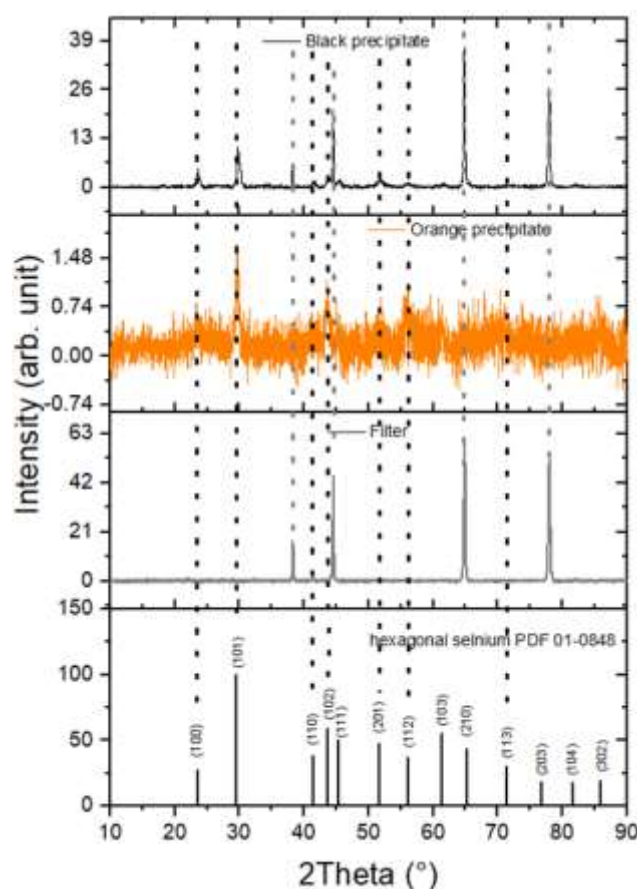
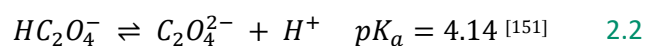
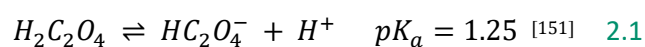
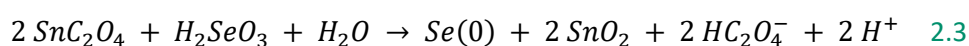


Figure 2.8: XRD analyses of Se precipitates: orange product formed during the solution preparation and black product, after a 2 day storage at 60 °C

It should be underlined that at RT and a pH of 2.5, oxalate ions should be in the form of HC_2O_4^- according to the values of the associated acid dissociation constants (reactions 2.1 and 2.2):



Consequently, the solubility of the oxalate salt (NaHC_2O_4) should be intermediate between those of $\text{Na}_2\text{C}_2\text{O}_4$ and $\text{H}_2\text{C}_2\text{O}_4$, which are respectively of 37 g.L^{-1} (0.28 mol.L^{-1})^[158] and of 108 g.L^{-1} (1.2 mol.L^{-1})^[159] at RT. However, solid products corresponding to hydrate oxalate, $\text{NaHC}_2\text{O}_4 \cdot \text{H}_2\text{O}$, were observed in the solution at RT with concentration of $\text{Na}_2\text{C}_2\text{O}_4$ of 0.2 M. Therefore, slightly increasing the bath temperature from RT to 30°C avoids the precipitation of oxalate ions. After a 2 day storage at 60°C , a pink precipitate is also observed. After filtration, we found it was composed of a red and a white precipitate. Both of them showed the presence of hydrate sodium oxalate according to PDF 70-0570 (Figure 2.9). We can suppose that after several days, tin is not complexed anymore by oxalate and gives rise to SnO_2 following reaction 2.3:



This equation is based on the fact that, after 2 days, XRD analyses revealed the presence of hydrate oxalate, $\text{NaHC}_2\text{O}_4 \cdot \text{H}_2\text{O}$, (Figure 2.9) and black selenium (Figure 2.8 black). However, no tin species was found by XRD, either because in too low quantity, or amorphous or, because this species is soluble in our electrolyte solution.

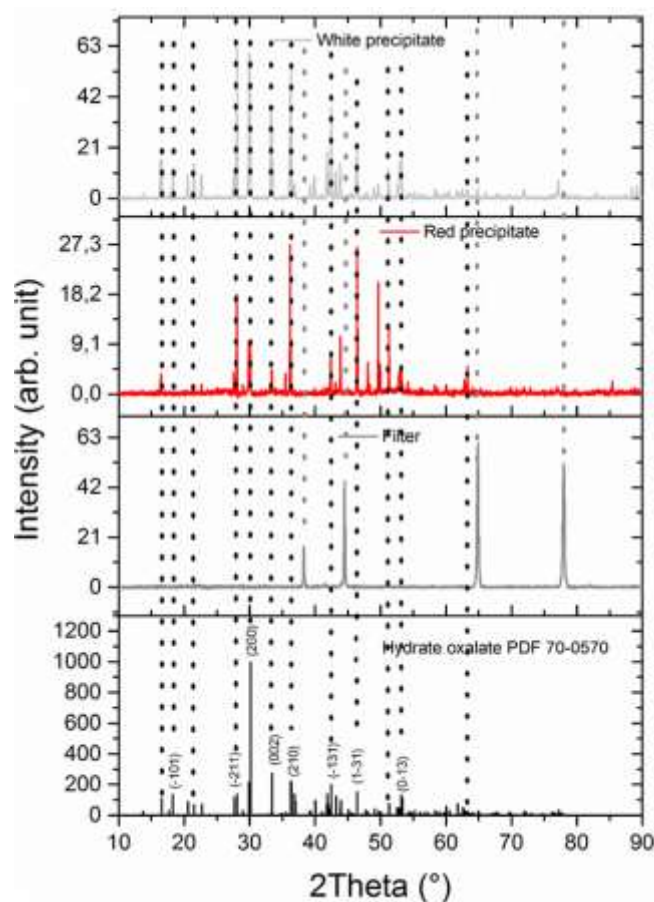


Figure 2.9: XRD analyses on oxalate precipitates obtained after a 2 day storage at 60°C

To conclude, the electrolyte solution is prepared at 30 °C as follow:

1. Dissolution of 0.2 M of KCl in water
2. Addition of 0.2 M of $\text{Na}_2\text{C}_2\text{O}_4$ and waiting until complete dissolution
3. Acidification at pH=2.5 using HCl 6 M
4. Addition of 20 mM of $\text{SnCl}_2 \cdot 2\text{H}_2\text{O}$
5. The addition of 5 mM of $\text{Na}_2\text{SeO}_3 \cdot 5\text{H}_2\text{O}$ will gradually be made just prior to the electrodeposition

c. Time evolution of the bath

From the previous section, the stability of electrolyte solution is optimized for a temperature of 30 °C. The stability of the complete electrolyte solution, as a key behavior, was studied with the follow-up of the aging of 3 samples stored at 30 °C (Figure 2.10). Higher relative quantities than the initial ones can be occasionally obtained (>100 %). These values are greater than 100 % of a maximum of 10 %, which is in the same range of the uncertainty of the ICP. A one day storage causes a small decrease of Sn, of maximum 2.99 % against 6.4 % for Se. At 3 days, Sn quantity does not change with a maximum loss of 2.49 % whereas Se content decreases up to maximum 20.68 %. Finally, for a 7 day storage, the Sn loss increases up to maximum 3.98 % and that of Se evolves to maximum 14.4 %. Globally we can observe that the Se(IV) concentration is more affected by aging than the Sn(II) concentration. To optimize the depositions, we suggest to use the electrolyte solution in a maximum of 1 day storage. Moreover, in order to preserve the Se concentration, we chose to add Na_2SeO_3 just before electrodeposition, the rest of the electrolyte solution being prepared and kept at 30 °C, following the order of addition shown in Figure 2.6.

Sn				Se			
Relative quantity (%)	100	100	100	Relative quantity (%)	100	100	100
t = 1 days	102.05	97.01	109.24	t = 1 days	96.12	93.60	105.97
t = 3 days	97.95	97.51	107.07	t = 3 days	83.47	85.20	79.32
t = 7 days	97.95	96.02	104.35	t = 7 days	89.59	85.60	86.78

Figure 2.10: Study of aging of three complete electrolyte solution samples

II. Electrochemical experiments

a. Electrochemical setup

All electrochemical experiments were carried out using an Autolab PGSTAT128N potentiostat controlled by the Nova 2.1 software. A three-electrode cell setup was used (Figure 2.11). The reference and counter electrodes were respectively a KCl-saturated AgCl/Ag electrode and a platinum wire. All the potential values will be given to this reference throughout the work. The CV experiments were performed using a glassy carbon disk electrode (0.07 cm^2) or a 300 nm platinum-coated glass electrode (0.025 cm^2 , from Kerdry, previously ACM) as working electrode. The glassy carbon disk electrode was used in order to get a better definition of the electrochemical signals with high hydrogen evolution reaction. The electrodeposition experiments were carried out with the same platinum-coated glass substrates, with a defined active surface close to 1 cm^2 . Platinum is advantageously chemically inert compared to copper or silver electrodes. It also avoids alloys like those observed between tin and gold and keep a good electrical conductivity. That is the reason why this metal was chosen as working electrode.

Before each experiment, all working electrodes were successively cleaned under a 10 minute sonication in acetone and ethanol. The part where the electrical contact was made, with a crocodile clip, was protected as much as possible with Teflon tape. The counter-electrode was regularly cleaned by an anodic etching treatment in 1 M NaOH. Some experiments were realized by separating the counter-electrode from the electrolyte solution. For this purpose, it was put in a compartment filled with a saturated KCl solution. The electrolyte solution temperature was maintained at $50\text{ }^{\circ}\text{C}$ (except for several CV experiments made at RT) thanks to heated water circulating inside the cell and a chiller from Julabo. The electrolyte solution was continuously deaerated under a continuous argon flux.

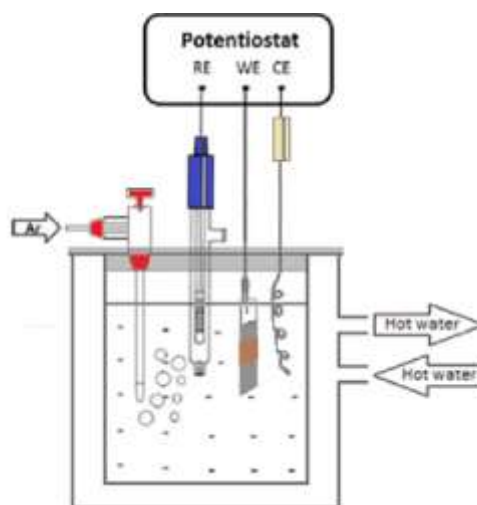


Figure 2.11: Schematic view of the experimental setup

b. Linear Sweep voltammetries (LSV) and cyclic voltammetries (CV)

For the study of the electrochemical systems, the Linear Sweep Voltammetries (LSV) were performed from the Open Circuit Potential (OCP) to the stop potential, using a scan rate of 10 mV.s^{-1} . The intensity was first recorded in the cathodic part and then in the anodic part.

For the CV experiments, the same scan rate was kept. The starting potential was fixed at the OCP and the potential was cathodically swept until the lowest vertex potential, E_1 (Figure 2.12). A diffusion cathodic peak (C) appears when M^{n+} cations are reduced into M and generate a thickness-limited layer. This peak is characterized by its minimum value of the intensity, i_p^C , reached at the peak potential, E_p^C . Then, the anodic part is scanned until the highest vertex potential, E_2 . An anodic stripping peak (A) appears at a peak potential E_p^A , with a maximum intensity of i_p^A . Its asymmetric shape makes it easy to recognize and means that the metallic layer deposited at C is oxidized into M^{n+} and dissolved. Finally, the potential is again reversed and stopped at the OCP. By switching the potential scan from the cathodic to the anodic direction, a first cross-over can appear, at a cross-over potential E_{co} . This value can be associated to the apparent equilibrium potential of the ion/metal M^{n+}/M system. A current crossover can be observed between the forward and the reverse direction and corresponds to a nucleation loop at a nucleation overpotential E_N . This phenomenon is typical of a conducting layer deposited on the working electrode and means that the reduction of M^{n+} cations requires large overpotential to form a nucleation and growth process.

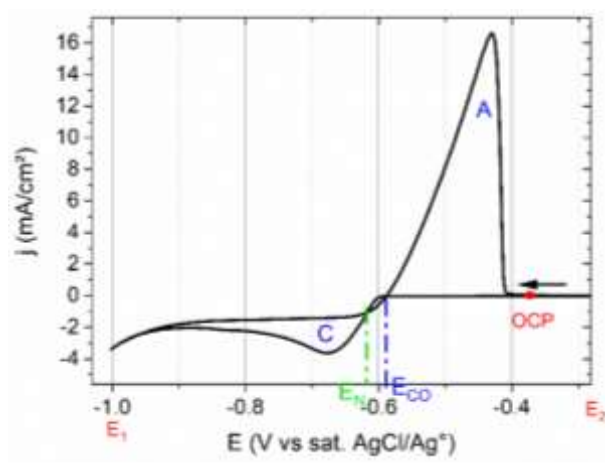


Figure 2.12: Typical cyclic voltammetry corresponding to a cathodic electrodeposition (C)/anodic stripping (A) system with the characteristic potentials : the Open Circuit Potential (OCP), the apparent equilibrium potential (E_{co}) and the nucleation overpotential (E_N)

c. Electrodeposition methods

Thanks to the preliminary CV analysis, an electrochemical window was defined, in which depositions were carried out by applying fixed potentials using potentiostatic continuous (Chapter 3) and pulse mode (Chapter 4). The samples were then systematically immersed in 0.01 M H₂SO₄, then rinsed by water then by ethanol.

The depositions performed in the continuous mode were conducted at different potentials and stopped when the desired charge quantity Q_{th} was reached. This charge quantity is calculated from the Faraday law for a targeted thickness and considering a 100 % faradaic yield (2.4):

$$Q_{th} = \frac{n F \rho_{SnSe} A h}{M_{SnSe}} \quad 2.4$$

Where Q_{th} , n , F , ρ_{SnSe} , A , h and M are respectively the theoretical charge quantity, the number of exchanged electrons, the Faraday constant (96480 C.mol⁻¹), the density of SnSe (6.192 g.cm⁻³), the deposition area, the thickness and the molar mass of SnSe (197.65 g.mol⁻¹). It should be underlined that, whatever the experiments, the deposition area was defined close to 1 cm² using Kapton tape.

In pulse deposition, the potential (or current) is switched between two values. Thus, a series of pulses, having same amplitude and duration is obtained (Figure 2.13) ^[160]. Different typical waveforms are possible depending on if unipolar (cathodic or anodic) or bipolar (both) pulse is chosen. We can cite pulse reverse or cathodic pulse followed by a period without current. The last one was investigated in this work (Chapter 4). A pulse is defined by a pulse duration called t_{ON} , during which, in our case, a potential is applied (E_{growth}) and the relaxation time t_{OFF} , during which the circuit is open (OCP) ^[161].

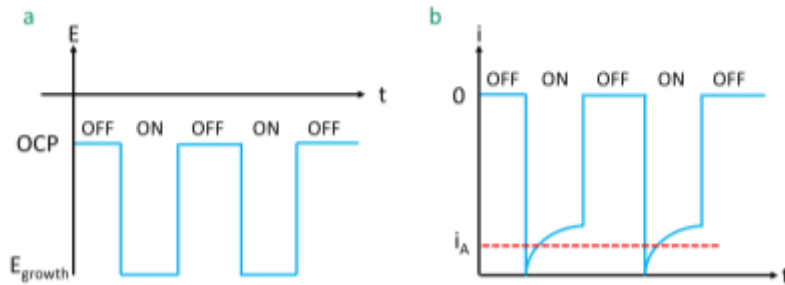


Figure 2.13: Typical pulse-potential waveform

From the estimated value of the average current (i_A) and the targeted value of Q_{th} the number N of required pulses can be calculated according to the following relationship (2.5):

$$Q_{th} = N i_A t_{ON} \quad 2.5$$

The pulse electrodeposition advantageously requires less or no additive than continuous deposition, generally reduced by 50 or 60 % ^[160]. Moreover, it should also improve the absolute limiting current density since the replenishment of ions in the diffusion layer occurs only during t_{OFF} .

- ✓ The SnSe bath is composed $\text{Na}_2\text{C}_2\text{O}_4$ and SnCl_2 as cationic precursors and is stored at 30 °C. Na_2SeO_3 is gradually added just before the experiments
- ✓ A three-electrode cell setup is used, the electrolyte solution is maintained at 50 °C and deaerated
- ✓ CVs and LSVs started from OCP to cathodic potentials at 10 mV.s^{-1}
- ✓ Continuous depositions under potentiostatic mode were realized for a fixed charge quantity
- ✓ Pulse potentiostatic depositions were performed at fixed applied potential during t_{ON} and at OCP during t_{OFF}

III. Microstructural characterizations

a. Sample preparation for analysis

To limit the roughness of the samples for a better quantitative chemical analysis by Electron Dispersive X-ray Spectroscopy (EDS), X-ray Photoelectron Spectroscopy (XPS) and Secondary Neutral Mass Spectrometry (SNMS), the samples were transferred on a non-conductive substrate according to the approach designed by Caballero-Calero *et al.* ^[162]. A piece of glass blade is glued onto the SnSe film using an epoxy based glue (Figure 2.14). After drying during at least 10 hours, the whole multilayer structure is immersed into liquid nitrogen which enables the separation of the film from the substrate.



Figure 2.14: Principle of the transfer process using glass blade

Although this process leads to SnSe films transferred on epoxy, the use of liquid nitrogen was found to be necessary, otherwise the separation would be impossible. Furthermore, SnSe deposit is

partially detached from the Pt layer. Nevertheless, this technique is adapted for EDS, XPS and SNMS analyzes since the surface state of the bottom side is mirror-like.

b. X-ray Diffraction (XRD)

The phase composition and crystallinity was determined using XRD thanks to a Bruker D8 Advance Diffractometer, equipped with a Cu-K α radiation source (1.54182 Å). The diffractometer was used at 40 mA and 40 kV. In the Bragg-Brentano configuration, X-ray beams are focused onto the sample with a wavelength of λ and an angle of θ (Figure 2.15). X photons are diffracted with an angle of 2θ from the incident beam with the same λ wavelength. The X photon flux varies according to the space direction and the detector measures their intensity.

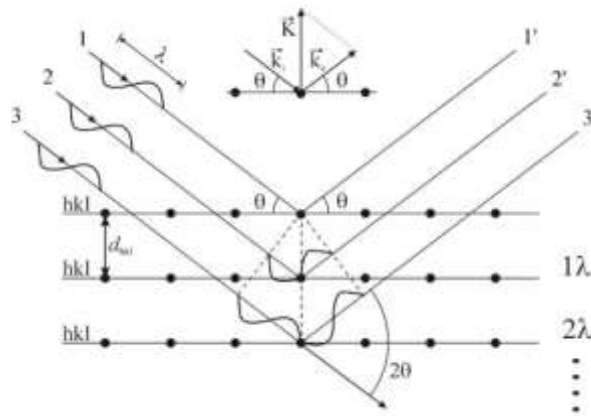


Figure 2.15: Scheme of the XRD principle ^[163]

Since λ has the same order of magnitude of the interatomic distances, the interferences of the X-rays will alternatively be constructive and destructive. The directions where the interferences are constructive, leading to the diffraction peaks, can be determined from the Bragg's law (equation 2.6):

$$2 d_{hkl} \sin \theta = n \lambda \quad 2.6$$

Where d_{hkl} , θ , n and λ are respectively the interplanar distance, the half-angle of deviation, the reflection order and the X-ray wavelength.

The result is a diffractogram where the diffraction peak intensity is plotted versus the 2θ angle. Thus, the phase composition, preferential orientations, lattice parameters and crystallite size can be determined from the pattern.

The diffraction peaks are indexed according to the Miller indexes, by comparing their angles with the theoretical ones based on JCPDS database (Joint Committee on Powder Diffraction Standards)

or COD database (Crystallography Open Database). The indexing process was realized using the EVA 5 software. We have to highlight that, since the diffraction peaks of the Pt substrate were in majority, in comparison with the contribution of the SnSe deposit, we adopted a Bragg-Brentano configuration, with a specific geometry (Figure 2.16). Here the tube and the detector were desynchronized by an angle of 10° . Consequently, the intensity of the main diffraction peak (111) of the textured Pt substrate, located at 39.54° , is strongly decreased.

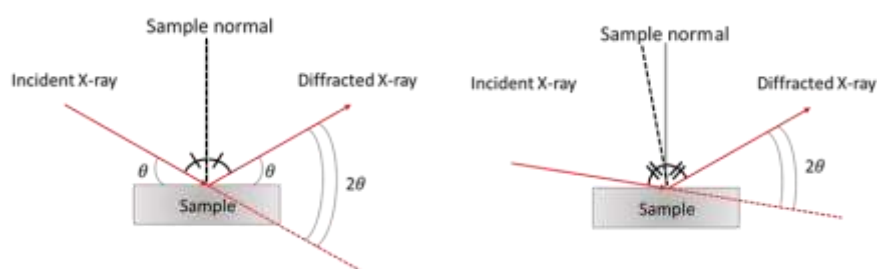


Figure 2.16: Comparison between the synchronized (left) and desynchronized (right) Bragg-Brentano configurations

c. Scanning Electron Microscopy (SEM)

To analyze the morphology of the samples, a Tescan Vega 2SBU was systematically used at a voltage of 30 kV. For high resolution images, a Philips XL30 S-FEG was occasionally used. The SEM is composed of an electron gun where a filament is submitted to an electrical field in order to extract electrons (Figure 2.17). They are then attracted into a diaphragm in order to concentrate the electron beam, before being accelerated due to the potential difference between the anode and the cathode. Thanks to electromagnetic lenses, the electron beam can be focused on the sample. The scan of the sample by the beam is ensured by deflection coils, electrically supplied by a scanning generator. When the electron beam reaches the sample, secondary electrons, backscattered electrons, Auger electrons, and also X-rays are emitted and can be collected by the appropriate detector.

The secondary electrons (SE) originate from ionizations occurring on the surface of the sample and have low energy. They give information about the topography of the sample. Backscattered electrons (BSE) can arise from greater depth with higher energies and occur when the primary electrons have reacted quasi elastically with the atomic nuclei of the sample. Since the amount of emitted BSE depends on the chemical elements, chemical phase contrasts can be observed.

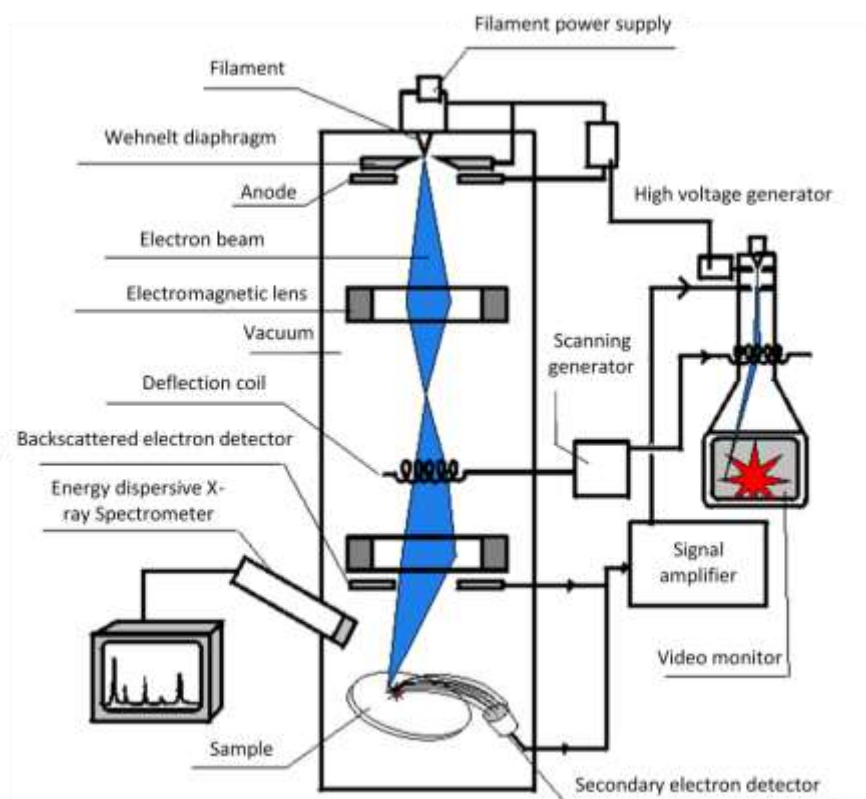


Figure 2.17: Scheme of the operating principle of a SEM ^[164]

d. Energy Dispersive X-ray Spectroscopy (EDS)

In order to complete the SEM analyses, semi-quantification was performed using a Bruker nano XFlash 410-M Spectrometer. The sample composition was determined making the average of 4 zones quantified at a $\times 15000$ magnification from the PB-ZAF calculation method. It is a standardless and self-calibrating spectrum analysis procedure. The PB-ZAF analysis is developed on modified ZAF matrix correction formulas adapted to light elements and based on the characterization of the bremsstrahlung and the contribution of the atomic numbers (Z), of the absorption (A) and of the fluorescence (F). X-ray intensities are calculated regarding the bremsstrahlung background and the peak intensities. The elements can be identified thanks to the energy of the X-rays. However, in order to optimize the semi-quantitative analysis, which can be impacted by the roughness, the EDS analyses were preferentially performed on the bottom face of the samples, which has a mirror-surface state.

e. Transmission Electron Microscopy (TEM)

SnSe lamellas were analyzed using an ACCEL ARM 200F High Resolution Transmission Electron Microscope, which is double aberration-corrected, both in probe-forming optics and in image-forming optics. SnSe 1D nanostructures were deposited on a TEM carbon grid and were analyzed using a Philips CM200 microscope. The principle of TEM is similar to the light microscope but the device uses a beam of electron to focus on thin samples (Figure 2.18). The microscope is also composed of an electron source from which electrons are ejected and further accelerated through an anode. Then, magnetic condenser lenses focus the electron beam onto the sample. The detectors are placed at the opposite side of the source in order to collect the electrons passing through the sample.

TEM has several operating modes including conventional imaging, scanning TEM imaging (STEM), electron diffraction and spectroscopy. When the incident electron beam reaches the samples, an image is formed from the interaction of the electrons with the sample. High resolution TEM enables an observation at atomic scale, useful to see defects such as dislocations or grain boundaries. When the objective aperture is inserted in the back focal of the objective lens, the diffracted beams interfere with each other and with transmitted beam forming an interference pattern. The result is a phase-contrast imaging for HRTEM imaging. The resulting figure can be analyzed by Fast Fourier Transform calculation and the crystal structure as well as the lattice parameters and preferential orientations can be determined. Scanning Transmission Electron Microscopy (STEM) is similarly used as SEM, the difference taking place in the interaction volume, decreased since the sample is thinner^[165]. The scans are performed either in Bright Field (BF) mode or in High Angle Annular Dark Field (HAADF) mode. In the BF mode, a diaphragm is placed to select the transmitted beam, thus 100 % of the electrons are transmitted in absence of sample and the image appears clear. In case of HAADF mode, another diaphragm is used to select scattered electrons. In absence of sample, all of the electron beam is transmitted and no electrons are scattered, thus the image is black. When a sample is introduced, an annular dark field image is generated thanks to scattered electrons at high angle^[166]. This mode is highly dependent on the atomic number: high atomic number elements lead to more scattered electrons and thus to brighter image.

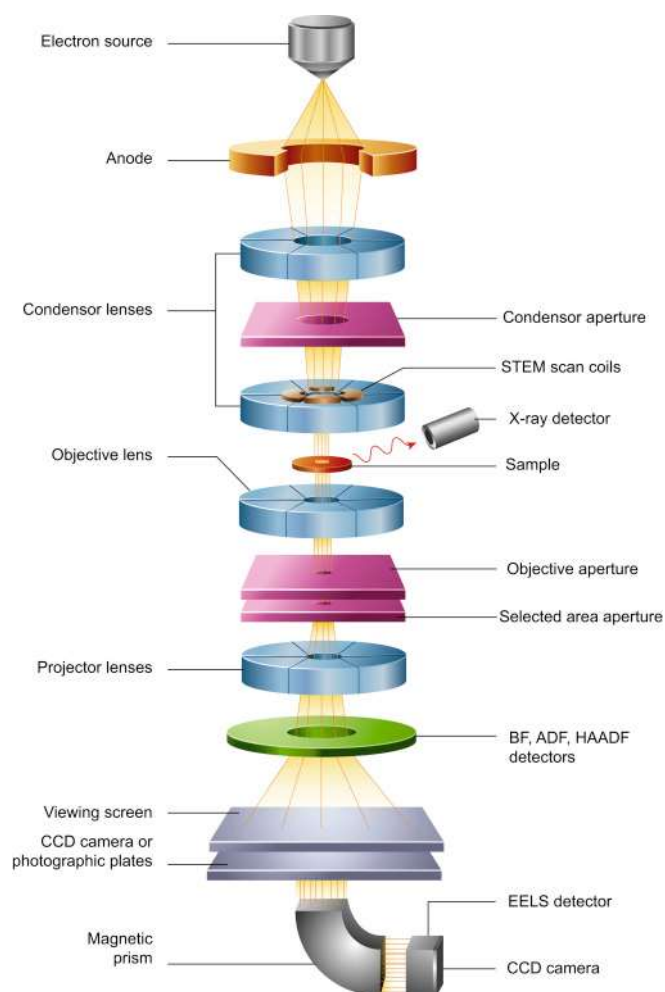


Figure 2.18: Scheme of the operating principle of a TEM ^[167]

f. Focused Ion Beam (FIB)

SnSe lamellas were prepared using FIB, from a SEM-FIB Helios Nanolab 600i-FEI system. Coupled to a SEM device, imaging is possible during the process of lamellas fabrication. A Liquid Metal Ion Source is usually used but a plasma source can replace the first one (Figure 2.19). Here the source is a Ga^+ source. A condenser lens is used to focus the ion beam. The blanking and Faraday cup are used to deflect the beam off the sample and measure the ion current. The circular beam shape is ensured by octupoles ^[168]. First, platinum was electronically and then ionically deposited to protect the zone of interest. According to the tilt angle, the shape and thickness of the sample can be tuned. Thus, 50 nm thick lamellas can be made. Ion beam is focused on both sides of the interesting zone, in order to dig up and down. Tilting the sample progressively thins it out.

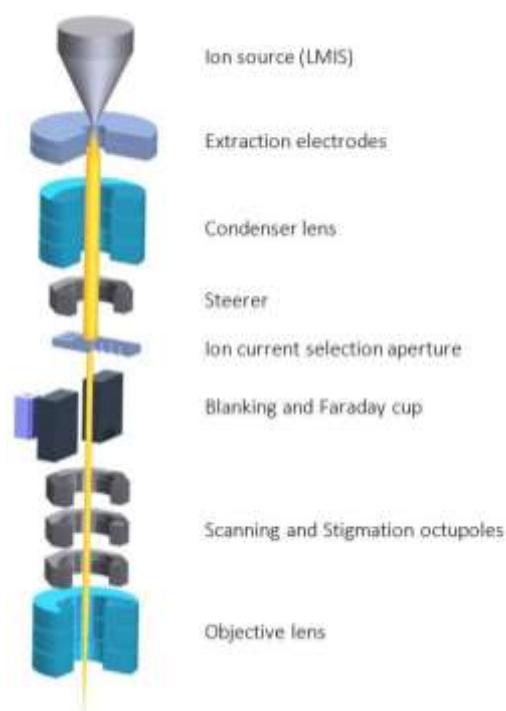


Figure 2.19: Schematic view of a FIB system ^[168]

The microstructure of the deposits will systematically be characterized using:

- ✓ XRD in a Bragg-Brentano configuration desynchronized of 10 °
- ✓ SEM using a voltage of 30 kV and EDS preferentially made on bottom face
- ✓ Occasional TEM characterizations using on lamellas prepared by FIB

IV. Other chemical characterization techniques

a. Inductively Coupled Plasma-Optical Emission Spectroscopy (ICP-OES)

An ICP-OES Avio 200 from Perkin Elmer was used to study the time dependence stability of the electrolyte solution and to determine the chemical composition of deposits after chemical etching. After dilution, generally in diluted acidic medium HNO_3 2 %, the sample is injected into an argon plasma thanks to a pneumatic system called nebulizer (Figure 2.20). Then, inside the nebulization chamber, the smaller particles are selected by different physical segregation methods, such as sedimentation, centrifugation or impact on an obstacle. The plasma, having a temperature until 10000 K ionizes the

molecules of the samples. A detector then measures the light emitted when the molecules return to their fundamental state ^[169]. The analysis can be performed either in radial or in axial view. The radial view consists in detecting the light perpendicularly to the plasma. Thus, less plasma is analyzed, less light is emitted and so this method is less sensitive. However, this method reduces the interferences and matrix effects thus the precision is improved ^[170]. In the axial view, the light is parallel to the plasma which leads to high sensitivity. Nevertheless, interferences impact the precision.

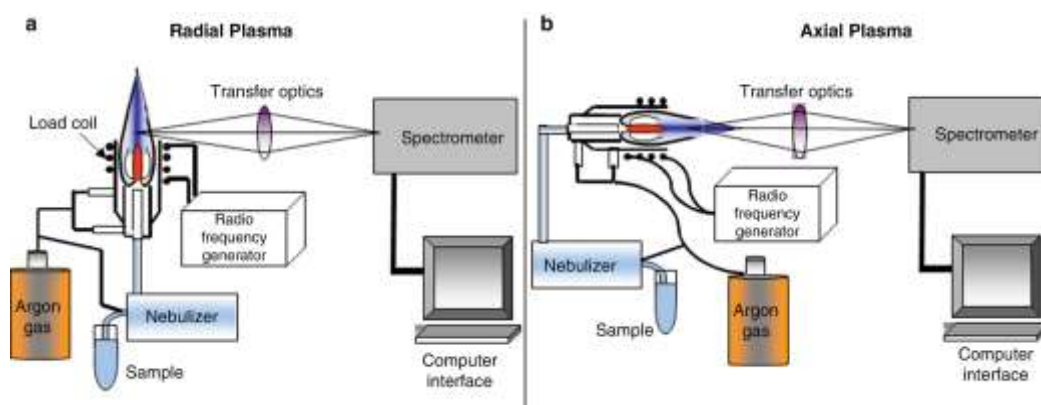


Figure 2.20: Principle of the operating process of an ICP-OES instrument ^[171]

b. Conversion Electron Mössbauer Spectrometry (CEMS)

A conventional spectrometer from Wissel with a flowing gas (96 % He, 4 % CH₄) proportional counter Rikon-5 were used for analyzing the samples. The error on all of the ¹¹⁹Sn Mössbauer spectra was $\pm 0.1 \text{ mm.s}^{-1}$. A radioactive source, fixed on the shaft of a vibrator to ensure a constant velocity, emits γ photons having a certain energy ^[172] (Figure 2.21). When the transition energy of both the radioactive source and the sample are identical, the nuclear resonance appears. In case of solid samples, the nuclear resonance occurs without recoilless resonance absorption. The nuclear resonance is strongly decreased for gas or liquid, thus, Mössbauer spectrometry is only adapted to solid samples. Moreover, this phenomenon is only observed for transitions from excited to fundamental states having energies lower than 100 keV. That is the reason why only 44 elements can be studied and 16 are used as radioactive sources. Among the most studied elements, we can find ⁵⁷Fe, ¹¹⁹Sn, ¹¹⁹Sb, ¹⁹⁷Au and rare earth isotopes ^[173].

The source is adapted to the studied isotope, in this work ¹¹⁹Sn is then used to study tin in SnSe. When the γ photons reach the sample, it in turn emits Auger electrons, backscattered electrons, X and γ photons. In transmission MS, the sample is placed between the source and the detector and γ photons are detected but the entire sample is analyzed in thickness. In the case of CEMS, which is a

surface analysis, the sample is placed inside a flowing gas counter and a thickness of about 300 nm is analyzed, depending on the material. Backscattered electrons are detected in this case. The flowing gas counter delivers pulses proportional to the energy of ionized particles that go through it. Here He is ionized and CH₄ is used as a cut-off gas. Compared to transmission configuration, CEMS improves the signal on noise ratio.

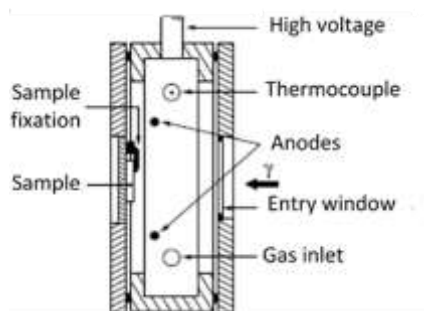


Figure 2.21: Scheme of a flowing gas counter ^[173]

During the experiment, the nuclei undergo splitting of energy levels, due to electrical and magnetic fields, called hyperfine interactions. They are quantifiable thanks to three parameters:

- The isomer shift which is linked to the oxidation degree, the nuclear spin, the coordination, the chemical bonding and the ligands
- The quadrupolar splitting which is related to the asymmetry of the charge distribution
- The magnetic hyperfine splitting which results from the interaction between the nuclei and the magnetic field

All parameters can be adjusted from least-square fitting, which was made using the Winnormos (Wissel) program. The quality of the obtained spectrum reflects the crystalline quality of the sample: fine lines indicate good crystallinity whereas widening or overlapping means defects, topologic and/or chemical disorder or relaxation phenomenon.

c. Raman spectrometry

To complete the film composition analysis, in addition to XRD, Raman spectra were recorded from a Horiba Jobin Yvon LabRam HR 800 spectrometer with a laser having a wavelength of 532 nm, in Madrid. The laser power and the integration time were adjusted according to each sample, to maximize the signal without damaging the material. The system consists of a continuous laser that emits a monochromatic wavelength which is then focused by a microscope lens at the surface the sample (Figure 2.22). The sample can advantageously be liquid or solid, which makes it an analysis of

interest, especially since it is relatively non-destructive. A turntable allows to correctly place the sample with respect to the laser. The laser spot size depends on the laser wavelength as well as the microscope objective. For standard Raman microscope, the spot size varies from 0.5 to 10 μm . The damages were first detected from the images given by the optical microscope. In the case of severe induced degradation the Raman spectra can also be significantly affected.

When the laser interacts with the sample, it emits light, but with a different frequency. This frequency change is called the Raman effect and this change depends on the frequencies of the chemical bonds present in the sample. During the experiment, the major part of the diffused light is provided by the Rayleigh scattering (without frequency variation). Thus a filter is placed between the sample and the detector to be sensitive to wavelengths really close to the incident one. The intensities and frequencies of the Raman scattered light vary according to the nature of the chemical bonds or the temperature. Moreover, processing the measurement in different conditions helps to determine the crystal structure ^[174]. Stretching modes occur at higher energies and thus at higher wave numbers than bonding modes, which occur at lower energies and are dependent of the compactness of the structure. The intensity increases for covalent bonds and is very weak for ionic bonds. Finally, this analysis can be quantitative since the intensity is related to the concentration of the different species.

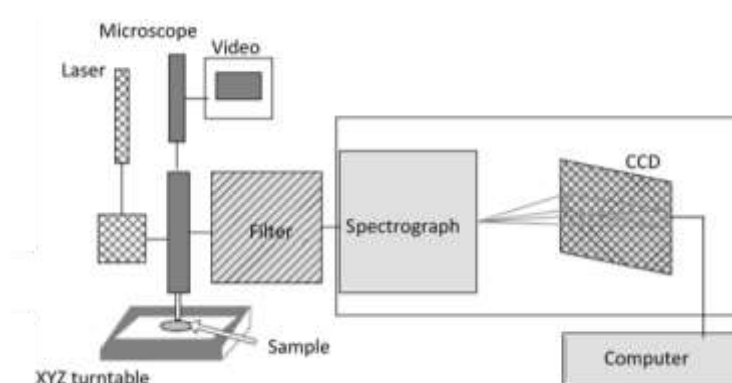


Figure 2.22: Scheme of Raman spectrometer ^[174]

d. Secondary Ion and Neutral Mass Spectrometry (SIMS and SNMS)

The depth profile obtained by SIMS was determined using an IMS-7F and Cs^+ ions bombardment on the top face. The analyzes carried out by SNMS were performed on the bottom face of the samples, which gives a better depth resolution at the vicinity of the substrate. For SNMS experiments, an INA-X, SPECS GmbH with an Ar^+ ions bombardment was used on bottom face of the

samples. A 350 V sputtering potential as well as a current density about 1 mA.cm^{-2} were maintained at a frequency of 100 kHz and with a 80 % duty cycle. The post-ionized neutral particles were directed into a quadrupole mass spectrometer Balzers QMA 410. A Nb mask was employed to maintain the erosion area into a 3 mm diameter circle. In order to get the sputtered depth and to calculate the sputtering rate, a profilometer (Amphios XP-I) was used.

SIMS and SNMS advantageously give quantitative results in agreement with the real concentrations under stationary conditions while techniques like XPS tend to give concentrations deviating from the reality ^[175]. Indeed, XPS needs an appropriate calibration and long sputtering time which represents strong effort. That is the reason why SIMS and SNMS are beneficial for depth profile analyzes and the control of sample material removal. A first difference between SIMS and SNMS is the strong matrix effects in secondary ion formation, which is absolutely eliminated in SNMS technique.

The equipment are similarly composed of a vacuum chamber, where a plasma is maintained at a high frequency (Figure 2.23). This plasma, containing ions (Cs^+ for SIMS, Ar^+ for SNMS), bombards the sample which leads to atomic collision cascade ^[176]. As a result, either the primary ions (from the plasma) are stopped or backscattered. Another possibility is the generation of secondary ions generated by the sputtering itself (1 % of the emitted particles) or neutral atoms inducing ions by post-ionization inside the plasma (99 % of the emitted particles). Thus, the secondary ions are analyzed by SIMS and the SNMS analyzes the ions produced by post-ionization. The residual gas ions are suppressed providing ion optics. Finally, the secondary particles are then accelerated to a quadrupole mass spectrometer, supplemented with a secondary electron multiplier in order to evaluate qualitatively the sputtered depth. Semi-quantitative results can be obtain, from calculation based on the dataset of the sensitivity values.

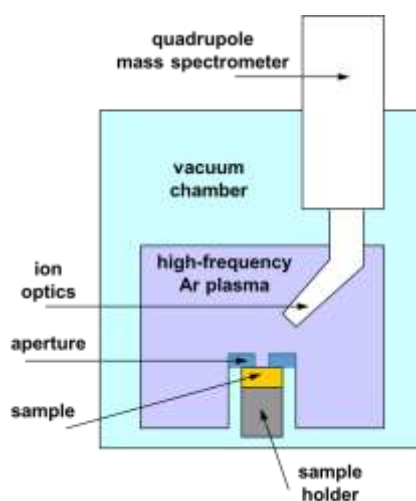


Figure 2.23: Schematic view of a SNMS system

e. X-ray photoelectron spectroscopy

To investigate the oxidation degrees of Sn and Se, top face surface analyses were performed with a spectrometer integrating OMICRONnano material. A conventional power of 300 W (15 kV and 20 mA) was applied. The system is equipped by an Al anode, without monochromator. If necessary, cleaning of the samples was made using Ar ions accelerated at a voltage of 5 kV and a current between 35-40 μA , during 3 to 9 minutes. This cleaning step enables to remove adsorbed species such as CO_2 or even water coming from ambient atmosphere.

X-ray photons provided by a source are bombarded onto a sample (Figure 2.24). The sample is thus ionized and emits photoelectrons. These photoelectrons go through optics to be slow down, before going into an analyzer. Since the photoelectrons have energies depending on the chemical elements, it allows to determine the chemical composition of our deposits. The chemical state of each element can also be determined since energy shifts occur with the chemical state. This analysis is only possible on solids and all elements except H and He, since they just have valence electrons. Moreover, this method can be quantitative if at least 5 % of the analyzed elements are present ^[177].

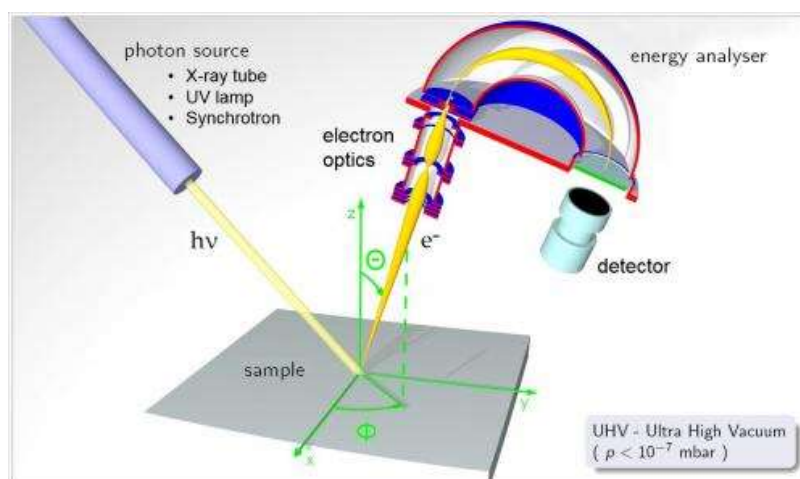


Figure 2.24: Scheme of the operating principle of the XPS ^[178]

f. Ellipsometry

Samples were optically characterized by ellipsometry. Variable angle spectroscopic ellipsometry measurements were carried out using a phase-modulated setup (UVISSEL, Horiba Jobin Yvon). The optical interface was modeled using the commercially available DeltaPsi2 software. Typical $\Delta - \Psi$ spectra were recorded for incidence angles between 60° and 70° in steps of 5° . The wavelength of the spectrum was 260 nm-860 nm in steps of 5 nm.

A light source is collimated and linearly polarized thanks to a polarizer (Figure 2.25). After reaching the sample, the light, whose polarization is modified, is reflected through an analyzer before being detected. The modification of the polarization is dependent on the studied surface. From the polarization of the incident light and the intensity of the reflected light, different physical properties can be obtained from wave-matter interaction modelling ^[179]. These properties can be the thickness with a precise resolution (range of Angstrom), optical constants or optical bandgap ^[180]. For the study of SnSe films, as non-transparent layer, this technique is of great interest for determining the optical constants n (real refractive index), k (extinction coefficient) and consequently determining the optical bandgap through the absorption coefficient α . The measurement at given incident angle and wavelength enable to determine the values of n and k , from modelling, thanks to equation 2.7:

$$N = n - ik \quad 2.7$$

Where N is the complex refractive index and i the imaginary number. The optical constant can alternatively be expressed by the complex dielectric function

$$\varepsilon = \varepsilon_1 + i\varepsilon_2 \quad 2.8$$

$$\text{with } \varepsilon_1 = n^2 - k^2 \quad 2.9 \quad \text{and } \varepsilon_2 = 2nk \quad 2.10$$

Then, α is determined from equation 2.11:

$$\alpha = \frac{4\pi k}{\lambda} \quad 2.11$$

Where α , k and λ are respectively the absorption coefficient, the extinction coefficient and the light wavelength.

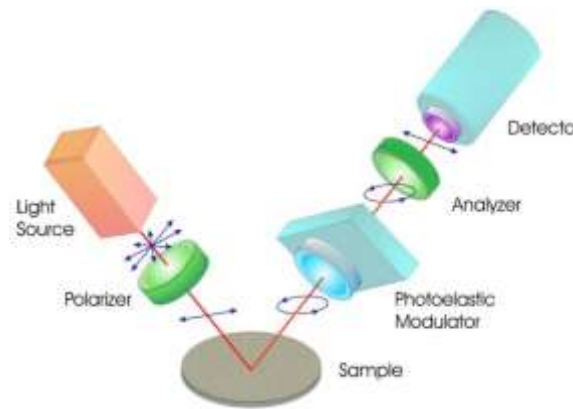


Figure 2.25: Scheme of the ellipsometry principle ^[180]

Additional characterizations were made by:

- ✓ ICP to investigate the bath stability and the chemical composition of the deposits after etching
- ✓ CEMS to exhibit the oxidation degree of tin in the films
- ✓ Raman spectrometry to investigate the presence of additional phases undetectable by XRD
- ✓ SIMS and SNMS to study the in-depth homogeneity of the deposits
- ✓ XPS to reveal surface oxidations degrees of Sn and Se and potential other elements
- ✓ Ellipsometry to determine the optical bandgap

Conclusion

This second chapter exposes the whole materials and methods used during this thesis. Thus, in the first part we reported the electrochemical bath composition, as well as its optimization and its long term relative stability. The setup and procedure adapted to the electrodeposition were also described. The second part focuses on the techniques systematically devoted to the microstructural characterization of SnSe deposits. Some characterizations by TEM were also performed from lamellas prepared by FIB. Finally, in the last part, we reported the other techniques we used, allowing the determination of the chemical composition and the oxidation degrees of the elements. Gap values could be obtained from ellipsometry.

Ce second chapitre expose l'ensemble des matériels et méthodes utilisés au cours de cette thèse. Ainsi, en première partie nous avons reporté la composition du bain électrochimique, ainsi que son optimisation et sa stabilité relative sur le long terme. Le montage ainsi que la procédure adaptés à l'électrodéposition ont également été décrits. La seconde partie se focalise sur les techniques systématiquement employées pour la caractérisation microstructurale des dépôts de SnSe. Quelques caractérisations par TEM ont également été effectuées à partir de lames préparées par FIB. Enfin, en dernière partie, nous avons reporté les autres techniques auxquelles nous avons eu recours permettant la détermination de la composition chimique et des degrés d'oxydations des éléments. Des valeurs de largeur de bande interdite (gap) pourront être obtenues par ellipsométrie.

Chapter 3.

Continuous
electrodeposition of
SnSe films

Introduction

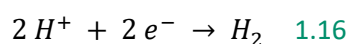
This third chapter introduces the studies devoted to the synthesis of SnSe films under continuous potentiostatic mode. In order to understand the SnSe electrochemical system, the electrochemical stability window, as well as the tin and selenium systems will be separately investigated in the first part. From the study of the complete electrolyte solution, an electrodeposition potential window will be defined. The influence of the deposition potential and the growth time as well as the counter-electrode on the quality of the films will be investigated. Deep characterizations both from a microstructural and chemical composition point of view will highlight the best deposits.

Ce troisième chapitre présente les études consacrées à la synthèse de films de SnSe en mode continu potentiostatique. Afin de comprendre le système électrochimique de SnSe, le domaine d'électroactivité ainsi que les systèmes de l'étain et du sélénium seront étudiés séparément en première partie. A partir de l'étude de la solution électrolytique complète, une fenêtre de potentiels d'électrodéposition sera définie. L'influence du potentiel et du temps de déposition ainsi que celle de la contre-électrode sur la qualité des films sera investiguées. Des caractérisations approfondies tant du point de vue microstructural que de la composition chimique permettront de mettre en évidence les meilleurs dépôts.

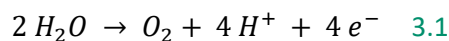
I. Study of the electrochemical systems

a. Electrochemical stability window

To investigate the electrochemical behavior of the supporting electrolyte, that is to say only diluted KCl and acidified at a pH of 2.5, a LSV was recorded on GC (Figure 3.1 black line). The reduction reaction of H^+ into H_2 starts from -1.66 V vs AgCl/Ag (reaction 1.16).



The oxidation of H_2O into O_2 is observed from 1.87 V vs AgCl/Ag (reaction 3.1). On platinum-coated glass, the solvent decomposition occurs at lower overpotentials since the reduction and oxidation are respectively observed from -0.80 V and 1.13 V vs AgCl/Ag (Figure 3.1 grey line). Since the stability window is reduced on platinum, we conclude that platinum has a catalytic behavior.



When adding oxalate salt, the electrochemical stability window becomes smaller, ranging from -0.90 V to 0.96 V vs AgCl/Ag on GC (Figure 3.1 black dashes). On platinum, the window is reduced again, from -0.32 V to 0.73 V vs AgCl/Ag (Figure 3.1 grey dashes). The catalytic behavior of platinum is thus confirmed in presence of oxalate. Moreover, the presence of oxalate salt decreases the electrochemical stability window.

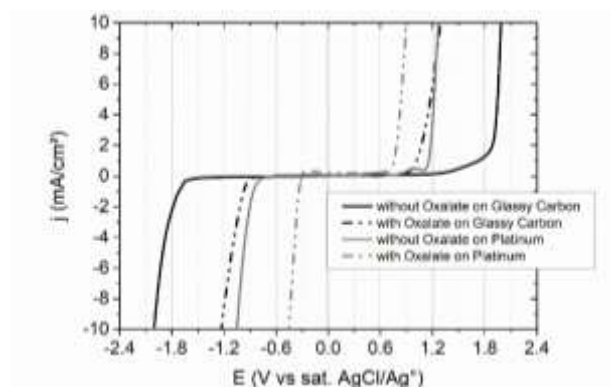


Figure 3.1: LSVs on the electrolyte solution containing 0.2 M KCl and with or without 0.2 M $\text{Na}_2\text{C}_2\text{O}_4$ at 50 °C and pH=2.5 ^[181]

In order to be sure that this decrease is due to the solvent decomposition and not to redox reactions associated to oxalate, we investigated the electrochemical stability window in presence of oxalate at various pH (Figure 3.2 a). According to the standard redox potential of $\text{CO}_2/\text{H}_2\text{C}_2\text{O}_4$, ($E_{\text{CO}_2/\text{H}_2\text{C}_2\text{O}_4}^0 = -0.48 \text{ V vs NHE} = -0.68 \text{ V vs AgCl/Ag}$) ^[151], the oxidation is expected at higher overpotential than the potential window of the solvent. As it can be seen, the electrochemical stability window is shifted to more cathodic potentials as the pH increases. Moreover the potential window is reduced from 1.30 V at pH=0.35 to 1.14 V at pH=3.5.

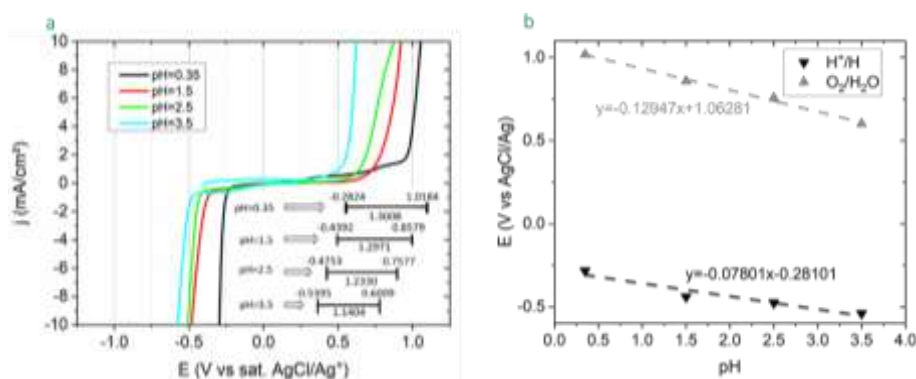


Figure 3.2: (a) Typical LSVs and (b) variation of the solvent decomposition potentials with the pH in the electrolyte solution containing 0.2 M KCl and 0.2 M $\text{Na}_2\text{C}_2\text{O}_4$ at 50 °C on Pt electrode

Chapter 3. Continuous electrodeposition of SnSe films

To explain this observation, the equilibrium potential of the H^+/H_2 couple, E_{H^+/H_2} , can be obtained following equations 3.2:

$$E_{H^+/H_2} = E_{H^+/H_2}^0 + \frac{R T}{2 F} \ln \frac{a_{H^+}^2}{a_{H_2}} \quad 3.2 \text{ a}$$

$$E_{H^+/H_2} = E_{H^+/H_2}^0 + \frac{R T}{2 F} \ln \frac{[H^+]^2}{P_{H_2}} \quad 3.2 \text{ b}$$

$$E_{H^+/H_2} = E_{H^+/H_2}^0 - \frac{2.3 R T}{2 F} \log P_{H_2} + \frac{2.3 R T}{F} \log [H^+] \quad 3.2 \text{ c}$$

By considering $P_{H_2} = 1 \text{ atm}$ and a temperature $T = 323 \text{ K}$, we obtain equation 3.2 d:

$$E_{H^+/H_2} = E_{H^+/H_2}^0 - 0.064 \text{ pH} \quad 3.2 \text{ d}$$

Where E_{H^+/H_2}^0 , R , a_{H^+} and a_{H_2} are respectively the standard potential of the H^+/H_2 couple, the universal gas constant ($8.314 \text{ J.mol}^{-1}.\text{K}^{-1}$), the chemical activity of H^+ and the chemical activity of H_2

Thus an increase of the pH obviously decreases the equilibrium potential. A comparison can be made between the experimental values and the calculated ones according to the equation 3.2 d. The experimental values were graphically estimated at a current density of -5 mA.cm^{-2} and reported in Figure 3.2 b. A dependence of -0.078 pH is found by a linear fit. The absolute value of this slope is higher than the expected one (0.064). This difference may result from several reasons such as non-equilibrium state, approximations on the calculation or protonation of oxalate which changes the pH. Whatever the reason, the observed evolution of the cathodic limit appears to be governed by the pH.

A similar reasoning can be made for the anodic part, considering E_{O_2/H_2O} as the equilibrium potential of the O_2/H_2O couple following equations 3.3:

$$E_{O_2/H_2O} = E_{O_2/H_2O}^0 + \frac{R T}{4 F} \ln \frac{a_{O_2} a_{H^+}^4}{a_{H_2O}^2} \quad 3.3 \text{ a}$$

$$E_{O_2/H_2O} = E_{O_2/H_2O}^0 + \frac{R T}{4 F} \ln (P_{O_2} [H^+]^4) \quad 3.3 \text{ b}$$

$$E_{O_2/H_2O} = E_{O_2/H_2O}^0 + \frac{2.3 R T}{4 F} \log P_{O_2} + \frac{2.3 R T}{F} \log [H^+] \quad 3.3 \text{ c}$$

By considering a partial pressure P_{O_2} equal to 1 atm we obtain equation 3.3 d:

$$E_{O_2/H_2O} = E_{O_2/H_2O}^0 - 0.064 \text{ pH} \quad 3.3 \text{ d}$$

Where E_{O_2/H_2O}^0 , a_{O_2} and $a_{H_2O}(=1)$ are respectively the standard potential of the O_2/H_2O couple, and the chemical activities of O_2 and of H_2O

As before, we can compare the experimental values with the calculated ones (Figure 3.2 b). The experimental points, graphically estimated at 5 mA.cm^{-2} , are well aligned and give rise to slope close to -0.13. The absolute value of this slope is almost two times higher than the expected one (0.064) and remains unexplained. The overall results confirm the lower overpotentials at higher pH. Although there is a difference between the values, we consider that the anodic limit is governed by the oxygen evolution reaction.

To conclude, the evolution with the pH confirms that the reduction and oxidation limit of the electrochemical stability window is governed by the solvent and not to oxalate.

b. Study of Sn electrochemical system

In order to prepare the electrodeposition of SnSe films, it is necessary to understand the separate electrochemical behavior of the precursors. Thus we firstly studied the Sn electrochemical system at various conditions. Before the explanation of the preliminary electrochemical studies, the composition of the electrolyte solution is reminded in Figure 3.3.

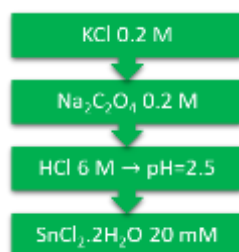
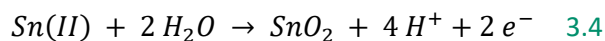
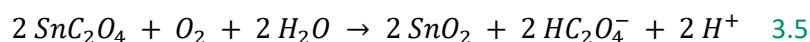


Figure 3.3: Composition of the electrolyte solution for Sn electrochemical studies

As it can be seen in Figure 3.4, the Sn electrochemical system is reversible, with a reduction peak C1 at -0.65 V vs AgCl/Ag, corresponding to the reduction of Sn(II) into Sn(0) (reaction 1.15) and an anodic stripping peak A1 at -0.43 V vs AgCl/Ag, which is due to the reverse reaction. A broad and weak anodic peak, A2, about 0.85 V vs AgCl/Ag may occur from the oxidation of Sn(II) into Sn(IV). This species should be SnO_2 as a passive layer, because we never saw the associated reduction peak (reaction 3.4). Moreover, from the Pourbaix diagram (Figure 1.11 and Figure 2.1), we expect its generation according the equation 3.4.



An increase of the temperature to 50 °C slightly increases the current density of the reduction reaction (Figure 3.4 a). The related anodic stripping peak A1 has also a higher current density, which means that the quantity of deposited Sn is improved at 50 °C. By comparing the voltammeteries in absence and in presence of sodium oxalate (Figure 3.4 b), the reduction potential of Sn(II) into Sn(0) is clearly shifted to more negative potentials since the reduction peak is observed at -0.53 V vs Ag/AgCl without oxalate. Moreover, switching the direction of the potential scan to the anodic direction generates a cross-over, called E_{CO} , which is associated to the apparent equilibrium potential of the Sn(II)/Sn system. Without oxalate, this value is of -0.46 V vs AgCl/Ag. In comparison with the standard redox potential which is -0.34 V vs AgCl/Ag^[15,136], this difference can be explained by the activity of the cation and/or a possible complexation with chloride. A shift of the E_{CO} value to -0.6 V vs AgCl/Ag in presence of oxalate appears. This phenomenon is in agreement with the hypothesis of a complexation between oxalate and tin. Another important point is the stability of the solution (Figure 3.4 c). Indeed, after a 2 day storage at 60 °C, the signals due to the redox reactions are considerably reduced, even canceled and the solution remains unusable. According to the Pourbaix diagram (Figure 2.1), this could be due to the dissociation of tin oxalate, leading to the formation of SnO₂ according to the following reaction 3.5:



However, the formation of a soluble chelated Sn(IV) species cannot be excluded. Finally, in order to prepare the electrodeposition on platinum, a CV was recorded on this substrate (Figure 3.4 d). The use of platinum as a working electrode increases the current density and slightly shifts the reduction potential from -0.68 V to -0.63 V vs AgCl/Ag. Furthermore, an additional peak, C0, precedes the C1 peak at -0.54 V vs AgCl/Ag. This peak can come from UPD of Sn on Pt, or the reduction of the solvent as suggested by the electrochemical stability window (Figure 3.1). The formation of Sn UPD layers has been discussed in the literature since the discovery of the promoting effect of the Sn adlayer on Pt to the oxidation of various compounds (like CO and CH₃OH)^[182–187].

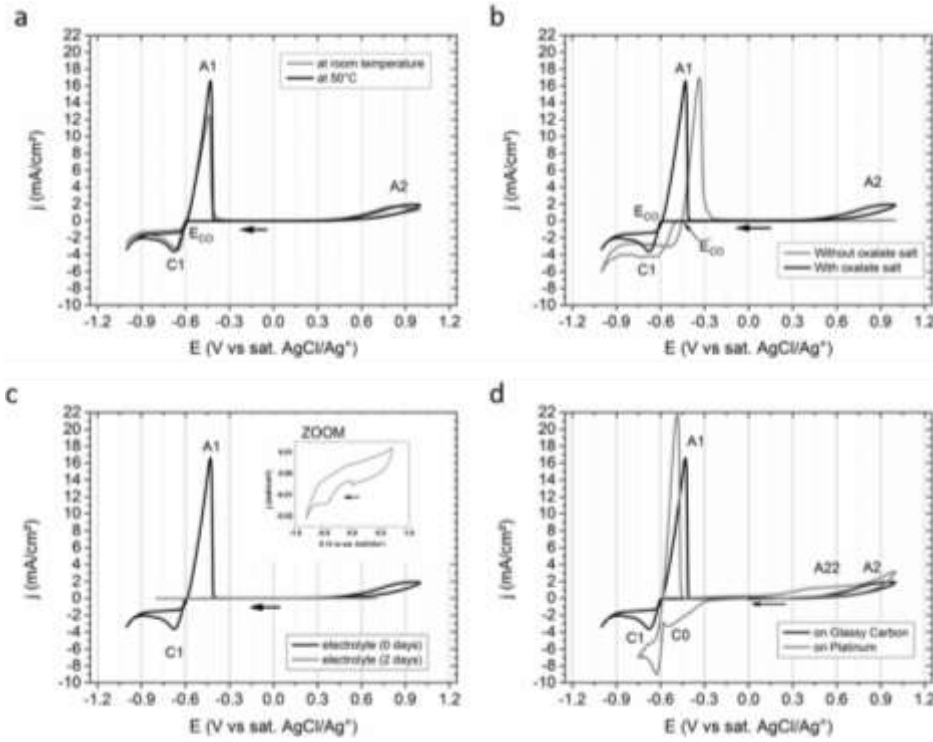


Figure 3.4: Typical CV of Sn electrolyte solution: influence of (a) the temperature, (b) the complexing agent, (c) the time and (d) the substrate ^[181]

To complete the electrochemical study of tin in this electrolytic bath, we performed several CVs on a rotating GC electrode in order to determine the diffusion coefficient of Sn(II) by the Levich method (equation 3.6). This study was made at RT and at 50 °C in an electrolyte solution in presence of oxalate salt. Without oxalate, the solution becomes cloudy, thus disturbing the evolution of the current. We graphically measured a current at -0.75 V vs AgCl/Ag, considered as a diffusion limit current. Then, the Levich equation was used to obtain the value of the diffusion coefficient.

$$i_{lim} = -0.621 n F A C D^{2/3} \nu^{-1/6} \omega^{1/2} \quad 3.6$$

Where i_{lim} , n , F , A , C , D , ν and ω are respectively the diffusion-limited current (in A), the number of involved electrons (here 2), the Faraday constant (96480 C.mol⁻¹), the electrode area (0.07 cm²), the Sn(II) concentration (20 mmol.L⁻¹ i.e. 2.10⁻⁵ mol.cm⁻³), the Sn(II) diffusion coefficient (value in cm².s⁻¹), the kinematic viscosity of water (10⁻² cm².s⁻¹) and the angular rotation rate (in rad.s⁻¹). Concerning the kinematic viscosity, we have approximated the value at 50 °C to that at 20 °C.

As it can be seen on the CVs (Figure 3.5), a plateau can be easily reached at RT, whereas it is more difficult at 50 °C. This is typical of dendrite-forming metal. To solve this problem, a higher sweep rate as well as a lower Sn(II) concentration can be used. Moreover, the pre-deposition of a smooth Sn layer helps to avoid the formation of dendrites. Moreover, at high rotation rates, the system becomes

Chapter 3. Continuous electrodeposition of SnSe films

disturbed and there is no further linear relation between the intensity and the rotation rate. However, for lower rotation rates, we can deduce a linear relation, which confirms the diffusion control. Diffusion coefficients of $5.46 \pm 0.77 \times 10^{-6} \text{ cm}^2.\text{s}^{-1}$ at RT and $2.89 \pm 2.32 \times 10^{-5} \text{ cm}^2.\text{s}^{-1}$ at 50 °C were obtained. The increase of the diffusion coefficient with T is in agreement with the observation in Figure 3.4 a.

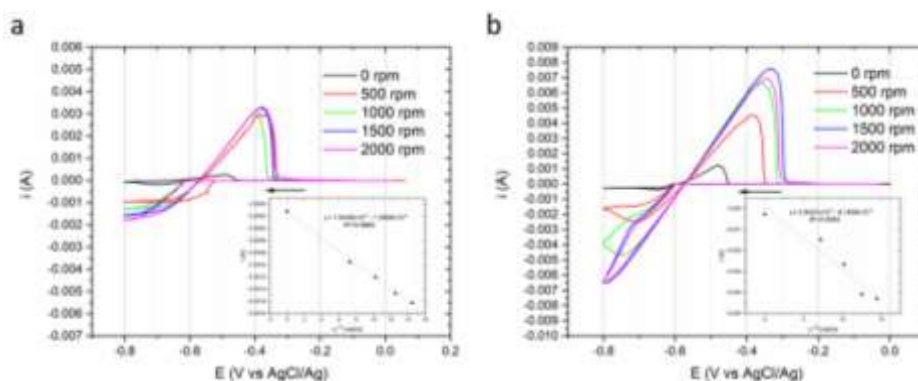


Figure 3.5: Determination of the diffusion coefficient of Sn in presence of sodium oxalates on GC: (a) at RT and (b) at 50 °C ^[181]

Various and opposed values of the Sn(II) diffusion coefficient are available at RT in the literature data, according to the electrolyte solution composition (Table 3.1). The results depend on the Sn(II)/additive ratio. Globally, when this ratio increases, i.e. the chelating effect is lower, the diffusion coefficient logically increases. Thus the use of additive may slow down the diffusion. The value we obtained at RT is for a Sn(II)/additive ratio of 0.1. In comparison with the value reported without additive, of $8.67 \times 10^{-6} \text{ cm}^2.\text{s}^{-1}$, it is not surprising to get a lower diffusion coefficient in presence of oxalate. Moreover, the value we determined at RT is in the same range of those obtained in presence of gluconate or thiourea at higher ratios. It should be highlighted that the results are sometimes controversial in the literature data since smaller diffusion coefficients are obtained for larger ligands.

$D \times 10^6 (\text{cm}^2.\text{s}^{-1})$	5.46	7.55	0.6	1.3	7.6	8.67	1.11	7.05	6.05	1.0
Precursor	SnCl ₂	SnCl ₂	SnCl ₂		SnCl ₂ 0.14 M					x
Additive	oxalate	Sulfate + gluconate	Gluconate		thiourea					citrate
[Sn(II)]/[additive]	0.1	0.2 + 0.5	0.25	0.375	0.5	1:0	0.14	1.4	14	0.2
Reference	This work	[92]	[93]		[96]					[188]

Table 3.1: Diffusion coefficient of Sn(II) measured at RT using different electrolyte solutions (the blue value was theoretically calculated)

Chapter 3. Continuous electrodeposition of SnSe films

From the Stokes-Einstein relation (equation 3.7), the solvated species radius can be calculated following:

$$D_{Sn(II)} = \frac{k_B T}{6 \pi \eta r} \quad 3.7$$

Where $D_{Sn(II)}$, k_B , T , η and r are respectively the Sn(II) diffusion coefficient, the Boltzmann constant ($1.38 \times 10^{-23} \text{ J.K}^{-1}$) the temperature, the absolute viscosity ($1.005 \times 10^{-3} \text{ Pa.s}$ at RT and 0.535×10^{-3} at 50°C [189]) and the solvated species radius

Thus, radii of 3.98 \AA and 1.53 \AA are obtained at RT and 50°C respectively. These results are very surprising. According to the atomic radii of Sn (1.45 \AA), C (0.7 \AA) and O (0.6 \AA), the value of 3.98 \AA is close to the radius of Sn complexed by oxalate. The value of 1.53 \AA , obtained at 50°C , is close to uncomplexed Sn, which is in contradiction with the CV experiments (Figure 3.4). Additional and complementary experiments should be made to confirm the diffusion coefficients, specifically the value determined at 50°C . Indeed, this value must be overestimated because of the dendrite formation.

To conclude:

- ✓ The reversible electrochemical Sn(II)/Sn was identified with and without oxalate salt on GC and Pt electrode.
- ✓ The chelating effect of oxalate on Sn(II) was logically proven by the induced negative shift of the cathodic reduction.
- ✓ As expected the increase of the bath temperature from RT to 50°C increases the diffusion coefficient of Sn(II).

c. Study of Se electrochemical system

For the electrochemical studies of the Se(IV)/Se system, the electrolyte solution is prepared as followed (Figure 3.6).

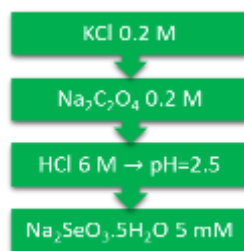
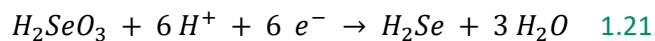
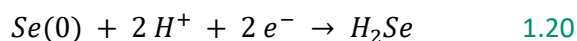
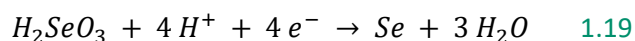
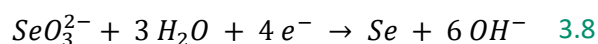


Figure 3.6: Composition of the electrolyte solution for Se electrochemical studies

First of all, from the CVs presented in Figure 3.7 we can say that the electrochemical system of Se(IV)/Se in the electrolyte solution is irreversible, with no anodic stripping peak. At RT, the voltammogram exhibits a broad cathodic peak C2' at -0.73 V vs AgCl/Ag. By increasing the bath temperature up to 50 °C, an additional shoulder, namely C1', appears at -0.62 V vs AgCl/Ag (Figure 3.7 a). Thus, we suggest that, C1' and C2' are respectively related to the reduction of Se(IV) into Se(0) (reaction 1.19) and Se(0) into H₂Se (reaction 1.20). At RT, the reduction process is a 6 electron reaction (reaction 1.21) and solid Se is not deposited.



Because there is no anodic stripping peak, it is not possible to estimate an apparent equilibrium potential of the H₂SeO₃/Se system. Lukinskas *et al.* mentioned a standard redox potential of -0.57 V vs AgCl/Ag for SeO₃²⁻/Se (reaction 3.8) [136].



This value is close to that of the C1' peak, where Se(0) is deposited. The potential of C2' is here different from the standard redox potential of Se/H₂Se system of -0.60 V vs AgCl/Ag [103].

The irreversible behavior of Se was rarely confirmed. Indeed, articles highlighted the reversible behavior of Se on PtO-free platinum [114] or on GC [112]. On (100) and (111) single crystalline gold electrode [109], oxidation peaks are distinguished and attributed to anodic stripping of bulk Se and UPD of Se.

By comparing with the Sn(II) electrochemical studies, we can say that oxalate does not react as a complexing agent in relation to Se(IV). It should be underlined that there is no apparent shift and

from the work of Ju *et al.*, we exclude a complexation of Se by oxalate ^[156] (Figure 3.7 b). However, for an unexpected reason, the current density in presence of oxalate is strongly improved. We suggest an additional current due to the reduction of the solvent. On platinum, the current density increases again and the signal is noisier, due to generation of H₂Se (Figure 3.7 c). We can guess a shoulder C1', preceding C2' which can be assigned to reduction of Se(IV) into Se(0) and/or the solvent decomposition since the decrease of the current density occurs at the same potential in Figure 3.1.

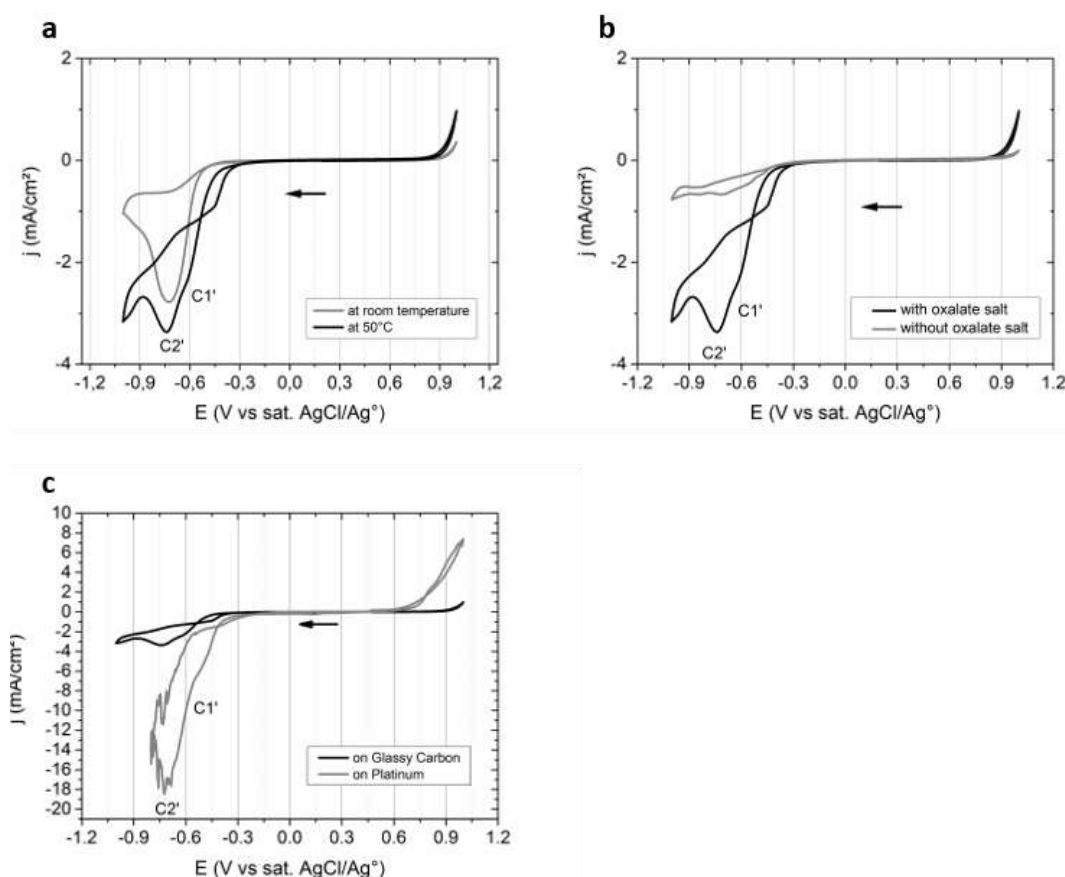


Figure 3.7: Typical CV experiments of a Se(IV) electrolyte solution: (a) influence of the temperature, (b) the complexing agent and (c) the substrate ^[181]

To complete this study, the diffusion coefficient of Se(IV) was determined in presence of oxalate salt, at RT and at 50 °C. The procedure was conducted using the Levich approach. The apparent diffusion limit current was graphically estimated at -0.7 V vs AgCl/Ag, on the forward scans (initial surface state), where the current is supposed to correspond to the cathodic reduction of Se(IV) in Se(0). The study on the diffusion coefficient of Se(IV) was more difficult than for Sn(II). Se deposit tends to remain on the electrode as previously said (Chapter 1), which strongly modifies the surface state of the electrode. No well-defined plateau was obtained but we could determine diffusion coefficients, respectively of $1.15 \pm 0.04 \times 10^{-6} \text{ cm}^2 \cdot \text{s}^{-1}$ at RT and $4.29 \pm 4.07 \times 10^{-6} \text{ cm}^2 \cdot \text{s}^{-1}$ at 50 °C. These

Chapter 3. Continuous electrodeposition of SnSe films

coefficients are lower than those obtained for Sn(II), which were respectively of $5.46 \pm 0.77 \times 10^{-6} \text{ cm}^2.\text{s}^{-1}$ at RT and $2.89 \pm 2.32 \times 10^{-5} \text{ cm}^2.\text{s}^{-1}$ at 50 °C.

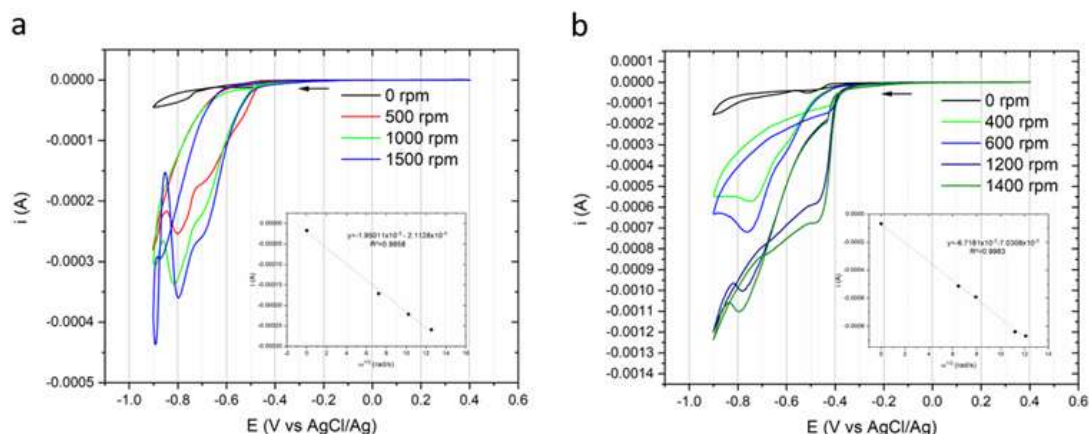


Figure 3.8: Determination of the diffusion coefficient of Se in presence of sodium oxalates on GC: (a) at RT and (b) at 50 °C ^[181]

To the best of our knowledge, few studies were devoted to the Se(IV) diffusion coefficient in aqueous media (Table 3.2). The value determined at RT in this work is almost tenfold lower than that reported from an electrolyte containing HClO₄ and citric acid, known as a complexing agent. This result is surprising since we did not demonstrate a complexation between Se(IV) and oxalate. However, the use of additive may slow down the diffusion thus a decrease of the diffusion coefficient can be possible. It should be underlined that the values we determined are close to those obtained using H₂SO₄. The pH of 2.5 corresponds to a HCl concentration of 3.16 mM which is strongly far from that H₂SO₄ used by the authors.

$D \times 10^6 \text{ (cm}^2.\text{s}^{-1}\text{)}$	1.15 (RT) 4.29 (50°C)	11.0	8.0	2.93
Precursor	H ₂ SeO ₃ 5mM	SeO ₂ 0.1 mM	H ₂ SeO ₃ 0-1.4 mM	Na ₂ SeO ₃ 1.14 mM
Electrolyte	KCl 0.2 M Na ₂ C ₂ O ₄ 0.2 M pH=2.5	HClO ₄ 0.1 M	Citric acid 0.4 M +CuSO ₄ 1 mM	H ₂ SO ₄ 254.89 mM
Reference	This work	[115]	[190]	[191]

Table 3.2: Diffusion coefficients of Se(IV) measured at RT using different electrolyte solutions

To compare with Sn system, we also determined the solvated species radius following the Stokes-Einstein relation (equation 3.7).

Radii of 1.89 Å and 1.03 Å are estimated at RT and 50 °C respectively, taking into account the change of the viscosity. These results remain also surprising. Specific comparative studies with the literature data would be interesting for a better knowledge of the results. The value of 1.03 Å, seems to correspond to the radius of free Se (Se^{4+}). To be more confident with the values we determined, other complementary experiments should be made. Moreover, as previously mentioned, no plateau was reached which implies uncertainties, specifically at 50 °C. We can suggest the 6 electron process instead of the 4 process.

d. Study of SnSe electrochemical system

The electrochemical behavior of the complete electrolyte solution (Figure 3.9) was investigated on platinum, in order to compare them with the results obtained both for Sn and Se electrochemical systems.

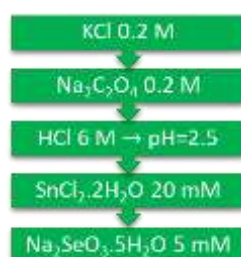


Figure 3.9: Composition of the electrolyte solution for SnSe electrochemical studies

It should be noticed that it was decided to introduce a Sn(II) excess over Se(IV) according to the literature ^[15,23,147,192]. Despite a diffusion control process, we cannot explain the Sn(II) excess by the previous determined diffusion coefficients. Indeed, we obtained higher diffusion coefficients for Sn(II), which means that Sn(II) is faster than Se(IV). If we suggest the deposition of SnSe as a codeposition from the reduction of Sn(II) into Sn(0) (reaction 1.15) and of Se(IV) into Se(0) (reaction 1.19), the observed limiting current density j_{obs} can be expressed depending on Sn and Se individual contributions (j_{Sn} and j_{Se}) following equation 3.9 ^[193]:

$$j_{obs} = j_{Sn} + j_{Se} \quad 3.9$$

Since the reductions are diffusion-limited processes, as proved by our study (Figure 3.5 and Figure 3.8), the individual contributions are given by the relations 3.10 and 3.11:

$$j_{Sn} = -\frac{2 F D_{Sn(II)}}{\delta_{Sn(II)}} C_{Sn(II)} \quad 3.10$$

$$j_{Se} = -\frac{4 F D_{Se(IV)}}{\delta_{Se(IV)}} C_{Se(IV)} \quad 3.11$$

Where $D_{Sn(II)}$, $D_{Se(IV)}$, $\delta_{Sn(II)}$, $\delta_{Se(IV)}$, $C_{Sn(II)}$ and $C_{Se(IV)}$ are respectively the diffusion coefficients, the thickness of the diffusion layer and the concentration of Sn(II) and Se(IV)

At a deposition time t , the amount of Sn and Se mole deposited follow equations 3.12 and 3.13:

$$n_{Sn} = -\frac{D_{Sn(II)}}{\delta_{Sn(II)}} C_{Sn(II)} t \quad 3.12$$

$$n_{Se} = -\frac{D_{Se(IV)}}{\delta_{Se(IV)}} C_{Se(IV)} t \quad 3.13$$

The Sn/Se ratio can be estimated following equation 3.14:

$$\frac{n_{Sn}}{n_{Se}} = \frac{D_{Sn(II)} \delta_{Se(IV)} C_{Sn(II)}}{D_{Se(IV)} \delta_{Sn(II)} C_{Se(IV)}} \quad 3.14$$

Making the hypothesis the diffusion is linear, it implies Cottrell equation:

$$j = n F C \sqrt{\frac{D}{\pi t}} \quad 3.15$$

Specially, δ can be replaced following equation 3.16:

$$\delta = \sqrt{\pi D t} \quad 3.16$$

Finally, taking into account the Sn/Se mole ratio in the film, equal to 1 and replacing δ according to equation 3.16, we obtain equation 3.17:

$$\frac{C_{Sn(II)}}{C_{Se(IV)}} = \sqrt{\frac{D_{Se(IV)}}{D_{Sn(II)}}} \quad 3.17$$

From the determined diffusion coefficients, this approach suggests theoretical [Sn(II)]/[Se(IV)] ratio of 0.39, instead of an experimental ratio of 4 in the literature data. We suggest the ratio we use enables to prevent a deficit in Sn(II) precursor due to its hydrolysis into SnO_2 .

In Figure 3.10 a, a first CV is displayed between -0.75 V and 1 V vs AgCl/Ag. Two cathodic peaks, C0'' and C1'', are respectively observed at -0.52 V and from -0.6 V vs AgCl/Ag. By reversing the scan direction, three anodic peaks appear, A1'', A2'' and A3'', respectively at -0.54 V, 0.11 V and 0.81 V vs AgCl/Ag. When the lower potential is modified up to -0.55 V vs AgCl/Ag, A1'' disappears since the reduction occurring at C1'' is not reached. Thus we deduce that these two peaks C1'' and A1'' are associated. Their positions are close to those of the system of Sn(II)/Sn(0) (Figure 3.4 d). Moreover, the asymmetric shape of the A1'' peak is characteristic of a stripping peak. Thus we deduce that C1'' is related to the reduction of Sn(II) into Sn(0) (reaction 1.15) and A1'', to the anodic dissolution of Sn. In comparison with the CVs performed on Sn and Se electrolyte solution, the position of the C0'' is close to that of C0 but also to that of Se deposition. Thus, this peak is either due to Se deposition from reaction 1.19 or UPD of Sn or the solvent decomposition as suggested by the electrochemical stability window (Figure 3.1). After the C0'' peak, the signal becomes noisy which can be related to the co-generation of H₂Se (reaction 1.20).

For a better understanding, additional experiments were made by applying pause times of 30 s and 60 s at -0.55 V vs AgCl/Ag (Figure 3.10 b). Very slight but not sufficient differences are observed in terms of intensity and position of the A2'' and A3'' peaks, which means they cannot be related to C0''. Hence, A2'' and A3'' remain, for the moment, unexplained. They must be determined either from surface analyzes with and without anodic scans after the deposition or by EQCM.

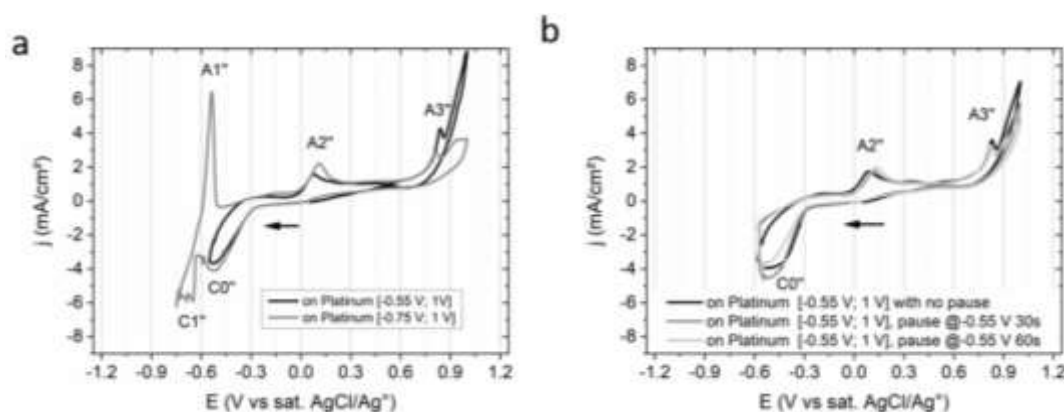
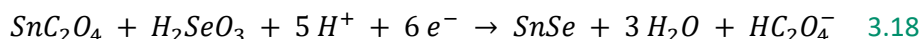
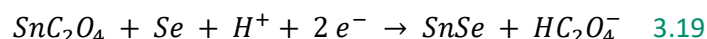
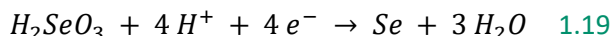


Figure 3.10: CV experiments on the complete electrolyte solution: (a) with different lower potential and (b) different pause times

In comparison with the CVs made on Sn electrolyte solution and Se electrolyte solution, the synthesis of SnSe is expected around the C0'' peak. Two mechanism are possible. The first, suggested by Ham *et al.* involved the uptake of six-electron (reaction 3.18) to reduce Se(IV) into Se(-II) which then further precipitates with Sn(II) to generate SnSe ^[137].



Another possibility is a two-step mechanism where Se(IV) is firstly reduced into Se(0) from reaction 1.19, followed by a two-electron mechanism (reaction 3.19), as similarly reported by Lu *et al.* ^[146] and Ham *et al.* ^[137] or for Bi₂Te₃ ^[194]:



Preliminary electrochemical studies revealed:

- ✓ Unfortunately a smaller electrochemical stability window using oxalate and Pt as working electrode
- ✓ The reversibility of the Sn(II)/Sn system and the chelating effect of oxalate salt on Sn(II)
- ✓ Either UPD of Sn or solvent decomposition on Pt electrode
- ✓ The irreversibility of Se system
- ✓ Lower Se(IV) diffusion coefficients than Sn(II)
- ✓ A potential window for deposition of SnSe from -0.4 to -0.7 V vs AgCl/Ag

II. Electrodeposition of SnSe films

a. Study of the chronoamperometric curves

According to the preliminary study, an electrochemical window was defined. Thus, depositions were carried out from -0.4 V to -0.7 V vs AgCl/Ag. However, in this potential window, the potentials from -0.5 V to -0.6 V vs AgCl/Ag were found to exhibit the best deposits and were specifically investigated. The influence of the growth time and the influence of the counter-electrode from the electrolyte solution were also studied.

For a fixed applied coulometric charge, the deposition time decreases when the potential is more cathodic (Figure 3.11). A first linear evolution of the deposition time is observed from -0.4 V to -0.5 V vs AgCl/Ag. Another one is observed from -0.5 V to -0.6 V vs AgCl/Ag. However, in this range of potentials, this decay is less important. Large uncertainties are linked to a more or less large number of experiments. Moreover, for comparison purposes, the coulometric charge was normalized at -12.7

$\text{C}\cdot\text{cm}^{-2}$. At -0.4 V, -0.45 V and -0.7 V vs AgCl/Ag, the deposition times are completely different, which is not compatible with a single diffusion-limited process. Since the current density may be similar whatever the potential, the deposition time should be in the same range. Thus, side reactions influence the current density and the deposition time.

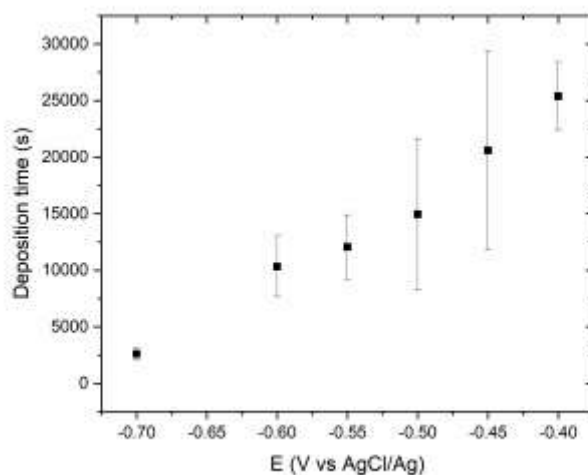


Figure 3.11: Influence of the applied potential on the deposition time for a charge quantity normalized at $-12.7 \text{ C}\cdot\text{cm}^{-2}$

As the deposition potential decreases, the chronoamperometric curves tend to become noisier with a decrease of the current density (Figure 3.12). This is due to the hydrogen evolution and/or the H_2Se production, as suggested by the presence of bubbles on the working electrode during the electrodeposition. For fixed coulometric charges of -9.07, -12.7 and -18.1 C, we expect to get films with thicknesses of 5, 7 and 10 μm respectively. We observe that the deposition time increases with the expected thicknesses (Figure 3.12 a, b and c). However, an unexpected change in the current density is observed, depending on the applied potential. As it can be seen, the current density becomes more cathodic as the applied potential decreases. This might come from side reactions occurring during the deposition. Moreover, the geometric active area was defined with uncertainty, which can slightly modify the current densities.

Few experiments were made by separating the counter-electrode (Figure 3.12 d), in order to avoid the influence of opposite reactions during the depositions. Indeed, the formation of a deposit is observed on the counter-electrode during the electrodeposition experiments. For this purpose, the counter-electrode was put in a compartment filled with a saturated KCl solution. The current density tends to increase, despite the uncertainty on the active area and thus the deposition time for same Q_{th} also increases.

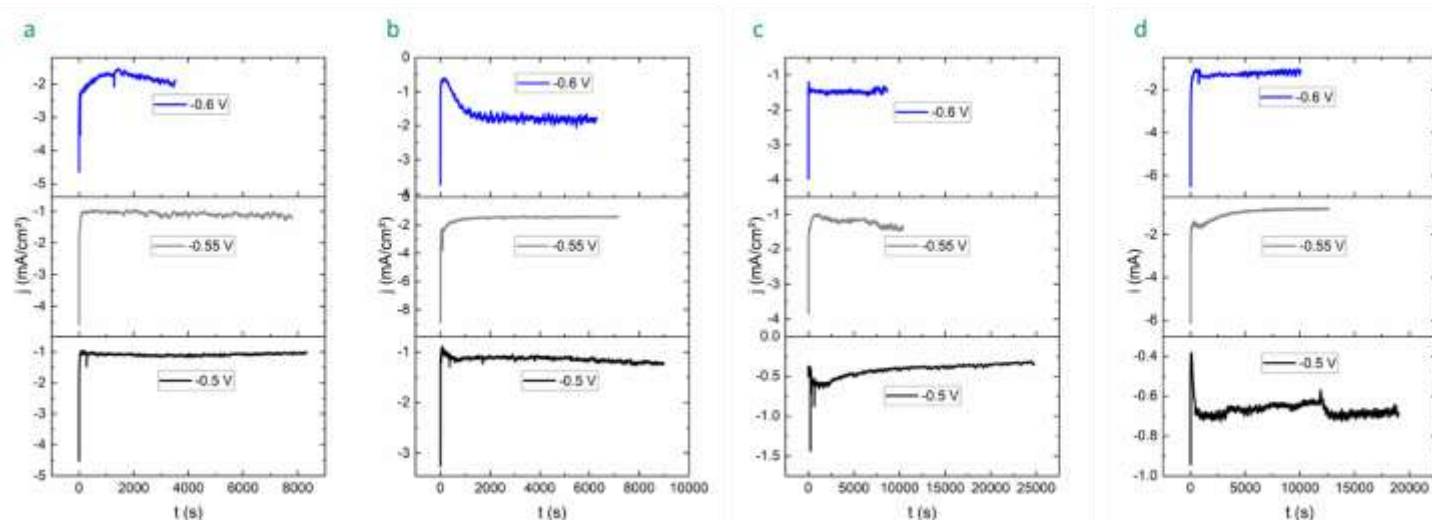


Figure 3.12: Typical chronoamperometric curves of the electrodeposited samples: (a) $Q_{th} = -9.07$ C, (b) $Q = -12.7$ C, (c) $Q_{exp} < -12.7$ C and (d) for separated counter-electrode at -12.7 C. The area were not defined for the plots in figure d.

The chronoamperometric curves revealed:

- ✓ A diffusion-limited process hindered at -0.4 V, -0.45 V and -0.7 V vs AgCl/Ag
- ✓ Deposition times in the same range from -0.5 V to -0.6 V vs AgCl/Ag but slight change of the current density, maybe due to hydrogen evolution
- ✓ Different deposition times and current densities when separating the counter-electrode

b. SEM characterizations

Deposits were analyzed on the top face by SEM. For $Q_{exp} = -12.7$ C, samples deposited at -0.4 V and -0.45 V vs AgCl/Ag exhibit two morphologies which can be due to the presence of different phases (Figure 3.13 a and b). From -0.5 V to -0.6 V vs AgCl/Ag the films exhibit needle-like grains with improved covering as the deposition potential decreases (Figure 3.13 c, d and e). Aggregates are observed whatever the potential but bigger agglomerates are generated at -0.6 V vs AgCl/Ag. At -0.7 V vs AgCl/Ag, the deposits are powdery, sometimes non-adhering to the substrate and occasionally red (Figure 3.13 f). This morphology is probably due to amorphous selenium, which is generated from the reaction between H_2Se and H_2SeO_3 (reaction 1.22).

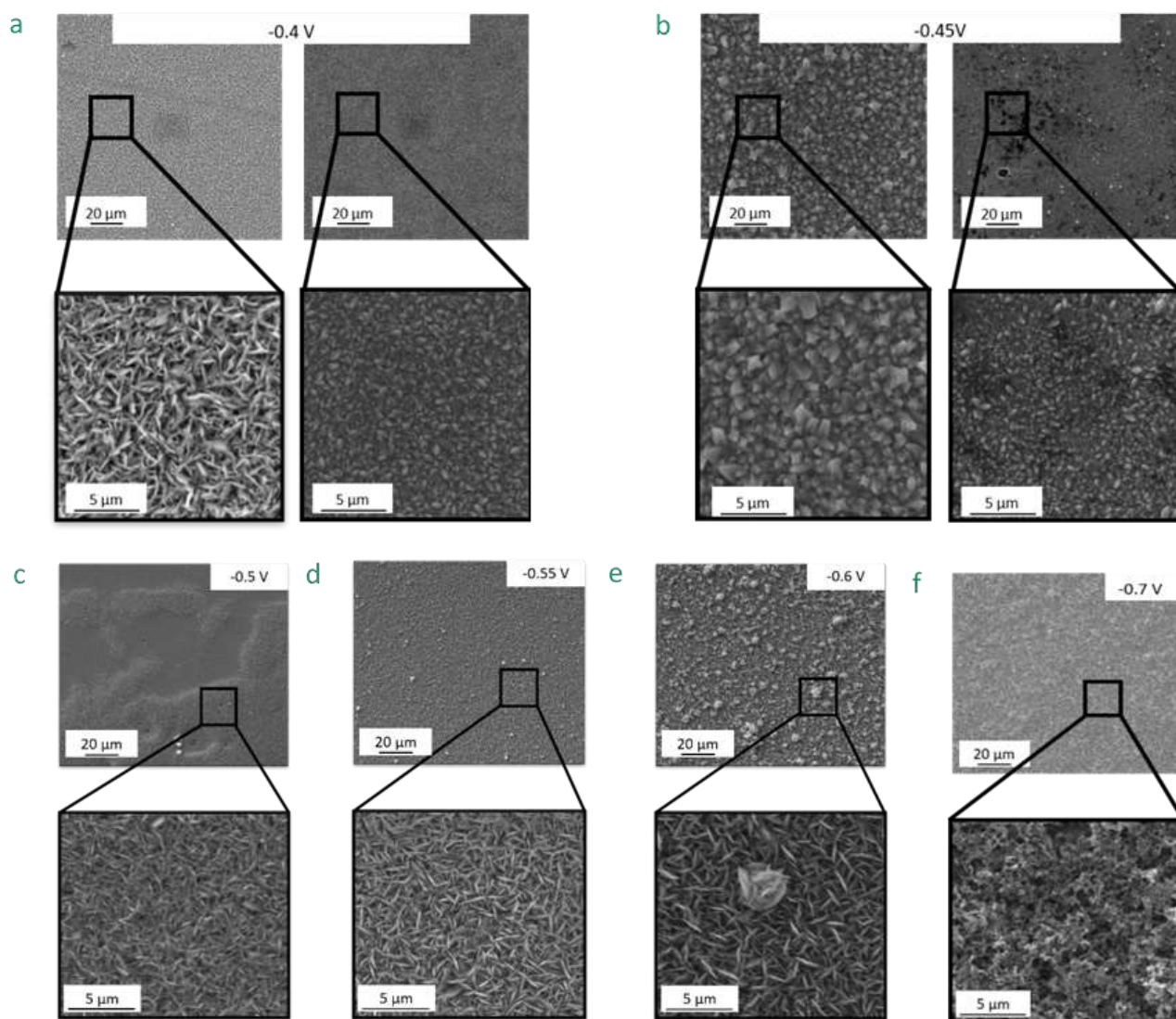
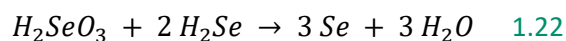


Figure 3.13: Top face SEM scans of as-deposited samples until -12.7 C: (a) -0.4 V, (b) -0.45 V, (c) -0.5 V, (d) -0.55 V, (e) -0.6 V and (f) -0.7 V vs AgCl/Ag. For -0.4 and -0.45 V the images correspond to two typical parts of the inhomogeneous surface

In the potential range from -0.5 v to -0.6 V vs AgCl/Ag, several samples show nuclei (Figure 3.14). In comparison with the needle-like grains, it seems that there are different growth rates and/or progressive nucleation. These nuclei seem to be “seeds” for the future needles as proved by the aggregate highlighted by the red circle.

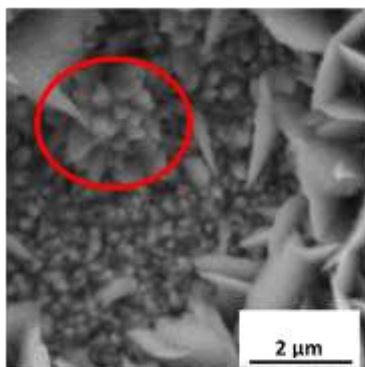


Figure 3.14: SEM image of a sample exhibiting smaller grains

This spherical morphology was also encountered for longer deposition times (coulometric charge of -18.1 C) as well as when the depositions were performed with separation of the counter-electrode (Figure 3.15 left). This kind of morphology was occasionally observed for low deposition times (coulometric charge of -9.07 C). Thus, we can suggest phenomena at long deposition times such as corrosion or side reactions. The influence of the counter-electrode on the SnSe deposition remains ambiguous. We observe that the morphology is different with or without separation of the counter-electrode. Moreover, deposits were often observed on the counter-electrode (Figure 3.15 right). They surprisingly contain rich Se content. The oxidation of Se(IV) into Se(VI) is not excluded explaining this deposit. Another hypothesis could be the oxidation of H_2Se into Se(0). Moreover, looking at the chronoamperograms (Figure 3.12 d), the nucleation and growth processes might be different from those without separation (Figure 3.12 b). Thus, if the current density is different, the grain size can also differ, as well as the thickness.

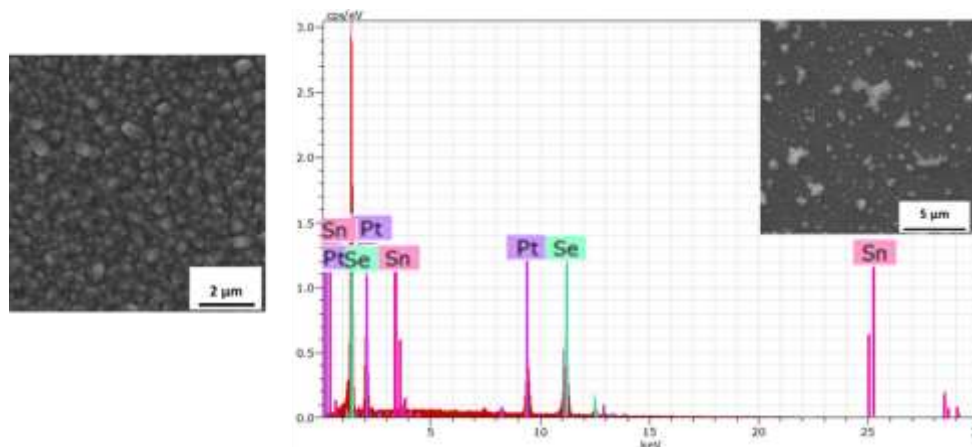


Figure 3.15: SEM images of (left) a sample deposited with separated counter-electrode and (right) the counter-electrode deposit with EDS spectrum

After transfer, all samples exhibit a smooth and mirror surface state, in contrast to the top face. Since the transfer process involves immersion into liquid nitrogen, cracks are always generated (Figure 3.16).

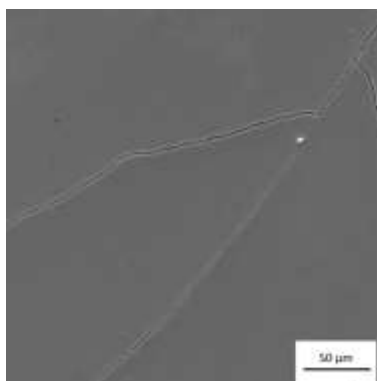


Figure 3.16: SEM image of a deposit after transfer process

Nevertheless, we took advantage of this technique to perform EDS analyzes on the bottom face (Figure 3.17). All samples exhibit a stoichiometry close to 1:1, except for -0.7 V vs AgCl/Ag. Because of their powdery morphology, the samples synthesized at -0.7 V vs AgCl/Ag are more difficult to detach from the platinum-coated glass and a non-negligible part of the film remains on the substrate. Thus, a strong incertitude on the composition is obtained. Indeed, one sample revealed high Sn concentration whereas another one exhibited a stoichiometry close to 1:1. Nevertheless, it is not surprising to find a Sn enrichment from more cathodic potentials, according to the CV studies (Figure 3.4 and Figure 3.10). The deposits realized in the potential range from -0.40 V to 0.65 V vs AgCl/Ag generally exhibit a small Se excess lower than 3 at.%, which is in the analysis incertitude.

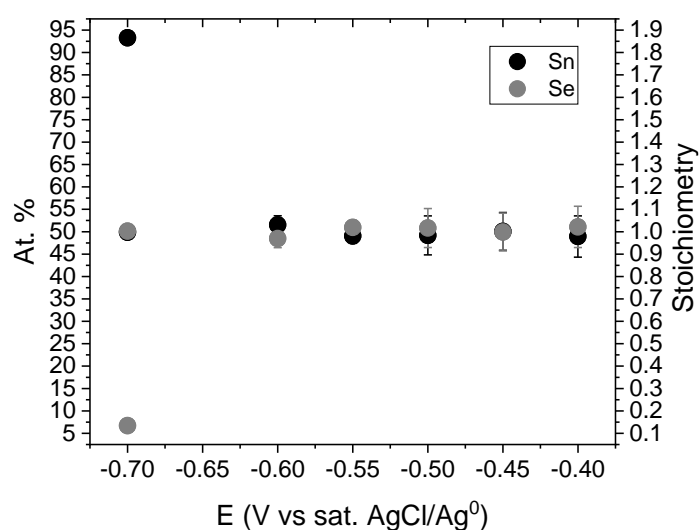


Figure 3.17: Influence of the deposition potential on the film composition: EDS analysis on the bottom surface

From the SEM analyzes we found that:

- ✓ The deposits made at -0.4 V and -0.45 V vs AgCl/Ag exhibit two morphologies which can reveal the presence of two phases with slight Se excess. Thus, these values of potential are not selected.
- ✓ The deposits made at -0.7 V vs AgCl/Ag are powdery and Sn rich. Also they are not retained for further analysis.
- ✓ From -0.5 V to -0.6 V vs AgCl/Ag, needle-like grains are observed until -12.7 C whereas spherical grains are observed either at longer deposition times or by separating the counter-electrode. A stoichiometry close to 1:1 is generally found.
- ✓ A Se-rich deposit is synthesized on the counter-electrode

c. TEM characterizations

The thickness of the deposits could not be obtained using profilometry, because of high roughness of the sample. The best way to obtain it was from TEM and/or STEM micrographs performed on lamellas prepared by FIB (Figure 3.18). The average thicknesses of each sample are reported in Table 3.3. The theoretical thicknesses were calculated from the Faraday law (equation 2.4):

Deposition potential (V vs AgCl/Ag)	-0.5	-0.55	-0.6
Experimental thickness (μm)	0.85	0.65	1.3
Coulometric charge (C.cm^{-2})	-6.35	-5.06	-5.06
Theoretical thickness (μm)	3.50	2.79	2.79
Faradaic yield (%)	24.29	23.29	46.59

Table 3.3: Influence of the deposition potential on the thickness and faradaic yield

As it can be seen, the experimental thicknesses are strongly far from the expected ones, which lead to bad faradaic yields. This can be explained by side reactions such as the generation of H_2Se . At -0.6 V vs AgCl/Ag, the decrease of the current density (such as in Figure 3.12 a), driven not only by H_2Se but also by Sn deposition, may benefit for the deposition and gives rise to thicker deposits.

Chapter 3. Continuous electrodeposition of SnSe films

From -0.5 V to -0.6 V vs AgCl/Ag, the samples exhibit needle-like grains and good compacity. The grains seem to be quite homogenous, but darker color in several points can reveal the presence of other phases since the HAADF mode is sensitive to phase contrast.

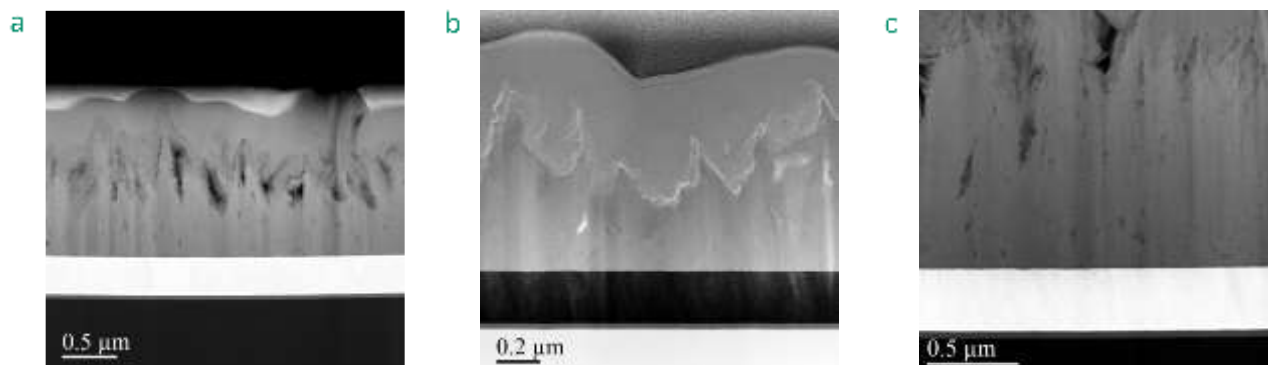


Figure 3.18: STEM-HAADF micrographs on samples deposited at (a) -0.5 V, (b) -0.55 V and (c) -0.6 V vs AgCl/Ag

EDS analyses were performed on the samples deposited from -0.5 V to -0.6 V vs AgCl/Ag (Figure 3.19). For each potential, a stoichiometry close to 1:1 was found with a slight Sn excess. An interesting information is the presence of oxygen whatever the potential, with general atomic percentages from 5 to 10 at.%. The presence of SnO_2 is therefore possible according to the electrochemical behavior of Sn (Figure 1.11, Figure 1.22 and relation 3.4). This potential presence of oxide was not observed by SEM. However, the TEM results are more precise but potentially not representative of the whole sample. We cannot exclude in-plane heterogeneities, as well as incertitude with the SEM - EDS from the SEM or in-depth gradient.

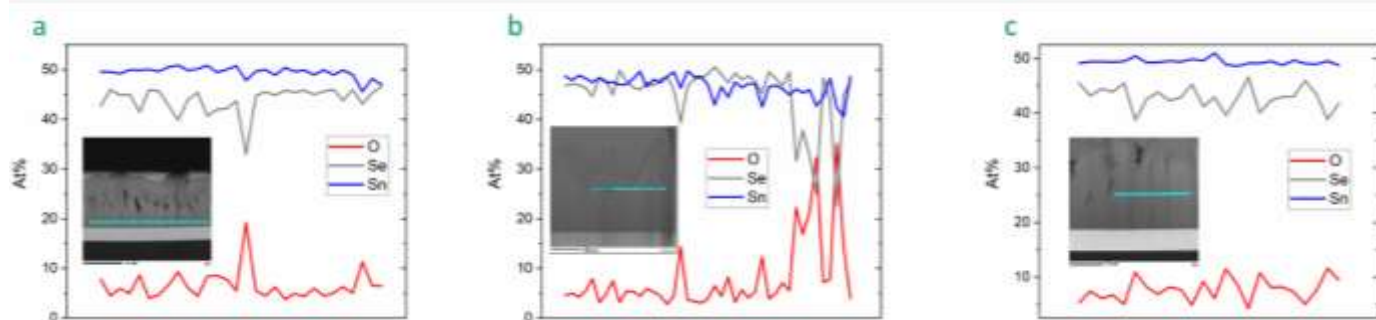


Figure 3.19: TEM – EDS analyses on the sample deposited at (a) -0.5 V, (b) -0.55 V and (c) -0.6 V vs AgCl/Ag

Besides, FFT analyses made on the samples confirmed the presence of SnSe. The presence of secondary phases (Figure 3.20 a and b) is suggested since their interplanar distances are different from

those obtained from SnSe (Figure 3.20 b and c and Appendix 1). From the COD database, these phases can be SnSe₂, Sn or Se₈ but need to be confirmed.

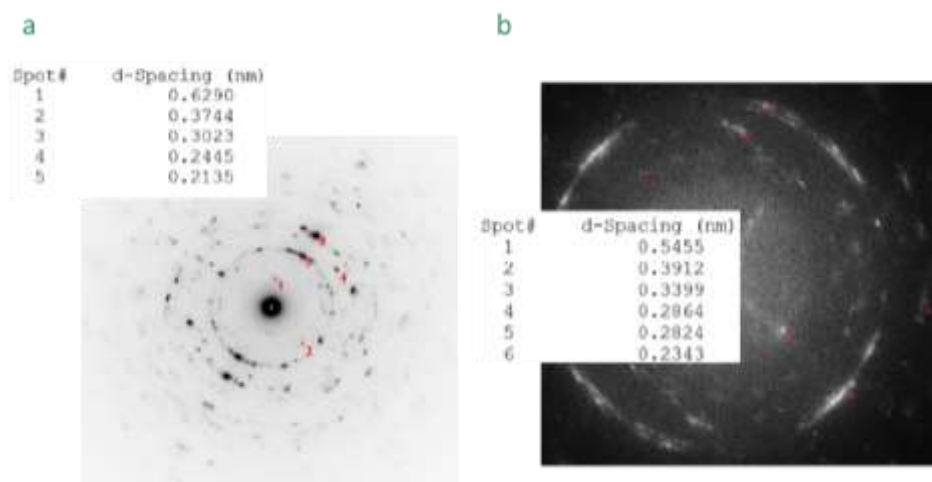


Figure 3.20: FFT results obtained on lamellas

From the TEM analyzes we found that:

- ✓ Thicker deposits are obtained at -0.6 V vs AgCl/Ag thanks to better faradaic yield
- ✓ The faradaic yield is low, from 23 to 47 %, because of side reactions (H₂Se)
- ✓ FFT reveals SnSe and secondary phases (SnSe₂, or Sn or Se₈)
- ✓ The lamellas have composition close to 1:1 with slight Sn excess. In contrast to EDS-SEM analysis, the presence of oxygen is detected, suggesting the presence of SnO₂.

d. XRD characterizations

Samples were analyzed by XRD on the bottom face to avoid the contribution of the Pt substrate (Figure 3.21). For all samples, the presence of SnSe indexed into the orthorhombic structure (*P n m a* space group) was confirmed and is in agreement with the stoichiometries previously found (Figure 3.17 and Figure 3.19). The coulometric charge as well as the applied potential were not found to strongly influence the patterns. Indeed, the intensities, the occurrence or disappearance of certain peaks differ even for deposits at same potential and/or same charge quantity. Shifts from the positions given by the COD card are observed maybe due to evolution of the lattice parameters due to deviation from the stoichiometry. We noticed that SnSe crystallizes with a preferred orientation along the (111)

plane. Finally, the weakest diffraction peaks are obtained at -0.7 V vs AgCl/Ag since these samples have low crystallinity, as suggested by the SEM analysis (Figure 3.13 f).

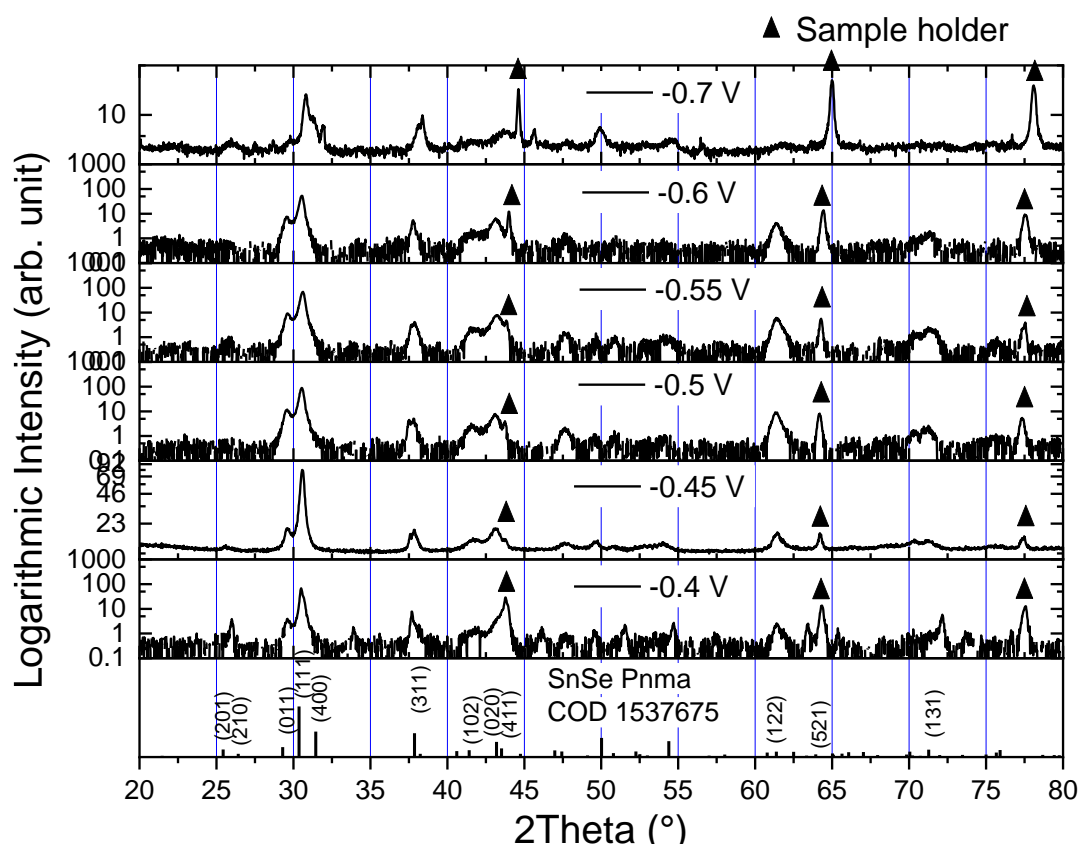


Figure 3.21: XRD patterns of samples deposited until -12.7 C after transfer process ^[181]

As previously mentioned, deposits were often observed on the counter-electrode and some of them were also analyzed by XRD (Figure 3.22). The typical XRD pattern surprisingly exhibit peaks indexed into the hexagonal structure of Se(0). Although this result is in agreement with the high Se proportion observed by EDS (Figure 3.15 right), it is not expected from the experimental details. Furthermore, we assume the generation of Se(-II) during the electrodeposition (reactions 3.18 and 3.19) at the working electrode. At the counter-electrode, oxidations occur during the cathodic electrodeposition process at the working electrode. Thus, the presence of Se(0) deposit on the counter-electrode, from a bath containing Se(IV), is possible from oxidation of Se(-II) produced at the working electrode. The growth time is long enough, an enrichment of the electrolyte solution in Se(-II) is possible during the electrodeposition, leading to the oxidation of Se(-II) into Se(0) on the counter-electrode.

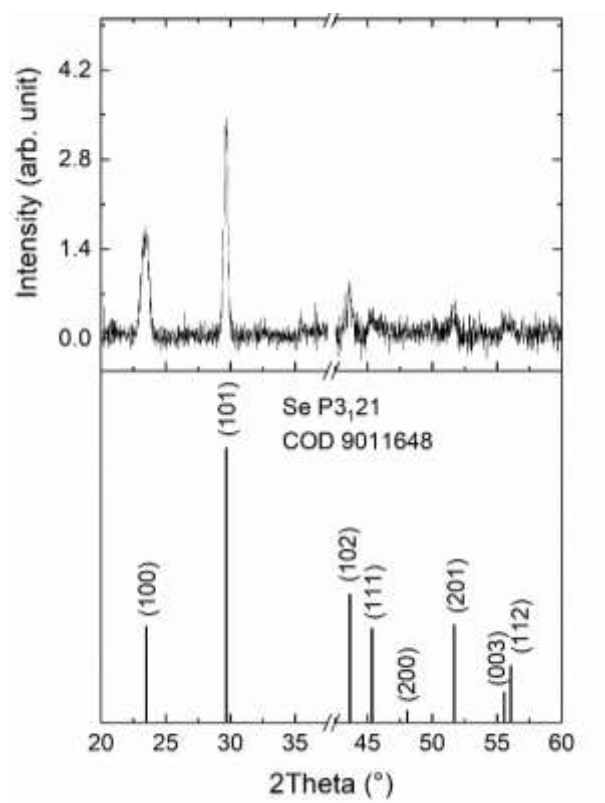


Figure 3.22: XRD pattern of a deposit on the counter-electrode

From the XRD analyzes we found SnSe indexed in the orthorhombic structure with (111) preferential plane, in agreement with the stoichiometry close to 1:1. Moreover, Se(0) was detected on the counter-electrode.

e. CEMS characterizations

Mössbauer analyzes were made on samples deposited from -0.5 V to -0.7 V vs AgCl/Ag (Figure 3.23). Due to low amount of deposit, the analyzes were unsuccessful for those made at -0.4 V and -0.45 V vs AgCl/Ag. From -0.5 V to -0.6 V vs AgCl/Ag, the spectra exhibit a doublet at an isomer shift of 3.4 mm.s^{-1} . It thus reveals the presence of Sn(II) and was expected from SnSe. The quadrupolar splitting was measured between 0.75 and 0.8 mm.s^{-1} for all samples, whatever the deposition potential and time. Moreover, the same spectra are obtained for samples deposited by separating the counter-electrode. Hence, we cannot deduce any change in symmetry or chemical environment.

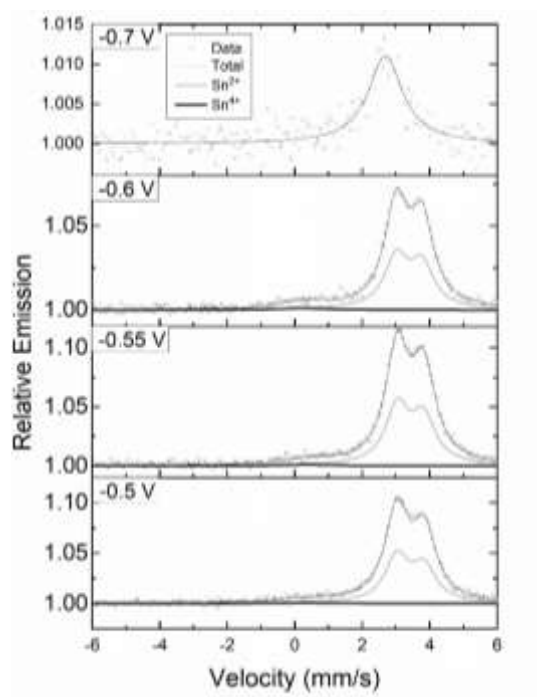
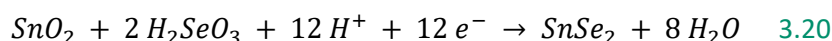


Figure 3.23: Mössbauer spectra of the as-deposited sample ^[181]

A singlet is surprisingly found at an isomer shift between 0.13 to 0.4 mm.s⁻¹, indicating the presence of unexpected Sn(IV). In comparison with the doublet, the singlet intensity is very weak, which means that Sn(IV) is in low concentration. This can be the reason why no Sn(IV) phase was detected by XRD. Bernardes-Silva *et al.* reported an isomer shift of 0.07 mm.s⁻¹ for SnO₂ ^[195], which is different from the values of this work. The presence of the Sn(IV) singlet could be explained by the presence of another phase, SnSe₂, generated according to [equation 3.20](#):



Since the Sn(IV) singlet is also observed for deposits made by separating the counter-electrode, we suggest that SnO₂, involved in the reaction, comes from the bath preparation, as mentioned in the [equation 2.3](#). The SnSe₂ phase would be in agreement with the EDS obtained from SEM analyzes ([Figure 3.17](#)). Finally, the spectrum of the sample made at -0.7 V vs AgCl/Ag exhibit a large singlet at an isomer shift of 2.5 mm.s⁻¹ which indicates the presence of Sn(0). This result is in agreement with the CV experiments ([Figure 3.4 d](#) and [Figure 3.10 a](#)). However, the XRD revealed the presence of SnSe, by analyzing the samples after transfer process. We suggest that SnSe was deposited on the first layers (bottom) and was consequently detected by the XRD analysis. On the contrary, the upper layers, with powdery Sn, was analyzed by CEMS. CEMS is a surface characterization, thus taking into account the ability of Sn to generate dendrites, the Sn(II) signal can be hidden by the Sn(0) singlet. Finally, the large signal is in favor of a low crystallinity.

From the CEMS analyzes, Sn(II) was determined for samples deposited from -0.5 V to -0.6 V vs AgCl/Ag, in agreement with SnSe. A low Sn(IV) signal was also found, that can be assigned to SnSe₂ or SnO₂. At -0.7 V vs AgCl/Ag, Sn(0) was detected, in agreement with the CV experiments. By comparison with XRD analysis, heterogenous composition in thickness is suspected at -0.7 V vs

f. Raman characterizations

To go further on the microstructural analysis, we performed Raman analyzes. For $Q=-12.7$ C (Figure 3.24 a), all of the spectra surprisingly exhibit bands at 70 cm⁻¹, from 90 to 130 cm⁻¹, from 144 to 156 cm⁻¹ and from 181 to 187 cm⁻¹. It should be underlined that SnSe films generally exhibit bands at 109, 130 and 150 cm⁻¹, assigned to B_{3g}, two A_g vibration modes of SnSe [57–59]. Shifts can occur depending on the symmetry, phonons, bonding strengths and distortions so we can have a deviation from the values reported in the literature.

- According to Luo *et al.*, the first band at 70 cm⁻¹ can be attributed to an A_g vibration mode of SnSe. This band may appear because of the laser excitation (only at a laser wavelength of 532 nm) [66].
- The wide band from 90 to 130 cm⁻¹ is probably due to a shoulder between B_{2u} mode of SnSe [141,150,196] and E_g mode of SnSe₂ [63]. This wide band can also hide the B_{3g} vibration mode of SnSe, which commonly appears at 109 cm⁻¹. Indeed, the spectra at -0.45 V, -0.6 V and -0.7 V vs AgCl/Ag show bands with maximum position from 115 to 117 cm⁻¹ (related to SnSe₂) and we can guess, on almost all spectra, a weak band with maximum position from 95 to 97 cm⁻¹ (related to SnSe).
- The band from 144 to 156 cm⁻¹ is attributed to an A_g vibration mode of SnSe appearing between 140 and 150 cm⁻¹ [57–59,141,150,196].
- The last band appearing from 181 to 187 cm⁻¹ is attributed to the A_{1g} vibration mode of SnSe₂ [63]. The presence of this phase is in agreement with the Sn(IV) singlet observed in CEMS and the slight Se excess, measured from EDS - SEM. It should be noticed that an A_g vibration mode of SnSe was attributed to a band at 179 cm⁻¹ for In-doped SnSe films [150]. However, it was reported only once.

Increasing the deposition time modifies the typical spectrum (Figure 3.24 b), whatever the potential but the previous one can also be observed.

- It seems that SeO_2 bands, due to B_{2g} , A_{1g} and E_g modes are expressed respectively close to 50, 62 and 245 cm^{-1} [197].
- E_g and A_{1g} vibration modes of SnSe_2 are still observed about 119 and 184 cm^{-1} .
- Two bands appear around 132 and 143 cm^{-1} . They may be attributed to A_g modes of SnSe as previously reported [196]. The first band is sometimes hidden by the E_g and A_g bands.

It should be underlined that the bands at 50, 132, 143 and 245 cm^{-1} can also be attributed to vibration modes of Se [199]. However, the presence of Se phase suggests an intense and well define band around 250 cm^{-1} which is not observed here.

Although the TEM analyzes revealed an overall Sn excess they also revealed the presence of oxygen. Thus we suggest that SnSe is predominant, with SnSe_2 and SeO_2 as secondary phases.

Finally, spectra were recorded on the cross-sections of samples (Figure 3.24 c). Although the spectra appear to be different from the others, the same characteristic bands are present.

- For the sample deposited at -0.5 V vs AgCl/Ag, the A_{1g} vibration mode has a surprisingly high signal whereas the E_g signal is shortened. The SnSe A_g vibration mode at 70 cm^{-1} is easily determined but the others are more difficult to find.
- The sample deposited at -0.55 V vs AgCl/Ag shows an intense E_g band whereas the A_{1g} band is weak. The A_g mode at 143 cm^{-1} is high in comparison with the one at 70 cm^{-1} .

To conclude, all bands were attributed from comparison with the literature according to the data reported in Table 3.4:

Chapter 3. Continuous electrodeposition of SnSe films

Experimental position in this work (cm ⁻¹)	Standard position (cm ⁻¹)	Compound	Vibration mode	Reference(s)
50	47-48 (50)	SeO ₂ (Se)	B _{2g} (E ₂)	[197] ([199])
62	57-59	SeO ₂	A _{1g}	[197]
70	71	SnSe	A _g	[66]
90-130	108/96/119	SnSe/SnSe/SnSe ₂	B _{3g} /B _{2u} /E _g	[57-59] [57-59,141,150,196] [63]
115-119	119	SnSe ₂	E _g	[63]
132	130 (128)	SnSe (Se)	A _g (E ₃)	[57-59] ([199])
143	144 (143)	SnSe (Se)	A _g (E)	[189] ([199])
144-156	140-150	SnSe	A _g	[57-59,141,150,196]
184-187	185	SnSe ₂	A _{1g}	[63]
245	250-253 (254)	SeO ₂ (Se)	E _g (E ₂)	[197] ([199])

Table 3.4: Summary of the data of vibration modes in comparison with the literature

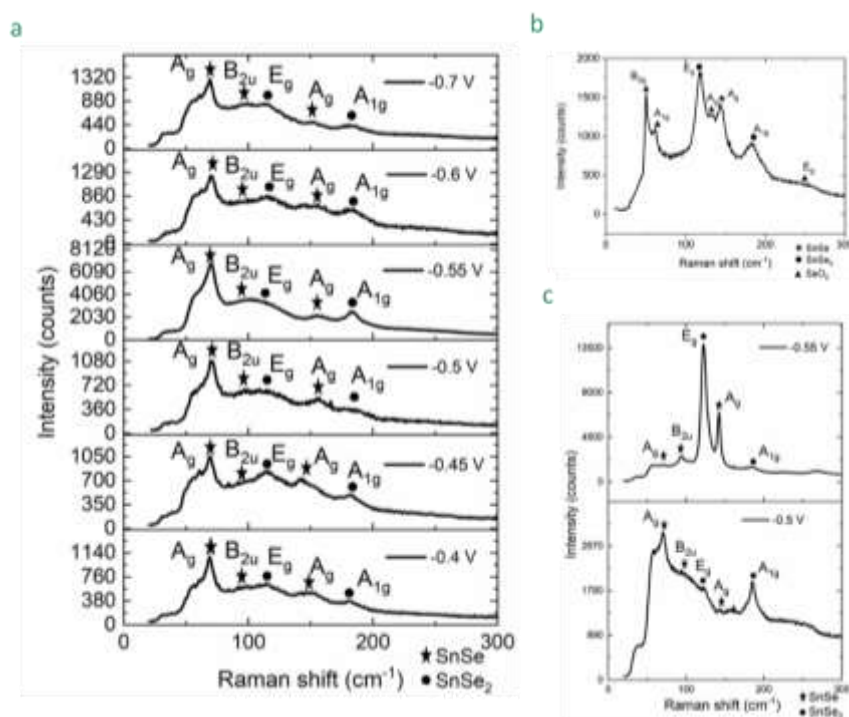


Figure 3.24: Raman spectra of the as-deposited samples: (a) with $Q_{exp} = -12.7$ C (b) with $Q_{exp} = -18.1$ C and (c) on the cross-section of samples

- ✓ The Raman analyzes revealed the presence of SnSe as well as SnSe₂ and SeO₂, in agreement with CEMS and supposed by TEM.
- ✓ At longer deposition time, the presence of Se seems also to be revealed.

g. SIMS/SNMS characterizations

The in-depth homogeneity of the films was firstly investigated by SIMS, on non-transferred samples (Figure 3.25). Whatever the deposition potential, the information taken from the spectra are similar. Indeed, the deposits are quite homogenous along the growth direction since the Sn and Se intensities vary with an overall parallel evolution, which means that the Sn/Se ratio is almost constant in the depth of the films. Moreover, oxygen is present, at least on the surface for the sample deposited at -0.5 V vs AgCl/Ag since its signal decreases rapidly (Figure 3.25 a). We can suspect the presence of oxygen inside the film for the others, since their evolution are parallel to Sn and Se signals (Figure 3.25 b and c). The presence of oxygen was also found by TEM analyzes. It can be due to oxidation from exposure to air or small amount of SnO₂ or SnC₂O₄. The depth profiles enable to approximately determine the thickness of the films since a complete sputtering of the SnSe depth is assured when Sn and Se intensities start to decrease. Thus, we respectively deduce thicknesses of 490 nm, 1.9 μ m and 1.6 μ m for the samples deposited at -0.5 V, -0.55 V and -0.6 V vs AgCl/Ag. The first thickness may be underestimated since the signal drastically fall. Moreover, we cannot exclude loss of matter or porosity since the deposits made at this potential exhibit the worst covering. At -0.55 V and -0.6 V vs AgCl/Ag, taking into account the faradaic yields previously obtained (Table 3.3), we expected thicknesses respectively of 1.24 μ m and 2.59 μ m. Consequently, from the observed thickness, the faradaic yield is overestimated at -0.6 V vs AgCl/Ag.

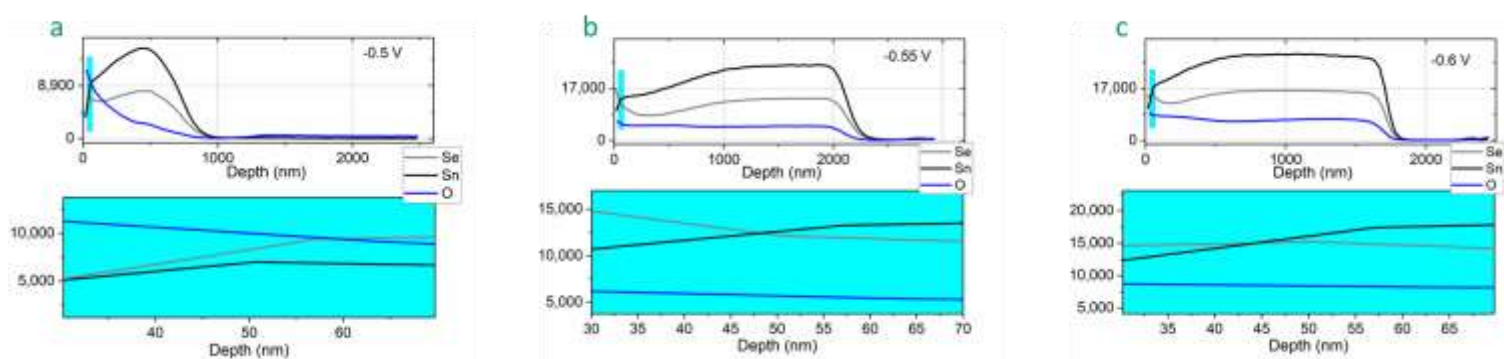


Figure 3.25: Depth profiles obtained on as-deposited samples by SIMS

Chapter 3. Continuous electrodeposition of SnSe films

Other films were studied by SNMS on transferred samples, since this technique is sensitive to roughness (Figure 3.26). Reverse depth profiles were thus made on roughness as small as possible which optimizes the measurements. Like SIMS depth profiles, we find a good in-depth homogeneity of the films thanks to an overall parallel evolution of the Sn and Se intensities, whatever the potential. Thus, we expect a quasi-constant Sn/Se ratio in the depth of the films. The sample deposited at -0.6 V vs AgCl/Ag is less homogenous due to its rougher morphology (Figure 3.26 c). Moreover, the presence of oxygen can be suggested but its intensity does not vary in the same way of Sn and Se intensities. It is higher in the beginning of the sputtering, probably because of exposure to air resulting in surface oxidation. In the end of the analysis of the samples deposited at -0.5 V and -0.55 V vs AgCl/Ag, the O intensity is higher than that inside the film, sign that the glue was sputtered (Figure 3.26 a and b). Like previously, the presence of O can also be explained by SnO_2 or SnC_2O_4 or oxidation from exposure to air. Finally, it was possible to determine an approximate thickness for each sample. Thus, the samples deposited at -0.5 V, -0.55 V and -0.6 V vs AgCl/Ag were respectively found to be 1 μm , 700 nm and 900 nm thick. Taking into account the faradaic yields previously obtained (Table 3.3), we expected thicknesses of 1.4 μm , 1.4 μm and 2.3 μm . The deviations from the expected thicknesses can be either due to overestimation of the faradaic yields or loss of matter.

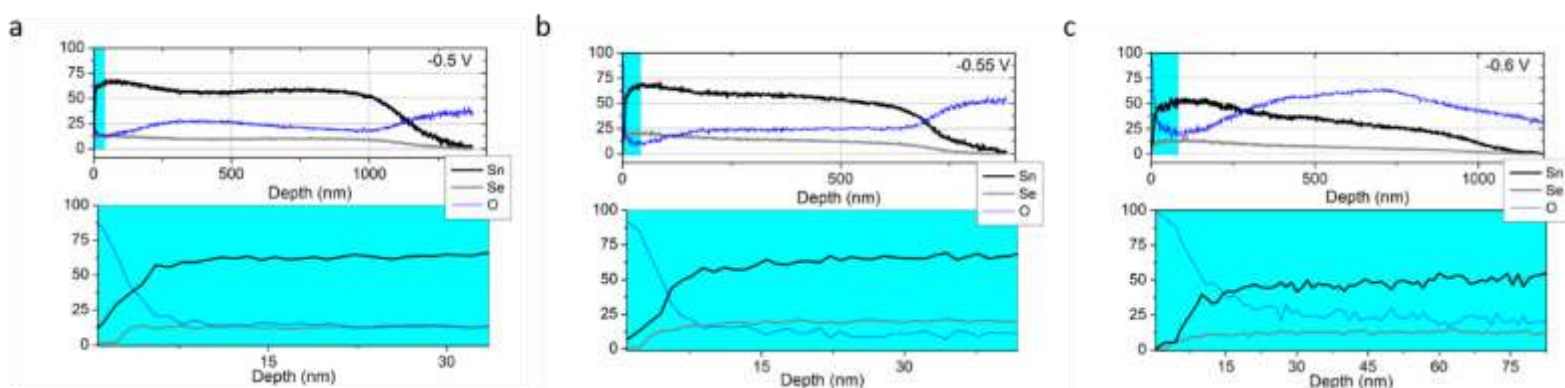


Figure 3.26: Reverse depth profiles obtained on as-deposited samples by SNMS ^[181]

Both SIMS and SNMS tend to show a good in-depth homogeneity, in terms of Sn and Se ratio. However, the analyzes also revealed the presence of oxygen that can come from exposure to air, resulting in surface oxidation. Finally, the thicknesses were generally lower than the expected ones but a loss of matter is not excluded, as well as overestimations of the faradaic yields.

Conclusion

In this chapter, we presented all the work dedicated to continuous electrodeposition of SnSe films. Preliminary studies prior to the electrodeposition enabled to define a deposition potential window. Thus, the deposits having the optimal morphology and composition close to $\text{Sn}_{1.0}\text{Se}_{1.0}$ are those deposited between -0.5 V and -0.6 V vs AgCl/Ag, without separation of the counter-electrode and for a minimum charge quantity of -12.7 C. Several analyzes showed the difficulty to get pure SnSe deposits. Indeed, Mössbauer and Raman spectrometries respectively show the presence of Sn(IV) and SnSe_2 as secondary phase, for optimized deposits between -0.5 V and -0.6 V vs AgCl/Ag. The presence of SeO_2 needs to be confirmed. XRD analyzes do not allow to highlight such secondary phases, which means they are either amorphous or in low quantity. However, their presence seems to be confirmed by TEM analyzes. Finally, SIMS/SNMS analyzes demonstrated a good in-depth homogeneity, as well as oxygen presence, probably caused by oxidation under atmosphere. The main results, in terms of composition and morphology, according to the applied potential, are summarized in [Figure 3.27](#).

The electrodeposition requires the use of a conductive substrate, as opposite to the electrical measurements, needing either a self-standing film, or a transferred film on a non-conductive substrate. We chose to transfer the SnSe films via the technique illustrated in [Figure 2.14](#). Although we tried to optimize this method, it was impossible to obtain an adequate process to the electrical measurements (without loss of deposit and induced cracks). Consequently, no electrical measurements were carried out.

Dans ce troisième chapitre, nous avons présenté tout le travail dédié à l'électrodéposition de films de SnSe en mode continu. Des études préliminaires à l'électrodéposition ont permis de définir une fenêtre de potentiels de déposition. Ainsi, les dépôts adoptant la morphologie et composition optimales proche de $\text{Sn}_{1.0}\text{Se}_{1.0}$ sont ceux électrodéposés entre -0,5 V et -0,6 V vs Ag/AgCl, sans séparation de la contre-électrode et pour une quantité de charge minimale de -12,7 C. Plusieurs analyses ont montré la difficulté d'obtenir des films purs de SnSe. En effet, les spectrométries Mössbauer et Raman montrent respectivement la présence de Sn(IV) et de SnSe_2 en phase secondaire, pour des dépôts optimisés entre -0,5 V et -0,6 V vs Ag/AgCl. La présence de SeO_2 nécessite d'être confirmée. Les analyses DRX ne permettent pas de mettre en évidence de telles phases secondaires, ce qui signifie qu'elles sont soit amorphes, soit en faible quantité. Cependant, leur présence semble être confirmée par les analyses MET. Enfin, les analyses SIMS/SNMS ont démontré une bonne homogénéité en profondeur, ainsi que la présence d'oxygène, probablement provoquée par une

Chapter 3. Continuous electrodeposition of SnSe films

oxydation à l'atmosphère. Les principaux résultats, en termes de composition et de morphologie, selon le potentiel appliqué, sont résumés sur la [Figure 3.27](#).

L'électrodéposition requiert le recours à un substrat conducteur, contrairement aux mesures électriques, nécessitant soit un film autosupporté, soit un film transféré sur un substrat non-conducteur. Nous avons ainsi choisi de transférer les films de SnSe via la technique illustrée en [Figure 2.14](#). Bien que nous ayons tenté d'optimiser cette méthode, il nous a été impossible d'obtenir un procédé adéquat aux mesures électriques (sans perte de dépôts et fissures induites). Par conséquent, aucune mesure électrique n'a été réalisée.

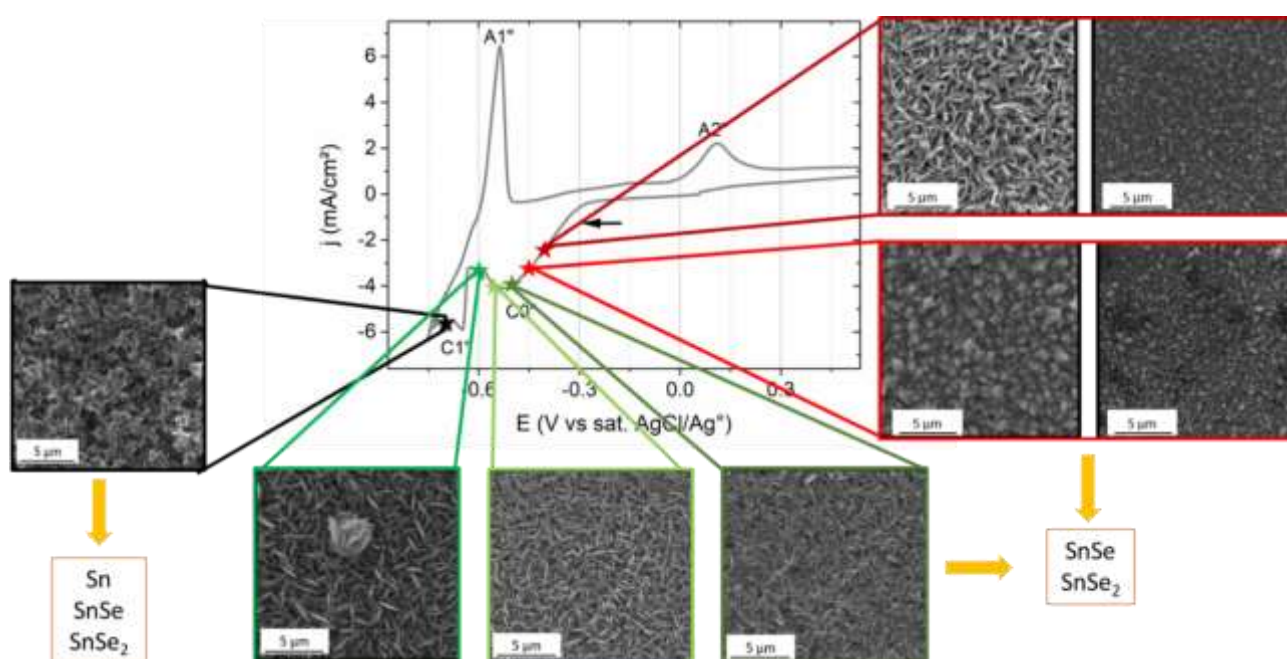


Figure 3.27: Dependence of the deposition potential on the composition and morphology of the films

Chapter 4.

Pulse electrodeposition of SnSe films

Introduction

In order to improve the quality of the deposits (crystallinity, morphology, compacity) and possibly the faradaic yield, it was decided, in this fourth chapter, to make deposits in pulse mode. The potentiostatic technique was preferred to the galvanostatic one for selectivity considerations. Indeed we have demonstrated in the [Chapter 3](#) that the electrodeposition of SnSe is strongly dependent on the applied potential. Moreover, the study only focuses on the synthesis at -0.55 V vs AgCl/Ag, this potential giving in continuous mode the best characteristics (stoichiometry, crystallinity, purity). In the first part, all of the electrodeposition parameters (t_{ON} , t_{OFF} and Q_{th}) will be defined. In the second part, the influence of the pulse duration (t_{ON}) on the deposits, mainly from a microstructural point of view will be investigated. The third part will focus on the optimization of the value of t_{OFF} , in order to limit the duration of the experiments. Consequently, a second series of results, for the optimized value of t_{OFF} , will be presented in the fourth part. Finally, the fifth part will be an introduction to doping of SnSe films by electrodeposition, aspects poorly treated regarding the literature. This part is intended to improve the electrical conductivity of SnSe films.

Afin d'améliorer la qualité des dépôts (cristallinité, morphologie, compacité) et éventuellement le rendement faradique, il a été décidé, dans ce quatrième chapitre, d'électrodéposer en mode impulsif. La technique potentiostatique a été préférée à la technique galvanostatique pour des considérations de sélectivité. En effet, nous avons démontré dans le [Chapitre 3](#) que l'électrodéposition de SnSe est fortement dépendante du potentiel appliqué. De plus, l'étude ne porte que sur la synthèse à -0.55 V vs Ag/AgCl, ce potentiel donnant les meilleures caractéristiques en mode continu (stœchiométrie, cristallinité, pureté). En première partie, l'ensemble des paramètres d'électrodéposition (t_{ON} , t_{OFF} et Q_{th}) sera défini. En seconde partie, l'influence de la durée de pulse (t_{ON}) sur les dépôts, principalement du point de vue microstructural sera étudiée. La troisième partie se focalisera sur l'optimisation de la valeur du t_{OFF} , afin de limiter la durée des expériences. Par conséquent, une seconde série de résultats, pour la valeur optimisée de t_{OFF} , sera présentée en quatrième partie. Enfin, la cinquième partie sera une introduction au dopage de films de SnSe par électrodéposition, aspect peu abordé dans la littérature. Cette partie est destinée à améliorer la conductivité électrique des films de SnSe.

I. Choice of the pulse mode

Pulse electrodeposition is of particular interest for the synthesis of anticorrosive coatings and semiconductors with controlled morphology and composition. The transfer kinetics, electrocrystallization and action of additives are influenced by the pulse parameters which are the pulse duration (t_{ON}), the relaxation time (t_{OFF}) and the pulse current or potential. If these parameters are not appropriately set, unexpected results can be obtained ^[161]. This method enables the reduction of additive concentration which can be a disadvantage in some cases, specifically for manufacturers. Moreover, the pulse method is more difficult to carry out. That is the reason why the procedure needs to be thoroughly planned before execution. The potentiostat equipments have also limited current capabilities and cause instability during high frequency pulse experiments. The advantages of using pulse electrodeposition are various. First of all, in comparison with DC electrodeposition, the replenishment of metal ions occurs only during t_{OFF} . The second advantage is by adjusting the pulse parameters, the composition, morphology and porosity can be tuned. Thus, reduced porosity, gas content and grain size as well as higher purity are usually observed. Hence, the mechanical and electrical properties of the deposits can be improved ^[90]. Finally, pulse electrodeposition enables to reduce even eliminate the additive fraction as compared to DC mode.

The variety of the materials investigated by pulse electrodeposition is huge. Unary compounds such as precious metals ^[201–203], as well as zinc ^[204], chromium ^[205], nickel ^[206] and tin ^[207] are the most studied by pulse electrodeposition. Alloys with those elements were also reported ^[208–212]. New architectures involving multilayers ^[213], nanostructures ^[192] and composites ^[214] are more and more elaborated. The method itself is modernizing by adding magnetic field ^[215] or ultrasonic ^[216] to the pulse process. The application fields are large, from simply the improvement of the properties and morphology like reduction or removal of tin whiskers ^[91] to deposition for printed circuit ^[217]. Optoelectronic ^[218], photovoltaic ^[219,220] and thermoelectric materials ^[221–223] earn interest in this synthesis method.

In this study, we investigated the effect of the pulse deposition on SnSe films. As presented in [Chapter 2 \(Figure 2.13\)](#), we decided to apply a cathodic potential during t_{ON} , followed by a period t_{OFF} during which the electrical circuit is open (zero current). This relaxation time must be sufficient to ensure a complete replenishment of Sn and Se species in the vicinity of the working electrode. That is the reason why an arbitrary value of t_{OFF} equal to 1 s was chosen in a first step. This value was reduced to 400 ms in a second step as described later in this chapter.

The investigation was made by varying the pulse duration (t_{ON}) from 50 ms to 500 ms. Due to limitations of the electrochemical equipment, it was not possible to decrease the t_{ON} below 25 ms, with unsuccessful tests. Moreover, the software does not allow to stop the experiments at a targeted charge quantity. Long-time experiments were not possible. Thus, a charge quantity of $Q_{th} = -2.4 \text{ C.cm}^{-2}$ was targeted by applying a fixed pulse number, by estimating a value of constant mean cathodic current (equation 2.5). The reached charge quantity was measured using an analogical coulometer.

For more simplicity and due to time limitations, all the experiments were made at the same cathodic potential during t_{ON} . As seen in Chapter 3, the quality of the deposits is strongly dependent on the deposition potential. Taking into account the morphology, the composition as well as the in-depth homogeneity, the best deposits are those synthesized at -0.55 V vs AgCl/Ag. That is the reason why we focus only on this potential for pulse deposition.

II. First set of results: pulse depositions with $t_{OFF} = 1 \text{ s}$

a. Effect on the double layer charging

The double layer charging occurs during t_{ON} . This electrical effect due to polarization of the electrode occurs with a strong transient current, which exponentially drops during the first ms. This additional current to the faradic one should mainly be dependent on the deposition potential. Thus, our first goal was to find the minimum value of t_{ON} that can be applied for the synthesis of SnSe films since the charging time should be lower than the pulse on-time.

The influence of the pulse duration on the double layer charging time was then investigated. For that, the contribution of the double layer charging was graphically estimated as described below. The tangent on the first points, where the charge is supposed to occur, is plotted (Figure 4.1). Then, for sake of simplification, a linear fit was performed according to the equation of the tangent (of type $y = ax + b$). Finally, the double layer charging time can be estimated by solving $ax + b = 0$ where x corresponds to the double layer charging time.

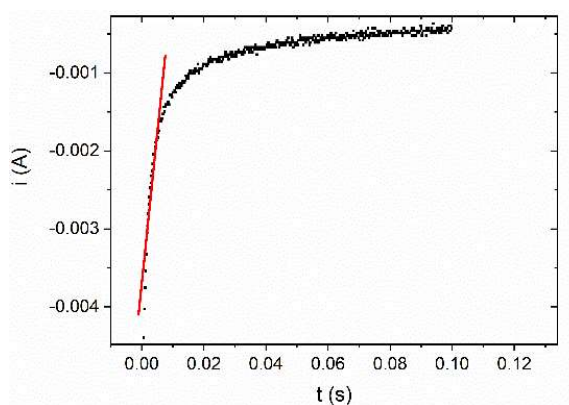


Figure 4.1: Determination procedure of the double layer charging time

Two series of experiments were made to ensure reproducibility, keeping a t_{OFF} of 1 s (Figure 4.2). As it can be seen, there is a surprising exponential evolution of the estimated double layer charging time with the applied value of t_{ON} . This result was not expected since only the applied potential and the current should have an influence on the double layer charge ^[161]. We cannot neglect the possible influence of other phenomena (corrosion, adsorption, side reaction) and uncertainty from the determination graphical method. Nevertheless, we estimated double layer charging times between 2 and 35 ms for t_{ON} ranging from 1 to 1000 ms. Thus, t_{ON} must be higher than these values to fully charge the double layer ^[212]. It should be noticed that the equipment devoted to the pulse electrodeposition may increase the double layer charging time ^[161].

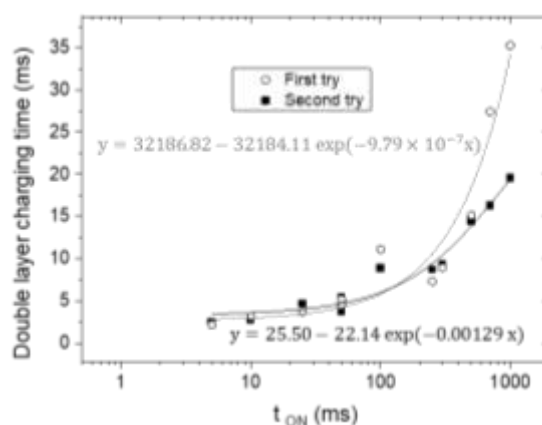


Figure 4.2: Evolution of the double layer charging time with t_{ON}

b. Study of the chronoamperograms

The current density was recorded during each electrodeposition experiment. For the sake of simplicity, the amplitude of the current density is represented in absolute value of the last pulse. The

origin of each pulse is set at $0 \mu\text{A}\cdot\text{cm}^{-2}$ and 0 s (Figure 4.3). As it can be seen, there is an increase of the amplitude as the pulse duration decreases. Since the experiments are made at the same applied potential (-0.55 V vs AgCl/Ag), such evolution is unexpected. We suggest that for shorter t_{ON} , side reactions can contribute to increase the absolute current density. It should be underlined that this observation is valid all along the electrodeposition process (Appendix 2). From the evolution of the current density with t_{ON} , we expect, for an equivalent total growth time, an increase of the absolute charge quantity when t_{ON} decreases.

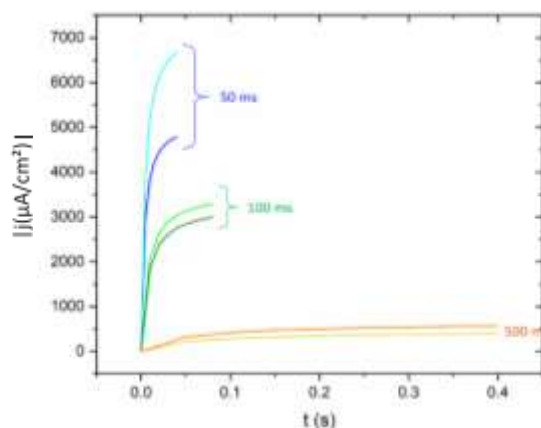


Figure 4.3: Typical chronoamperometric curves recorded for samples deposited with a t_{OFF} of 1 s

c. HRSEM and SEM characterizations

The morphology of the deposits was investigated by HRSEM (Figure 4.4). The morphology depends on the t_{ON} parameter. The deposits synthesized with t_{ON} of 50 ms exhibit the greatest grain size with platelet-like morphology. Progressively, the platelet-like grains give way to thinner needle-like grains by increasing the values of t_{ON} . This decrease of grain size may be related to the decrease in the absolute current density which leads to lower growth rates (Figure 4.3). Higher absolute charge quantities are expected at lower t_{ON} . It should be reminded that such morphology evolution was observed in DC electrodeposition in Chapter 3. Needle-like grains were obtained at -12.7 C whereas platelet-like to spherical grains were obtained for lower charge quantity. Moreover, according to Hansal and Roy, a too short t_{OFF} results in mass transport limitation (with incomplete replenishment of the reactive species), involving the formation of rough surface. On the contrary, a too long t_{OFF} is responsible of larger grain size^[161]. Thus, we cannot neglect the necessity to adjust t_{OFF} for each t_{ON} , specifically for 500 ms .

Aggregates can be found, specifically at a t_{ON} of 500 ms. It should be underlined that the use of a HRSEM with higher resolution was preferred to SEM since smaller grains are obtained in pulse mode in comparison with continuous mode. Thus, the grains are difficult to observe with a low resolution SEM. This phenomenon is in agreement with repeated short nucleation times in pulse deposition leading to compact film. As shown below by TEM analysis, the films are much thinner than those obtained in continuous mode since the targeted charge quantity is almost divided by 5, namely -2.4 C/cm^2 instead of -10.89 C/cm^2 . Consequently it was not possible to transfer the deposits onto a non-conductive substrate. Bottom face analyzes as well as cross sectional views were also impossible.

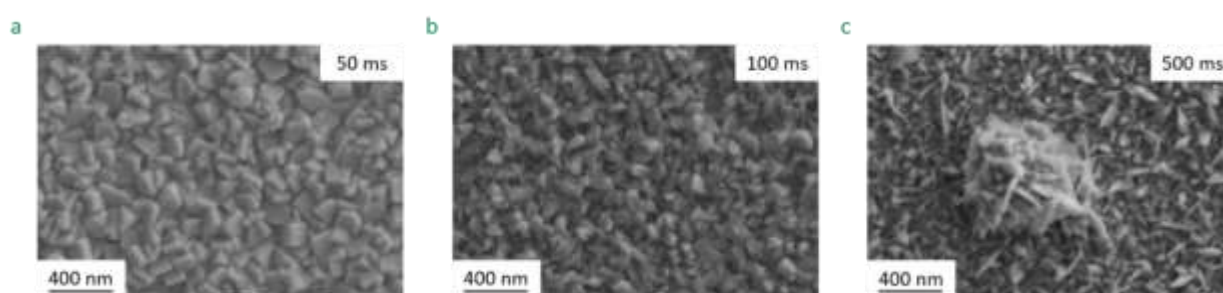


Figure 4.4: Typical HRSEM images of samples deposited at -0.55 V vs AgCl/Ag and t_{ON} of (a) 50 ms, (b) 100 ms and (c) 500 ms

Occasionally, heterogeneities were observed whatever the pulse duration. As shown in Figure 4.5 a and b, different grain sizes and morphologies can be randomly obtained in the same sample. It can be due to ineffective cleaning process of the substrate and the presence of local precipitates (yellow circles) and/or inhomogeneous distribution of the electrical field lines along the substrate.

For well distributed morphological irregularities on the sample, the current distribution can be a candidate. Three types of current distributions can be distinguished ^[161]:

- the primary current distribution depending on the geometry of the cell
- the secondary current distribution determined by the charge transfer reaction
- the tertiary current distribution which is mass transfer controlled

This can also explain why heterogeneities were obtained at 50 ms. Both primary and secondary current distributions may be responsible of such heterogeneities. Indeed, the primary current distribution is the least uniform and generates needles for kinetically low limited electrode materials with strong edge effect. The current circulation is easier towards points near the counter-electrode. Although the position of the working electrode should be the almost the same, we do not exclude displacement as well as tilt from previous positions. However, this effect should be relatively low. The secondary current distribution becomes less uniform at higher current density. At a t_{ON} of 50 ms, we observe the highest absolute current densities. It also depends on the polarization resistance of the

electrode surface. Hence this current distribution may have a strong influence. Finite element modelling of current distribution would be valuable for a better understanding of such effects.

In the wide field image we can see color contrasts as well as defects, which implies probable cleaning deficiency (Figure 4.5 c). While the samples were successively cleaned after each electrodeposition by H_2SO_4 , water and finally ethanol, the presence of solid products seems to persist on the films.

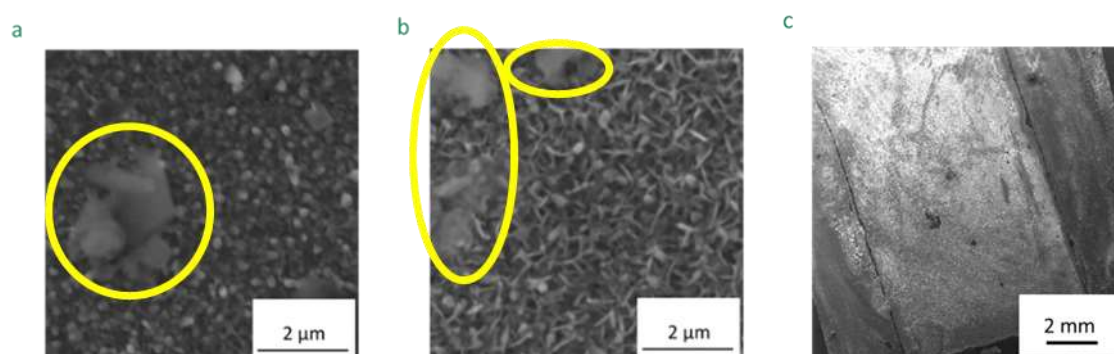


Figure 4.5: (a) and (b) SEM images of two zones of a same sample deposited with a t_{ON} of 50 ms and (c) and enlarged view

d. TEM characterizations

Several samples were analyzed by TEM from FIB slides (Table 4.1). They exhibit good compacity and according to the HAADF mode, a phase contrast is not obvious. For all samples, regular thickness with no cracks or holes is obtained. Individual grains of height almost equal to the thickness (for t_{ON} equal to 50 ms and 100 ms) are observed. The compacity seems to be improved as the t_{OFF} increases.

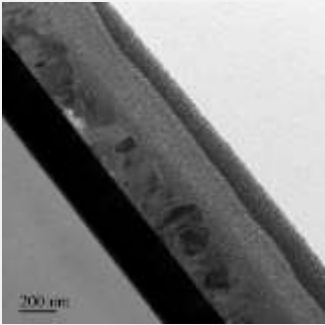
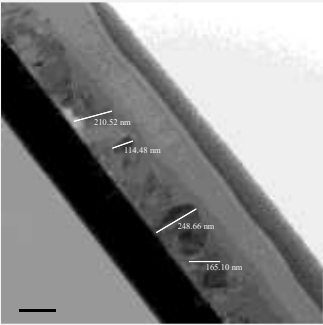
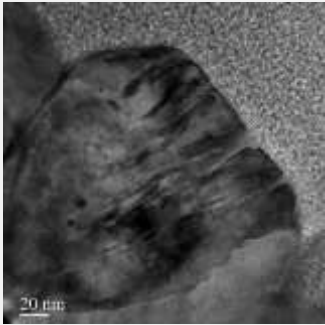
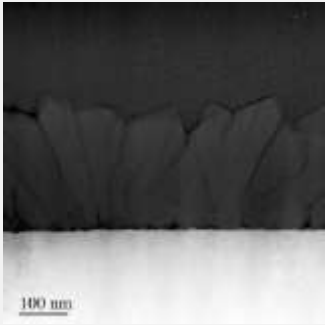
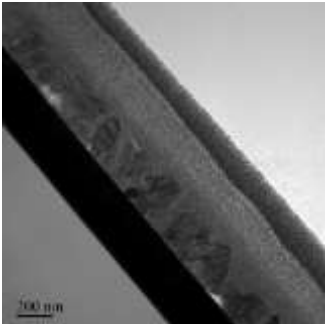
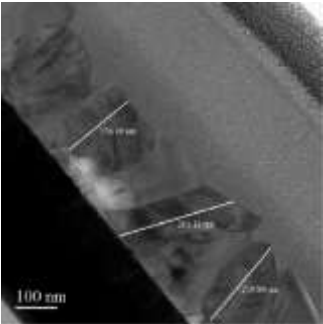
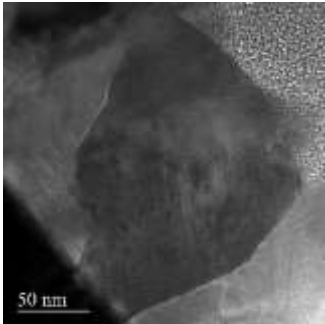
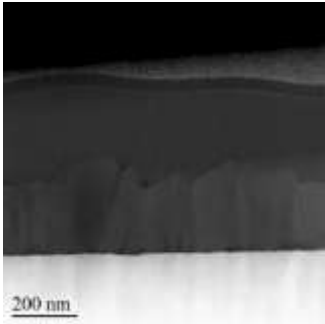
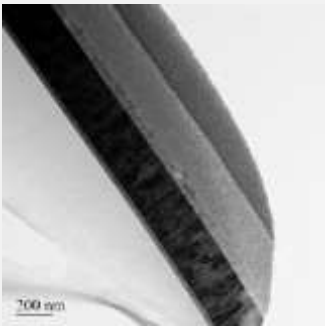
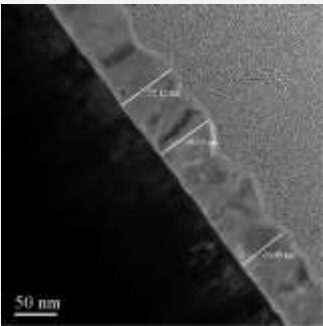
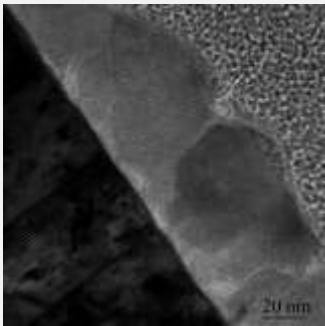
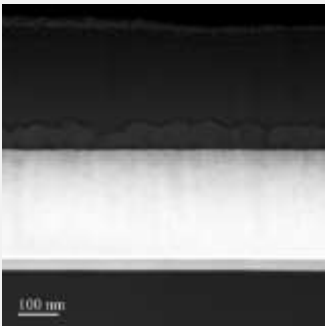
	TEM-BF	TEM-BF	HRTEM	STEM-HAADF
50 ms				
100 ms				
500 ms				

Table 4.1: TEM-BF, HRTEM and STEM-HAADF micrographs of samples deposited for t_{ON} of 50, 100 and 500 ms

Chapter 4. Pulse electrodeposition of SnSe films

An estimation of the related thicknesses can be made and is reported in Table 4.2. A decrease of the thickness is found when t_{ON} increases. This evolution is in agreement with the conclusions from the chronoamperometric curves (Figure 4.3). An apparent decrease of the faradic yield is determined. The faradic yield is only an estimation, since the theoretical charge quantity is based on a constant mean current. No measured value of the charge quantity was unfortunately available for this set of experiments. The faradaic yield determined from continuous mode at -0.55 V vs AgCl/Ag was 23.29 %. In pulse mode, the estimated faradaic yields are lower than this value. It seems that our method should be more optimized.

Pulse duration (ms)	50	100	500
Pulse number	12000	6000	1200
Total duration (s)	12650	6623	1692
Experimental thickness (nm)	~250	~200	~60
Theoretical charge quantity (C.cm ⁻²)	-4.09	-1.87	-0.72
Experimental charge quantity (C.cm ⁻²)	X	X	X
Theoretical thickness (μm)	2.26	1.03	0.40
Faradaic yield (%)	11.06	19.42	15.00

Table 4.2: Influence of the pulse duration on the thickness and faradaic yield

FFT analyzes confirmed the presence of SnSe. However, it seems that other phases are present since the interplanar distances are different from those of the COD database of orthorhombic SnSe (Appendix 1 and Table 4.3). This phase might be SnSe₂.

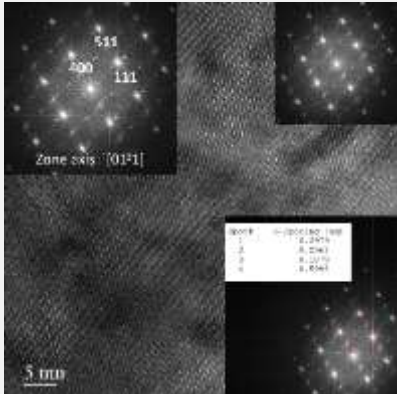
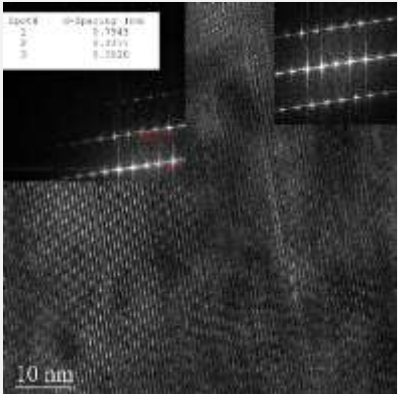
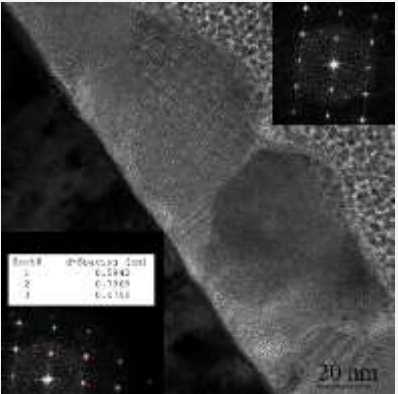
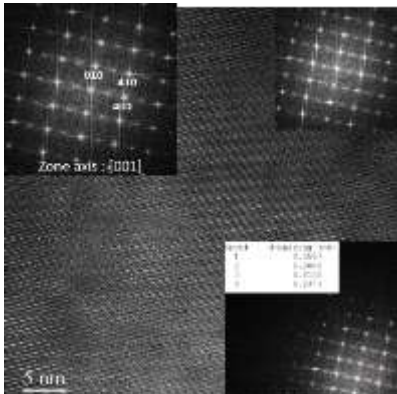
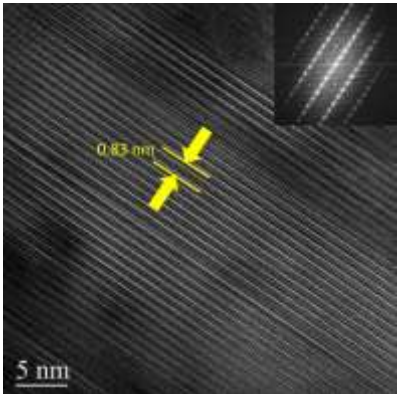
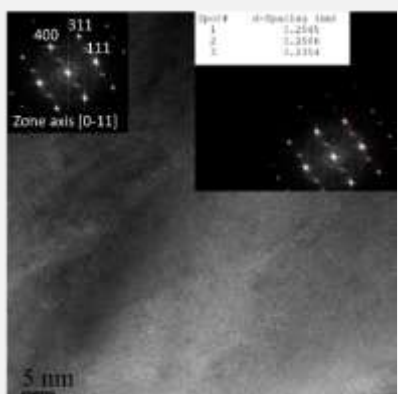
50 ms	100 ms	500 ms
		
		
		

Table 4.3: FFT results obtained on lamellas for different values of t_{ON} . The electron diffraction pattern are indexed according the SnSe orthorhombic phase

The composition of the films was determined by EDS (Figure 4.6). The samples synthesized with a t_{ON} of 50 and 100 ms show a Sn/Se ratio close to 1:1, in agreement with the expected SnSe. The sample synthesized at 500 ms exhibit a Sn excess. All samples reveal the presence of about 5 at.% of oxygen which can come from oxalate or SnO_2 . A surface oxidation under atmosphere is not excluded.

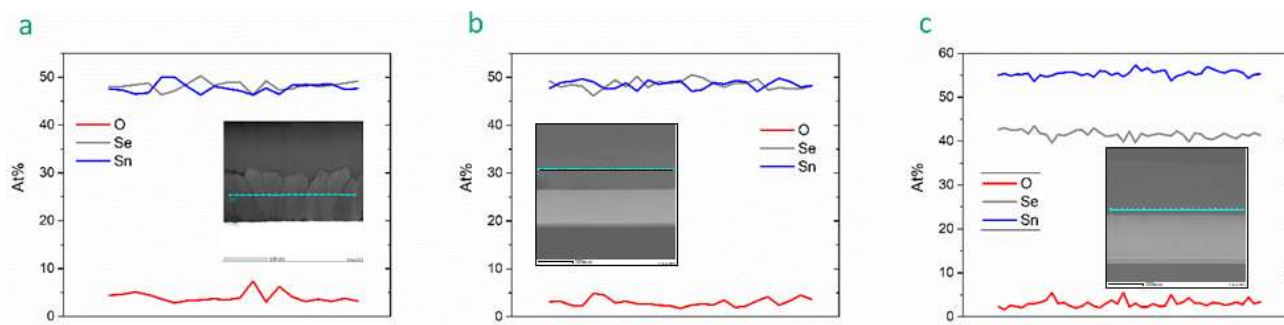


Figure 4.6: EDS analyzes on the samples deposited with a t_{ON} of (a) 50, (b) 100 and (c) 500 ms

It should be underlined that EDS analyzes on different grains as well as in depth do not reveal composition differences (Figure 4.7). Even if the oxygen content was not taken into account, a stoichiometry close to 1:1 is found in agreement with SnSe.

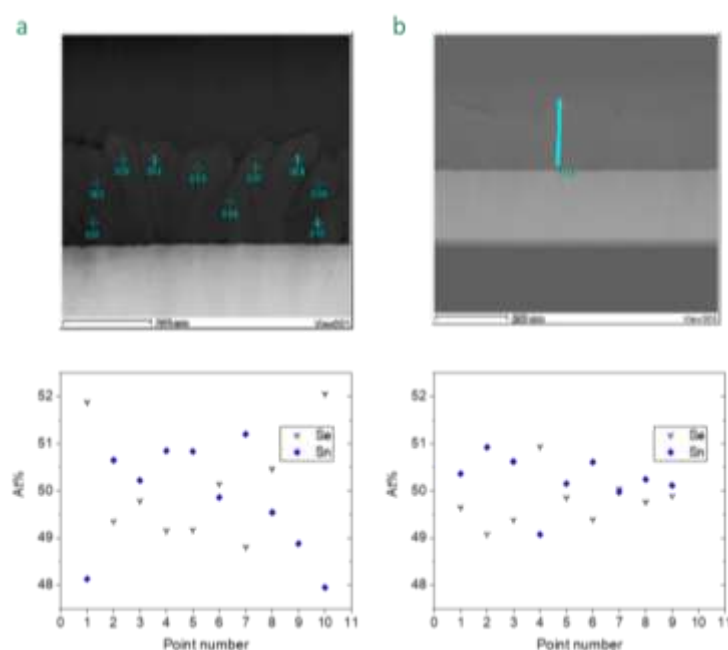


Figure 4.7: EDS analyzes on the samples deposited with a t_{ON} of 50 ms (left) on several grains and (right) in depth

e. XRD characterizations

XRD analyzes were recorded on top face of the samples and typical patterns are represented in Figure 4.8. All samples reveal the presence of SnSe indexed into the orthorhombic structure. Moreover, a preferential growth orientation is found to be perpendicular to the (111) plane. To get an idea of the evolution of the crystallinity, the crystallite size was estimated thanks the Debye-Scherrer equation (equation 4.1) and applied on the (111) peak of each samples as the most significant.

$$\tau = \frac{K\lambda}{\beta \cos \theta} \quad 4.1$$

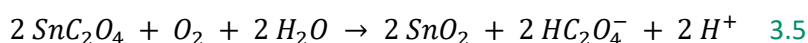
With τ, K, λ, β and θ are respectively the crystallites size, the dimensionless shape factor (equal to 0.89), the X-ray wavelength (1.5406 Å), the Full Width at Half-Maximum (FWHM) and the Bragg angle respectively

The (111) peak has a value of FWHM increasing with t_{ON} . It means the crystallite size decreases when the t_{ON} increases, as displayed in Table 4.4. This evolution is in agreement with the HRSEM analyzes (Figure 4.4). We suggest a decrease of the growth rates, as the t_{ON} increases, due to the decrease of the absolute current density (Figure 4.3).

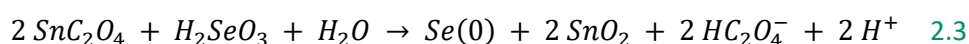
t_{ON} (ms)	Crystallite size (Å)
50	254.93 ± 28.93
100	237.23 ± 8.60
500	225.15 ± 9.08

Table 4.4: Evolution of the crystallite size with the t_{ON}

A decrease of the (111) peak intensity is observed when increasing t_{OFF} which suggests a decrease of the thickness (for the same XRD analysis parameters). This observation is in agreement with the evolution from TEM analyzes (Table 4.1). It should be underlined that few peaks could not be indexed according to the orthorhombic structure of SnSe. Minor and weak peaks at 33.4° and 51.06° can be respectively attributed to the (101) and (211) planes of SnO₂ according to the COD card n°1000062 (tetragonal structure, $P 4_2/m n m$ space group). It should be underlined that the peak at 25.5° could both be assigned to SnO₂ and SnSe. The presence of SnO₂ as secondary phase can be explained by the partial oxidation of Sn(II) into Sn(IV) (reaction 3.5).



In the chapter 2, we also highlighted the possible reaction between Sn(II) and Se(IV) generating SnO₂ (reaction 2.3).



Although these reactions suggest precipitations, the ICP analyzes did not reveal a loss in Sn concentration, suggesting the formation of a soluble Sn(IV) species. Finally, SnO_2 , can be generated from surface oxidation under atmosphere.

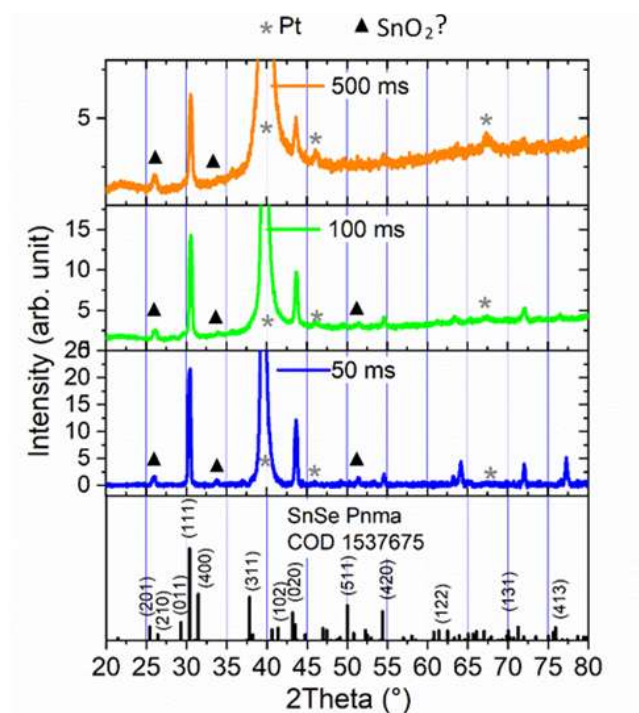


Figure 4.8: XRD analyzes on as-deposited samples by pulse method with $t_{OFF} = 1$ s and different values of t_{ON} : 50 ms, 100 ms and 500 ms.

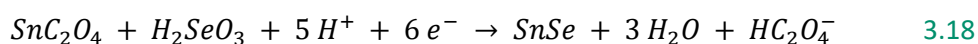
A first set of experiments was done, where a potentiostatic pulse method was developed for the synthesis of thin films. The influence of the value of t_{ON} , from 50 ms to 500 ms was in particular studied on the microstructure of the films with an applied potential equal to -0.55 V vs AgCl/Ag and a t_{OFF} value of 1 s. The results reveal:

- ✓ An unexpected dependence of the double layer charging time increasing with t_{ON}
- ✓ An unexpected dependence of the absolute steady state cathodic current density decreasing with an increase of t_{ON} , leading to thinner deposits as t_{ON} increases
- ✓ A dependence of the morphology with t_{ON} (from platelet-like to needle-like grains)
- ✓ Individual grains distinguished by TEM
- ✓ Unfortunately worse faradaic yields than those obtained from continuous mode
- ✓ Stoichiometric SnSe grains identified along the thickness and the film with no apparent precipitates or well defined second phase. A slight Sn excess for t_{ON} equal to 500 ms, as well as presence of O whatever the t_{ON}
- ✓ SnSe indexed according to the orthorhombic structure
- ✓ Crystallite size decreasing when t_{ON} increases, maybe related to the decrease of the absolute current density with t_{ON} , involving low growth rates

III. Second set of results: pulse deposition with reduced relaxation time

a. Optimization of the replenishment time

In order to limit the duration of the experiments (between around 1800 s and 24600 s for $t_{OFF}=1s$, (Table 4.5), there is a necessity to decrease the value of t_{OFF} . A determination of the lowest value of t_{OFF} without any disturbance can be made from the estimation of the replenishment time. It can be graphically estimated during the relaxation process. For that, we consider that the observed potential during t_{OFF} is governed by the Nernst relationship of the electrochemical system of Se(IV), Sn(II)/SnSe (equation 3.18) with the interfacial concentrations according to the following relation 4.2.



$$E_{Sn(II),Se(IV)/SnSe} = E_{Sn(II),Se(IV)/SnSe}^0 + \frac{RT}{6F} \ln \left(\frac{[H_2SeO_3] [SnC_2O_4] [H^+]^5}{[HC_2O_4^-]} \right) \quad 4.2$$

Therefore we estimate that the replenishment of the electroactive species at the electrode is finished when the observed potential is almost stabilized. The replenishment time is given by the intersection of both tangents of the potentiometric curve (Figure 4.9).

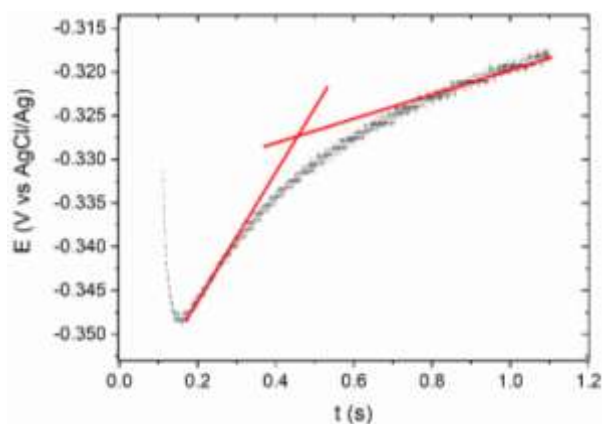


Figure 4.9: Graphical determination procedure of the replenishment time

Thus, the replenishment time was estimated by varying t_{ON} and keeping t_{OFF} at 1 s (Figure 4.10). Two series of experiments were carried out in order to assure repeatability. However, differences are observed for a same t_{ON} , due to the uncertainty from the graphical determination method. We observe a trend to decrease the replenishment time as t_{ON} increases. The reverse trend was expected since a longer t_{ON} leads to a decrease of the absolute cathodic current (Figure 4.3) and then generates a less important consumption of the Sn(II) and Se(IV) species. From all of the data, we arbitrary chose to define the replenishment time to a value of 400 ms, needed for a complete replenishment of Sn(II) and Se(IV) species. This estimated value of replenishment time is generally overestimated regarding the estimated values for each t_{ON} (Figure 4.10). However, the replenishment time must be prolonged due to the equipment limitations. A t_{OFF} higher than the replenishment time is also needed to ensure a complete replenishment^[161].

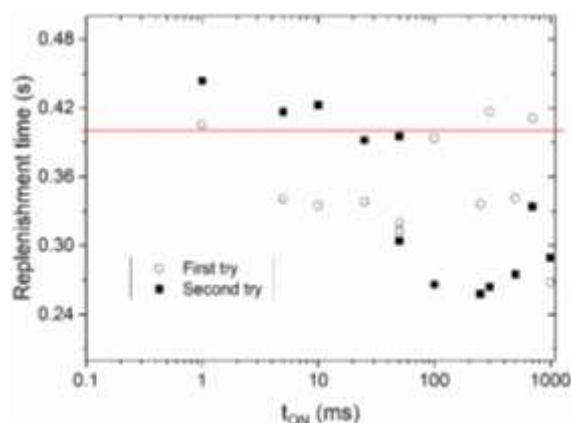


Figure 4.10: Variation of the replenishment time with t_{ON}

b. Study of the chronoamperograms

As previously mentioned, the t_{OFF} value was optimized and fixed at 400 ms instead of 1 s for all further deposits. Thus, the duration of the experiments are considerably reduced (Table 4.5). They are comprised between 1080 s and 5400 s instead of 1800 to 12600 s. It should be underlined that for each experiments, the average current was assumed to be equal to -4.0 mA which was the average absolute current for a t_{ON} of 50 ms. In fact, the absolute current is overestimated and the number of required pulses is consequently underestimated. Although it should not have any influence on the growth rate, these underestimations of pulse number might be responsible of the differences in reached charge quantities.

Q_{th} (C)	i_A (mA)	t_{ON} (ms)	t_{OFF} (ms)	$N = \frac{Q_{th}}{i_A t_{ON}}$	Deposition duration (s) $= N t_{ON}$	Experiment duration (s) $= N (t_{ON} + t_{OFF})$
-2.4	-4.0	50	1000	12000	600	12600
-2.4	-4.0	100	1000	6000	600	6600
-2.4	-4.0	500	1000	1200	600	1800
-2.4	-4.0	50	400	12000	600	5400
-2.4	-4.0	100	400	6000	600	3000
-2.4	-4.0	500	400	1200	600	1080

Table 4.5: Deposition parameters for a supposed deposition area of 1 cm²

The chronoamperometric curves of each experiments were systematically recorded. In order to compare them with the results obtained for t_{OFF} of 1 s (Figure 4.3), the last pulse of each experiment is represented in absolute value (Figure 4.11). Its origin is set at 0 $\mu\text{A}\cdot\text{cm}^{-2}$ and 0 s.

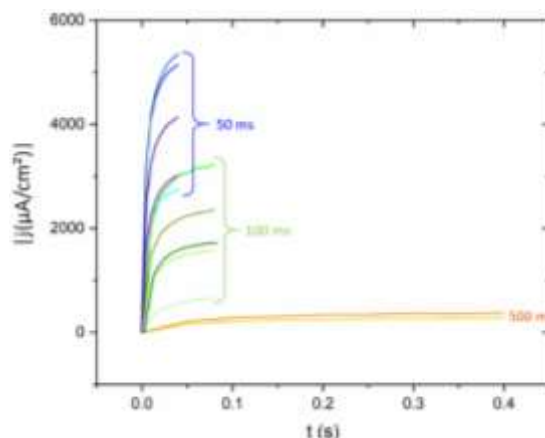


Figure 4.11: Chronoamperometric curves recorded for samples deposited with a t_{OFF} of 400 ms

It seems that there is no influence of t_{OFF} since similar current densities to those obtained with a t_{OFF} of 1 s are obtained. Moreover, we still observe a decrease of the current density with t_{ON} . Thus, we expect lower charge quantities and thicker deposits when decreasing the value of t_{ON} .

The optimization study of the relaxation time t_{OFF} revealed the following key points:

- ✓ A reverse dependence of the replenishment time with t_{ON} is observed in agreement with the influence of t_{ON} on the observed cathodic current
- ✓ The value of t_{OFF} was optimized to 400 ms with no influence on the observed current density, whose evolution with the t_{ON} is similar to that of $t_{OFF} = 1$ s

c. HRSEM and SEM characterizations

Samples deposited with an optimized t_{OFF} value of 400 ms were analyzed by HRSEM (Figure 4.12). The trend is similar to what we observed for a t_{OFF} of 1 s. Indeed, coarser grains are generated for a t_{ON} of 50 ms and the morphology changes to needle-like grains with higher values of t_{ON} . Aggregates are specifically found for deposits synthesized for t_{ON} equal to 500 ms. As mentioned for the samples prepared with a t_{OFF} of 1 s, we cannot neglect the necessity to readjust t_{OFF} for each t_{ON} . Larger grain sizes are obtained for too long t_{OFF} . On the contrary, an insufficient t_{OFF} leads to rough surfaces ^[161].

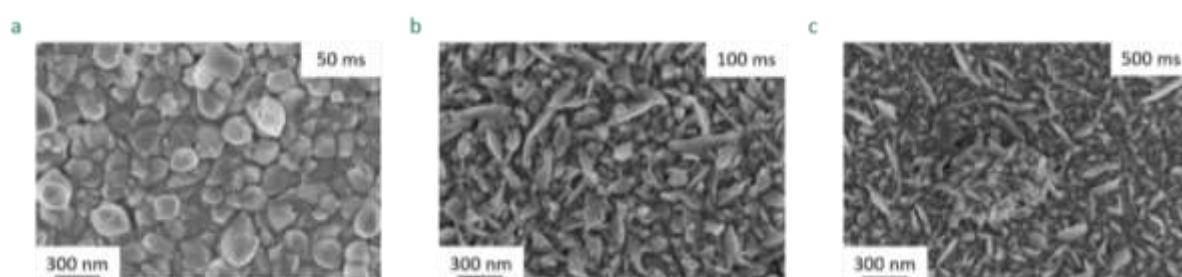


Figure 4.12: HRSEM images of samples deposited at -0.55 V vs AgCl/Ag and t_{ON} of (a) 50 ms, (b) 100 ms and (c) 500 ms

At macroscale, heterogeneities can be observed and may be induced by imperfect cleaning process (Figure 4.13). Moreover, discs and lines are present on the surface, suggesting either a non-uniform distribution of the current lines or either local pH variation during the electrodeposition process. It should be remind that the primary current distribution is the least uniform and can

contribute to the synthesis of needles for kinetically low limited electrode materials with strong edge effect. The secondary current distribution becomes less uniform at higher current density. This can explain why heterogeneities were encountered at lower t_{ON} . Since at 50 ms higher absolute current densities are reached, we suggest a strong influence of the secondary current distribution. We cannot neglect tilts and difference of positioning the working electrode, which can also impact the primary current distribution.

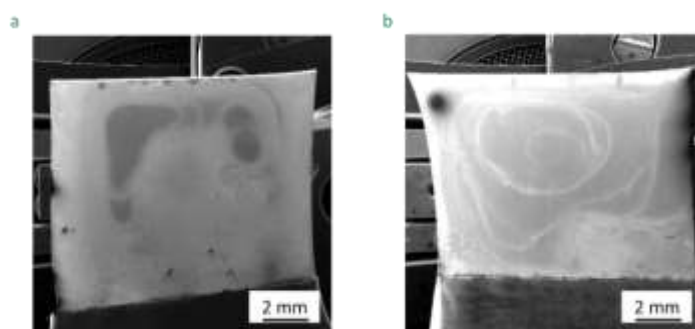


Figure 4.13: SEM images (wide-view) of samples deposited with t_{ON} of (a) 50 ms and (b) 100 ms

d. TEM characterizations

Lamellas, prepared by FIB, were analyzed by TEM (Table 4.6). First of all, from the HAADF mode, the samples do not seem to exhibit in-depth phase contrast. A good compacity is also found, whatever the t_{ON} . Individual grains are more difficult to distinguish in comparison with the films deposited at a t_{OFF} of 1 s (Table 4.1). The roughness also seems to be more important. This can be due to an insufficient t_{OFF} , resulting in an activation of growth centers, specifically at 500 ms ^[161].

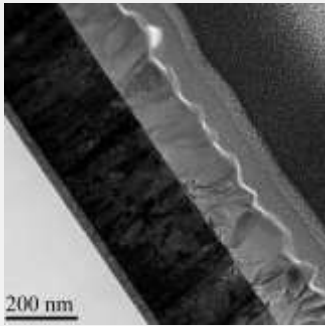
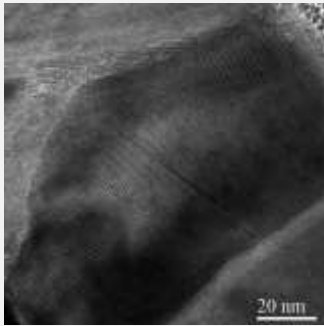
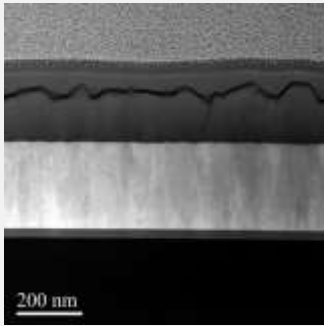
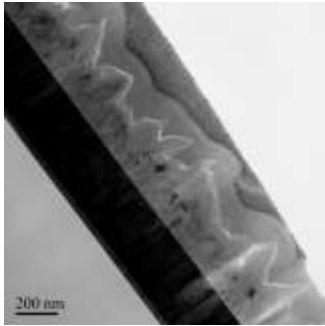
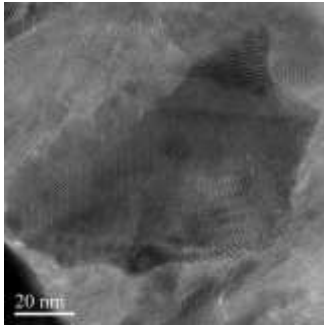
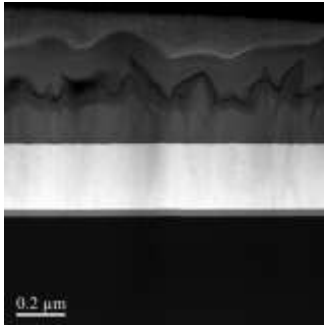
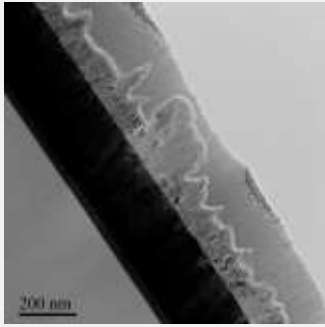
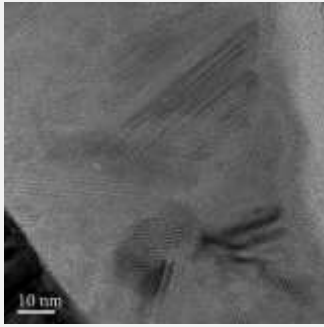
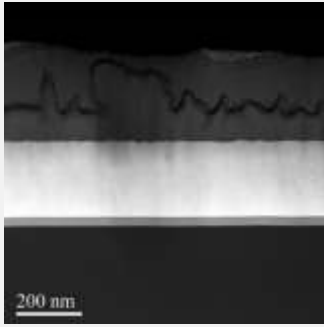
	TEM-BF	HRTEM	STEM-HAADF
50 ms			
100 ms			
500 ms			

Table 4.6: TEM-BF, HRTEM and STEM-HAADF micrographs of samples deposited for t_{ON} of 50, 100 and 500 ms

From the STEM micrographs, it was possible to estimate the thickness of each sample. They are reported in Table 4.7. No monotonous dependence is found with t_{ON} . Faradaic yields are calculated and they are lower than those from continuous mode (of 23.29 % at -0.55 V vs AgCl/Ag). It should be underlined that the sample deposited at a t_{ON} of 100 ms exhibit a slightly improved faradaic yield. The evolution tends to be similar to what we observed using a t_{OFF} of 1 s. Nevertheless, these faradaic yields being still too low, they confirm the contribution of side reactions and our method should be optimized.

Pulse duration (ms)	50	100	500
Pulse number	14400	7925	1655
Total duration (s)	6600	4050	1503
Experimental thickness (nm)	~160	~235	~100
Theoretical charge quantity (C.cm ⁻²)	-1.51	-2.08	-0.74
Experimental charge quantity (C.cm ⁻²)	-4.04	-1.71	-0.87
Theoretical thickness (nm) 1	833	1147	408
Theoretical thickness (nm) 2	2228	943	480
Faradaic yield (%)	7.18	24.92	20.83

Table 4.7: Influence of the pulse duration on the thickness and faradaic yield

The composition of the lamellas was investigated by EDS (Figure 4.14). A Sn/Se ratio, relatively close to 1/1 is found whatever the potential, in agreement with the SnSe phase. The sample prepared with a t_{ON} of 50 ms reveals a slight Sn excess whereas a slight Se excess is distinguished for the sample synthesized at a t_{ON} of 500 ms. It should be reminded that the sample deposited at a t_{ON} of 500 ms and a t_{OFF} of 1 s revealed, on the contrary, a Sn excess. Whatever the t_{ON} , oxygen is found with proportion around 10 at.%. Locally, the concentrations reach more than 25 at.%. In comparison with the films synthesized at a t_{OFF} of 1 s, the oxygen percentage is more important here. The deviation to the stoichiometry is also a more important for the film synthesized with a t_{ON} of 50 ms and a t_{OFF} of 400 ms.

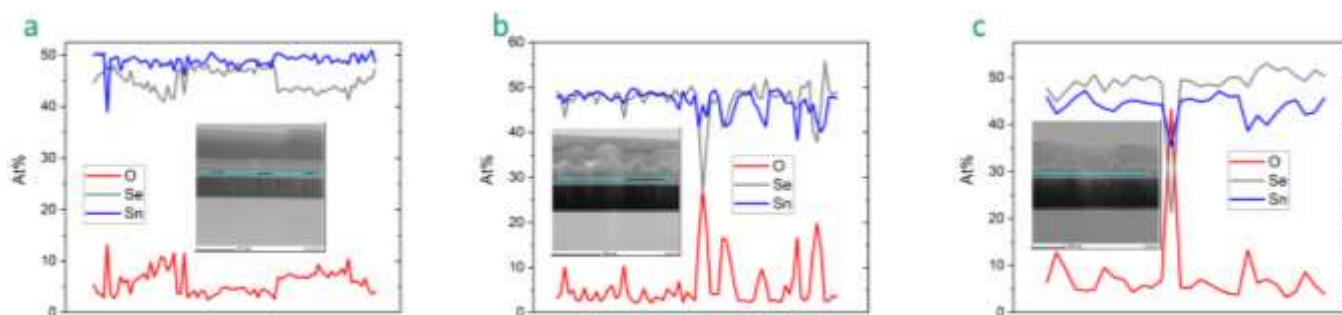


Figure 4.14: EDS analyzes on the samples deposited with a t_{ON} of (a) 50, (b) 100 and (c) 500 ms

An additional analysis was performed on the sample deposited with a t_{ON} of 100 ms to investigate the origin of oxygen (Figure 4.15). As proven by the quantification of the points number 7, 8 and 9, the oxygen content is major on the grain boundaries. However, we cannot conclude whether the oxygen is due to post-oxidation under atmosphere or a secondary phase generated during the electrodeposition.

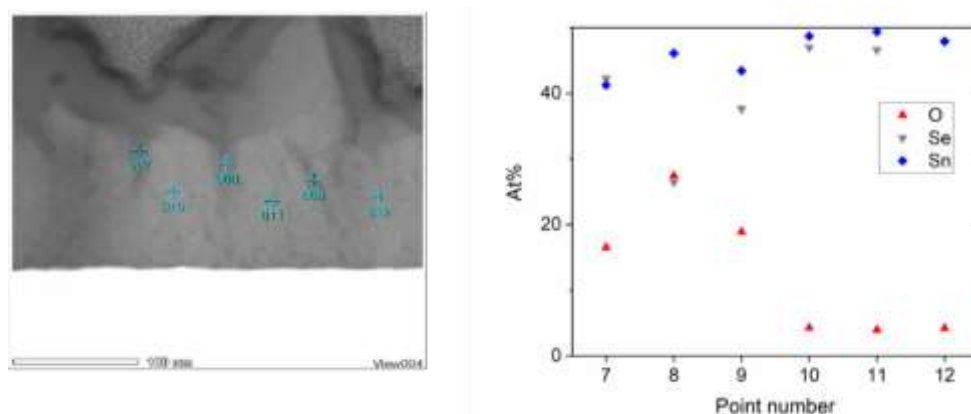


Figure 4.15: EDS analysis on grains boundaries of the sample deposited with a t_{ON} of 100 ms

e. XRD characterizations

The as-deposited samples were characterized by XRD. Typical patterns are represented in Figure 4.16. The presence of SnSe crystallized into the orthorhombic structure is confirmed whatever the value of t_{ON} . A preferential growth orientation perpendicular to the (111) plane is obvious for each t_{ON} . By decreasing the value of t_{ON} from 500 ms to 50 ms, the FWHM of the (111) peak decreases. Thus, the crystallite size increases when t_{ON} decreases, as proven by Table 4.8. This evolution is in agreement with the HRSEM observations (Figure 4.12).

t_{ON} (ms)	Crystallite size (Å)
50	397.72 ± 215.45
100	290.20 ± 75.50
500	241.10 ± 22.39

Table 4.8: Evolution of the crystallite size with the t_{ON}

Moreover, the diffraction peak intensity tends to decrease when t_{ON} increases. This observation suggests a decrease of the thickness by increasing the t_{ON} up to 500 ms, in agreement with the TEM cross section views (Table 4.6). The minor peaks at 33.5° , 36° and 51° are not indexed according to the orthorhombic structure of SnSe. By taking into consideration the EDS chemical analyses (Figure 4.14), the presence of SnO_2 as a secondary phase is not excluded.

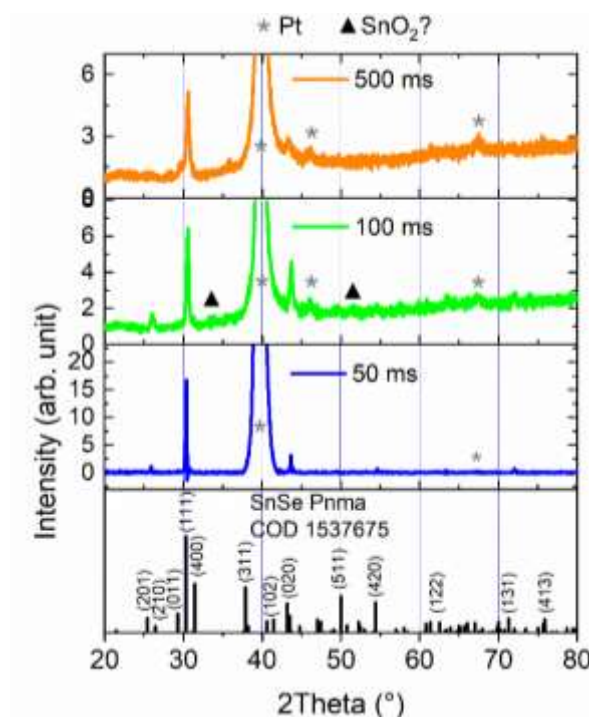


Figure 4.16: XRD analyzes on as-deposited samples

f. XPS characterizations

XPS analyzes were performed on samples elaborated with a t_{ON} from 50 to 500 ms. The spectra of Se 3d are represented in Figure 4.17. The Sn 3d spectra are shown in Figure 4.18. The Se 3d spectra of each sample exhibit one peak at 53.97, 53.76 and 53.41 eV for the samples deposited with t_{ON} respectively of 50, 100 and 500 ms. These binding energies are in agreement with that of Se(-II)

[49]. However, the samples prepared at a t_{ON} of 100 and 500 ms display a slight shoulder, around 56.0 and 55.98 eV respectively. The presence of Se(0) is possible but needs to be more investigated [136,224]. Finally, the last sample seems to show another shoulder at 50.33 eV which is not explained.

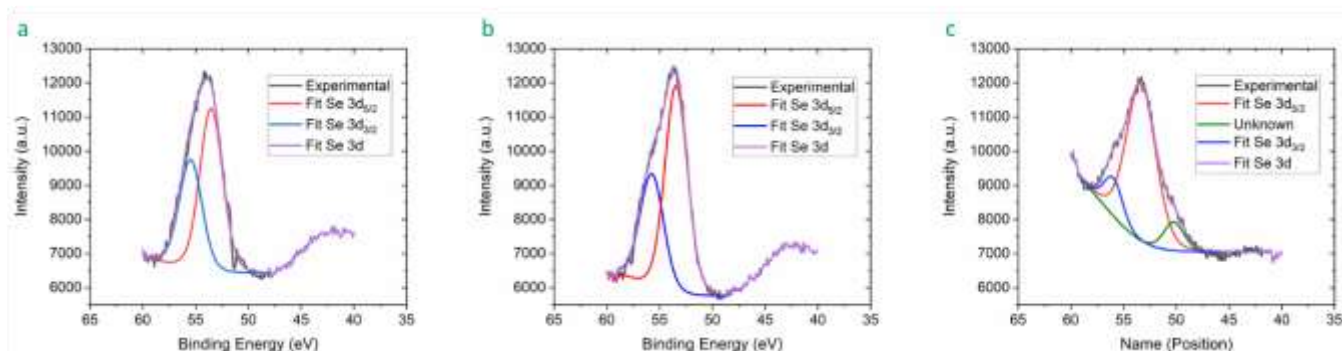


Figure 4.17: Se 3d XPS spectra of samples deposited with t_{ON} of (a) 50 ms, (b) 100 ms and (c) 500 ms

The three Sn 3d spectra reveal the presence of two peaks. For each sample, the Sn $3d_{3/2}$ and $3d_{5/2}$ peak can be deconvoluted in two peaks. The values are reported in Table 4.9.

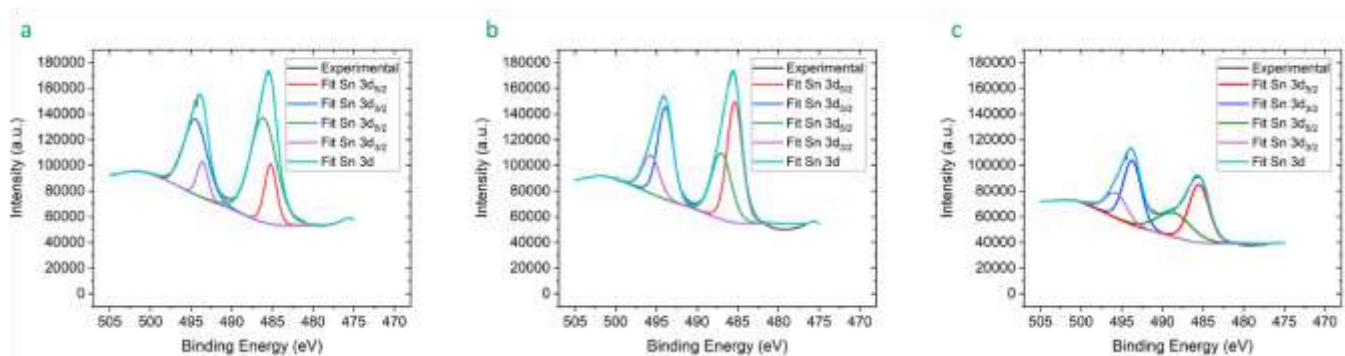


Figure 4.18: Sn 3d XPS spectra of samples deposited with t_{ON} of (a) 50 ms, (b) 100 ms and (c) 500 ms

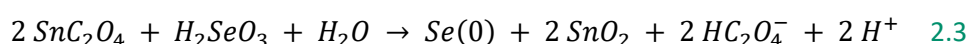
A slight evolution is observed with the t_{ON} . For Sn(II) in SnSe, the Sn $3d_{3/2}$ peak is expected around 494 eV [49,52,65,157]. Thus, our values are in agreement with the presence of Sn(II). Moreover, the values close to 495 eV can indicate the presence of Sn(IV) from SnSe₂ [65,225]. It should be underlined that the presence of SnO₂ cannot be excluded since the $3d_{3/2}$ and $3d_{5/2}$ peaks are respectively expected around 494.7 and 486.3 eV [226]. The $3d_{5/2}$ peaks generally appear at higher binding energies than those reported by the literature for SnSe [49,52,65,157]. From the literature data, these values can be in agreement with SnSe₂, as well as SnO₂ [65,225,226].

t_{ON} (ms)	Sn 3d _{3/2}		Sn 3d _{5/2}	
50	494.46	493.58	486.12	485.22
100	494.70	493.70	487.12	485.39
500	495.68	493.71	488.54	485.51

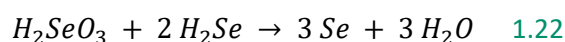
Table 4.9: Evolution of the Sn 3d_{3/2} and 3d_{5/2} binding energies with the t_{ON}

g. Raman characterizations

Raman spectra of samples deposited with t_{ON} of 50 and 500 ms were recorded (Figure 4.19). The bands located at 72, 133 and 144 cm⁻¹ suggest SnSe A_g vibration modes [196]. This interpretation is reinforced with the XRD analysis and the EDS results. Additionally the bands at 50, 61 and 245 cm⁻¹ could be attributed to B_{2g}, A_{1g} and E_g vibration modes of SeO₂ [197]. However, the bands at 50, 133, 144 and 245 cm⁻¹ can also be attributed to Se [199]. Nevertheless, a clear band near 250 cm⁻¹ related to Se would be expected and is not present. Thus we suggest more SeO₂ than Se. The presence of SeO₂ remains quite surprising. We can suggest a surface oxidation of Se(0) into SeO₂. Another hypothesis is that Se(0) could be generated from a spontaneous reaction between Se(IV) and Sn(II), however, this chemical reaction leads to immediate precipitation (reaction 2.3) and does not explain the generation of Se(0) and SeO₂ inside the films.



We suggest the formation of SeO₂ as follow. Since the electrodeposition occurs at a more negative potential than the hydrogen evolution and in diluted acidic medium, the formation of H₂Se is expected. For a sufficiently high H₂SeO₃ concentration, a disproportionation reaction generates amorphous selenium (reaction 1.22):



Then, SeO₂ is generated by oxidation of Se(0) in presence of dioxygen.

According to Anderson *et al.* the band at 119 and 245 cm⁻¹ can also be assigned to the presence of SeO₂. This, would be in agreement with the presence of oxygen as indicated by TEM analyzes. Whatever the t_{ON} , the spectra clearly exhibit also two bands at 119 cm⁻¹ and between 180 and 186 cm⁻¹. As previously observed and due to the bath electrochemical behavior, these bands could be

attributed to E_g and A_{1g} vibration modes of SnSe_2 [63]. We explain the presence of this phase from the partial oxidation in the bath of Sn(II) into Sn(IV) and the presence of Sn(IV) induces the following cathodic reduction (reaction 3.20):

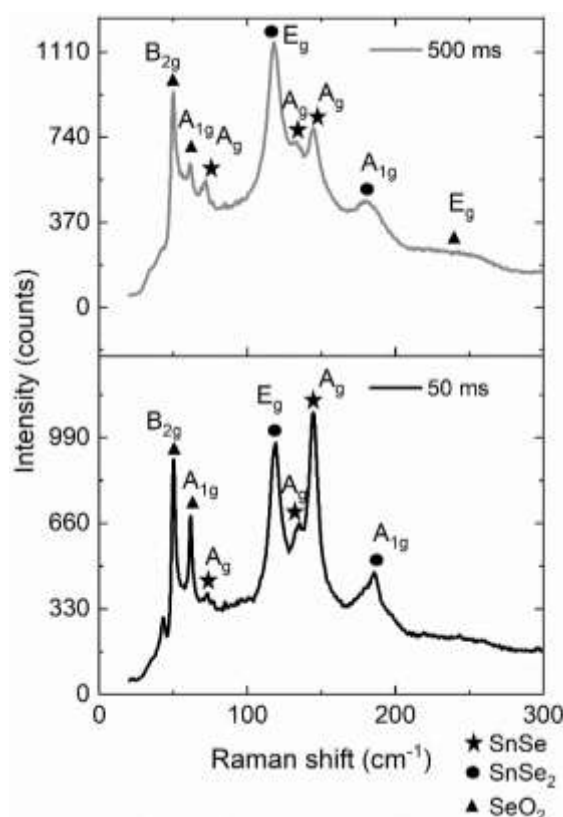
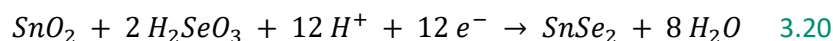


Figure 4.19: Raman spectra of as-deposited samples

h. Ellipsometric characterizations

Ellipsometry was used on samples in order to determine their optical bandgaps. Comparative analysis was realized on samples synthesized in continuous mode ($E = -0.55\text{V}$ vs AgCl/Ag), so called C-SnSe, and in pulse mode $t_{ON} = 100\text{ ms}$, $t_{OFF} = 400\text{ ms}$, $E = -0.55\text{V}$ vs AgCl/Ag , so called P-SnSe. Since the surface state of the P-SnSe samples apparently did not diffuse the polarized light after reflection with depolarization effects, measurements were done on as-deposited films. In contrast, the roughness of the C-SnSe sample was too important for reliable ellipsometric characterizations. Therefore the measurements were done on transferred samples. Due to the differences in terms of thickness between the samples, specific model was used. C-SnSe sample was considered as semi-infinite bulk and the dielectric function was calculated by a constrained spline approach (collaboration

Dr. M. Gilliot, LISM, Univ. Reims) ^[227]. C-Sample was modeled as thin film on platinum substrate, where the thickness was fitted to 51 nm, as well as the parameters of a dispersion relation approach (Tauc-Lorentz) were fitted. In both cases, the surface roughness was taken into account with final fitted values of 18 nm and 33 nm for C-SnSe sample and P-SnSe sample respectively.

The real and imaginary part of dielectric functions of the films are systematically compared with those of the literature, corresponding to single crystals ^[228] (Figure 4.20). Qualitatively the shapes of the spectra of the real part ϵ_1 and the imaginary part ϵ_2 for the P-SnSe sample are closer to literature data than the C-SnSe sample. In particular the amplitudes are lowered for the films synthesized in continuous mode. This observation can be linked to the differences of microstructure between the samples. Here C-SnSe sample shows deteriorated optical properties in comparison with P-SnSe sample.

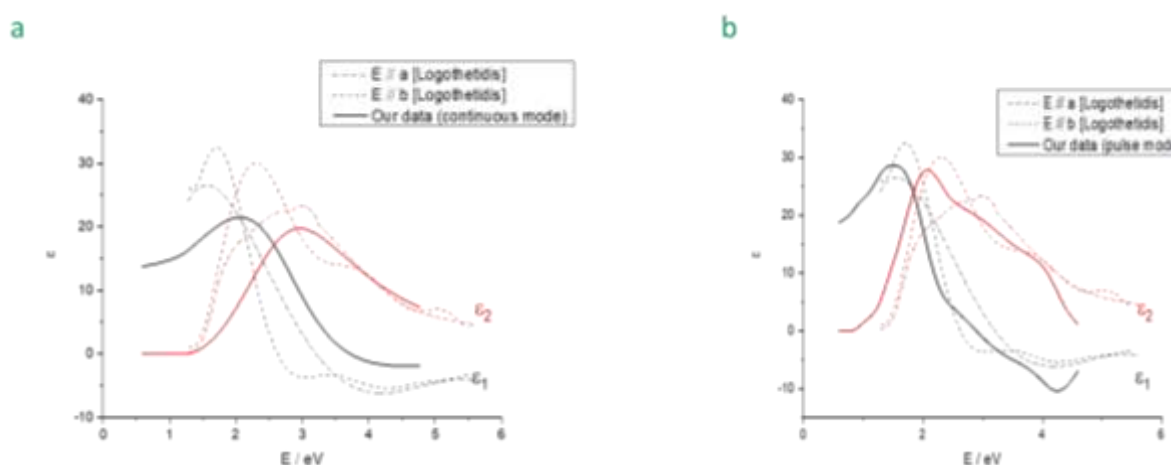


Figure 4.20: Comparison between the real part ϵ_1 and the imaginary part ϵ_2 of the dielectric function single crystals of orthorhombic SnSe for two different orientation and (a) SnSe films in continuous mode and (b) SnSe films in pulse mode

Optical band gaps can be extracted from the optical constant by using the graphical Tauc plot approach. Direct band gaps and indirect band gaps were graphically obtained and the related plots are shown in the Figure 4.21. The data are in the same range than in the literature data according to the UV-visible spectroscopy determinations ^[22–27]. Moreover, as expected from the literature data, the direct band gaps are higher than the indirect ones. For both hypotheses, the bandgap of samples obtained in continuous mode are lower than those synthesized in pulse mode. This observation has to be linked with the lower crystallite sizes of C-SnSe samples than for P-SnSe (from TEM images). Thus this trend appears to be opposed to the results of Shikha *et al.* and Ananthi *et al.* ^[30,31].

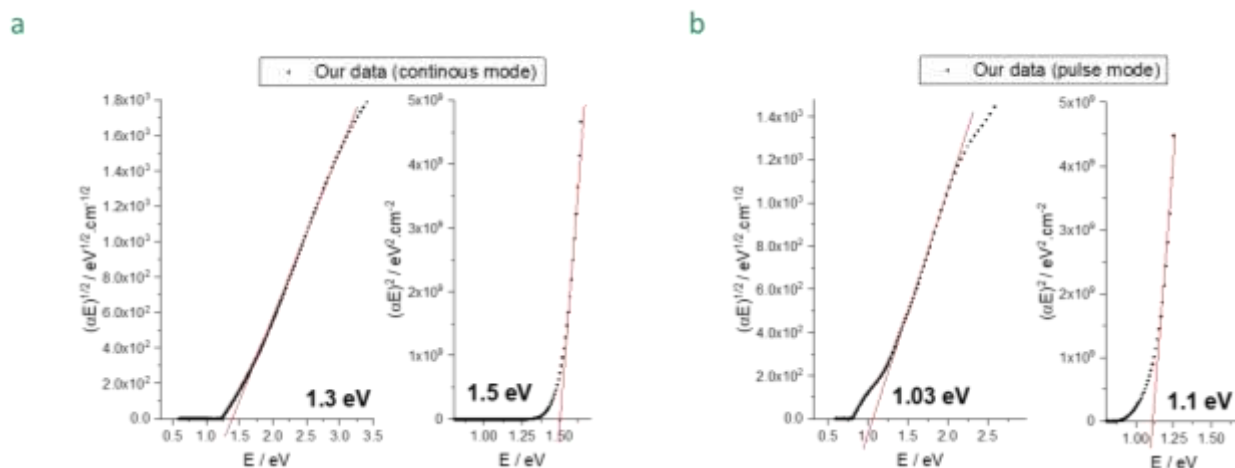


Figure 4.21: Tauc plot determination of the optical band gap for indirect and direct transitions of (a) SnSe films in continuous mode and (b) SnSe films in pulse mode

The samples deposited with a t_{OFF} of 400 ms exhibit:

- ✓ Rougher and more compact morphology with bigger grains than for t_{OFF} of 1 s
- ✓ Orthorhombic SnSe in presence of the minor phase SnSe_2 (proved by Raman) and probably SeO_2 (proved by Raman and oxygen content suggested by EDS)
- ✓ A dependence of the morphology with t_{ON} (from platelet-like to needle-like grains). This trend can be associated to the evolution of the current density.
- ✓ A thickness that tends to decrease when t_{ON} increases. This evolution is related to the decrease of the absolute current density when t_{ON} increases.
- ✓ Unfortunately faradaic yields in pulse mode are lower than that obtained using continuous mode (23.29 %).
- ✓ Faradaic yields were compared between a t_{OFF} of 400 ms and 1000 ms: except for $t_{ON} = 50$ ms, better values are obtained
- ✓ An evolution from slight Sn excess to slight Se excess as the t_{ON} increases
- ✓ Crystallite size decreasing when t_{ON} increases
- ✓ The presence of Sn(II) and Se(-II) according to XPS analyzes
- ✓ That Se(0), as well as Sn(IV) either from SnSe_2 or SnO_2 cannot be excluded according to XPS
- ✓ Ellipsometric measurements have enabled to determine the optical band gaps : 1.03 eV for an indirect transition and 1.1 eV for a direct transition. These values are lower than those of the samples obtained in continuous mode at -0.55 V vs AgCl/Ag : indirect band gap of 1.3 eV and direct band gap of 1.5 eV.

IV. Towards doping of SnSe films

a. Choice of the dopant

In the aim of improving the electrical properties of SnSe, an interesting approach consists in elaborating doped SnSe. The studied elements were Ag, Bi, Cd, Co, Cu, In, Ni, Pb, S, Sb, Te, Y and Zn. They were chosen according to the literature (Table 4.10).

Element	Ag	Bi	Cd	In	Pb	S	Sb	Y	Zn	Te	Cu	Co	Ni
p- or n-type	p	n	p?	p	p	p?	n/p	n	p	p	p	x	x
Compound	SnSe									SnTe	SnS	Co-Sn	Ni-Sn
Reference	[229]	[229]	[143]	[150]	[141]	[149]	[230]	[29]	[141]	[231]	[232]	[233]	[234]

Table 4.10: List of the possible dopants according to the literature

To choose the best dopants among these 13 elements, a first criterion to fulfill is the chemical compatibility of the additional compound with the electrolyte solution. Thus the electrochemical stability of the complete electrolyte solution was predicted, using the Spana software. For that, our electrolyte solution conditions were considered in terms of pH and concentration (Chapter 3, Figure 3.9). Consequently we predicted, from the related diagrams, that the cationic precursors Cd(II), In(III), Pb(II), Co(II) and Ni(II) should not generate reactions with Sn(II) and could be in the good range of the SnSe deposition potential window (Appendix 5, Appendix 6, Appendix 7, Figure 4.22 and Figure 4.24). In other words, Ag(I), Bi(III), S(VI), Sb(III), Te(IV) and Cu(II) were eliminated due to their oxidizing behavior towards Sn(II) (Appendix 3, Appendix 4, Appendix 8, Appendix 9, Appendix 12 and Figure 4.26). Y(III) and Zn(II) have a too negative reduction potential in comparison with the SnSe potential window (Appendix 10 and Appendix 11). Concerning Cu(II), we found that it should generate a reaction with Sn(II). However, Liu *et al.* successfully performed the electrodeposition of Cu-doped SnS films^[232]. Since SnS has a similar electrochemical behavior to SnSe, we have added Cu(II) to the list of the potential dopants. In an objective to a reduction potential close to that of SnSe formation, we decided to focus on Cu(II), Ni(II) and Co(II).

b. Chemical compatibility of Co(II)

From the Pourbaix diagram, Co may generate complexes with oxalate (Figure 4.22). It should be noticed that, to the best of our knowledge, no pK_s value was reported for the cobalt oxalate

complexes. At pH=2.5, the majority Co(II) species should be $\text{Co}(\text{C}_2\text{O}_4)_2^{2-}$. The redox potential of the $\text{Co}(\text{C}_2\text{O}_4)_2^{2-}/\text{Co}$ couple at pH=2.5 is -0.46 V vs SHE. This value is lower than that of the $\text{H}_2\text{SeO}_3/\text{Se}$ couple (0.49 V vs SHE) (Figure 2.3) and $\text{SnO}_2/\text{Sn(II)}$ couple (-0.23 V vs SHE) (Figure 2.1). Thus, the SnSe electrolyte containing Co(II) should be stable.

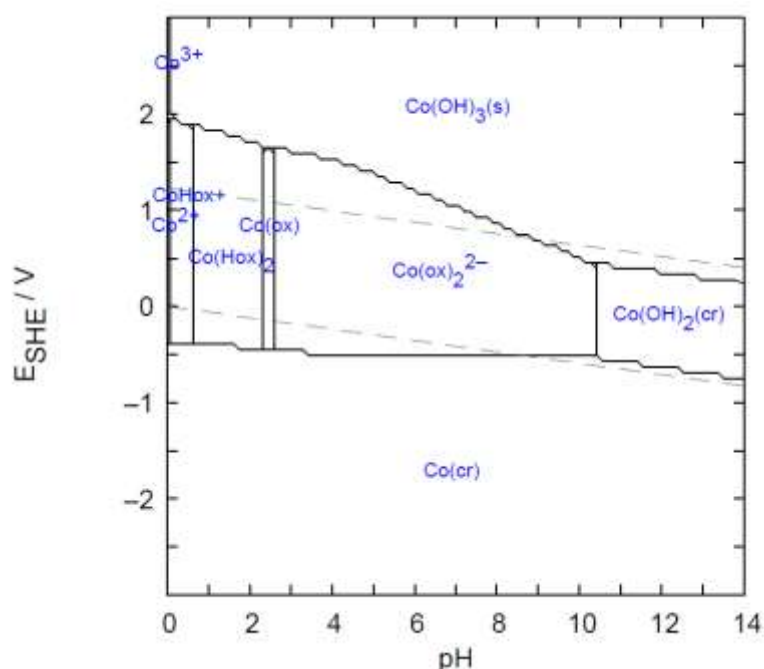
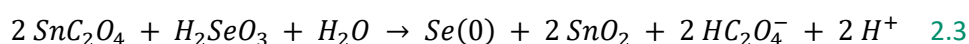


Figure 4.22: Calculated Pourbaix diagram of Co taking $[\text{Co(II)}]=2 \text{ mM}$, $[\text{C}_2\text{O}_4^{2-}]=0.2 \text{ M}$ and $[\text{Cl}^-]=0.2 \text{ M}$

After CV experiments of Co(II) in presence of 0.2 M oxalate salt, a red precipitate is observed in the bath. The XRD analysis revealed that this precipitate is CoC_2O_4 , as expected from the Pourbaix diagram (Figure 4.23 a). This observation highlights the bath instability. It should be mentioned that no defined cathodic and anodic stripping peaks were observed on the CV (Appendix 13). We suggest that Co(II) is no longer electroactive in presence of oxalate. Moreover, after a one day storage at RT, the SnSe electrolyte solution containing 20 mM of $\text{CoCl}_2 \cdot 6\text{H}_2\text{O}$ generated another precipitate NaHC_2O_4 . According to the XRD analysis, the one day storage at RT leads to precipitation of oxalate salt (Figure 4.23 b) maybe from dissociation of SnC_2O_4 as mentioned in reaction 2.3.



Taking into account the non-electroactivity and instability of Co(II) in the oxalate-based electrolyte solution of SnSe, it was no more considered as dopant.

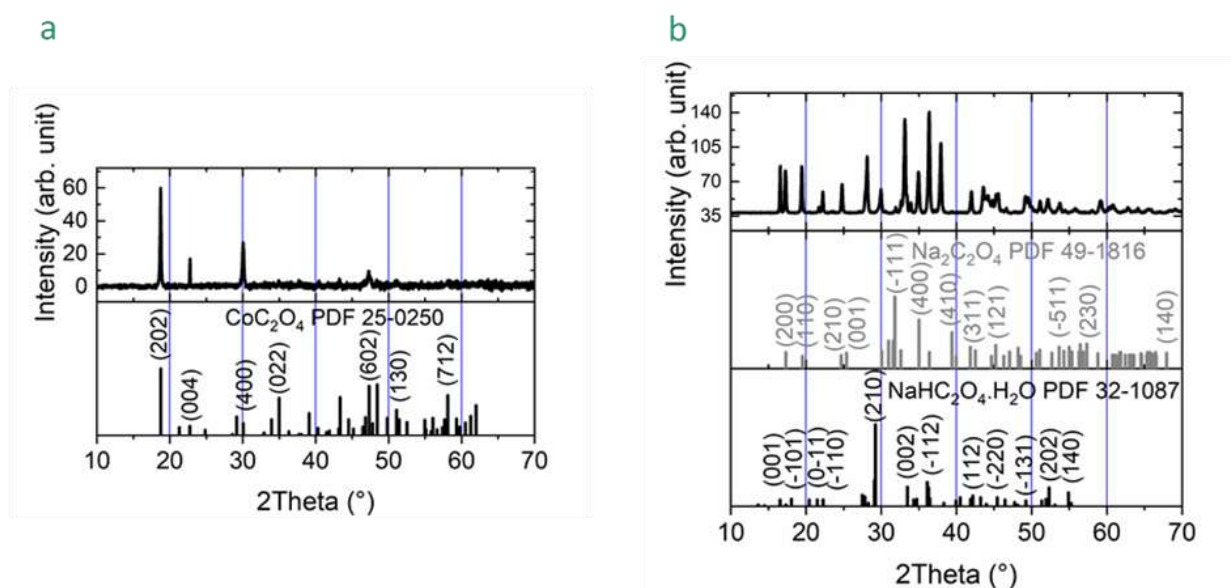


Figure 4.23: XRD analysis of a precipitate: (a) from 0.2 M oxalate and 20 mM $\text{CoCl}_2 \cdot 6\text{H}_2\text{O}$ and (b) from SnSe electrolyte solution with 20 mM $\text{CoCl}_2 \cdot 6\text{H}_2\text{O}$ after one day storage at RT

c. Chemical compatibility of Ni(II)

According to the calculated Pourbaix diagram and considering the electrolyte solution conditions, Ni(II) should also generate complexes with oxalate (Figure 4.24). At pH=2.5, the majority Ni(II) species should be $\text{Ni}(\text{C}_2\text{O}_4)_2^{2-}$. A K_s value of 1.42×10^{-7} was reported for NiC_2O_4 [235]. The redox potential of the $\text{Ni}(\text{C}_2\text{O}_4)_2^{2-}/\text{Ni}$ couple at pH=2.5 is estimated at -0.41 V vs SHE. This value is lower than those obtained for the $\text{H}_2\text{SeO}_3/\text{Se}$ couple (0.49 V vs SHE) (Figure 2.3) and $\text{SnO}_2/\text{Sn(II)}$ couple (-0.23 V vs SHE) (Figure 2.1). Thus, we expect a good chemical stability of the bath in presence of Ni(II).

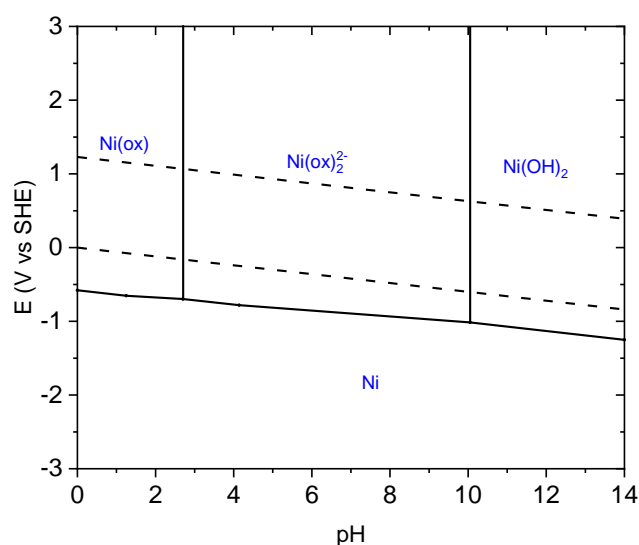


Figure 4.24: Calculated Pourbaix diagram of Ni taking $[\text{Ni(II)}]=2 \text{ mM}$, $[\text{C}_2\text{O}_4^{2-}]=0.2 \text{ M}$ and $[\text{Cl}^-]=0.2 \text{ M}$

The electrochemical behavior of Ni(II) in presence of oxalate salt was studied. However, no defined cathodic and anodic stripping peaks were obtained (Appendix 14). We suggest that Ni(II) is not electroactive in presence of oxalate. During the CV experiments, a precipitation occurred. The XRD analysis showed the precipitation of Ni(II) with oxalate (Figure 4.25 a), revealing the bath instability. Moreover, after a one day storage at RT, a selenium precipitate can be found, as proven by the XRD analysis (Figure 4.25 b). This precipitate may come from the spontaneous reaction between Sn(II) and Se(IV). Nevertheless, due to the possible non electroactivity and instability of Ni(II) in presence of oxalate salt, this element was also eliminated for the rest of the study.

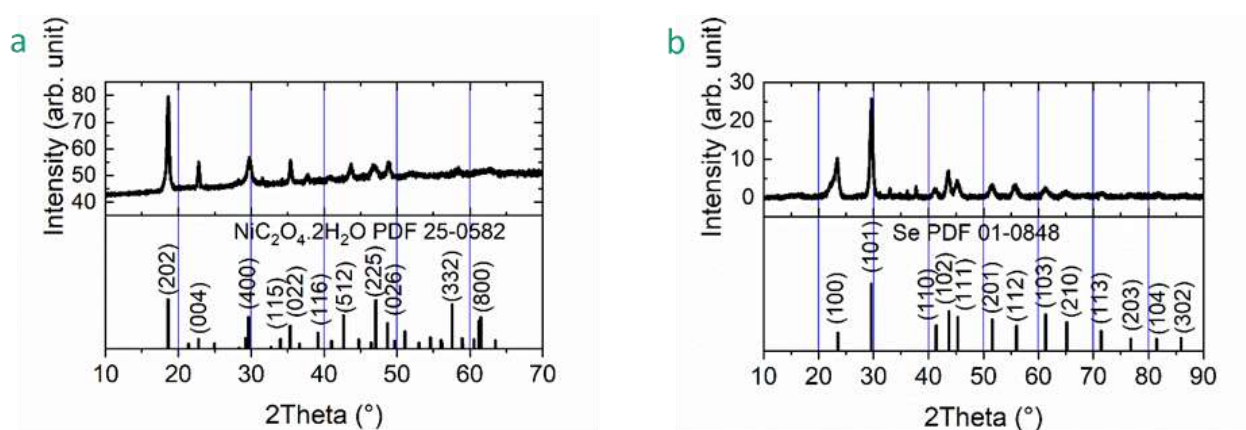


Figure 4.25: XRD analysis of a precipitate: (a) from 0.2 M oxalate and 20 mM NiCl₂·6H₂O and (b) from SnSe electrolyte solution with 20 mM NiCl₂·6H₂O after one day storage at RT

d. Chemical compatibility of Cu(II)

According to the Pourbaix diagram, Cu(II) should be complexed to oxalate and the majority species at pH=2.5 should be Cu(C₂O₄)₂²⁻ (Figure 4.26). K_s values of 3×10^{-8} and 4.43×10^{-10} were reported for CuC₂O₄. Unfortunately, we estimated a value of 0.09 V vs SHE of the Cu(C₂O₄)₂²⁻/Cu redox potential. Since this value is higher than that of SnO₂/Sn(II) (-0.23 V vs SHE), it suggests a reactivity between Cu(II) and Sn(II).

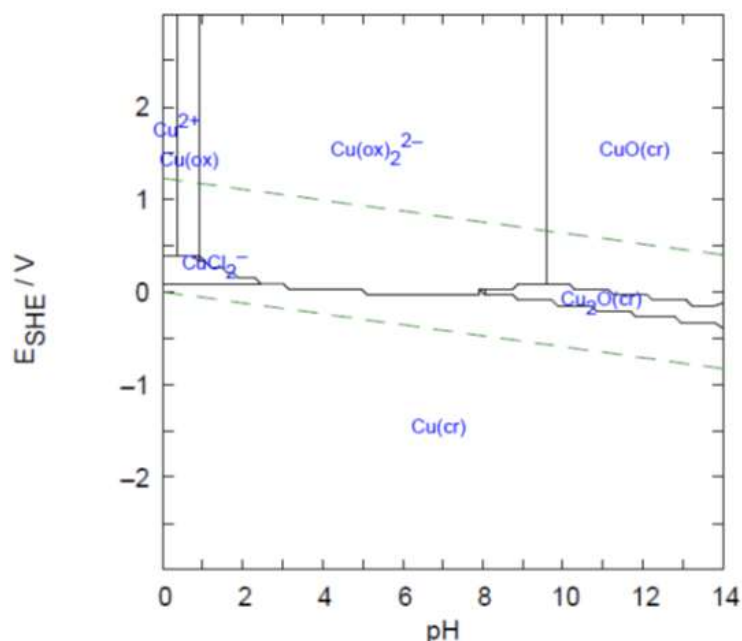


Figure 4.26: Calculated Pourbaix diagram of Cu taking $[Cu(II)]=2$ mM, $[C_2O_4^{2-}]=0.2$ M and $[Cl^-]=0.2$ M

In the electrolyte solution with 0.2 M oxalate and 20 mM $CuCl_2 \cdot 2H_2O$, a blue precipitate was generated (Figure 4.27 a). The XRD analysis showed that Cu(II) is easily complexed with oxalate. Two phases were detected which are CuC_2O_4 and $Na_2CuC_4O_8$. After a one day storage at RT, a solid product is also obtained. We determined by XRD that this product was mostly composed of oxalate salt (Figure 4.27 b). However, we have to keep in mind the trend of oxalate salt to precipitate at RT. Thus we cannot associate the precipitation of oxalate to an increase of the instability in presence of Cu(II).

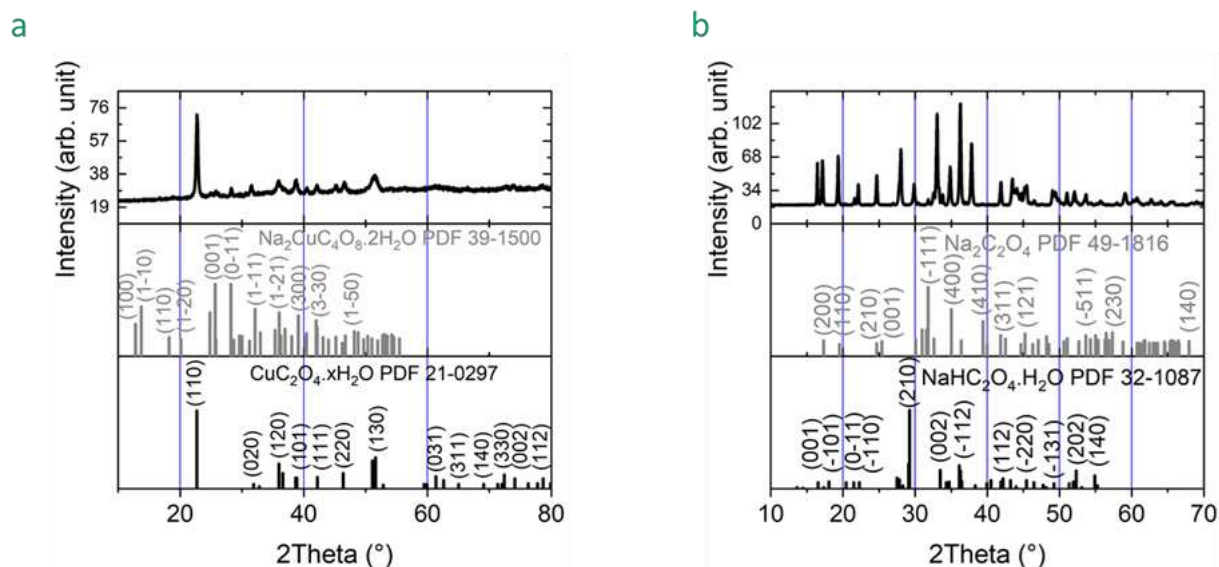


Figure 4.27: XRD analysis of a precipitate: (a) from 0.2 M oxalate and 20 mM $CuCl_2 \cdot 2H_2O$ and (b) from SnSe electrolyte solution with 20 mM $CuCl_2 \cdot 2H_2O$ after one day storage at RT

Chapter 4. Pulse electrodeposition of SnSe films

The stability of the electrolyte solution was evaluated by increasing the Cu(II) concentration until 0.57 mM (Figure 4.28). Without Cu(II), the electrolyte has an orange color due to the precipitation of Se (reaction 1.26 and Figure 2.8). When the Cu(II) concentration is increased up to 0.18 mM, the solution remains transparent. When the concentration is increased up to 0.57 mM, a precipitate progressively appears. That is the reason why it is suitable to perform the electrodeposition with a maximum Cu(II) concentration of 0.18 mM.

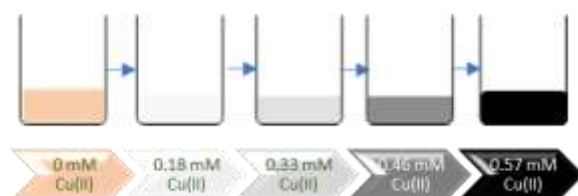


Figure 4.28: Evolution of the complete electrolyte with increasing Cu(II) concentration

After the preparation of the electrolyte solution containing Cu(II), the precipitates generated at concentrations of 0.46 mM of Cu(II) were filtered and analyzed by XRD (Figure 4.29). Several peaks unambiguously indicate the presence of crystallized KCl. The others seem to be more in adequation with Cu_2Se . The presence of this phase suggests the reduction of Se into Se(-II) as well as the reduction of Cu(II) into Cu(I). Another possible phase is $\text{Cu}_2\text{Se}_4\text{Sn}$. However, this phase cannot explain the peaks around 31° and 56° and would also involve the reduction into Se(-II).

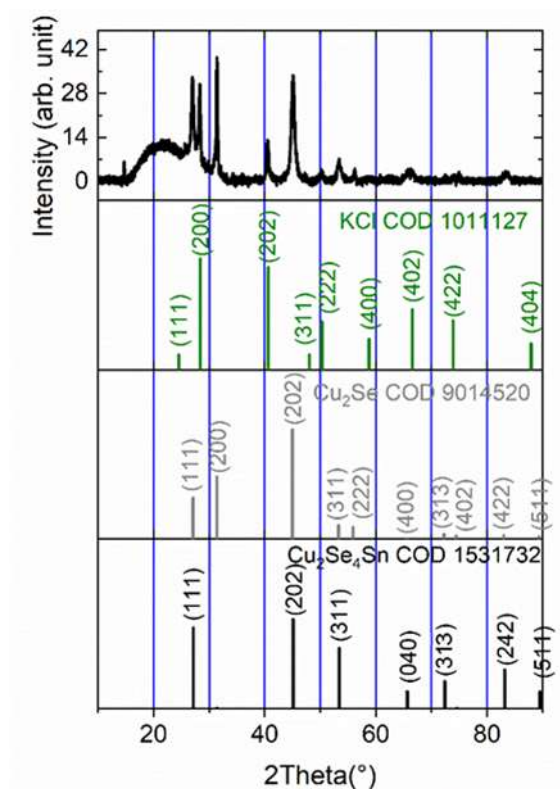
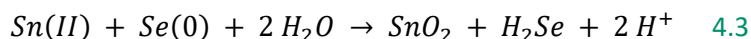
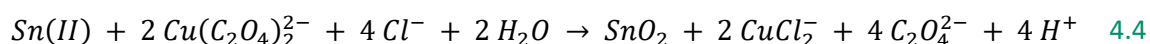


Figure 4.29: XRD analysis of precipitates from SnSe electrolyte solution with 0.46 mM $\text{CuCl}_2 \cdot 2\text{H}_2\text{O}$

We know that Se(IV) is reduced into Se(0) in presence of Sn(II) (reaction 1.26). According to the Pourbaix diagrams (Figure 2.1 and Figure 2.3), the standard potential of the SnO₂/Sn(II) system is a bit lower than that of Se(0)/H₂Se (-0.23 V vs SHE against -0.19 V vs SHE). Hence we suggest a reaction between Se(0) and Sn(II) following equation 4.3:



According to the Pourbaix diagram of copper, we cannot exclude the existence of CuCl₂⁻ at pH=2.5 (Figure 4.26). The redox potential of the Cu(C₂O₄)₂²⁻/CuCl₂⁻ is of 0.09 V vs SHE. Thus, a reaction may occur between Cu(C₂O₄)₂²⁻ and Sn(II) leading to the formation of SnO₂:



It is obvious that the SnSe electrolyte solution stability in presence of Cu(II) is lowered. Copper oxalate products as well as copper selenide salts were determined. However, the precipitations can be limited for a Cu(II) concentration lower than 0.18 Mm

e. Electrochemical study of the system Cu(II)-Sn(II)- Se(IV)/SnSeCu

The electrochemical behavior of Cu(II) was investigated at pH=2.5 from an electrolyte solution containing only 0.2 M KCl and 2 mM CuCl₂·2H₂O (Figure 4.30 a). Without oxalate, a large cathodic peak around 0.12 V vs AgCl/Ag is observed and related to the reduction of Cu(II) into Cu(I). Another peak, which is slightly shifted from -0.23 to -0.27 V vs AgCl/Ag as the scan rate increases is attributed to the reduction of Cu(I) into Cu(0). Two anodic stripping peaks are also observed. The first is slightly shifted from -0.06 to -0.07 V vs AgCl as the scan rate increases. The second anodic stripping peak is observed around 0.25 V AgCl/Ag. They are respectively attributed to the oxidation of Cu(0) into Cu(I) and of Cu(I) into Cu(II). This two step mechanism was also reported in aqueous chloride medium and is typical of the polarization effect induced by chloride ions [236–238]. We notice that the current density increases with the scan rate for each peak, which is typical of diffusion mechanisms. When oxalate is added to the electrolyte solution, one clear cathodic peak is observed between -0.62 and -0.65 V vs AgCl/Ag (Figure 4.30 b). This peak may be assigned to the direct reduction of Cu(II) into Cu(0). The fact that the cathodic peak is shifted to more negative potential suggests a complexation between Cu(II) and oxalate. Two anodic stripping peaks are still observed, one at -0.12 V and another one around 0.14 V vs AgCl/Ag. They are respectively attributed to the oxidation of Cu(0) into Cu(I) and of Cu(I) into Cu(II).

It should be underlined that the absolute current density of each cathodic peak also increases with the scan rate, which is typical of a diffusion mechanism.

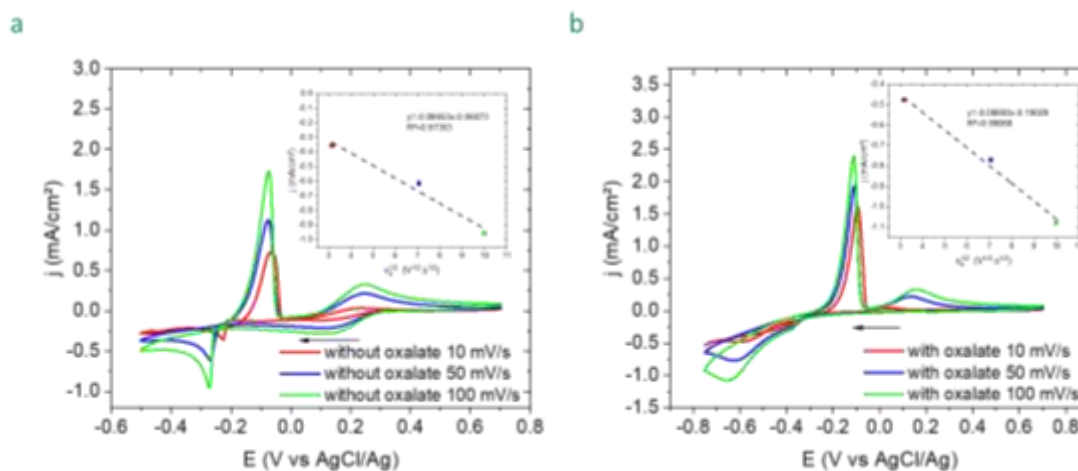
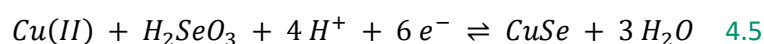
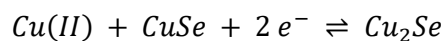


Figure 4.30: CV experiments on GC electrode, at 50 °C, on (a) the electrolyte solution containing KCl 0.2 M and CuCl₂·2H₂O 2 mM and (b) containing Na₂C₂O₄ 0.2 M and CuCl₂·2H₂O 2 mM

The behavior of the SnSe electrolyte solution (Chapter 3, Figure 3.9) containing Cu(II) was investigated (Figure 4.31 a). Without Cu(II), a cathodic peak, C1'' is observed at -0.71 V vs AgCl/Ag and attributed to the reduction of Sn(II) into Sn(0). In comparison with Figure 4.30 b, the reduction of Cu(II) into Cu(0) is expected in the same range but starts at more positive potentials. We suggest that, when adding Cu(II), the presence of the unique cathodic peak is due to the co-reduction of Cu(II) into Cu(0) and of Sn(II) into Sn(0). Without Cu(II), two anodic stripping peaks A1'' and A2'' are clearly observed at -0.56 V and around 0.06 V vs AgCl/Ag. The first is attributed to the oxidation of Sn(0) into Sn(II). The second may be related to the generation of SnO₂. When adding Cu(II) up to 0.18 mM, another stripping peak follows A2'', represented by *. We suggest this peak is due to the oxidation of Cu(I) into Cu(II), in comparison with Figure 4.31 b. The evolution of the CV with the Cu(II) concentration is a bit surprising. Indeed, the oxidation peak of Cu(0) into Cu(I) is not observed or hindered by the noisy signal before A2''. Only one additional cathodic peak, around -0.7V, is observed with an intensity, which randomly varies with the Cu(II) concentration. A1'' and A2'' current densities increase with the Cu(II) concentration (Figure 4.31 b and c). A1'' is completely shifted to -0.53 V vs AgCl/Ag when Cu(II) is added and A2'' is progressively shifted to 0.10 V vs AgCl/Ag as the Cu(II) concentration increases. If these peaks, at similar positions than in Sn and SnSe CV, would be attributed to Sn system, this behavior would not be expected. Thus, it seems these peaks are related to Cu system or to Cu-Se species as observed by Baral *et al.* and Thouin *et al.*, following equations 4.5 and 4.6 [190,239]:





4.6

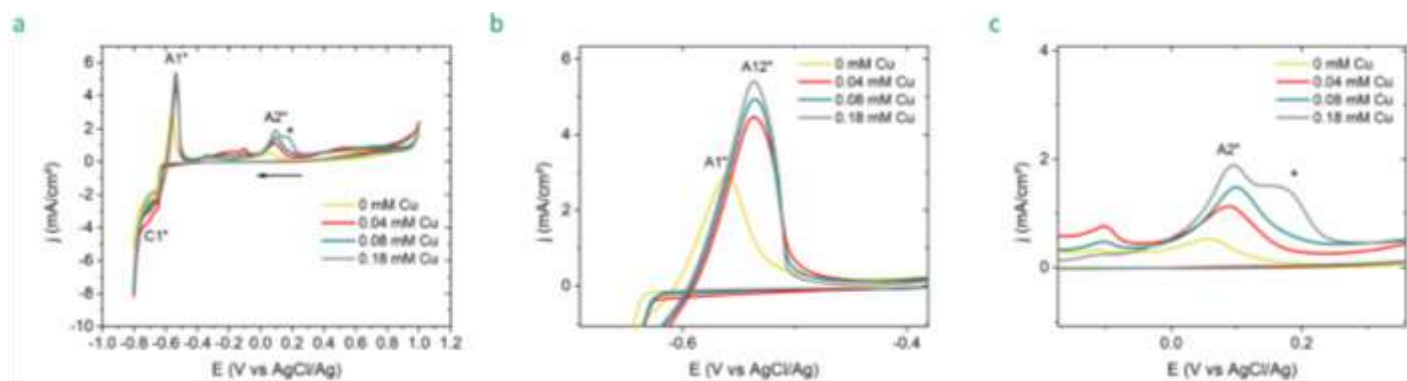


Figure 4.31: CV experiments on GC electrode, at 50 °C, on the complete SnSe electrolyte solution with $\text{CuCl}_2 \cdot 2\text{H}_2\text{O}$, (a) whole CV, (b) zoom on A1" and (c) zoom on A2"

- ✓ Ni, Co and Cu were envisaged as dopant for SnSe
- ✓ Ni and Co were excluded due to non-electroactivity and instability with oxalate
- ✓ Cu(II) complexes are observed in presence of oxalate
- ✓ Low Cu(II) concentration is needed to limit the formation of Cu_2Se

According to the preliminary electrochemical study, Cu(II) is electroactive in presence of oxalate salt. Moreover, in presence of oxalate, the reduction of Cu(II) into Cu(0) occurs at a lower overpotential which means Cu(II) can be complexed by oxalate. In addition, we found that the reduction potential is compatible with the deposition potential window of SnSe. We thus suggest the feasibility to elaborate $\text{Cu}_x\text{Sn}_{1-x}\text{Se}$ films. However, the preliminary study also revealed an instability of the bath in presence of Cu(II). To limit the precipitations, the Cu(II) salt may be introduced at a maximum concentration of 0.18 mM.

f. Pulse electrodeposition of $\text{Cu}_x\text{Sn}_{1-x}\text{Se}$

Similarly to the undoped SnSe films, pulse deposition of Cu-doped films was performed at -0.55 V vs AgCl/Ag with the optimized value of t_{OFF} of 400 ms. According to the characterizations of the undoped SnSe films (specifically TEM and XRD analyses), the most promising deposits are those

synthesized with a t_{ON} equal to 50 ms. That is the reason why we decided to keep this t_{ON} for the synthesis of Cu-doped films. The number of pulses was adjusted according to the targeted charge quantity of -2.4 C.cm^{-2} (equation 2.5). In the previous part, we revealed an instability of the bath in presence of Cu(II). We also explained that a decrease of the Cu(II) concentration is beneficial for the stability of the electrolyte solution. Thus, the experiments were performed with Cu(II) concentrations varying from 1 to 8 μM . For that, the electrolyte was prepared according a 2 step procedure. Firstly the SnSe electrolyte solution without copper salt was prepared as mentioned in Chapter 2 I. b. Then a 2 mM Cu(II) solution, as a stock solution, was preliminary prepared by dissolution of $\text{CuCl}_2 \cdot 2\text{H}_2\text{O}$ into water. Then the needed volume of this stock solution is added into the SnSe electrolyte solution before the electrodeposition to avoid any precipitation.

The chronoamperometric curves were systematically recorded for each sample. To study the influence of the Cu(II) concentration, only the last pulse for each concentration was represented in Figure 4.32 and compared with others. The origin was fixed at 0 s and 0 $\mu\text{A/cm}^2$. Since the Cu(II) concentrations are much lower in comparison with Sn(II) and Se(IV) concentrations, by a factor 250 and 62.5 respectively, the presence of Cu(II) should not greatly influence the current density. Thus, it is not surprising to find no clear dependence of the Cu(II) concentrations. A good reproducibility is observed, except the last experiment, namely LR20102801.

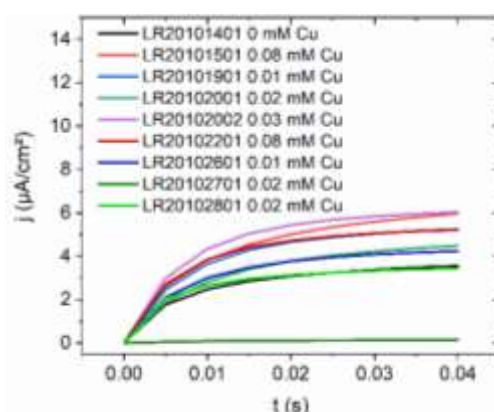


Figure 4.32: Chronoamperometric curves recorded for samples deposited with various Cu(II) concentrations

g. SEM characterizations

Since the films are thinner than those made in continuous mode, it was not possible to detach them from the substrate. Due to strong interaction between the electrons and the substrate, EDS analyzes were not performed. Thus, only top face analyzes were acquired on as-deposited samples.

Typical images are represented in Figure 4.33. Without Cu, as previously mentioned, two morphologies can be observed but the predominant is the one exhibiting platelet-like grains. When the Cu(II) concentration increases up to 0.03 mM, bigger grains having the same morphology are observed. Finally at a Cu(II) concentration of 0.08 mM, the samples exhibit coarser grains. The morphology is also different. We can guess nanoflowers which are close to SnSe films made by continuous mode. Thus, the presence of Cu seems to influence the morphology from 0.08 mM Cu(II). It should be underlined that the color of the deposits at this Cu(II) concentration changed, after several days. This is probably due to the oxidation of copper or of another phase involving Cu and is not suitable for the thermoelectric properties.

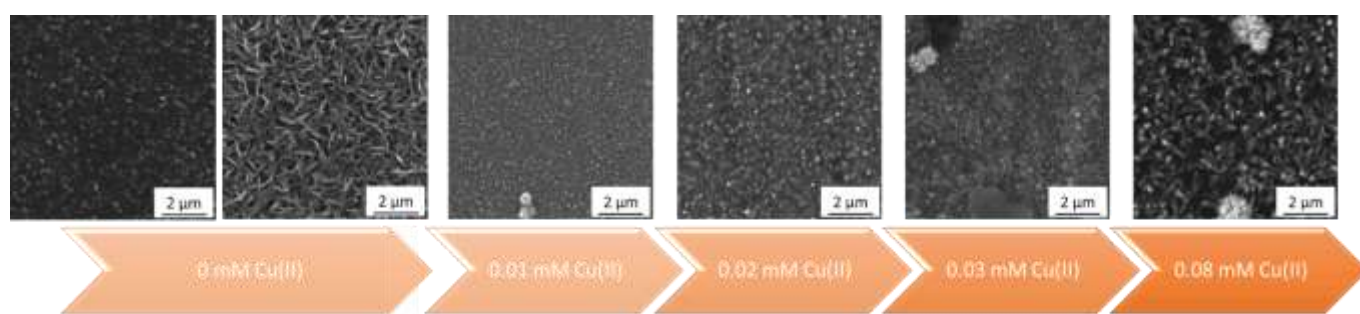


Figure 4.33: SEM images of samples deposited at different Cu(II) concentrations

h. XRD characterizations

The samples were analyzed on the top face by XRD. Typical patterns are shown in Figure 4.34. Whatever the Cu(II) concentration, the orthorhombic SnSe phase is determined with a preferential orientation along the (111) plane. However, the presence of Cu₂Se is not excluded since almost all the peaks can be double indexed into the Cu₂Se structure. Indeed, the peaks at 30.04, 43.25, 54.23 and 71.57 ° can be attributed to the (200), (220), (222) and (420) planes of Cu₂Se. However, since no additional peaks are observed in comparison with the pattern containing no Cu(II), we suggest all the peaks are related to the SnSe phase. The crystallite size randomly evolves with the concentration of Cu(II) (Table 4.11). Evolution of the crystallite size as well as shifts of the peaks are expected with replacement of Sn(II) by Cu(II). A drop of the crystallinity is observed at a concentration of 0.08 mM of Cu(II). According to the SEM analysis, we expected an increase of the crystallite size with the Cu(II) concentration (Figure 4.33) and we cannot explain the random evolution of the crystallite size. Finally, according to the reactivity of the electrolyte solution with Cu(II), the possible presence of Cu₂Se must be more investigated (reactions 4.5 and 4.6).

Cu(II) concentration (mmol.L ⁻¹)	Crystallite size (Å)
0	225.87 ± 7.10
0.01	197.70 ± 30.61
0.02	247.70
0.03	272.40
0.08	223.65 ± 73.75

Table 4.11: Evolution of the crystallite size with the Cu(II) concentration

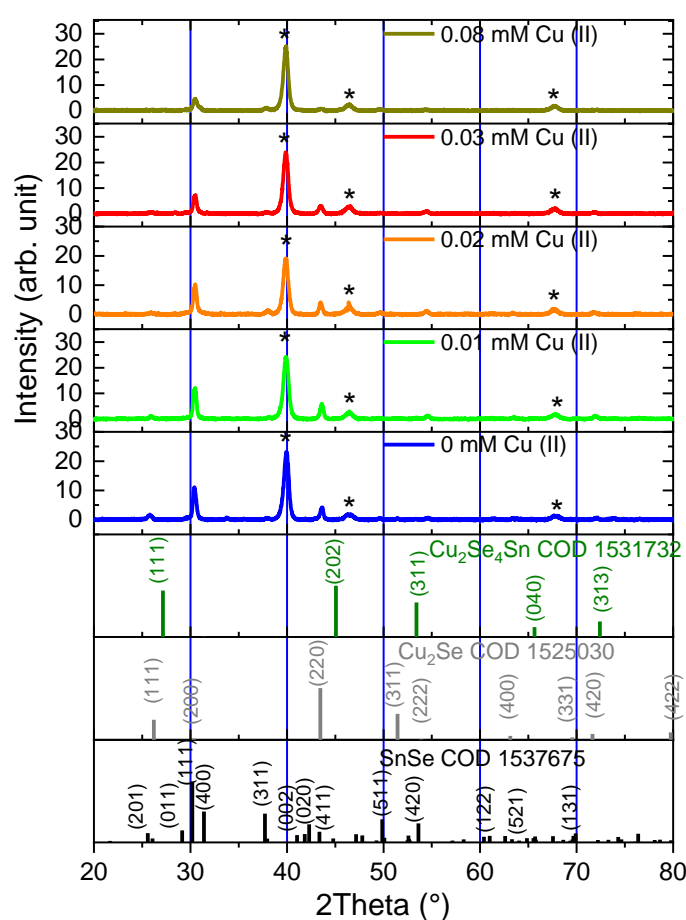


Figure 4.34: XRD analyzes on as-deposited samples with various Cu(II) concentration

- ✓ Electrodepositions were managed with Cu(II) concentrations between 0.01 and 0.08 mM
- ✓ The morphology is influenced by the Cu(II) concentrations
- ✓ It is difficult to see an evolution of the grain size with the Cu(II) concentration

Conclusion

This fourth chapter aimed to study the SnSe films deposited in pulse mode. In the first part, the electrodeposition conditions were set. The second part exposes the samples elaborated at a t_{OFF} of 1 s. Thus, we showed the unexpected effects of the t_{ON} on the double layer charging as well as the current density. Hence, we observed an influence of the t_{ON} on the morphology which tends to look like that of the deposits in continuous mode for higher t_{ON} , specifically 500 ms, although the charge quantities are not the same. When the t_{ON} increases, the grain size (XRD, TEM) and the film thickness decrease. It should be noticed that the faradaic yields are not improved by the pulse mode. After optimization of the t_{OFF} in the third part, similar results with a t_{OFF} of 400 ms were obtained in the fourth part. However, stronger oxygen contents were obtained. The comparison of the microstructures between the pulse modes and the continuous mode is contrasted. Smaller grain sizes (from SEM top views) are obtained using pulse electrodeposition, as opposite from the TEM cross views. This comparison must be moderated due to the difference of the reached charge quantities (at least fivefold lower). Although the films are thinner in pulse than in continuous mode, the XRD reveal a more important intensity of the (111) peak, corresponding to a more pronounced preferential growth. It is also possible that the pulse parameters need to be readjusted. Lower t_{OFF} values could be experienced for t_{ON} of 50 and 100 ms. Lower t_{ON} could also be tried. A higher t_{OFF} value should be applied for a t_{ON} of 500 ms. Finally, the fifth part represents an introduction to SnSe doping. In a first step, we explained how copper was chosen as dopant. Stability problems were highlighted, underlying the necessity to use a very low copper concentration. We showed the influence of the copper concentration on the morphology of the deposits. Nevertheless, it seems that there is no clear influence of the copper content on the microstructure. Other characterizations are needed to confirm or not the presence of other phases such as Cu_2Se .

Ce quatrième chapitre avait pour but d'étudier les films de SnSe déposés en mode impulsionnel. En première partie, les conditions d'électrodépositions ont été fixées. La seconde partie expose les échantillons élaborés à un t_{OFF} de 1 s. Nous avons ainsi montré les effets inattendus du t_{ON} tant sur la charge de la double couche que la densité de courant. Ainsi, nous avons observé une influence du t_{ON} sur la morphologie qui tend à ressembler à celle des dépôts en mode continu pour des t_{ON} plus élevés, spécifiquement 500 ms, bien que les quantités de charges ne soient pas les mêmes. Lorsque le t_{OFF} augmente, la taille de grains et l'épaisseur des films diminue (DRX, MEB). Il est à noter que les rendements faradiques ne sont pas améliorés par le mode impulsionnel. Après optimisation du t_{OFF} en troisième partie, des résultats similaires avec un t_{OFF} de 400 ms ont été

obtenus en quatrième partie. Cependant, de plus fortes teneurs en oxygène ont été obtenues. La comparaison des microstructures entre les modes impulsionnels et le mode continu est contrastée. Des tailles de grains plus petites (selon des vues MEB de dessus) sont obtenues en utilisant l'électrodéposition pulsée, ce qui est en contradiction avec les vues en coupes par MET. Cette comparaison doit être modérée en raison de la différence des quantités de charge atteintes (au moins cinq fois plus faibles). Bien que les films soient plus fins en mode impulsionnel qu'en mode continu, les analyses DRX révèlent une intensité plus importante du pic (111), correspondant à une croissance préférentielle plus prononcée. Il est également probable que les paramètres impulsionnels utilisés doivent être réajustés. De plus faibles valeurs de t_{OFF} peuvent être expérimentées pour les t_{ON} de 50 et 100 ms. De plus faibles t_{ON} peuvent également être testés. Une valeur plus élevée de t_{OFF} devrait être appliquée pour un t_{ON} de 500 ms. Enfin, la cinquième partie représente une introduction au dopage de SnSe. Dans un premier temps, nous avons expliqué comment le cuivre a été choisi comme dopant. Des problèmes de stabilités ont été mis en évidence, soulignant la nécessité d'utiliser une très faible concentration de cuivre. Nous avons montré l'influence de la concentration de cuivre sur la morphologie des dépôts. Néanmoins, il semble qu'il n'y ait pas d'influence claire de la teneur de cuivre sur la microstructure. D'autres caractérisations sont nécessaires pour confirmer ou non la présence d'autres phases telles que Cu_2Se .

Chapter 5.

Towards
electrodeposition of
SnSe nanowires

Introduction

This fifth chapter represents challenges, prospects and hopes concerning the development of the synthesis by electrodeposition of SnSe nanowires and nanotubes. To the best of our knowledge, no work has currently been published concerning the study of electrodeposited SnSe nanowires and nanotubes. That is the reason why the growth mechanism of these nanostructures is for the moment partially unexplained. However, the electrodeposition of Sn and of Se nanostructures has been reported. Both single and polycrystalline nanostructures can be elaborated, depending on the electrodeposition conditions as well as the chemical bath. The properties of SnSe nanowires synthesized by CVD ^[36,240,241], polyol ^[242] or solvothermal ^[39] processes were also described. Thus, the first two parts of this chapter will be devoted to a brief review of the literature. The first section will concern the electrodeposition of Sn nanostructures and the second one, the electrodeposition of Se nanostructures. The third part will introduce the first developments dealing with SnSe nanostructures. Finally, the last part will focus on our study on the electrodeposition of SnSe nanowires and nanotubes.

In this chapter, we chose the template-assisted electrodeposition as synthesis technique for these 1D nanostructures. This approach, introduced by C. R. Martin ^[243], is widely used due to its simplicity and the large range of accessible 1D nanomaterials. The technique is based on the use of a mesoporous membrane. Since the method of electrochemical growth involves electronic transfers to interfaces, a conductive substrate is necessary. For that, an adherent conductive layer is previously deposited by physical way on the template to ensure an electrical contact. This layer must be electrochemically inert, that is the reason why gold or platinum are generally chosen. The nanoporous membrane can be made of different materials such as polycarbonate or alumina. The material growth being confined within the pores, they impose the geometry of the nanostructures as well as their diameter. By applying a potential or a current density, the nanostructures progressively grow inside the pores. The growth is finished when the first nanostructures reach the top of the template, generating a blocking overgrowth layer at the top of the template (Figure 5.1).

Ce cinquième chapitre représente les challenges, perspectives et espoirs concernant le développement de la synthèse par électrodéposition de nanofils et nanotubes de SnSe. A notre connaissance, aucun travail n'a à ce jour été publié concernant l'étude de nanofils et de nanotubes de SnSe électrodéposés. C'est pourquoi le mécanisme de croissance de ces nanostructures est pour le moment partiellement inexpliqué. Cependant, l'électrodéposition de nanostructures Sn et de Se a été déjà reportée. Des nanostructures aussi bien mono que polycristallines peuvent être élaborées,

dépendant des conditions d'électrodéposition ainsi que du bain chimique. Les propriétés de nanofils de SnSe synthétisés par procédés CVD ^[36,240,241], polyol ^[242] ou encore solvothermal ^[39] ont également été décrites. Ainsi, les deux premières parties de ce chapitre seront dédiées à un bref panorama de la littérature. La première partie concernera l'électrodéposition de nanostructures de Sn et la seconde, l'électrodéposition de nanostructures de Se. La troisième partie présentera des premiers développements traitant de nanostructures de SnSe. Enfin, la dernière partie se concentrera sur notre étude sur les nanofils et nanotubes de SnSe électrodéposés.

Dans ce chapitre, nous avons choisi l'électrodéposition assistée par membrane comme technique de synthèse de ces nanostructures 1D. Cette approche, introduite par C. R. Martin ^[243], est largement utilisée en raison de sa simplicité et de la large gamme de nanomatériaux 1D accessibles. La technique est basée sur l'utilisation d'une membrane mésoporeuse. Puisque la méthode de croissance électrochimique implique des transferts électroniques aux interfaces, un substrat conducteur est nécessaire. Pour cela, une couche conductrice adhérente est préalablement déposée par voie physique sur la membrane afin d'assurer un contact électrique. Cette couche doit être électrochimiquement inerte, c'est pourquoi l'or ou le platine sont généralement choisis. La membrane nanoporeuse peut être de différents matériaux tels que polycarbonate ou alumine. La croissance du matériau étant confinée dans les pores, ceux-ci imposent la géométrie des nanostructures ainsi que leur diamètre. En appliquant un potentiel ou une densité de courant, les nanostructures croissent progressivement à l'intérieur des pores. La croissance est finie lorsque les premières nanostructures atteignent le haut de la membrane, générant une surcouche bloquante au sommet de la membrane (Figure 5.1).



Figure 5.1: Illustration des différentes étapes de l'électrodéposition assistée par membrane

I. Electrodeposition of Sn nanowires

a. Studies in ionic liquid

Taking into account the bad stability of Sn(II) salts in water, generating hydroxides or SnO₂ precipitation, ionic liquids under inert atmosphere were commonly used as electrolytes for its electrodeposition. Indeed, in addition to their high thermal stability, ionic liquids have a low vapor pressure and they enable a wide potential window, avoiding the hydrogen evolution ^[244]. To fabricate

nanowires, the research group of Elbasiony *et al.* focused their work on two ionic liquids. The baths are respectively 1-ethyl-3-methylimidazolium dicyanamide ([EMIm]DCA) and 1-butyl-1-methylpyrrolidinium dicyanamide ([Py1,4]DCA). To perform the electrodeposition of the nanowires, the group used polycarbonate membranes, previously sputtered by a hundred-nanometer-thick Cu or Au layer on one side. They obtained nanowires using galvanostatic pulse deposition with [Py1,4]DCA at -2 mA and $t_{ON}=1$ s and $t_{OFF}=4$ s. After dissolution of the membrane in dichloromethane, the nanowires have bunched together and the whole sample was fragile. Using [EMIm]DCA, the authors decided to deposit a Cu layer, as a supporting layer for the nanowires. They obtained freestanding nanowires, using continuous potentiostatic deposition, after dissolution of the membrane. A similar study, from Al Kiey *et al.* demonstrated the synthesis of freestanding nanowires from polycarbonate membranes after dissolution in dichloromethane, using 1-ethyl-3-methylimidazolium trifluoromethylsulfonate ([EMIm]TfO) [245]. They obtained nanowires 5 μm long nanowires but no information is mentioned about their crystallinity.

Without any template, Sn tends to be deposited in dendrites [246,247]. However, several ionic liquids promote freestanding with high aspect ratio Sn nanowires without any template. These ionic liquids are 1-butyl-1-methylpyrrolidinium chloride (BMP-Cl), 1-butyl-1-methylpyrrolidinium triflate (BMP-TFO), 1-ethyl-3-methylimidazolium methyl sulfate (EMIM-CH₃OSO₃) or 1-butyl-1-methylpyrrolidinium bis(trifluoromethylsulfonyl)imide (BMP-TFSI). If the ionic liquids are associated with SiCl₄, they act as additives in organic solvent, such as acetonitrile and propylene carbonate [248]. The anions from the ionic liquid, likely complexed with SiCl₄, adsorb on Sn crystallites and act as capping agent. Moreover the pyrrolidinium cations interact strongly with the working electrode during the electrodeposition, enhancing the 1D-growth.

b. Growth mechanism in alumina templates in aqueous and organic media

Other works reported the synthesis of Sn nanowires inside alumina membranes. Such membranes, well known to support high temperature thanks to their melting point close to 2100 °C, cause diffusion problems due to narrow pore diameter and high aspect ratio. Moreover, the bubbles generated by hydrogen evolution during the deposition would block access to the remaining pores. That is the reason why Lodge *et al.* decided to work with dichloromethane as electrolyte instead of water [249]. Their work showed, on the first hand, the increase of the electrodeposition time with the pore diameter, in agreement with the active surface increase. On the other hand, they confirmed the

limiting character of these membranes. They observed different length of nanowires with unfilled pores, sign of heterogeneous growth rates due to diffusion problems, which creates faster diffusion at some points. When a nanowire reaches the top, it overgrows and covers other pores, inhibiting the growth of neighboring nanowires (Figure 5.2).

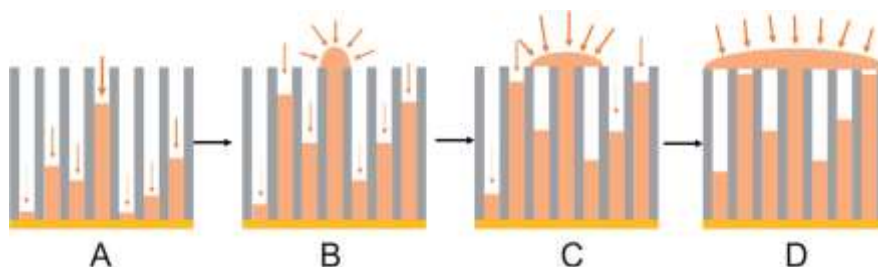


Figure 5.2: Schematic views of the different diffusion modes (linear, hemispheric) occurring during the electrodeposition process ^[249]

In this article, they suggest that such templates are also responsible for different morphologies of the deposit. They encountered three kinds of morphologies inside the same template:

- Sn Nanowires completely filling pores (most common)
- Sn Nanowires filling the central part of the pores but not touching the pore walls
- Sn nanotubes

Thus, the morphology seems to be directly linked to the pore wall chemistry. Indeed, alumina templates cannot only be associated to crystalline Al_2O_3 ^[250]. The anodization process generates several species like amorphous oxides, hydroxides or inclusions of the acid used during the process. Thus the presence of OH^- along the pores give to the template a significant chemical reactivity. Moreover, aluminum oxides and hydroxides are preferentially dissolved by diluted acid electrolyte solutions, like sulfuric, phosphoric or oxalic acid. If the ability of the electrolyte solution to penetrate the template is weak due to poor wettability, it will of course modify the synthesized nanostructures. Furthermore, nucleation differences are not excluded inside the pores, leading to various nanowire lengths. Finally, different growth rates and morphologies, which can also be related to the diffusion and the pore wall chemistry, lead to different nanowire lengths.

Other teams tried the electrodeposition of Sn in the same template but in aqueous media. It is the case of Luo *et al.* who show that it is possible to obtain single crystalline Sn nanowires exclusively when pre-depositing Cu nanorods ^[251]. They explain the change of crystallinity by the fact that, at smaller overpotential, nuclei with larger critical size are generated, favorable to single crystal growth. Moreover, the crystallinity of Cu nanorods is in favor of generating Sn single crystal nanowires. For

their part, still in a aqueous medium, Harlow *et al.* obtained polycrystalline nanopillars with a maximum length estimated to 16 μm and around 50 nm diameter ^[252].

Still using alumina template, Sharma *et al.* performed the pulse galvanostatic deposition in presence of tri-ammonium citrate and used a t_{ON} of 1 ms and t_{OFF} of 10 ms ^[253]. Increasing the current density modifies the nanostructures. Thus, the lowest current density generated nanorods with limited lengths from 5 to 8 μm and diameters from 209 to 253 nm. A higher current density led to thinner and shorter nanowires, with a length of 2 to 3 μm and a diameter from 146 to 240 nm. The higher used density of current enabled nanoribbon formation, large of 129 nm as well as nanowires long of 2 μm and wide of 40 nm. Since the template has pores of 200 nm in diameter, these results are surprising and unexplained. In another work, they also managed the pulse potentiostatic electrodeposition of Sn, from a bath based on PolyEthylene Glycol (PEG) and sulfuric acid ^[254]. Their results are similar to the previous ones: the morphology changes from nanorods to nanowires of various aspect ratio when the potential becomes more and more cathodic and the population of nanowires increases. They suggest also a slight dissolution of the membrane in acidic conditions, that can lead to higher wires diameters than the pores.

An alternative approach was explored by Djenizian *et al.*, with the use of TiO_2 nanotubes as guide layer ^[255]. The starting point to generate nanowires is on the top of the nuclei by applying a higher current density, this phenomenon being called the “tip effect” (Figure 5.3). Moreover, hydrogen evolution increases also with the polarization. Then the morphology of the nanostructures is also modified by a higher hydrogen evolution.



Figure 5.3: SEM image of Sn nanowires ^[255]

Shin *et al.*, according to theoretical and experimental findings, claim that, during the electrodeposition, the diffusion rate continuously increases into the pores, which has the effect to increasingly destabilize the nanowires growth ^[256]. Because the current density is higher on the top of the nanowires, their idea is to apply a thermal gradient between the bottom and the top of the

membrane (Figure 5.4). As a consequence, the diffusion rate being weaker for lower temperatures, the smaller nanowires catch up their growth delay and then a more uniform filling rate is obtained.



Figure 5.4: Scheme of the thermal gradient protocol across the template ^[256]

According to the review of Sn nanowires electrodeposition:

- ✓ The use of ionic liquids or organic solvents was preferred to avoid Sn hydrolysis
- ✓ The pre-electrodeposition of Au or Cu nanorods is a benefit for the crystallinity of the Sn nanostructures
- ✓ The growth inside alumina template is not uniform (different morphologies, filling rate, sizes)
- ✓ The evolution of H₂ bubbles can block pores
- ✓ Acid diluted electrolyte solutions can partially dissolve the membrane
- ✓ A change of morphology and/or crystallinity is expected with the applied deposition potential
- ✓ The nanostructures grow due to a difference of current density (tip effect)
- ✓ The hydrogen evolution may modify the morphology

II. Electrodeposition of Se nanostructures

The synthesis of Se nanowires by electrodeposition remains poorly studied. That is the reason why the following review, as exhaustive as possible, presents a list of only five articles. Steichen and Dale studied the template-free electrodeposition of Se nanostructures from 1-ethyl-3-methylimidazolium tetrafluoroborate chloride ([C2mim][BF₄]/[C2mim]Cl) ^[257]. They showed that the Se precursor has an importance for the nanostructures. Indeed, when SeCl₄ is used, amorphous

hemispheres are generated, whereas SeO_2 leads to trigonal crystallized nanorods. These nanorods in fact originate from trigonal nanocrystallites emerging from amorphous particles and act as seeds for the nanorod growth. It is like a liquid-solid phase transformation from amorphous to trigonal phase, which is improved when the temperature increases. Thus, the crystallinity of the nanorods is also enhanced by the temperature.

Zhang *et al.* used cetyltrimethylammonium bromide (CTAB) in aqueous bath for the generation of Se nanotubes by cyclic voltammetry ^[258]. This surfactant improves the electrolyte conductivity and adsorbs on the working electrode. The electrodeposition is explained by the fact that initial seeds are composed of CTAB micelles, which act as a soft template. The cationic radicals can be associated to HSeO_3^- or SeO_3^{2-} , which will then be adsorbed on the working electrode and reduced in $\text{Se}(0)$. The preferential growth remains in the seed direction and the current density is still higher on the tip. It should be underlined that increasing the scan rate generates nanoparticles. Decreasing the distance between the working and the counter-electrode gives rise to flower-like particles. Ramified nanotubes were also obtained by modifying the orientation of the working electrode. Furthermore, stirring the electrolyte modifies again the morphology. Finally, the study is also in agreement with the fact that a limited high temperature improves the crystallinity of the nanotubes. Indeed, below 60 °C, they obtained amorphous nanoparticles. No deposit was obtained beyond 90 °C, probably due to desorption phenomenon but this assumption remains to be verified.

Other groups studied the electrodeposition of Se using polycarbonate ^[259] and alumina templates ^[260,261]. All these works are in agreement with the synthesis of Se nanowires, crystallized into the trigonal structure. In both works of Kumar *et al.* ^[259,260], trigonal polycrystalline nanowires according to the space group $P 3_1 2 1$ (JCPDS card n°. 06-0362) are obtained whatever the template and with a good uniformity in terms of diameter (Figure 5.5). Concerning the work of Zhang *et al.* ^[261], the microstructural characterizations revealed the presence of the unexpected fcc structure, which should be generated at a high pressure. After annealing, they finally obtained the desired trigonal structure.

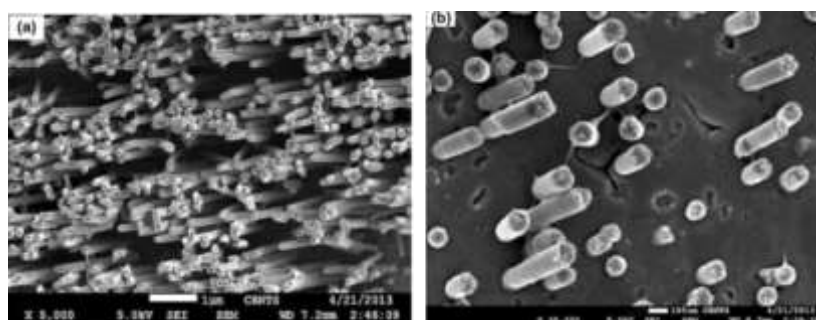


Figure 5.5: FESEM image of Se nanowires after dissolution of the membrane ^[259]

According to the review of Se nanostructures electrodeposition:

- ✓ Se nanostructures can be deposited without or with alumina or polycarbonate templates.
- ✓ Without template, the choice of the Se precursor determines the morphology and crystallinity.
- ✓ Without template, the position and orientation of the working electrode can also modify the morphology.
- ✓ The use of surfactant may influence the morphology.
- ✓ A change of morphology and/or crystallinity is expected with the bath temperature or by post annealing.

III. Study of SnSe nanostructures

a. Theoretical properties: first principles calculations

To have a better understanding of the thermoelectric properties, first principle calculations using DFT were made on a single wall SnSe nanotube. At room temperature, SnSe crystallizes into the orthorhombic structure with the Pnm space group, characterized by a quasi-lamellar structure. The b and c axes can be considered as in-plane equivalent axes and a as a cross-plane axis (Figure 5.6 a). Looking at a nanotube, three configurations can be considered but among them, the zigzag structure was studied. Being simulated as thermodynamically stable under ambient conditions, this nanostructure is obtained by rolling the single layer along the c -axis and gives rise to a star-like structure (Figure 5.6 b).

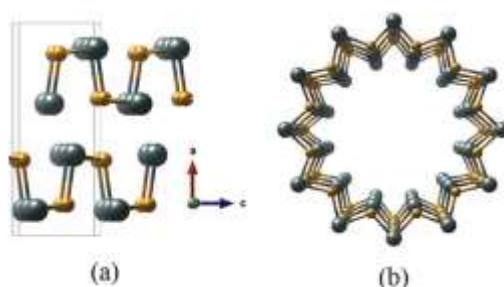


Figure 5.6: (a) Structure of a SnSe crystal and (b) top view of a SnSe nanotube ^[262]

In their work, Lin *et al.* determined a band gap between 1.47 eV and 1.55 eV ^[262]. Looking at the electronic band structure (Figure 5.7), they found that the valence band maximum (VBM) is very close to the second lowest one (VBM1), with only 0.103 eV of difference. The observation is similar for

the conduction band minimum (CBM), different from the second lowest (CBM1) of only 0.08 eV. The fact that they are at similar energy levels means they can be considered as quasi-direct band gap. Moreover, a first interest in thermoelectricity is to have such flat bands, giving a high carrier concentration at the same energy level which is in favor of a high Seebeck coefficient S .

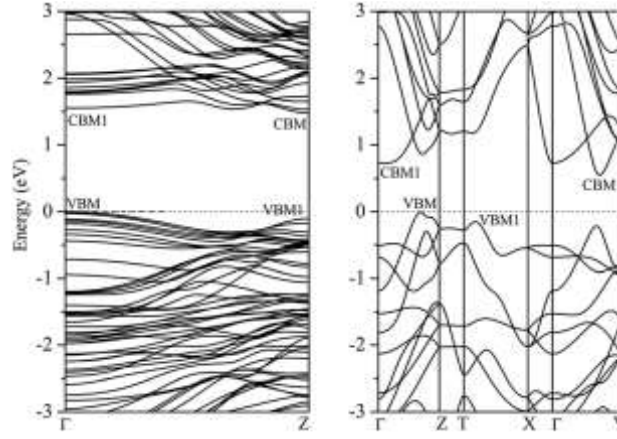


Figure 5.7: Electronic band structure of the single nanotube (left) and crystalline SnSe (right) ^[262]

Thus, simulated p-type SnSe nanotubes show a better S than crystalline SnSe (Figure 5.8). At 300 K, an enhancement of S is expected for a hole concentration of $1.5 \times 10^{20} \text{ cm}^{-3}$ with a value reaching approximately $275 \mu\text{V.K}^{-1}$, instead of $100 \mu\text{V.K}^{-1}$ for the bulk counterpart. According to the authors, this improvement can be linked to the chemical potential, which reaches the VBM1 and contributes to S . Concerning σ , it can be strongly influenced by the microstructural defects like atomic point defects, crystalline boundaries or impurities. Simulations on SnSe crystals showed that the carrier concentration is dominated by Sn vacancies, which can be extended to SnSe nanotubes.

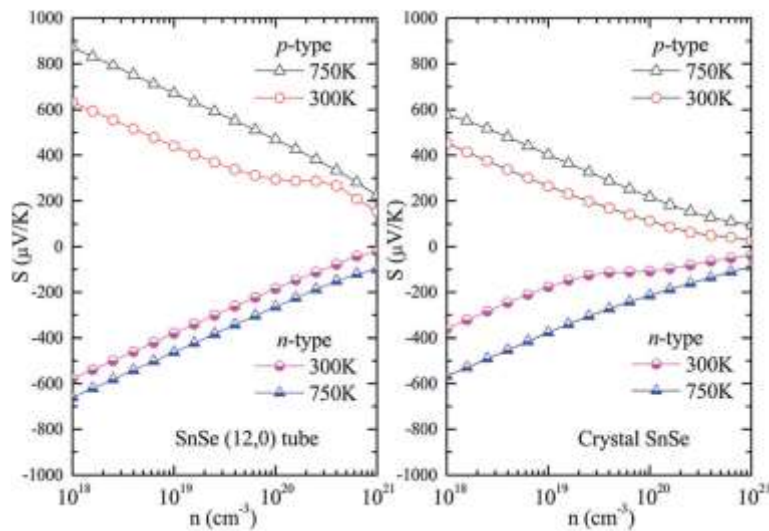


Figure 5.8: Dependence of the Seebeck coefficient with the carrier concentration (a) for a nanotube and (b) for crystalline SnSe ^[23]

The comparison of the lattice thermal conductivity was made between a nanotube and a crystal (Figure 5.9). The values were calculated by solving the Boltzmann transport equation. The nanotube exhibits a lattice thermal conductivity lower than that of the crystal, only $0.46 \text{ W.m}^{-1}\text{.K}^{-1}$ at 300 K. In the star-like structure, the distance between Sn and Se atoms is shorter than in the crystal due to rotation of the rings. Due to the specific geometry, there are more atoms in the unit cell of the nanotube (Figure 5.6) and then more vibration modes. Moreover, the phonon lifetime is significantly shortened which leads to a lower value of κ .

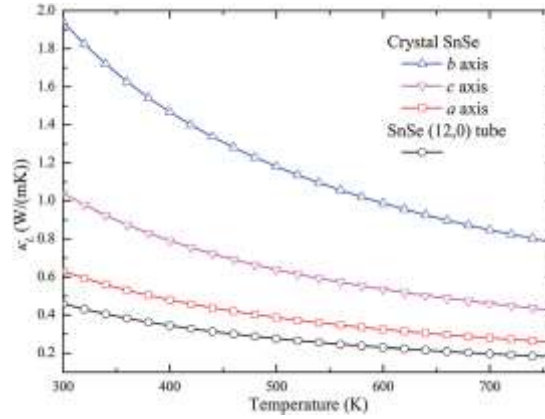


Figure 5.9: Evolution of the lattice thermal conductivity with the temperature ^[262]

If we consider the lower simulated value of κ and the higher value of S and if we assume to keep a suitable value of σ with p-doping, the figure of merit can be significantly enhanced (Figure 5.10). Thus, Lin *et al.* found that ZT can be comprised between 3.5 and 4.6 at 750 K, for an optimum doping concentration of $6.3 \times 10^{20} \text{ cm}^{-3}$, whereas the typical experimental ZT values for the crystal are in the range of 0.6 up to 2.6 according the authors ^[16]. Such improvement should be due to both the degenerated band structure, leading to a higher thermopower and the reduced lattice thermal conductivity.

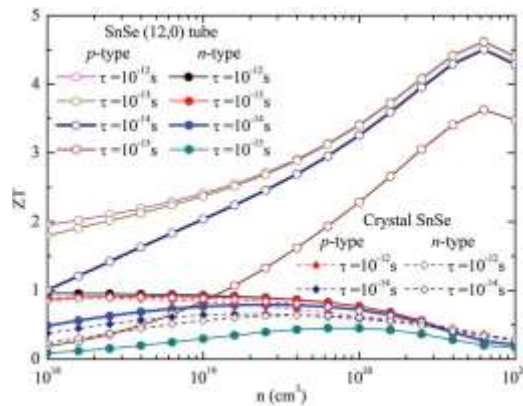


Figure 5.10: Evolution of the figure of merit with the carrier concentration for different scattering times: comparison between SnSe nanotube and SnSe crystal ^[262]

b. Synthesis and properties

To the best of our knowledge, the first synthesis of SnSe nanowires was managed by Shen *et al.* in 2003 ^[242]. Using the polyol method, they have obtained SnSe nanowires with a mean diameter of 50 nm and a length of 10 μm but SnO_2 was also detected inside the nanostructures. Unfortunately, their method could not promote the achievement of pure SnSe nanostructures.

In 2004, Han *et al.* synthesized, by coprecipitation, SnSe nanorods at room temperature from aqueous solution ^[263]. Firstly, they introduced elemental Se and NaOH into distilled water and heated the bath. This solution generated Na_2Se and Na_2SeO_3 . Then, $\text{SnCl}_2 \cdot 2\text{H}_2\text{O}$ was added into a solution containing trisodium citrate, before adding NaOH, in order to complex Sn(II) salt. Finally, both solutions were mixed together, the reaction between Na_2Se and complexed Sn(II) leading to the precipitation of SnSe nanostructures. The morphology is related to the complexing strength of the ligand. Thus nanorods with high purity and diameters comprised between 80 and 100 nm were obtained from trisodium citrate as a complexing agent for Sn. Replacing trisodium citrate by EDTA changes the morphology into nanosheets and nanoparticles, whereas tartaric acid leads to nanosheets. Moreover, modifying the concentration of the complexing agent influences also the nanorod diameters.

Zhao *et al.* performed in 2006 the synthesis of polycrystalline SnSe nanowires and nanotubes inside an alumina template. Infiltration of $\text{Sn}(\text{SePh})_4$ is carried out into the template followed by thermolysis at 350 $^\circ\text{C}$ ^[264]. Concerning alumina templates, we must keep in mind the fact that they contain defects along the pore walls. Consequently, the presence of a large number of defects inside the pores will increase the chemical reactivity of the template, specifically for smaller diameters. Here for a pore diameter of 25 nm, nanowires were generated. In contrast, nanotubes, having terminating caps on the top, were found for pore diameters from 180 to 1000 nm.

By a solution-liquid-solid mechanism, Liu *et al.* performed the synthesis of single-crystalline SnSe nanowires by heating all the precursors in a flask until 290 $^\circ\text{C}$ ^[265]. In this way, smooth nanowires with diameters averaging 20 nm and lengths from hundreds of nm to tens of μm were obtained. The direct and indirect band gaps were determined, using UV-visible-near IR spectroscopy, at 1.55 and 1.12 eV respectively, which seems to be in agreement with theoretical values ^[262].

An ionic liquid-assisted solvothermal synthesis was made by Zhang *et al.*, in presence of 1-butyl-3-methyl imidazole chloride ($\text{Bmim}[\text{Cl}]$), which plays a huge role in controlling the morphology of the nanostructures ^[39]. To investigate the growth mechanism of the obtained nanostructures, they studied the concentration of the ionic liquid and the time synthesis dependence. Without ionic liquid, regular nanoplates with a thickness of 30 nm were obtained. Adding 2 g of ionic liquid led to bark-like

structures composed of SnSe nanoparticles. The ionic liquid promotes the nanoparticles aggregation only if its concentration is sufficient. In that case, micelles are generated, stabilizing the solution (Figure 5.11). For higher concentrations, nanoparticles aggregate into nanorods interlinked in shape of nanorafts. Bmim⁺ cations interact with Se(-II) anions present on chalcogenide particles surface and tend to self-assembly into ordered structures stabilized by π - π interactions, perpendicularly to SnSe particles. Beyond 10 g of ionic liquid, the viscosity became too important and led to irregular particle aggregation.

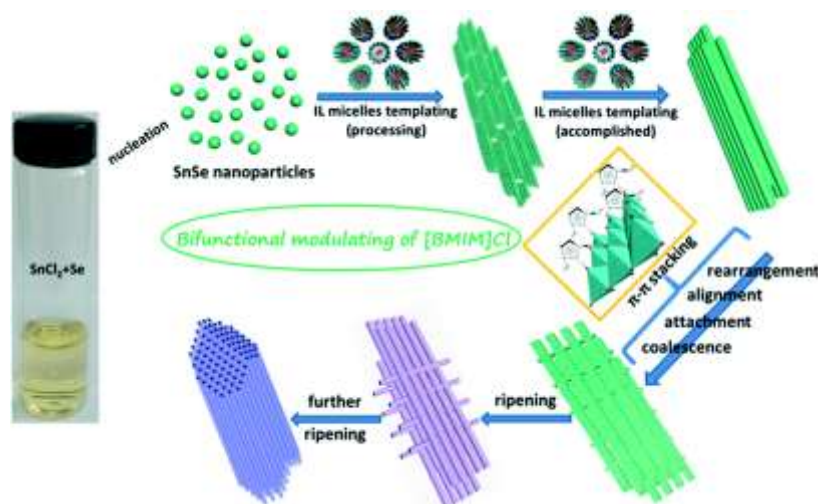


Figure 5.11: Illustration of the synthesis process of SnSe nanostructures via micelle templating ^[39]

To conclude about the time dependence of the synthesis, characterizations were made at different reaction times, using an ionic liquid quantity of 4 g. Thus, amorphous tiny nanoparticles were obtained for the minimum time of 1h. This result is in agreement with the Ostwald rule. Then, by increasing the reaction time, the nanoparticles aggregated from polycrystalline plates to rod-like subunits and nanorafts composed of nanorods. The TEM analysis showed that these nanorods were in fact composed of a single-crystal core and a 10 nm thick polycrystalline shell. The authors suggest that the nanorafts growth occurs mainly via the connection of the nanorods through the polycrystalline shell. After 24 h, disassembled single-crystal nanorods were obtained by the ripening of nanorafts. All the synthesized nanostructures absorb the light in the visible and the near IR wavelength range and by the way their optical band gaps were determined (Table 5.1).

	Nanoparticles	Nanoplates	Nanorafts	Nanorods
Indirect gap (eV)	0.91	0.93	0.8	0.86
Direct gap (eV)	1.61	1.74	1.70	1.42

Table 5.1: Optical band gaps of SnSe nanostructures ^[39]

There is no general trend concerning the band gap of the nanostructures, except that all the direct gaps are blue shifted. The indirect gaps match with that of bulk SnSe. Nanorods and nanorods have lower indirect gaps but it is not the case for the direct gap of nanorods. Furthermore, the lowest value of the direct gap for the nanorods is also not explained. It seems to be closer to that of the bulk material.

Butt *et al.* performed the synthesis of SnSe nanowires by a Vapor Liquid Solid (VLS) mechanism^[36]. SnSe powder was put inside a crucible and heated, and gold seeds were used to catalyze the reaction. They obtained single-crystalline orthorhombic SnSe nanowires without any secondary phase. Diameters between 30 and 40 nm and lengths of tens of μm were measured. According to UV-vis-NIR spectroscopy, they obtained a direct gap of 1.03 eV and an indirect gap of 0.92 eV. Different positions of the crucible in the furnace lead to different temperatures. Thus the coldest end at 200 °C, generated sheet-like structures. Going progressively to the center promoted disk or plate-like structures, on which the nanowires started to grow, as indicated by the Au catalyst on the tips of nanowires. Cuboid structures were observed at 400 °C. The optimized and uniform nanowires were synthesized at 550 °C.

The same synthesis method was employed by Zheng *et al.* who obtained nanowires with diameter close to 80 nm and length of about 3 μm ^[240]. Their results show a high photoconductive gain, good responsivity, excellent detectivity and fast response speed under near-infrared illumination. Hernandez *et al.* went further by measuring the thermoelectric properties of individual SnSe nanowires in comparison with the temperature and the nanowires diameter^[241]. As well as the previous work, no secondary phase was found, sign of pure SnSe but they showed the presence of Sn vacancies, as expected by theoretical studies^[262].

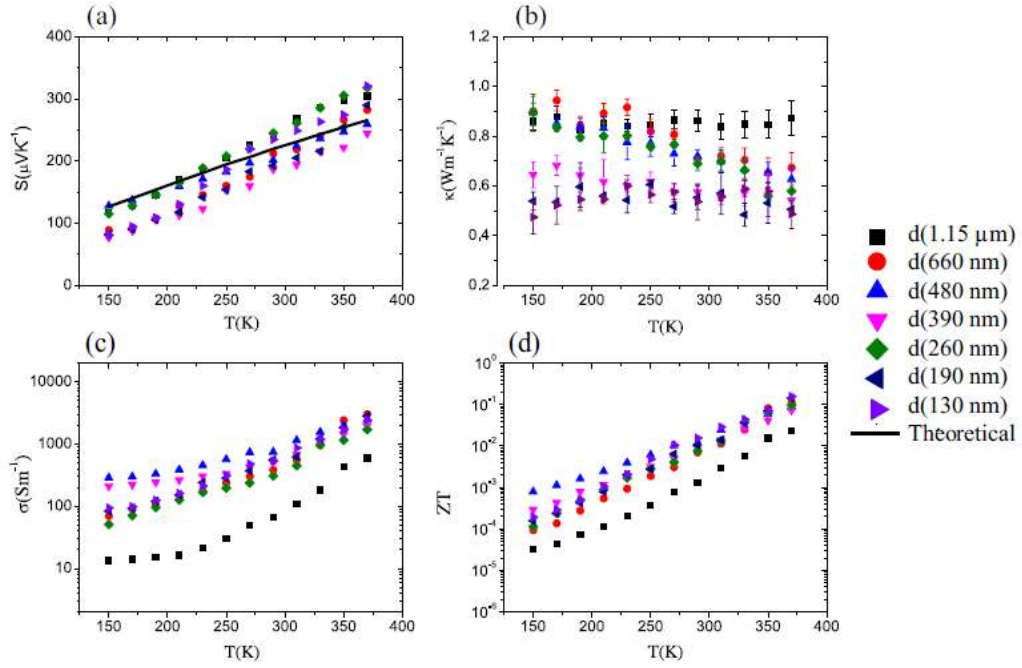


Figure 5.12: (a) Seebeck coefficient, (b) thermal conductivity, (c) electrical conductivity and (d) ZT obtained for SnSe nanowires ^[241]

No clear dependence of S with the diameter is demonstrated here. Indeed, the overall values tend to vary from 100 to 250 $\mu\text{V.K}^{-1}$ between 150 and 370 K and are in good agreement with those obtained by simulation (Figure 5.12 a). On the contrary, a strong influence of the diameter is observed on κ (Figure 5.12 b). But it does not show a clear dependence on the temperature. σ was obtained by four-probe measurement and after measuring the diameter of the nanowires with SEM and TEM (Figure 5.12 c). It is very difficult to say if there is an influence of the diameter, specifically for high temperatures. But the values are weak, in the range of 1000 S.m^{-1} at 370 K. As a result, no strong influence of the nanowires diameter is observed on ZT even if it seems to be improved by reducing the diameter and reaches its maximum of 0.156 at 370 K (Figure 5.12 d). Although κ is reduced compared to the bulk material and S is quite good, σ contributes to decrease the ZT . Nevertheless, this study shows the interest in SnSe nanowires as a new p-type material for thermoelectric applications.

From the review on SnSe nanostructures, we found that:

- ✓ High bandgap values for nanotubes are expected in comparison with crystalline bulk SnSe
- ✓ An enhancement of S is theoretically expected for nanotubes compared to the bulk SnSe
- ✓ A strong decrease of κ is also predicted by decreasing the dimensionality
- ✓ A maximum ZT value should be obtained between 3.5 and 4.6 at 750 K for nanotubes
- ✓ SnSe nanostructures were synthesized by other methods than electrodeposition
- ✓ Single to polycrystalline SnSe nanowires or nanotubes (with or without terminating caps) can be obtained as well as other morphologies (sheets, rafts, particles)
- ✓ SnO_2 can eventually be co-generated
- ✓ The use of ligand or surfactant influences the morphology
- ✓ First experimental results show that S and σ do not clearly vary with the diameter of the nanostructures
- ✓ A better influence of the diameter of the nanostructures on κ is experimentally observed
- ✓ The measured values of ZT are in the same range whatever the diameter of the nanowires

IV. Electrodeposition of SnSe nanostructures in alumina templates

a. Preliminary study of the alumina templates

1. Geometric characteristics

Commercial alumina membranes from Whatman with nominal values of pore diameters of 0.1 μm were used for all the experiments (supplier data). Before performing the electrodeposition, we studied the microstructure of the membrane, in order to precisely determine the real active surface, that will condition the electrodeposition duration.

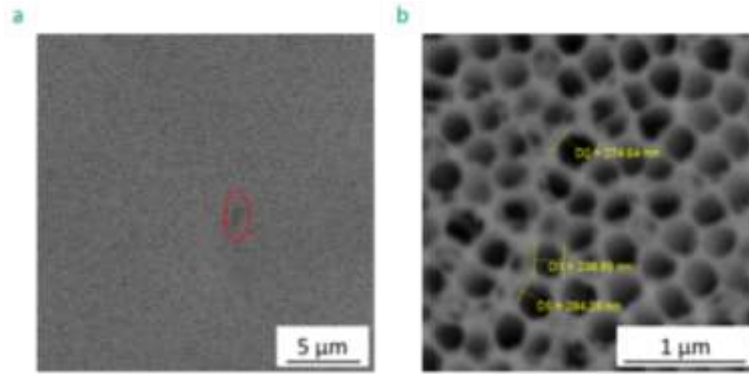


Figure 5.13: Top SEM views of a 0.1 μm pore membrane

Different zones on the membranes were analyzed by SEM visualizations. It should be noted that the samples were previously sputtered with carbon. As it can be seen on the membrane (Figure 5.13), the pores are irregular in terms of size and morphology. It can of course impact the electrodeposition process and lead to different morphologies between nanowires, as encountered by Lodge *et al.* ^[249]. Cracks are visible on the top of the membrane (red circle), but it is difficult to say if they are due to the sputtering metallization process or not. The sputtering process should not create any defect due to heating effect because alumina is thermally stable (melting point of 2050 °C). Moreover, these membranes are protected by a polymer ring which, sometimes, can be distorted or melted during the metallization process and leading to the break the membrane. Furthermore, a thin polymer film, that can be easily dissolved by acetone, seems to be partially present on the membrane.

To determine an average pore density and an average pore diameter, 8 areas of exactly 1 μm^2 were examined. Inside each area, four well-defined pores were measured in order to obtain an average diameter as accurate as possible. An unexpected pore diameter value of $0.2968 \pm 0.0368 \mu\text{m}$ (D_{pore}) was obtained, which is almost triple than expected, regarding the supplier data. This result can be explained due to the anodization process, the pore diameter highly depending on the used experimental parameters. From several top views, we deduce that the pore density (N_{pore}) is 9.75 pores per μm^2 , or $(9.75 \pm 1.28) \times 10^8$ pores/ cm^2 . This value is in the range of such AAO templates.

Cross-sectional SEM scans also confirm that the pore diameter is in the range of 200 nm (Figure 5.14 a). The membranes were found to have an average thickness (h) of $62.11 \pm 1.47 \mu\text{m}$ (Figure 5.14 b).

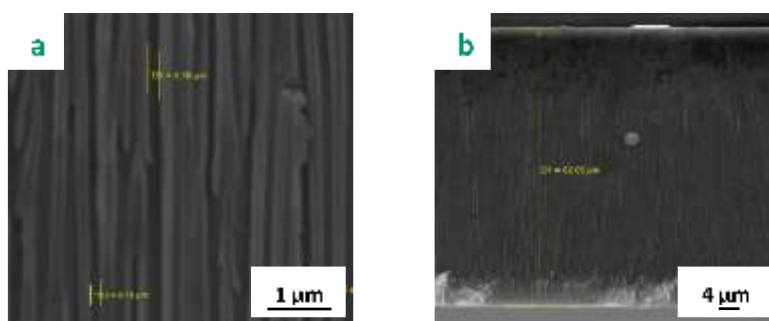


Figure 5.14: Cross section SEM views of 0.1 μm diameter membrane: (a) high and (b) low magnification

All the determined values are reported in Table 5.2.

Nomial value	$N_{pore}/\mu\text{m}^2$	N_{pore}/cm^2	$D_{pore}(\mu\text{m})$	$h(\mu\text{m})$
0.1 μm	9.75	$(9.75 \pm 1.28) \times 10^8$	0.2968 ± 0.0368	62.11 ± 1.47

Table 5.2: Geometrical characteristics of the templates determined by SEM

2. Determination of the exposed and real surfaces

The charge quantity of an electrochemical reaction is directly linked to the electrochemical active surface of the electrode, so-called real surface. If we assume one reaction, the calculation of this charge quantity is related to the amount of deposited nanostructures through the Faraday law. The problem is that the real surface can be higher than the expected one from the geometrical dimensions of the exposed area.

The estimation of the real surface is possible for example by the analysis of the UPD peaks of adsorbed dihydrogen onto Pt electrode. In this focus, we chose to perform the same procedure developed by Rodríguez *et al.* ^[266].

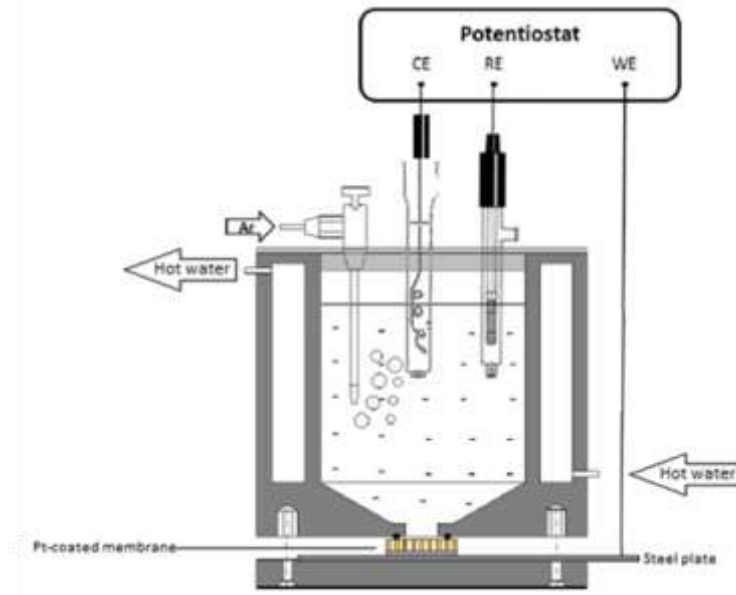


Figure 5.15: Schematic representation of the PVC electrochemical cell (adapted from ^[267])

The alumina membranes were sputtered with a Pt layer on one side and they were used as the working electrode (WE). The reference electrode (RE) was a saturated KCl AgCl/Ag electrode and a Pt wire was used as a counter-electrode (CE). The template was maintained horizontally into a PVC cell, the Pt-coated side put down, in contact with a steel piece, in order to assure an electrical contact (Figure 5.15).

The cell enables an immersion of the electrolyte with a radius of 0.499 cm (R_{cell}). Thus, the immersed surface, corresponding to the surface of the membrane in contact with the electrolyte, is given by the following relation 5.1:

$$S_{imm} = \pi \times R_{cell}^2 \quad 5.1$$

With this cell, a surface of 0.784 cm² is immersed in the electrolyte (S_{imm}). If we consider all the accessible pores, we can estimate the exposed surface (S_{exp}) according to the relation 5.2:

$$S_{exp} = S_{imm} \times N_{pore/cm^2} \times \pi \times \left(\frac{D_{pore}}{2}\right)^2 \quad 5.2$$

Finally, the volume of pores that can be filled (V_{fill}) during the deposition is determined from the exposed surface and the membrane thickness (relation 5.3):

$$V_{fill} = S_{exp} \times h \quad 5.3$$

Chapter 5. Towards electrodeposition of SnSe nanowires

Considering that the pore diameters are close for both kind of membranes, it is not surprising to determine similar exposed surfaces and volumes (Table 5.3).

	R_{cell} (cm)	S_{imm} (cm ²)	D_{pore} (μm)	S_{exp} (cm ²)	h (μm)	V_{fill} (cm ³)
"0.1 μm" membrane	0.499	0.784	0.2968	0.534	62.11	3.31×10^{-3}

Table 5.3: Parameters of the template using the PVC cell

A cyclic voltammetry was made on a solution of 0.5 M H₂SO₄ with a scan rate of 50 mV/s, at room temperature. The reference electrode was a saturated KCl AgCl/Ag electrode and a Pt wire was used as a counter electrode. A typical cyclic voltammogram is represented in Figure 5.16 a. Three zones can be distinguished: the double layer region, the oxygen region and the hydrogen region. We focus on the latter (Figure 5.16 b). A first broad signal **1** corresponds to the reduction of protons and their adsorption onto the electrode. For the signal **2**, the adsorbed hydrogen is converted into dihydrogen.

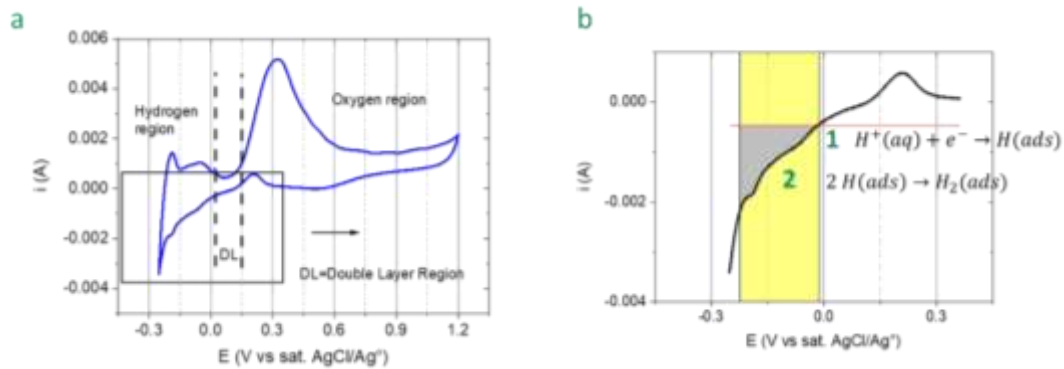


Figure 5.16: Cyclic voltammogram of a 0.5 M H₂SO₄ solution vs Ag/AgCl (left) and zoom on the hydrogen evolution zone (right)

The calculation of the charge quantity is firstly made by integration for both peaks. The result of the integration is 1.66×10^{-4} A.V. Secondly, dividing by the scan rate, we obtain a charge quantity of 3.32×10^{-3} C. Finally, to calculate the real surface we use the following relation 5.4 :

$$S_{real} = \frac{Q N_A}{F d_m} \quad 5.4 \text{ [266]}$$

Where S_{real} , Q , N_A , F and d_m are respectively the real surface, the charge quantity (3.32×10^{-3} C), the Avogadro constant ($6.02 \times 10^{23} \text{ mol}^{-1}$), the Faraday constant (96480 C.mol^{-1}) and the polycrystalline Pt constant evaluated by Anderson criterion ($1.3 \times 10^{15} \text{ cm}^{-2}$). In this way we obtain a real surface of 15.93 cm^2 .

The calculation of the exposed and real surfaces is to keep in mind for the rest of this part, specifically for the chronoamperometric and voltammetric curves respectively. In comparison with the

exposed surface, we find a ratio S_{real}/S_{exp} of 30. In comparison with Schoenleber's thesis, this result is not surprising ^[267]. Indeed, for alumina membrane with pore diameter of 100 nm, he determined a ratio of 32, using the same method.

An explanation of this result is that the sputtering process occurred also along the walls of the template, until a height of several μm , and not only at the bottom (Figure 5.17).

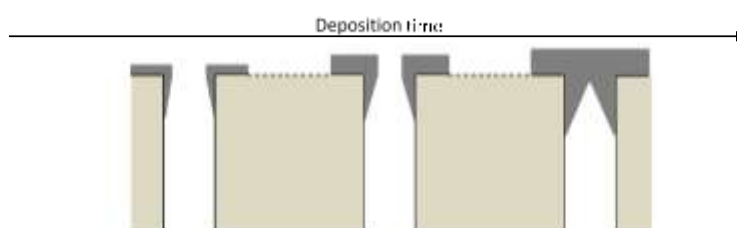


Figure 5.17 : Cross view schematic representation of the metallization occurring inside the template (adapted from ^[267])

b. Study of the electrochemical system

Before any electrodeposition process, we should perform preliminary electrochemical studies. First of all, we studied the electrolyte solution containing 0.2 M of KCl, 0.2M of $\text{Na}_2\text{C}_2\text{O}_4$ and 20 mM of $\text{SnCl}_2 \cdot 2\text{H}_2\text{O}$. The pH was adjusted to 2.5 before adding the Sn(II) salt. The electrolyte solution was maintained at 50 °C and degassed under argon before the experiment. The electrochemical setup was the same as described in the previous section. An alumina membrane, sputtered with a Pt layer on one side was used as the working electrode (WE). Prior to the electrodeposition experiments, a sonication treatment was occasionally carried out on templates, either in deionized water or in the electrolyte solution. Not using sonication can induce the presence of air inside the membrane, which can inhibit the growth in some pores. The reference electrode (RE) was a saturated KCl AgCl/Ag electrode and a Pt wire was used as a counter-electrode (CE). The cell used for the study of the electrochemical system was the PVC cell (Figure 5.15).

The cyclic voltammetry of Sn(II) shows a wider deposition potential window than what we observed using Pt-coated glass (Figure 5.18). The shoulder C0, preceding C1, can be due to the Sn UPD. Moreover, taking into account our study of the electroactivity domain, a reduction of the electrolyte is not excluded (see Chapter 3). The reduction of Sn(IV), coming from partial oxidation of Sn(II) as well as the reduction of dissolved oxygen remain also possible. It seems that the reduction of Sn(II) into Sn(0), corresponding to the peak C1, starts from -0.7 V vs Ag/AgCl, instead of -0.62 V vs Ag/AgCl. Thus

C1 is shifted to more negative potentials. Nevertheless, this peak being large and flat, we do not exclude other reduction processes and the superposition with another peak. The anodic stripping is observed, represented by A1. At higher potential, the strong increase of the current is due to the oxidation of Sn(II) into SnO₂ and the formation of O₂.

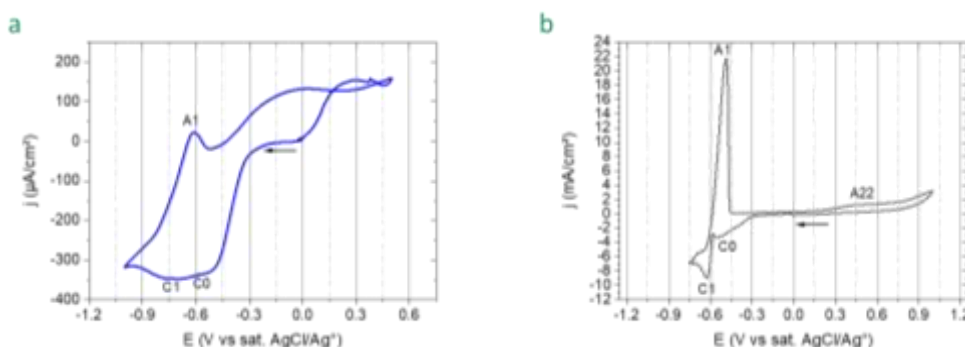


Figure 5.18: CV of a 20 mM SnCl₂.2H₂O solution at 10 mV/s, 50 °C: (a) in alumina membrane ($S_{\text{real}}=15.93 \text{ cm}^2$) and (b) on Pt-coated glass ($S=0.025 \text{ cm}^2$)

A cyclic voltammetry was realized by replacing Sn(II) by 5 mM of Na₂SeO₃.5H₂O (Figure 5.19 a). In this voltammogram, two cathodic peaks can be seen. The first, C1', is associated to the reduction of Se(IV) into Se(0), at -0.52 V vs Ag/AgCl. The peak C2', at -0.75 V vs Ag/AgCl, corresponds to the reduction of Se(0) into Se(-II). Both peaks are slightly cathodically shifted compared to our study on Pt-coated glass (Figure 5.19 b).

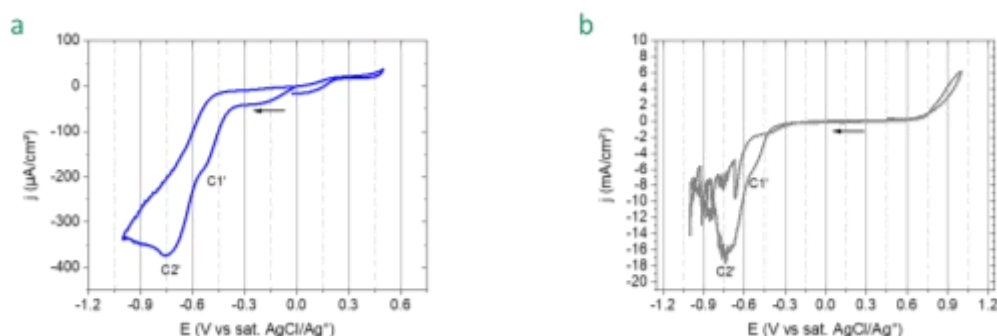


Figure 5.19: CV of a 5 mM Na₂SeO₃.5H₂O solution at 10 mV/s, 50 °C: (a) in alumina membrane ($S_{\text{real}}=15.93 \text{ cm}^2$) and (b) on Pt-coated glass ($S=0.025 \text{ cm}^2$)

The complete electrolyte, including Sn(II) and Se(IV) salts, was also studied (Figure 5.20 a). The shape of the curve is similar to that of Sn, apart from an additional cathodic peak C2'' at -0.94 V vs Ag/AgCl (Figure 5.18). Two less pronounced peaks or shoulders, called here C1'' and C0'', are also detected. By comparing with the electrochemical behavior of the same electrolyte on Pt-coated glass (Figure 5.20 b), different hypothesis can be made about the origin of the peaks :

- Since the C0'' peak is almost at the same position of C0 (Figure 5.18), the same possible processes can be associated, namely the UPD of Sn, or reduction of the solvent, or Sn(IV) or otherwise oxygen. From the electrochemical behavior of this bath on platinum disc, this potential window can be associated to the cathodic reduction of SnSe.
- C1'' is associated to the deposition of Sn(0).
- A1'' corresponds to the anodic stripping of Sn(0).
- C2'' should be associated to the reduction of H⁺ coming from partially dissociated H₂C₂O₄.
- The further increase of the anodic density of current is due to the oxidation of Sn(II) to SnO₂.

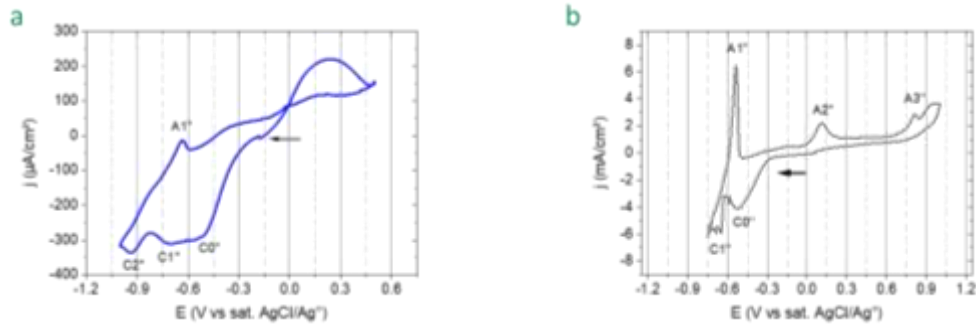


Figure 5.20: CV of 20 mM SnCl₂.2H₂O and 5 mM Na₂SeO₃.5H₂O solution at 10 mV/s, 50 °C: (a) in alumina membrane ($S_{\text{real}}=15.93 \text{ cm}^2$) and (b) on Pt-coated glass ($S=0.025 \text{ cm}^2$)

To conclude, the deposition potential window seems to be wider and shifted to more cathodic potentials than on Pt-coated glass electrode. Consequently, electrodepositions of SnSe nanostructures were performed in a potential window ranging from -0.5 V to -0.8 V vs AgCl/Ag.

c. Electrodeposition of SnSe nanostructures

A first set of electrodeposition experiments was performed using the 0.1 μm membranes and the PVC cell described in Figure 5.15. Using the Faraday law, we can estimate the charge quantity, necessary to fill the membrane, considering a faradaic yield of 100 % (equation 5.5):

$$Q = \frac{n F \rho_{\text{SnSe}} V_{\text{fill}}}{M_{\text{SnSe}}} \quad 5.5$$

Where Q , n , F , ρ_{SnSe} , V_{fill} and M_{SnSe} are the charge quantity, the number of involved electrons (here $n=6$), the Faraday constant (96480 C.mol^{-1}), the SnSe volume weight (6.192 g.cm^{-3}),

the AAO filling volume ($3.31 \times 10^{-3} \text{ cm}^3$) and the SnSe molar weight ($197.65 \text{ g.mol}^{-1}$) respectively. Thus, to completely fill the membrane, a minimum charge quantity of -60.83 C is needed.

1. Typical chronoamperograms during template electrodeposition

Generally, the chronoamperogram shape allows to know if the filling is reached or not (Figure 5.21).

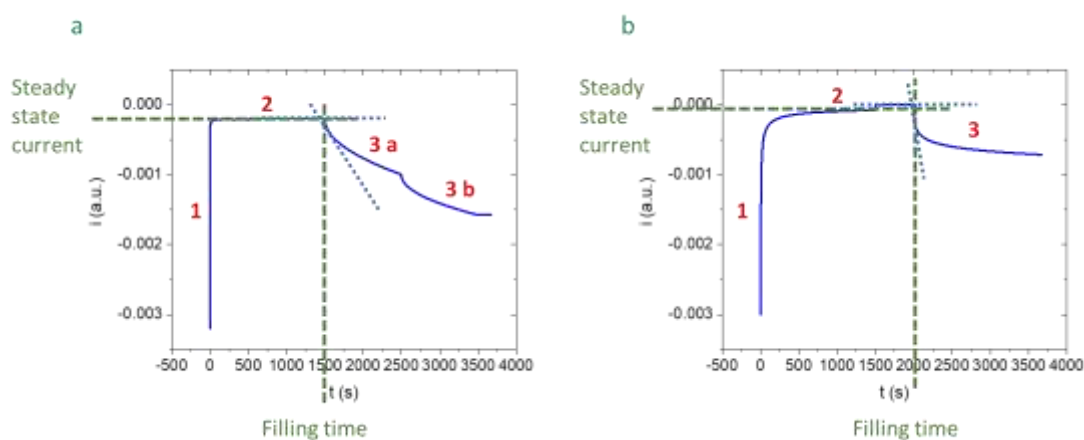


Figure 5.21: Typical chronoamperograms during the template electrodeposition of (a) nanowires and (b) nanotubes

The initial sharp transient current drop (step 1) is associated to the double-layer charge and to the nucleation step. Then the current stabilizes during the growth of the nanowires or nanotubes (step 2). During this step, the pore filling is promoted from the steady state current density, until the filling time. When the filling is reached, an overgrowth layer is generated on the top of the membrane. Consequently an increase of the absolute value of the current can be observed due to the increase of active surface. Proenca *et al.*, working on the electrodeposition of Ni nanotubes and nanowires, highlighted the following differences between the related chronoamperograms from the step 3^[268]. Indeed, according to them, the overgrowth of the nanowires is a double-step process. Firstly, nanowires reach the top of the membrane, generating polygonal heads associated with a current decrease (step 3 a) (Figure 5.22). Secondly, the growth rate of the overgrowth film exceeds that of the nanowires (step 3 b), leading to another increase of the absolute current. For nanotubes, spherical heads are generated. The overgrowth is a one step process with an associated strong decrease of the current (step 3).

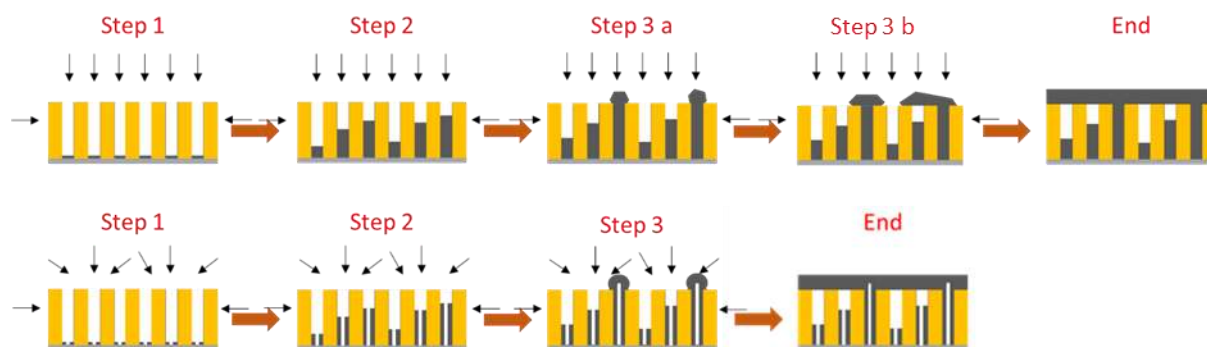


Figure 5.22: Illustration of the growth mechanism of nanowires (up) and nanotubes (down) (adapted from ^[267])

Samples were deposited by continuous deposition at a fixed applied potential between -0.5 V and -0.8 V vs AgCl/Ag, after systematic cathodic linear sweep voltammetries. The corresponding chronoamperograms were systematically recorded.

2. Influence of the counter-electrode

Several samples were made without separation of the counter-electrode (Figure 5.23 a and c). In comparison with the typical chronoamperograms (Figure 5.21), the curves of the samples do not show the typical filling curve. This is significant of an incomplete filling process. On the contrary, by separating the counter-electrode, the membrane filling can be reached earlier and typical filling curves can be observed (Figure 5.23 b and d). That is the reason why the counter-electrode was systematically immersed in a separate compartment filled with 0.1 M KCl solution. This is because the whole current is not devoted to the electrodeposition of the nanostructures but other reactions occur like hydrogen evolution, especially at -0.8 V vs AgCl/Ag. On the counter-electrode, oxidations occur and they should disrupt the electrolyte solution without separate compartment.

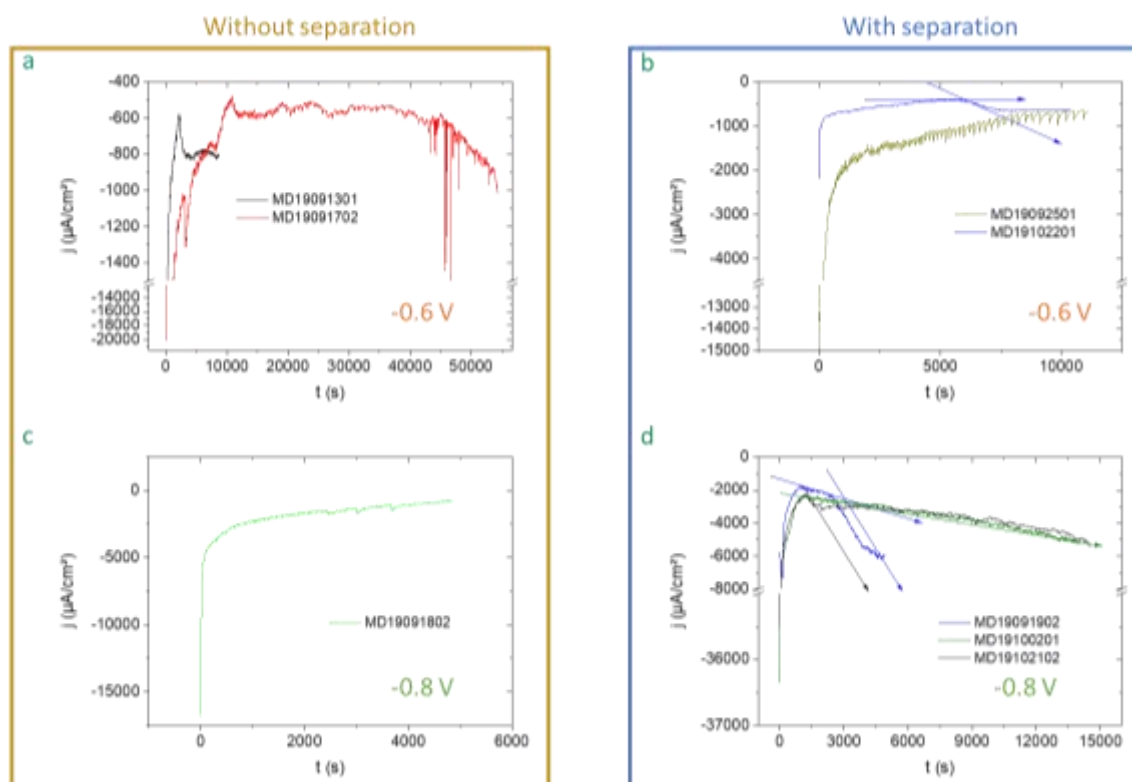


Figure 5.23: Chronoamperometric curves of the as-deposited samples (a) -0.6 V without separation, (b) -0.6 V with separation, (c) -0.8 V without separation and (d) -0.8 V with separation ($S_{\text{exp}}=0.53 \text{ cm}^2$)

3. Influence of the applied potential

The evolution of the curves with the applied potential was also investigated. The Figure 5.24 gathers all the growth experiments realized from -0.55 V down to -0.8 V vs AgCl/Ag, with separation of the counter-electrode. A first observation is that the sample deposited at -0.55 V vs AgCl/Ag does not seem to have filled the membrane. The sample MD19092501 -0.6 V also seems to reveal incomplete growth, as well as current instability. The other potentials show better filling curves with shapes close to those expected. We can note that a similar shape of the theoretical curve represented in Figure 5.21 a is observed for most of the samples synthesized at -0.65 V vs AgCl/Ag and below. Although this phenomenon is hardly observable, the presence of nanowires for this potential window is possible and needs to be confirmed. From -0.7 V to -0.8 V vs AgCl/Ag, strong increases of the absolute current are observed, probably due to hydrogen evolution. At -0.8 V vs AgCl/Ag, for the samples MD19100201 and MD19102102, the hydrogen evolution is responsible of the strong increase of the absolute current what hides the expected plateau of the nanowire growth. Thus, for the rest of this study, only samples with the expected filling curves, with defined filling time marked with arrows, will be considered in the potential window from -0.6 V to 0.8 V vs AgCl/Ag.

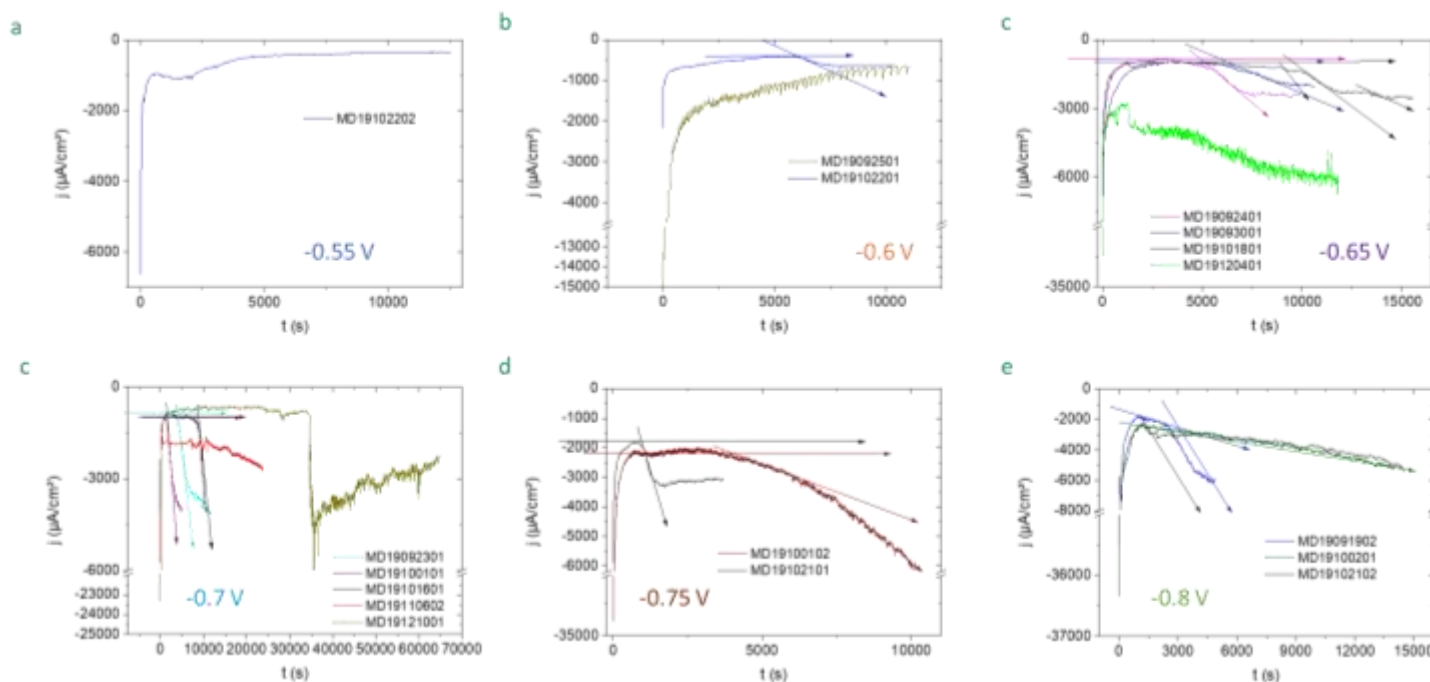


Figure 5.24: Chronoamperograms of the as-deposited samples (a) -0.55 V, (b) -0.6 V, (c) -0.65 V, (d) -0.7 V, (e) -0.75 V and (f) -0.8 V vs AgCl/Ag with separation of the counter-electrode ($S_{\text{exp}}=0.53 \text{ cm}^2$)

4. Filling time, steady state current and filling charge quantity

A general trend is that the deposition rate becomes faster when the applied potential becomes more cathodic (Figure 5.25 a). This observation is similar to what we observe for films deposition in continuous mode (Chapter 3). Moreover, the steady state current density tends to decrease with the applied potential (Figure 5.25 b). No influence of the value of the applied potential is observed on the filling charge quantity (Figure 5.25 c), which appears to be roughly constant. Moreover, the reached coulometric charge should not be sufficient to fill the membrane in comparison with the theoretical one (-60.83 C from geometrical considerations). Consequently nanowires or nanotubes with lengths mostly lower than $60 \text{ }\mu\text{m}$ are expected. Indeed, an average charge quantity of -4 C should lead to a filling volume of $2.21 \times 10^{-4} \text{ cm}^3$ and thus to an average length of $7.89 \text{ }\mu\text{m}$. Although all the values were graphically estimated with varying degrees of uncertainty, the unreproducible values can also come from leaking problems of the cell or sonication treatment in water. Moreover, we do not exclude membranes with different pore diameters. Due to the bath instability, generation of precipitates during the electrodeposition, such as $\text{Se}(0)$ or SnO_2 , may also occur and would block pores.

Furthermore, bubbles due to H_2Se and/or H_2 can also prevent access to several pores. Finally, different active surfaces and sputtering can lead to different growth rates.

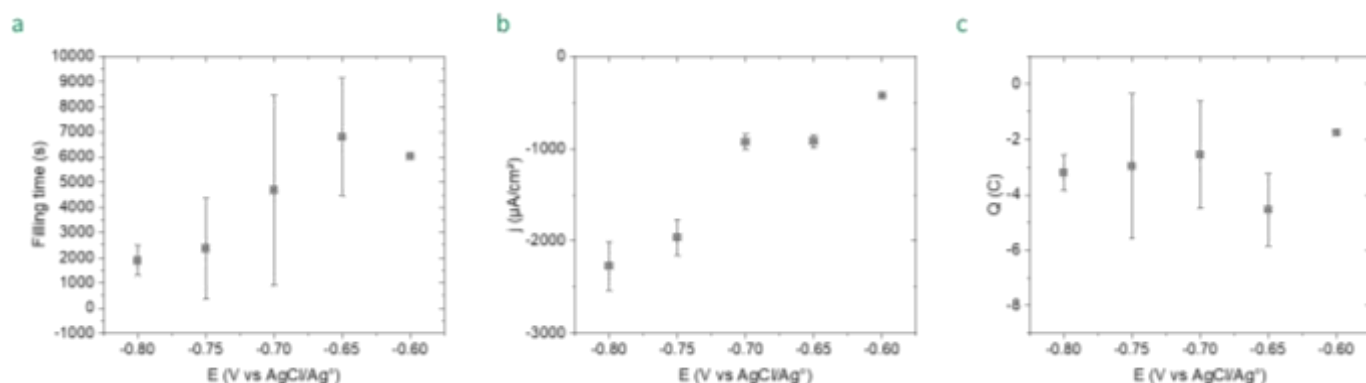


Figure 5.25: Deposition parameters of the as-deposited samples in the PVC cell dependence of the deposition potential of: (a) the filling time, (b) the steady state current density and (c) the filling charge quantity

d. Microstructural characterization

1. XRD characterizations

The Figure 5.26 shows typical XRD patterns of the as-deposited samples at different applied potentials. Because the analyses were made on unpolished samples, the presence of several peaks can be due to the overgrowth layer or some impurities on the top of the membrane. At -0.6 V vs AgCl/Ag, the diffractogram display relative lower signal on noise ratio but SnSe can be indexed according to the orthorhombic structure thanks to the peaks (111), (400), (002) and (501). A manual lattice adjustment was applied to fit the theoretical data from the COD card n°1537675 as best as possible with the pattern. Thus, the initial lattice parameters of $a = 11.37000 \text{ \AA}$, $b = 4.18600 \text{ \AA}$ and $c = 4.43900 \text{ \AA}$ were adjusted to $a = 11.19437 \text{ \AA}$, $b = 4.15390 \text{ \AA}$ and $c = 4.41898 \text{ \AA}$. Other peaks, not indexed according to SnSe structure, suggest the presence of impurities. At -0.65 V vs AgCl/Ag, SnSe is observed, specifically by the (011), (111), (400) and (222) peaks. At -0.65 V and -0.7 V vs AgCl/Ag, the main peaks (111) and (400) suggest a preferential growth orientation. Taking into account the fact that all the diffraction peaks, except the (011) one, can be indexed also in Sn tetragonal structure, the presence of Sn cannot be excluded as a secondary phase. From -0.7 V to -0.8 V vs AgCl/Ag, (220), (211), (301), (122), (321), (420) and (411) Sn peaks with increasing intensities are strongly detected. According to the cyclic voltammetry, the presence of Sn is possible at more negative deposition potential, instead of SnSe. Because of the presence of the diffraction peaks corresponding to the (111)

and (400) plans of SnSe, the exclusive generation of Sn at this potential needs to be confirmed by additional analyses.

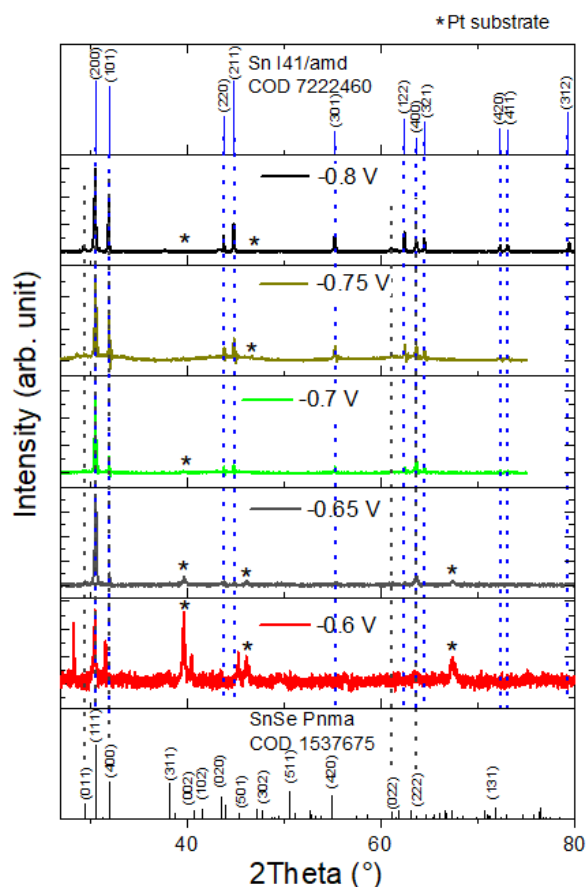


Figure 5.26: XRD patterns of the as-deposited samples

To have an idea of the evolution of the crystallinity, the crystallite size was estimated thanks the Debye-Scherrer equation and applied on the (111) peak of each samples, which is the most intense peak for all of the patterns. The values show a small trend that needs to be further confirmed. From -0.6 V to -0.65 V vs AgCl/Ag, the crystallite size increases (Table 5.4). When Sn appears, the trends is totally reversed and the crystallite size decreases. An exception is observed at -0.7 V vs AgCl/Ag which exhibit the lowest crystallite size and highest standard deviation.

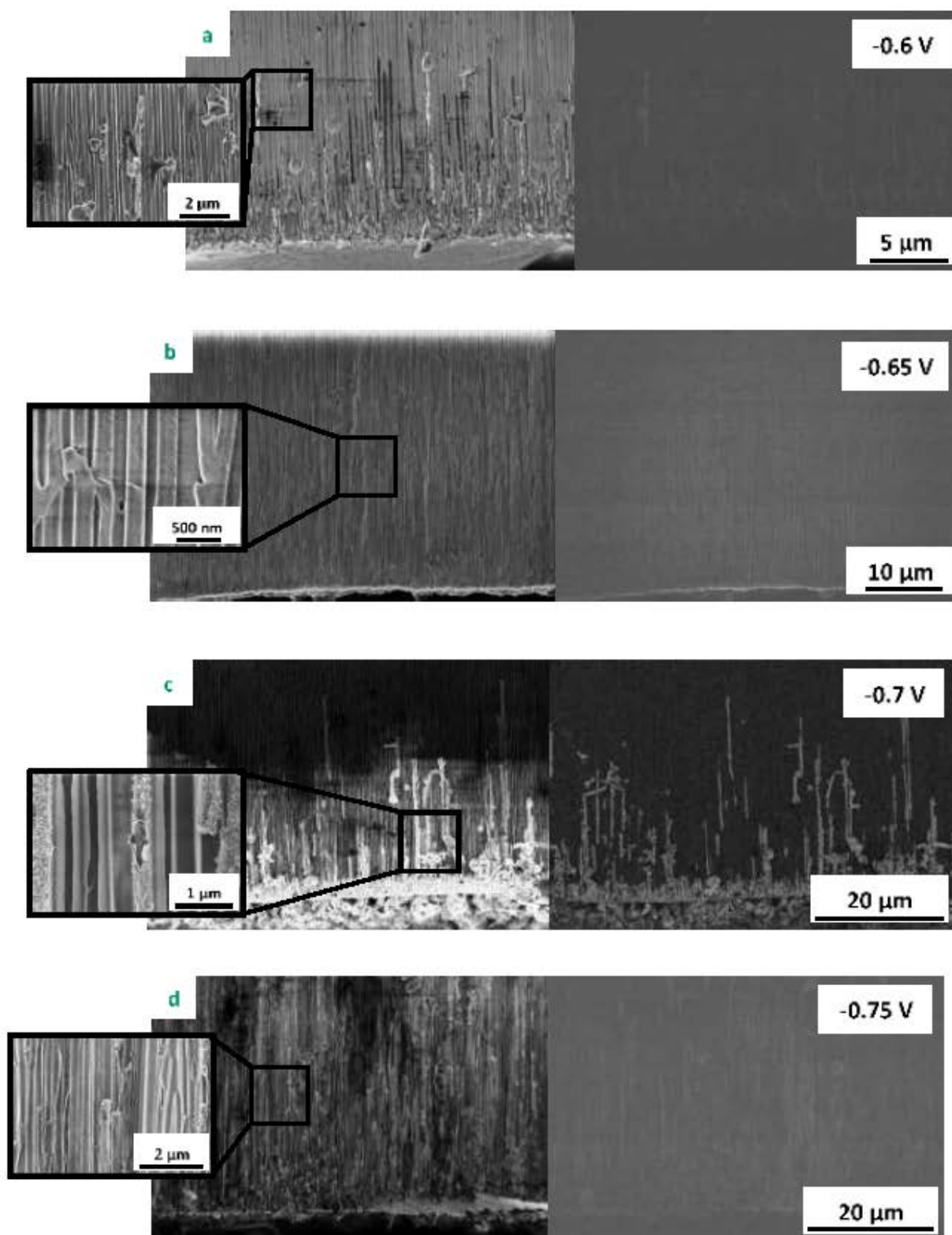
Deposition potential	Crystallite size (Å)
-0.6 V	611.4
-0.65 V	654.7 ± 88.3
-0.7 V	599.6 ± 129.8
-0.75 V	686.0 ± 36.8
-0.8 V	644.9 ± 94.5

Table 5.4: Crystallite sizes determined for each patterns using the Debye-Scherrer equation

2. HRSEM characterizations

Characterizations using High Resolution SEM were made on cross-sectional views. As expected from the obtained charge quantities, the samples generally exhibit partial filling and no overgrowth from nanowires or nanotubes could be seen on top views. Lengths from 2 to 8 µm were often measured, in agreement with the theoretical length of 7.89 µm calculated for a mean rough value of -4 C. The sample deposited at -0.6 V vs AgCl/Ag reveals the presence of rough nanostructures with low crystallinity which can explain the large SnSe peaks obtained by XRD (Figure 5.27 a). Salts are observed, which is in agreement with the not indexed additional peaks on the XRD.

By applying more cathodic fixed potentials, several typical morphologies can be observed. Thus, it was decided to highlight the deposits with the best growth fronts, as a function of the applied potential, considering the others as failures. Made at -0.65 V vs AgCl/Ag, the sample MD19093001 seems to show a smooth covering of the pores by the deposit along the membrane thickness, confirmed by the BSE image (Figure 5.27 b). The difficulty to distinguish between the nanostructures and the membrane suggest the presence of nanotubes instead of nanowires. By decreasing the potential, the sample MD19110602 -0.7 V, shows rough and granular nanotubes, with different lengths, not filling every pores. A growth front of about 20 µm can be roughly distinguished from the SE views (Figure 5.27 c). In the same sample, we can see nanotubes with terminating caps or nanowires, sometimes not touching the pore walls, like similarly reported by Lodge *et al.* ^[249]. Figure 5.27 d, e and f show probable Sn nanowires, according to the deposition potentials of -0.75 and -0.8 V vs AgCl/Ag and the related XRD patterns. Smooth nanostructures are present filling the porosities with a growth front of about 40 µm.



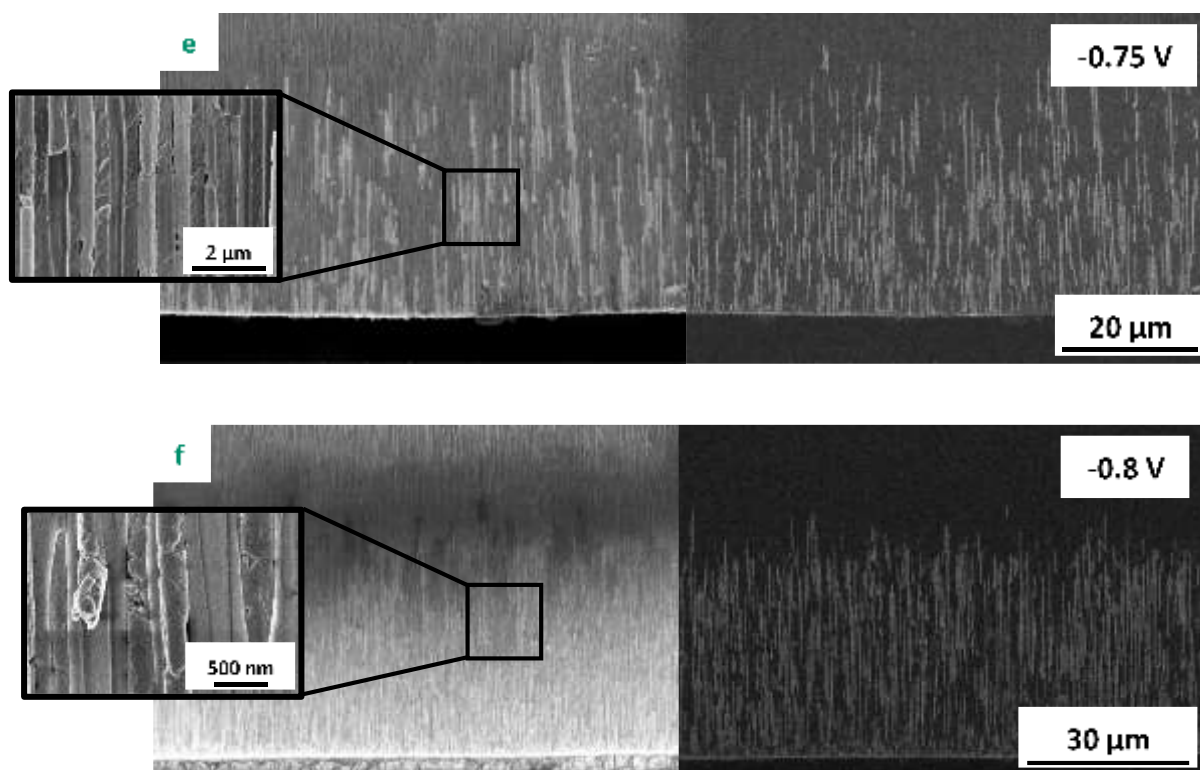


Figure 5.27: Cross-sectional HRSEM scans of samples in SE (left) and BSE (right) modes:

(a) MD19102201 -0.6 V , (b) MD19093001 -0.65 V, (c) MD19110602 -0.7 V, (d) MD19092302 -0.75 V, (e) MD19100102 -0.75 V and (f) MD19102102 -0.8 V

3. TEM characterizations

The influence of the applied potential between -0.65 V and -0.8 V vs AgCl/Ag was studied by TEM analyzes. For this purpose 4 samples corresponding to 4 different potentials were examined after dissolution of the membrane in 4 M NaOH at 40 °C followed by rinsing in water then ethanol. The first sample, called MD19101801, synthesized at -0.65 V vs AgCl/Ag shows likely nanotubes with diameters in the range of 300 nm and several grains on them (Figure 5.28 a). This is in agreement with the fact that, at this potential, we expect to have SnSe, according to the CV (Figure 5.20 a) and the XRD (Figure 5.26). Furthermore, the SEM images suggest the presence of nanotubes instead of nanowires (Figure 5.27 b). Unfortunately, EDS acquisition was not possible to get the chemical composition, since the nanostructures were completely destroyed under the effect of electron beam focusing.

The sample MD19101601 made at -0.7 V vs AgCl/Ag shows what could be a “skeleton”, as a remaining part of a nanotube (Figure 5.28 b), in agreement with the SEM images (Figure 5.27 c). We make the hypothesis that this morphology results from the chemical etching post-treatment. However

it was possible to record an EDS spectrum which reveals the a low amount of Sn (Figure 5.29 a). From the CV and XRD, we expect the presence of Sn but because of the used method to dissolve the membrane, which led to a considerable loss of matter, the EDS analysis comprises large uncertainties and no conclusion can be drawn.

In the sample MD19102101 (-0.75 V vs AgCl/Ag), we can distinguish two kinds of nanotubes (Figure 5.28 c). On the left, the image seems to correspond to a multi-wall nanotube with ripples because darker, with a diameter around 600 nm. On the right, the nanotube is smoother and more transparent and has a diameter close to 1 μm . This value is strongly higher than the pore diameter and can be explained by a partial dissolution of the membrane during the deposition, expanding the pores. It should be remind that Sharma *et al.* also obtained higher and unexplained diameters starting from 200 nm in diameter of pores ^[253].

Finally, the sample MD19102102, made at -0.8 V vs AgCl/Ag was analyzed (Figure 5.28 d). A smooth nanotube is distinguished and small grains are visible through it. The nanotube, having a diameter of 120 nm, is, according to the EDS (Figure 5.29 b) only composed of Sn, which is expected from the XRD and the CV.

The presence of nanotubes instead of nanowires can be explained by the potential gas evolution (H_2Se , H_2) occurring during the SnSe/Sn deposition.

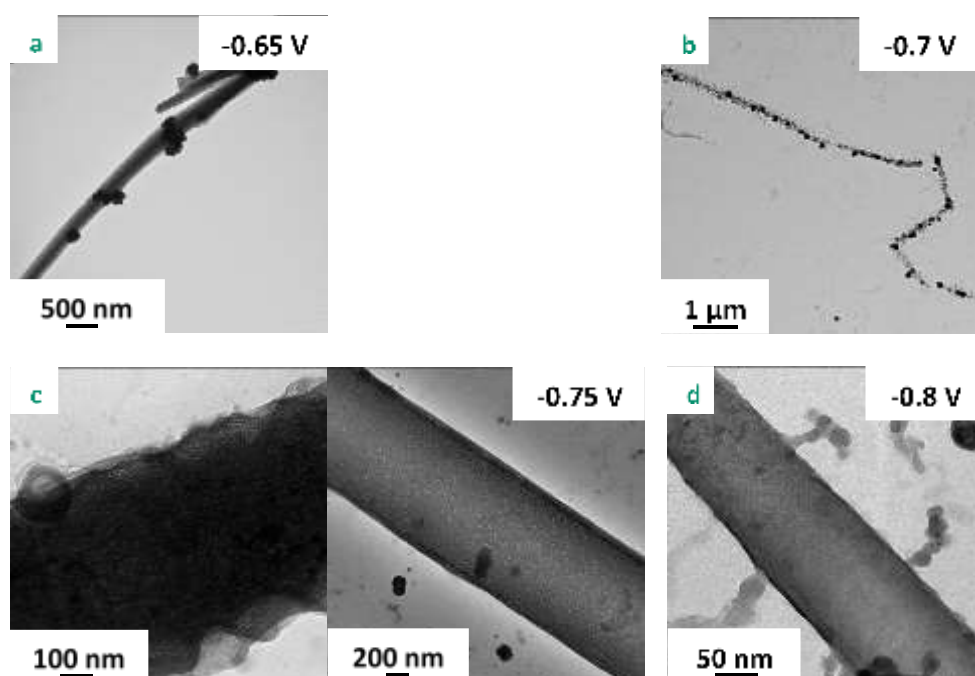


Figure 5.28: TEM images of the samples: (a) MD19101801 -0.65 V, (b) MD19101601 -0.7 V, (c) MD19102101 -0.75 V and (d) MD19102102 -0.8 V

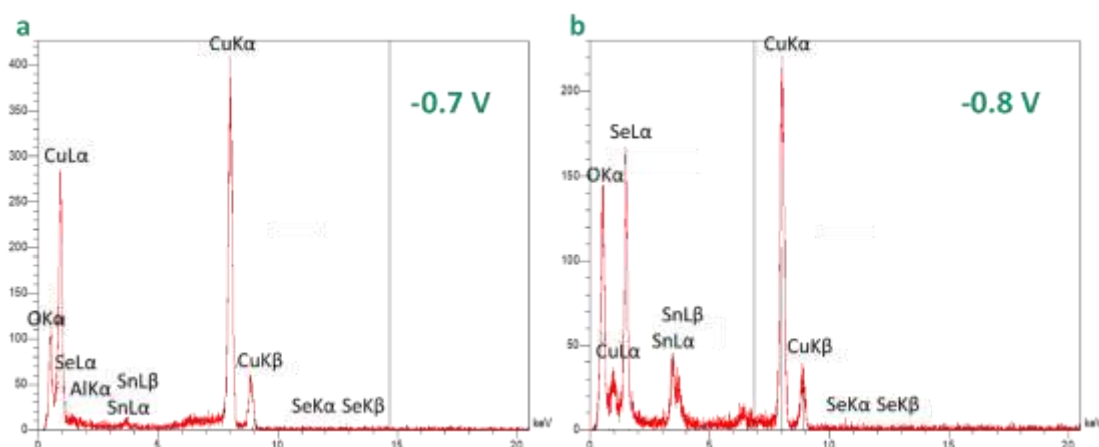


Figure 5.29: EDS spectra on (a) MD19101601 -0.7 V and (b) MD19102102 -0.8 V

4. Raman characterizations

Raman spectroscopy was made on cross section of samples deposited from -0.65 V to -0.8 V vs AgCl/Ag (Figure 5.30). The obtained spectra are similar for all the samples: 4 bands can be attributed to A_g (70 cm^{-1}), B_{3g} (107 cm^{-1}), A_g (125 cm^{-1}) and A_g (151 cm^{-1}) vibration modes of SnSe. The band at 187 cm^{-1} is due to A_{1g} mode of SnSe_2 . On the first hand, we confirm the presence of SnSe at more cathodic potentials, which was not obvious from the XRD and the SEM analyses. On the second hand, the Raman spectra indicate the presence of SnSe_2 , which was not observed by XRD. We can note that the shoulder between the B_{3g} and A_g modes, specifically observable for samples deposited at -0.65 V and -0.7 V vs AgCl/Ag, can be attributed to a vibration mode of SnSe_2 [63]. Moreover, it seems that the peaks are more and more separated and well defined when the deposition potential decreases. It means that there is a modification of the crystallinity with the deposition potential.

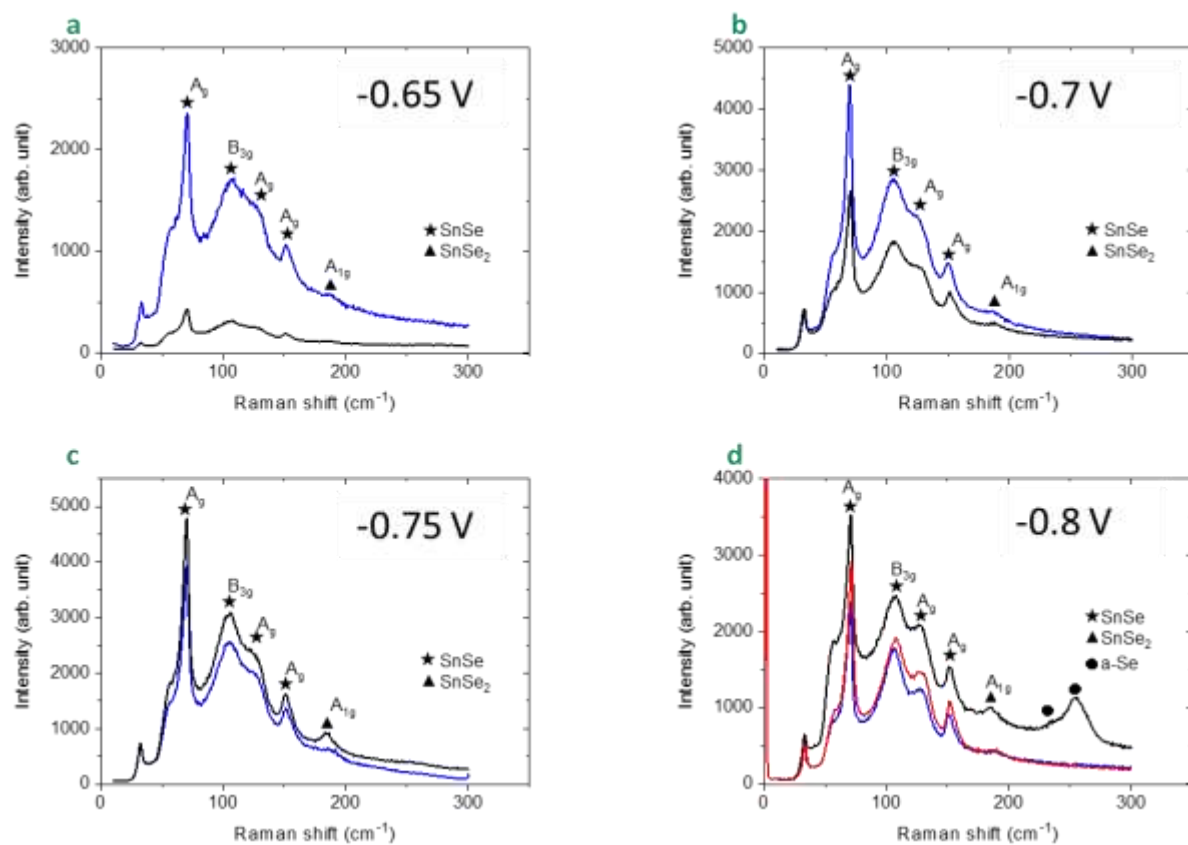


Figure 5.30: Raman spectra recorded on cross section of samples deposited at (a) -0.65 V, (b) -0.7 V, (c) -0.75 V and (d) -0.8 V

Our study revealed that:

- ✓ From the geometry of the used AAO membranes, we can expect nanostructures having a diameter close to 200 nm and a length of 60 μm
- ✓ The real surface of the membranes is around 55 fold higher than the exposed surface due to the metallization process of the membranes
- ✓ The deposition potential window of SnSe is wider and shifted to more negative potentials, namely from -0.65 V to -0.8 V vs AgCl/Ag
- ✓ We can predict, from the chronoamperograms if nanowires or nanotubes were deposited
- ✓ From the shape of the chronoamperograms, the limited coulometric charge and the cross section views, the complete filling of the membranes is rarely reached
- ✓ The deposition rates are faster by separating the counter-electrode
- ✓ The negative current density and the deposition duration generally decrease with the negative applied potential
- ✓ Nanostructures are crystallized according to the orthorhombic phase of SnSe with evolution of the crystallite size depending on Sn appearance
- ✓ SnSe nanotubes are deposited until -0.7 V vs AgCl/Ag and Sn nanowires at more cathodic potentials
- ✓ The deposited nanostructures generally have lengths between 2 and 8 μm
- ✓ The best samples exhibit lengths until 40 μm
- ✓ Nanotubes with higher diameters than expected were observed by TEM
- ✓ The presence of SnSe was confirmed by Raman analysis with the potential presence of SnSe₂
- ✓ An evolution of the Raman spectra with deposition potential is observed. This may be due to an evolution of the crystallinity.

Conclusion

This fifth chapter aimed to study in an introductory way the SnSe nanostructures. In the first part, a review concerning the electrodeposition of tin nanowires was described. As a result, different and non-aqueous media were identified. Moreover, various morphologies were obtained with the template synthesis (alumina membranes). In the second part we reported the few works on the electrodeposition of selenium nanostructures. The obtained nanostructures are dependent, among others, on the temperature and the utilized precursor. Since, to our knowledge, the electrodeposition of SnSe nanowires and/or nanotubes has never been reported, we discussed, in the third part, about the properties obtained via other synthesis methods. Finally, in the fourth and last part, we exposed our first results. It should be underlined that during this thesis, our sputtering device encountered several problems. We highlighted, only in the end of these works, that several membranes suffer from an insufficient metallization. That is the reason why our results sometimes lack reproducibility. Similarly, the electrochemical cell used for the experiments, contributed to this irreproducibility due to its configuration and leaks. Nevertheless, a deposition potential window could be established, starting from -0.6 V vs AgCl/Ag, which appears wider and more cathodic than for the film synthesis. It should be noticed that the nanostructures were deposited by separating the counter-electrode from the electrolyte solution, reducing the duration of the growth experiments. Nevertheless, the membranes were partially filled, whatever the applied experimental conditions. Moreover, we showed an evolution of the nanostructure crystallinity with the applied potential. Similarly, these first results tend to illustrate a tin enrichment towards more cathodic potentials. The analyzes by microscopy indicate the presence of SnSe nanotubes, having larger diameters than those of membrane pores. This can be explained by a partial dissolution of the membranes by our electrolyte solution. Finally, Raman analyzes also reveal the presence of SnSe₂ as potential byproduct.

Ce cinquième chapitre avait pour objectif d'étudier de manière introductive les nanostructures de SnSe. En première partie, une revue concernant l'électrodéposition de nanofils d'étain a été décrite. Il en résulte que des milieux différents et non aqueux ont été utilisés. Par ailleurs, des morphologies diverses ont été obtenues avec la synthèse par matrice (membranes d'alumine). En seconde partie nous avons reporté les quelques travaux relatant de l'électrodéposition de nanostructures de sélénium. Les nanostructures obtenues sont dépendantes entre autres de la température et du précurseur utilisé. Dans la mesure où, à notre connaissance, l'électrodéposition de nanofils et/ou nanotubes de SnSe n'a jamais été reportée, nous avons discuté, en troisième partie, des propriétés

obtenues via d'autres méthodes de synthèse. Enfin, en quatrième et dernière partie, nous avons exposé nos premiers résultats. Il faut souligner qu'au cours de cette thèse, notre appareil de métallisation a rencontré divers problèmes. Ce n'est qu'à la fin de ces travaux qu'il a été mis en évidence que certaines membranes avaient une métallisation insuffisante. C'est pourquoi nos résultats manquent parfois de reproductibilité. De même, la cellule électrochimique utilisée pour les expériences, a contribué à cette faible reproductibilité de par sa configuration et ses fuites. Néanmoins, une fenêtre de potentiels de déposition a pu être établie, partant de -0,6 V vs Ag/AgCl, qui apparaît plus étendue et cathodique que pour la synthèse de films. Il est à noter que les nanostructures ont été déposées en séparant la contre-électrode de la solution électrolytique, réduisant les durées de synthèse. Malgré tout, les membranes n'ont été que partiellement remplies quelles que soient les conditions expérimentales appliquées. Par ailleurs, nous avons montré une évolution de la cristallinité des nanostructures avec le potentiel appliqué. De même, ces premiers résultats tendent à illustrer un enrichissement en étain vers des potentiels plus cathodiques. Les analyses par microscopie indiquent la présence de nanotubes de SnSe, ayant des diamètres plus importants que ceux des pores des membranes. Ceci peut être expliqué par une dissolution partielle des membranes par notre solution électrolytique. Enfin, les analyses Raman révèlent également la présence de SnSe₂ en tant que coproduit.

General conclusion and prospects

This thesis work concerns the SnSe film synthesis by electrodeposition in view of a typical application of a thermoelectric autonomous sensor. Mainly elaborated in bulk shape, thermoelectric materials are more and more studied at lower dimensionality in the aim of decreasing the thermal conductivity. Concerning SnSe, its thermoelectric properties were poorly studied in film form and even less when it was electrodeposited. Having failed to achieve an adequate transfer process to electrical measurements, this thesis manuscript focuses on the synthesis and characterizations, mainly chemical, of SnSe by electrodeposition.

In a first step, after exposing the fundamental principles of thermoelectricity and the expectations concerning SnSe, several physico-chemical properties of SnSe were described. A review of the conventional elaboration methods of SnSe films as well as the obtained physical properties was also written. Based on a state of the art concerning electrodeposition of tin, selenium and of SnSe, an electrochemical bath was defined. It was thus chosen to work in oxalate medium, biodegradable compound, to limit tin(II) hydrolysis. Moreover, using a tin(II) salt instead of tin(IV) contributes to the bath instability but decreases the energetic consumption. The electrodeposition of selenium is also accompanied by side reactions which cause among others apparition of amorphous selenium. An acidic medium and a temperature higher than ambient favor crystallization of selenium. According to the literature, the syntheses were therefore performed at 50 °C with a tin(II) excess.

An instability of the electrolyte, in the long term, was highlighted, associated to the reactivity between tin(II) and selenium(IV). In order to optimize the syntheses, it was decided to gradually incorporate selenium, at a temperature of 30 °C before each electrodeposition procedure. This limits on the first hand the selenium(0) precipitation and oxalate precipitation on the second hand. Nevertheless, this instability is relative and the solution can be stored à 30 °C during 7 days.

A preliminary study to the syntheses was carried out in order to investigate the electrochemical systems of tin and of selenium separately. The complexation between Sn(II) and oxalate was highlighted. A slower diffusion of Se(IV) was determined in comparison with Sn(II). The electrochemical study of the complete electrolyte solution enabled to define a deposition potential window. The morphology and chemical composition of the deposits was studied as a function of the applied potential, in continuous mode. As a result, the best deposits are those deposited between -0.5 and -0.6 V vs AgCl/Ag. Although having an atomic composition close to 1:1, the different characterization techniques show a secondary phase, SnSe₂. The presence of another secondary phase, SeO₂, remains to be confirmed by other characterization techniques. The morphology turned out to

be dependent on the electrodeposition time, as well as the possible separation of the counter-electrode.

In order to improve the quality of the deposits, potentiostatic pulse electrodeposition was studied. The potential exhibiting the best deposits in terms of morphology and chemical composition was chosen during the growth pulses. Two series of experiments were performed with two different relaxation times. The two series revealed an unexpected evolution of the current density with the pulse durations, which has an influence on the morphology and the crystallinity of the deposits. Thus, thinner deposits and including smaller grains are obtained by increasing the pulse duration. Unfortunately, the faradaic yields are not improved in comparison with the continuous mode. The presence of SnSe_2 is confirmed and oxygen seems to be more abundant. Thus, the pulse conditions need to be more optimized. Nevertheless, it should be underlined that the experiments in pulse mode were done with limited and lower coulometric charge quantities than in continuous mode. Therefore, this feature should be improved in the future. Values of gaps are relatively close to the literature. First trials to doping by copper were carried out. Although adding copper increases the solution instability, the first trials are encouraging and show an influence of the copper concentration on the morphology of the deposits.

This thesis manuscript is the first work, regarding the literature, to pay attention to the electrodeposition of SnSe nanowires and nanotubes. That is the reason why a review concerning the electrodeposition of tin and selenium nanostructures was firstly realized. The methods already utilized to synthesize SnSe nanostructures as well as their properties were reported. The electrodeposition of SnSe nanostructures was then performed in continuous mode. Despite problems related to the metallization (Figure 5.31) and the electrochemical setup, SnSe nanostructures were obtained. Their crystallinity has proved to be dependent on the deposition potential. In addition, tin nanowires were also observed at more cathodic potentials. In order to overcome the encountered difficulties as well as lack of reproducibility, another configuration is envisaged, similar to that of films (Figure 2.11). The metallized face of the membrane would be attached on a glass slide through the use of double-sided copper tape. First tests show the usefulness of pre-depositing few hundreds nm of silver, in order to improve the crystallinity and the growth front of the SnSe nanostructures by reducing the hydrogen evolution reaction. The first trials are encouraging.

A key point of this thesis should concern the measurement of thermoelectric properties of SnSe films. Despite several unsuccessful trials, the deposits were either too cracked to be measured, or too adherent to be detached. The measurement of the electrical properties requiring either a self-standing film, or on a non-conductive substrate, it is important to find a new transfer method. An

alternative consists in electrodepositing the material of interest on a conductive polymer. When detached, the whole constitutes in a hybrid film whose thermoelectric properties are very interesting. First trials, using PEDOT-PSS as conductive polymer, were carried out and show the feasibility of electrodepositing SnSe. Another option would consist in using a metal as conductive substrate, having a melting temperature lower than that of SnSe, in order to detach it without risk of degrading it.

Conclusion générale et perspectives

Ce travail de thèse concerne la synthèse de films de SnSe par électrodéposition en vue d'une application de type capteur autonome thermoélectrique. Principalement élaborés sous forme massive, les matériaux thermoélectriques sont de plus en plus étudiés à plus faible dimensionalité dans un objectif de diminution de la conductivité thermique. Concernant SnSe, ses propriétés thermoélectriques n'ont été que peu étudiées sous forme de films et encore moins lorsque celui-ci était électrodéposé. N'ayant pu parvenir à un procédé de transfert adéquat aux mesures électriques, ce mémoire de thèse se focalise sur la synthèse et les caractérisations, principalement chimiques, de SnSe par électrodéposition.

Dans un premier temps, après avoir exposé les principes fondamentaux de la thermoélectricité et les attentes concernant SnSe, quelques propriétés physico-chimiques de SnSe ont été décrites. Une revue des méthodes d'élaborations conventionnelles de films de SnSe ainsi que les propriétés physiques obtenues a été également rédigée. Sur la base d'un état de l'art concernant l'électrodéposition de l'étain, du sélénium et de SnSe, un bain électrochimique a été défini. Il a ainsi été choisi de travailler en milieu oxalate, composé biodégradable, afin de limiter l'hydrolyse de l'étain(II). Par ailleurs, utiliser un sel d'étain(II) au lieu d'étain(IV) contribue à l'instabilité du bain mais diminue la consommation énergétique. L'électrodéposition du sélénium s'accompagne également de réactions secondaires qui provoquent entre autres l'apparition de sélénium amorphe. Un milieu acide et une température supérieure à celle de l'ambiante favorisent la cristallisation du sélénium. En accord avec la littérature, les synthèses ont donc été effectuées à 50 °C avec un excès d'étain(II).

Une instabilité de l'électrolyte, sur le long terme, a été mise en évidence, associée à la réactivité entre l'étain(II) et le sélénium(IV). Afin d'optimiser les synthèses, il a été décidé d'incorporer graduellement le sélénium, à une température de 30 °C avant chaque procédure d'électrodéposition. Ceci limite d'une part la précipitation du sélénium(0) et d'autre part la précipitation d'oxalate. Néanmoins, cette instabilité est relative et la solution peut être conservée à 30 °C durant 7 jours.

Une étude préalable aux synthèses a été menée afin d'étudier les systèmes électrochimiques de l'étain et du sélénium séparément. La complexation entre l'étain(II) et l'oxalate a été mise en évidence. Une diffusion plus lente du sélénium(IV) par rapport à l'étain a été déterminée. L'étude électrochimique de la solution électrolytique complète a permis de définir une fenêtre de potentiels de déposition. La morphologie et la composition chimique des dépôts a été étudiée en fonction du potentiel appliqué, en mode continu. Il en résulte que les meilleurs dépôts sont ceux déposés entre -0,5 et -0,6 V vs Ag/AgCl. Bien qu'ayant une composition atomique de l'ordre de 1:1, les différentes

techniques de caractérisations montrent une phase secondaire, SnSe_2 . La présence d'une autre phase secondaire, SeO_2 , reste à confirmer par d'autres techniques de caractérisation. La morphologie s'est avérée dépendante du temps d'électrodéposition, ainsi que la séparation éventuelle de la contre-électrode.

Afin d'améliorer la qualité des dépôts, l'électrodéposition en mode impulsionnel potentiostatique a été étudié. Le potentiel affichant les meilleurs dépôts en termes de morphologie et composition chimique a été choisi pendant les pulses de croissance. Deux séries d'expériences ont été menées avec deux temps de relaxation différents. Les deux séries ont révélé une évolution inattendue de la densité de courant avec les temps de pulse, ce qui influe sur la morphologie et la cristallinité des dépôts. Ainsi, des dépôts plus fins et contenant des grains plus petits sont obtenus pour des durées de pulse croissantes. Malheureusement, les rendements faradiques ne sont pas améliorés par rapport au mode continu. La présence de SnSe_2 est confirmée et l'oxygène semble être plus abondant. Les conditions impulsionnelles nécessitent donc d'être plus amplement optimisées. Il faut néanmoins souligner que les expériences en mode impulsionnel ont été menées pour des quantités de charges coulométriques limitées et plus faibles que celles en mode continu. Par conséquent, cette caractéristique devra être améliorée à l'avenir. Des valeurs de largeurs de bandes interdites sont relativement proches de la littérature. Des premiers essais de dopage au cuivre ont été effectués. Bien que l'ajout de cuivre augmente l'instabilité de la solution, les premiers essais sont encourageants et montrent une influence de la concentration de cuivre sur la morphologie des dépôts.

Ce mémoire de thèse est le premier travail, au regard de la littérature, à s'intéresser à l'électrodéposition de nanofils et de nanotubes de SnSe . C'est pourquoi une revue concernant l'électrodéposition de nanostructures d'étain et de sélénium a été tout d'abord réalisée. Les méthodes déjà utilisées pour synthétiser les nanostructures de SnSe ainsi que leur propriétés ont été reportées. L'électrodéposition de nanostructures de SnSe a ensuite été menée en mode continu. Malgré des problèmes liés à la métallisation (Figure 5.31) et au dispositif électrochimique, des nanostructures de SnSe ont été obtenues. Leur cristallinité s'avère dépendante du potentiel de déposition. De plus, des nanofils d'étain ont également été observés aux potentiels plus cathodiques. Afin de pallier les difficultés rencontrées ainsi que le manque de reproductibilité, une autre configuration est envisagée, analogue à celle des films (Figure 2.11). La face métallisée de la membrane serait fixée sur une lame de verre via un scotch double face en cuivre. Des premiers essais montrent l'utilité de pré-déposer quelques centaines de nm d'argent, afin de diminuer la co-réduction du solvant et ainsi d'améliorer la cristallinité et le front de croissance des nanostructures de SnSe . Les premiers essais sont encourageants.

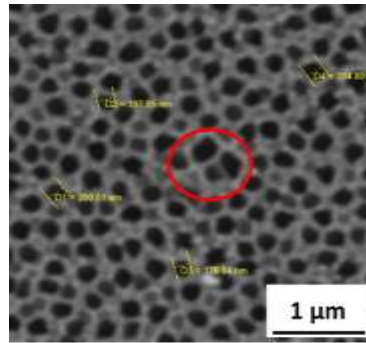


Figure 5.31: Image MEB de dessus d'une membrane illustrant la métallisation incomplète

Un point clé de cette thèse devait concerner la mesure des propriétés thermoélectriques des films de SnSe. Malgré plusieurs tentatives infructueuses, les dépôts se sont avérés soit trop fissurés pour être mesuré, soit trop adhérents pour être détachés. La mesure des propriétés électriques nécessitant soit que le film soit autosupporté, soit sur un substrat non conducteur, il est important de trouver une nouvelle méthode de transfert. Une alternative consiste à électrodéposer le matériau d'intérêt sur un polymère conducteur. Une fois détaché, l'ensemble constitue un film hybride dont les propriétés thermoélectriques sont très intéressantes. Des premiers tests, en utilisant le PEDOT-PSS comme polymère conducteur, ont été effectués et montrent la faisabilité de l'électrodéposition de SnSe. Une autre option consisterait à utiliser comme substrat conducteur un métal dont la température de fusion serait plus basse que celle de SnSe afin de le détacher sans risquer de le dégrader.

Appendices

Appendix 1.

Pattern: COD 1537675 Radiation: 1,54060 Quality: Qualité inconnue

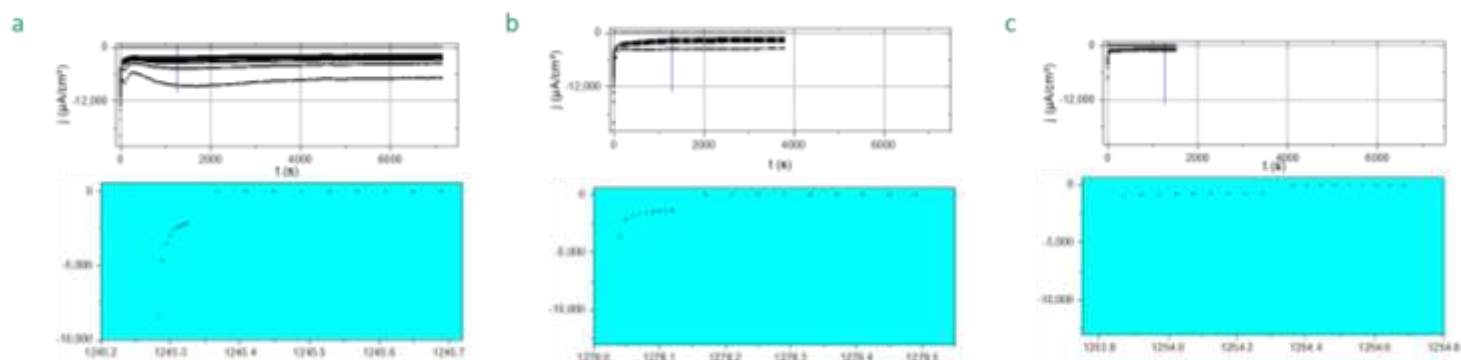
Formula Name Name (mineral) Name (common) Status Ambient		SeSn Statut inconnu Yes															
Lattice: S.G.:		Orthorhombique P n m a (62)		Mol. weight = Volume [CD] = 211,27 Dx = Dm = l/lcor = 8,380													
a = 11,37000 b = 4,18600 c = 4,43900 a/b = 2,71620 c/b = 1,06044		Z = 4															
		</															

Pattern: COD 1537675 Radiation: 1,54060 Quality: Qualité inconnue

Formula Name Name (mineral) Name (common) Status Ambient			SeSn Statut inconnu Yes																	
Lattice: S.G.:			Orthorhombique P n m a (62)			Mol. weight = Volume [CD] = 211,27 Dx = Dm = l/lcor = 8,380														
a = 11,37000 b = 4,18600 c = 4,43900 a/b = 2,71620 c/b = 1,06044			Z = 4																	
Référence primaire Chattopadhyay T.K., Pannetier J., von Schnering H.G., "Neutron diffraction study of the structural phase transition in Sn S and Sn Se", Journal of Physics and Chemistry of Solids 47 (1986) 879-885.						d	2θ	I	h	k	l	d	2θ	I	h	k	l			
						1,32210	71,272	147	-1	-3	-1	1,12360	86,560	8	-6	-3	0			
						1,31250	71,874	5	-4	0	-3	1,11190	87,701	6	-4	-2	-3			
						1,31080	71,982	41	-7	0	-2	1,11090	87,800	53	-7	-2	-2			
						1,28790	73,469	42	-8	-1	-1	1,10450	88,441	16	-1	0	-4			
						1,26530	75,004	49	-5	-2	-2	1,10140	88,755	11	-10	0	-1			
						1,25590	75,664	90	-3	-3	-1	1,09790	89,113	11	-9	0	-2			
						1,25260	75,898	12	-4	-3	0	1,09720	89,185	19	-10	-1	0			
						1,25240	75,912	139	-4	-1	-3	1,09380	89,537	25	-7	0	-3			
						1,25090	76,020	12	-7	-1	-2	1,09080	89,850	11	-4	-3	-2			
						1,24020	76,794	8	-5	0	-3	1,06800	92,316	6	-1	-1	-4			
						1,23270	77,348	8	-7	-2	-1	1,06700	92,428	9	-5	-2	-3			
						1,21510	78,683	44	-9	0	-1	1,06500	92,653	14	-3	0	-4			
						1,20550	79,433	40	-4	-3	-1	1,06200	92,993	59	-9	-1	-2			
						1,20150	79,750	35	-1	-2	-3	1,05830	93,415	6	-7	-1	-3			
						1,19690	80,118	23	-8	0	-2	1,05410	93,901	134	-2	-1	-4			
						1,18910	80,752	20	-5	-1	-3	1,05080	94,287	62	-9	-2	-1			
						1,18700	80,924	13	-6	-2	-2	1,04830	94,582	40	-5	-3	-2			
						1,18180	81,355	50	-2	-2	-3	1,04650	94,796	48	0	-4	0			
1,17580	81,859	81	-8	-2	0	1,03900	95,699	32	-8	-2	-2									
1,17500	81,926	33	-1	-3	-2	1,02960	96,862	29	-7	-3	-1									
1,16690	82,619	84	-9	-1	-1	1,02500	97,443	9	-8	0	-3									
1,16630	82,671	26	-6	0	-3	1,01880	98,241	41	-6	-2	-3									
1,15660	83,519	8	-2	-3	-2	1,01520	98,711	47	0	-3	-3									
1,15110	84,009	49	-3	-2	-3	1,01190	99,147	9	-10	0	-2									
1,15080	84,035	36	-8	-1	-2	1,01110	99,254	6	-1	-3	-3									
1,14880	84,215	105	-5	-3	-1															
1,13660	85,332	6	-8	-2	-1															
1,12780	86,159	16	-3	-3	-2															
Wavelength: h:			1,54060			Filter: d-spacing:			Non spécifié											
SS/FOM:																				

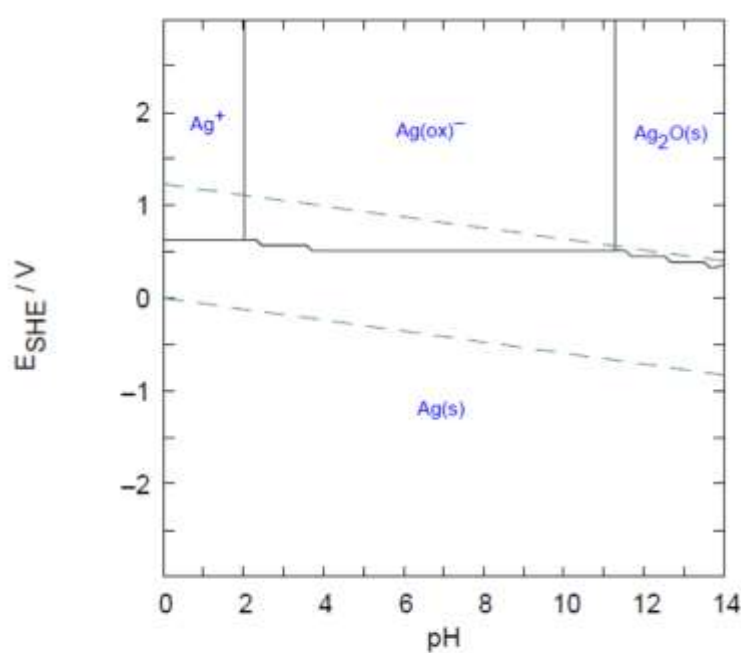
SnSe COD card n°1537675

Appendix 2.



Chronoamperometric curves of samples deposited with a t_{OFF} of 400 ms and t_{ON} of: (a) 50 ms, (b) 100 ms and (c) 500 ms

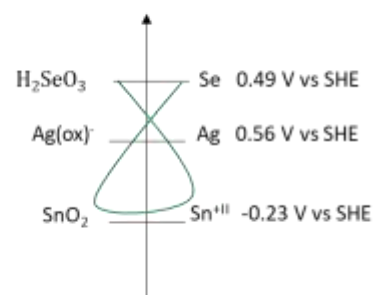
Appendix 3.



$[Ag^+] = 2 \text{ mM}$
 $[Na_2C_2O_4] = 0.2 \text{ M}$
 $[Cl^-] = 0.2 \text{ M}$

At pH=2.5

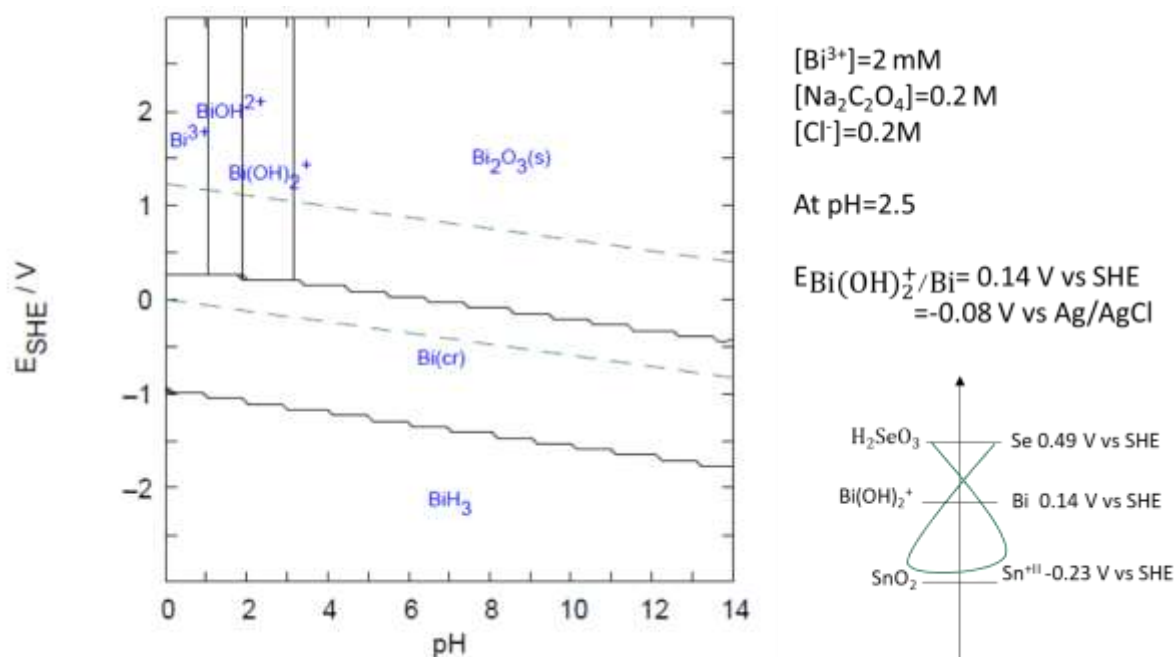
$E_{Ag(ox)^-/Ag} = 0.56 \text{ V vs SHE}$
 $= 0.34 \text{ V vs Ag/AgCl}$



$K_S = 5.40 \times 10^{-12} / 3.5 \times 10^{-11}$ (ars-chemia.net) for $Ag_2(ox)$ against 1.77×10^{-10} for AgCl

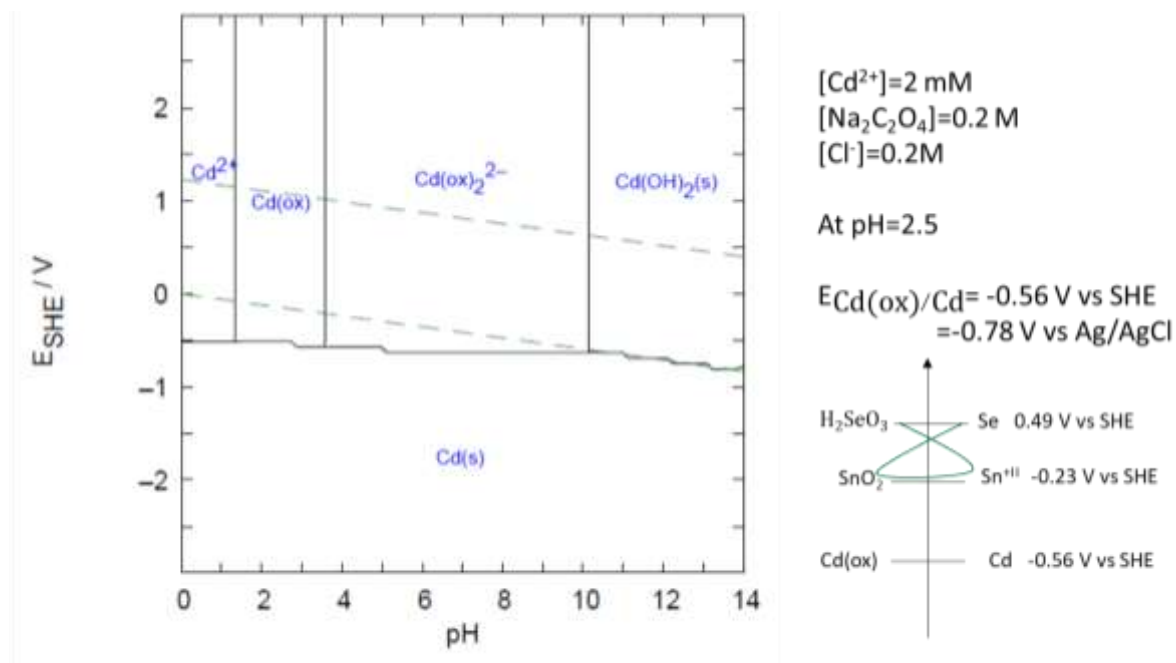
Calculated Pourbaix diagram of Ag

Appendix 4.



Calculated Pourbaix diagram of Bi

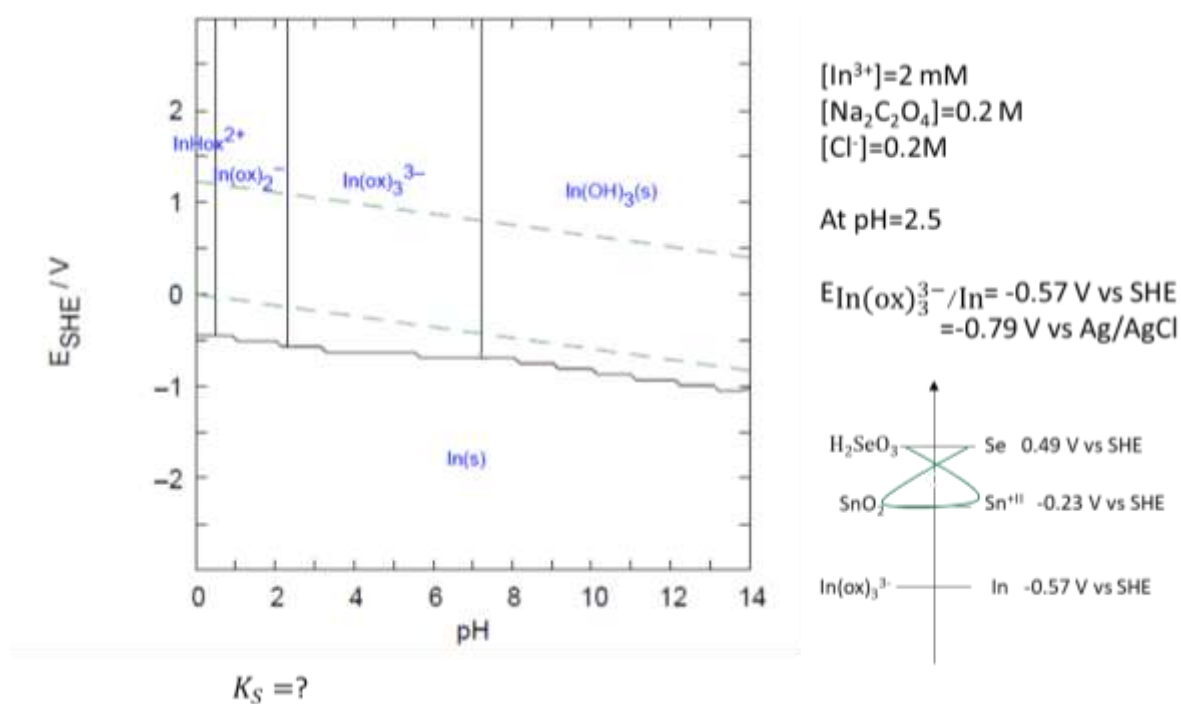
Appendix 5.



$K_S = 1.42 \times 10^{-8} / 9.1 \times 10^{-8}$ (Zeng et al. 2020) for $Cd(ox).3H_2O$ and 2.32×10^{-9} for $Cd(ox).H_2O$

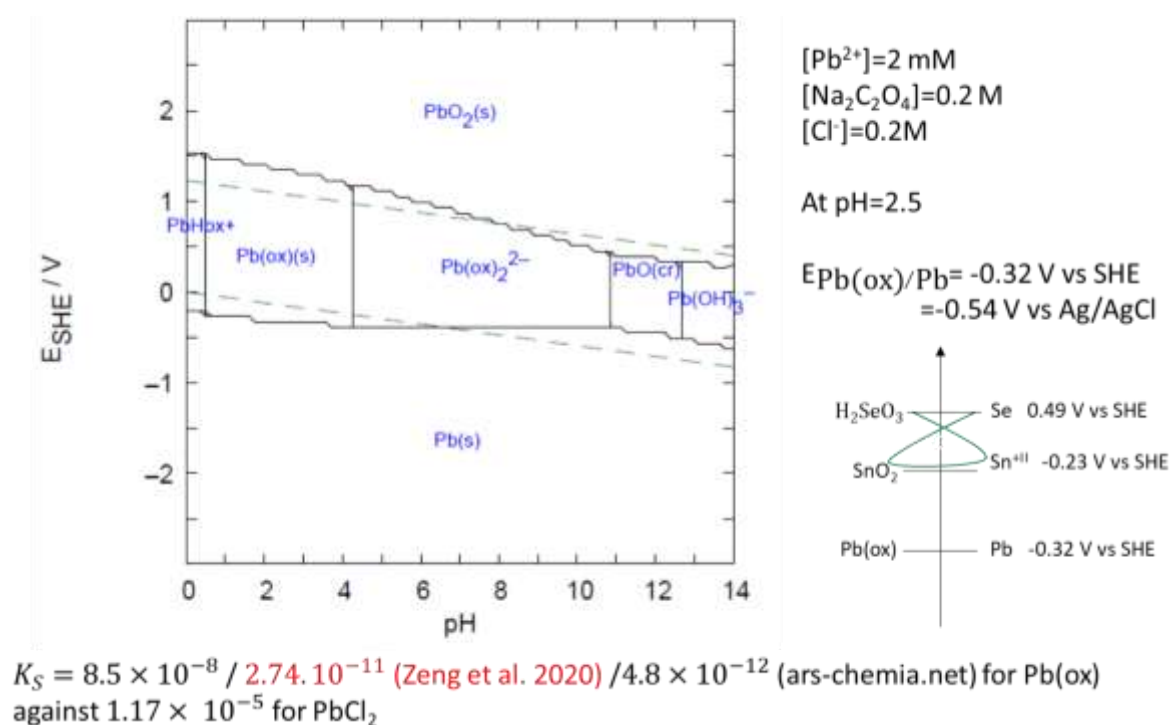
Calculated Pourbaix diagram of Cd

Appendix 6.



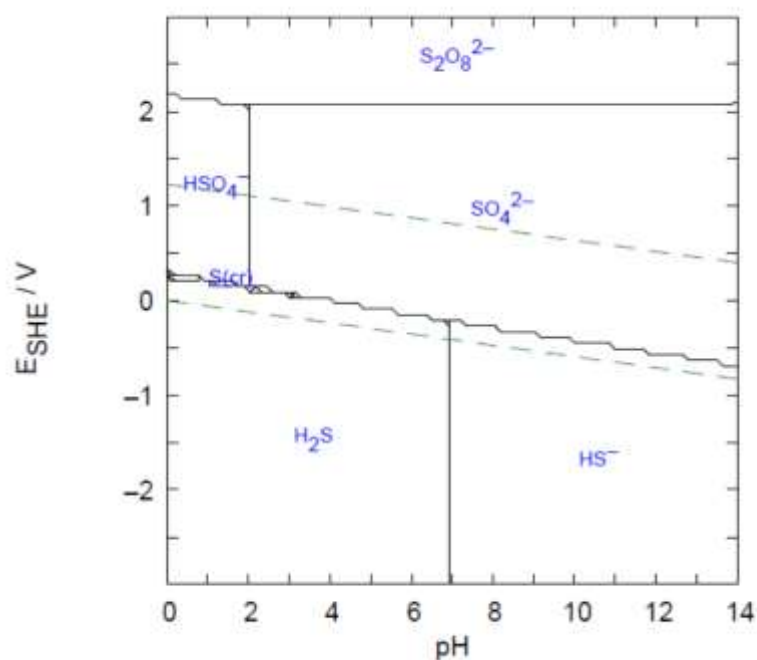
Calculated Pourbaix diagram of In

Appendix 7.



Calculated Pourbaix diagram of Pb

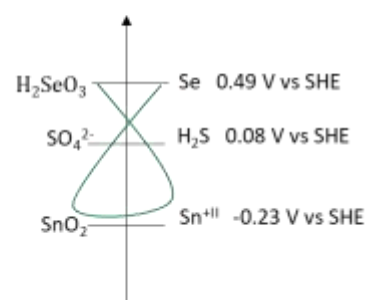
Appendix 8.



$[SO_4^{2-}] = 0.5 \text{ mM}$
 $[Na_2C_2O_4] = 0.2 \text{ M}$
 $[Cl^-] = 0.2 \text{ M}$

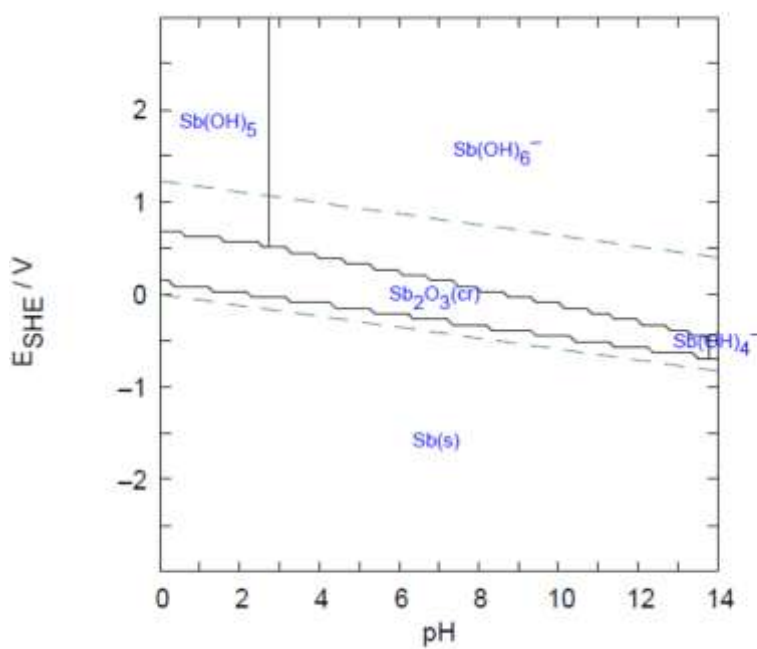
At pH=2.5

$E_{SO_4^{2-}/H_2S} = 0.08 \text{ V vs SHE}$
 $= -0.14 \text{ V vs Ag/AgCl}$



Calculated Pourbaix diagram of S

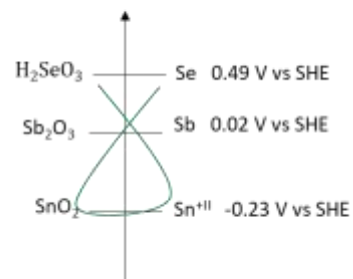
Appendix 9.



$[Sb(OH)_3] = 2 \text{ mM}$
 $[Na_2C_2O_4] = 0.2 \text{ M}$
 $[Cl^-] = 0.2 \text{ M}$

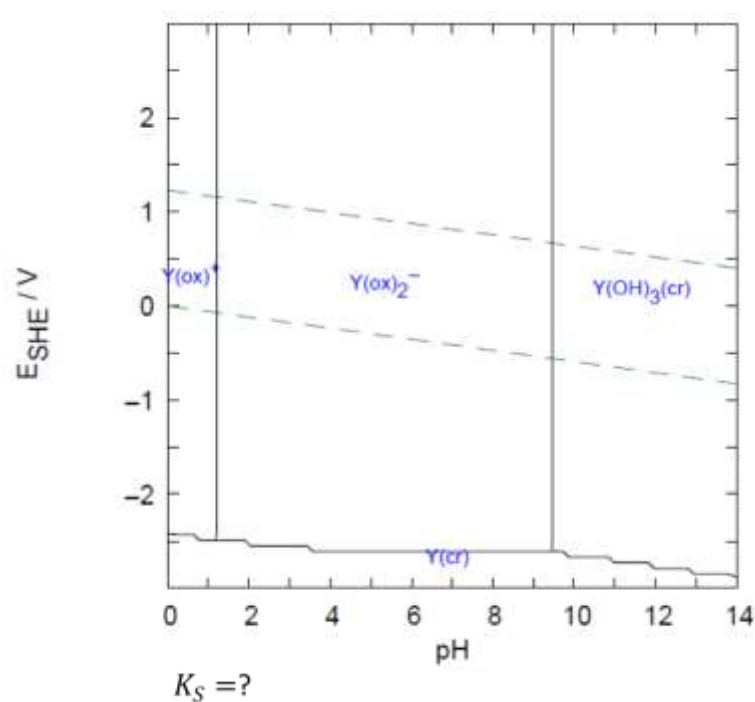
At pH=2.5

$E_{Sb_2O_3/Sb} = 0.02 \text{ V vs SHE}$
 $= -0.20 \text{ V vs Ag/AgCl}$



Calculated Pourbaix diagram of Sb

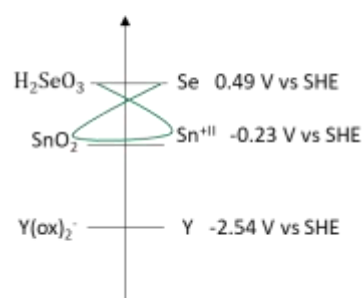
Appendix 10.



$[Y^{3+}] = 2 \text{ mM}$
 $[Na_2C_2O_4] = 0.2 \text{ M}$
 $[Cl^-] = 0.2 \text{ M}$

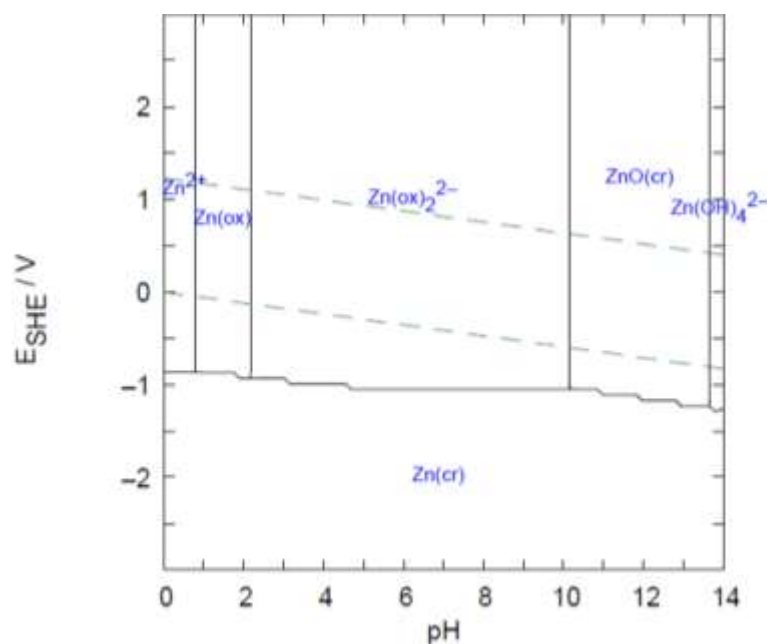
At pH=2.5

$E_{Y(ox)_2^-/Y} = -2.54 \text{ V vs SHE}$
 $= -2.76 \text{ V vs Ag/AgCl}$



Calculated Pourbaix diagram of Y

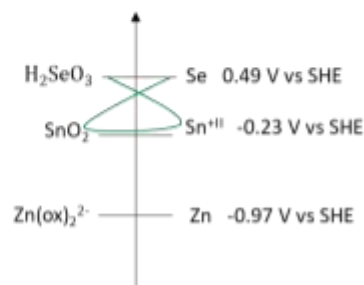
Appendix 11.



$[Zn^{2+}] = 2 \text{ mM}$
 $[Na_2C_2O_4] = 0.2 \text{ M}$
 $[Cl^-] = 0.2 \text{ M}$

At pH=2.5

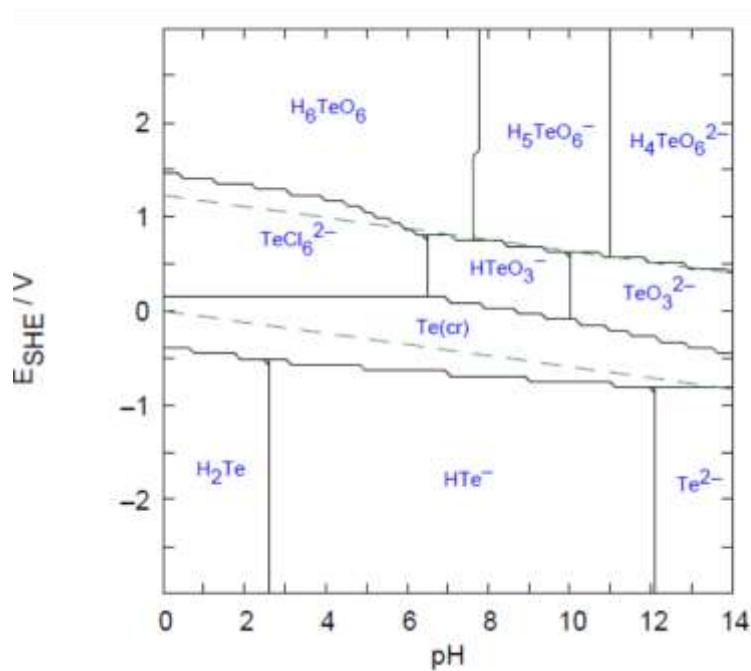
$E_{Zn(ox)_2^{2-}/Zn} = -0.97 \text{ V vs SHE}$
 $= -1.19 \text{ V vs Ag/AgCl}$



$K_S = 1.38 \times 10^{-9}$ for $Zn(ox) \cdot 2H_2O$ (Zeng et al. 2020) / 2.7×10^{-8} (ars-chemia.net)

Calculated Pourbaix diagram of Zn

Appendix 12.



$[H_2TeO_3]=0.5 \text{ mM}$

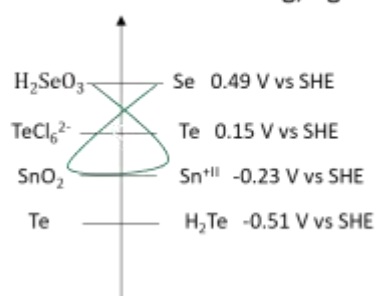
$[Na_2C_2O_4]=0.2 \text{ M}$

$[Cl^-]=0.2 \text{ M}$

At pH=2.5

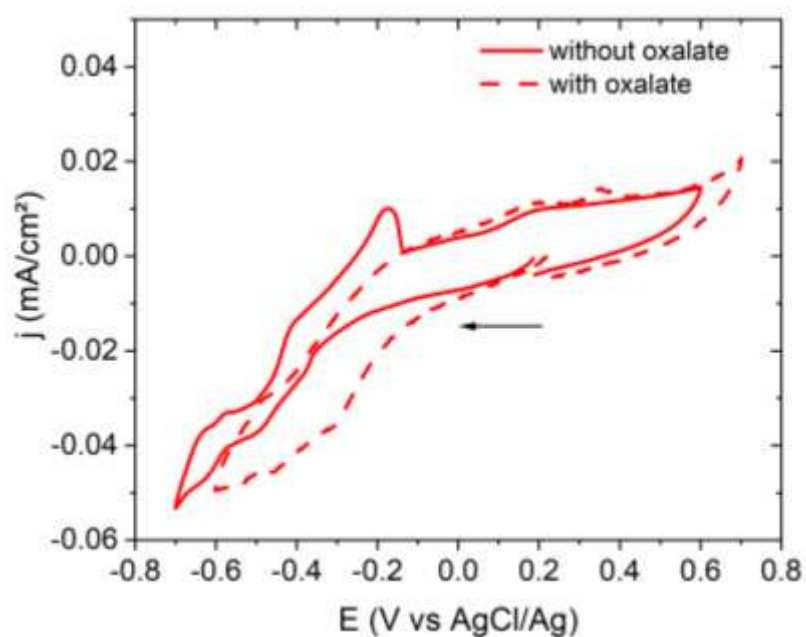
$E_{TeCl_6^{2-}/Te} = 0.15 \text{ V vs SHE}$
 $= -0.07 \text{ V vs Ag/AgCl}$

$E_{Te/H_2Te} = -0.51 \text{ V vs SHE}$
 $= -0.73 \text{ V vs Ag/AgCl}$



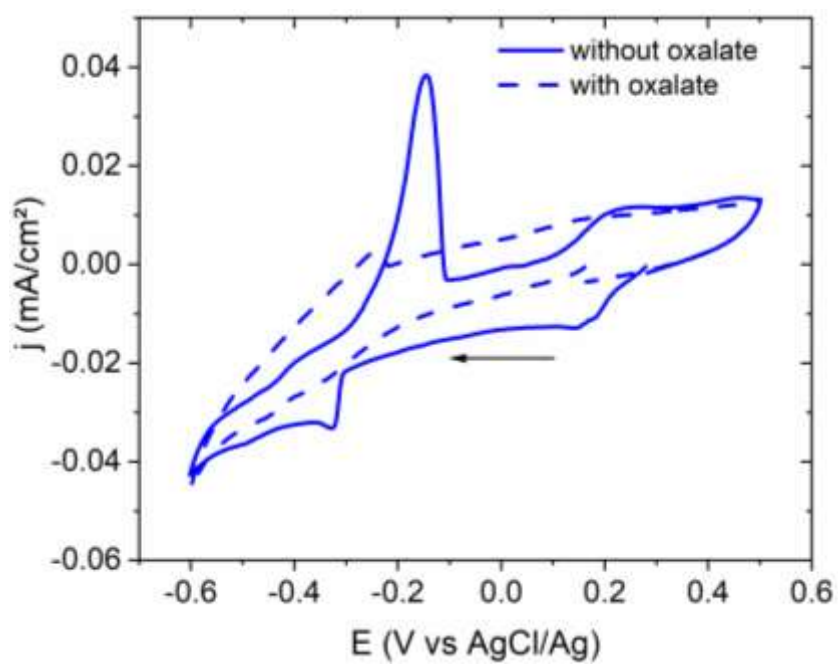
Calculated Pourbaix diagram of Te

Appendix 13.



CV experiments on GC electrode, at 50 °C, on the electrolyte solution containing KCl 0.2 M and $CoCl_2 \cdot 6H_2O$ 2 mM

Appendix 14.



CV experiments on GC electrode, at 50 °C, on the electrolyte solution containing KCl 0.2 M and $\text{NiCl}_2 \cdot 2\text{H}_2\text{O}$ 2 mM

References

All internet references were consulted between February 1st 2018 and April 30th 2021

- [1] D. Champier, in *Tech. Ing.*, **2018**, p. 31.
- [2] <http://corporate.renault-trucks.com/fr/les-communiqués/recuperer-la-chaleur-des-gaz-d-echappement-pour-reduire-la-consommation.html>
- [3] W. Liu, Q. Jie, H. S. Kim, Z. Ren, *Acta Mater.* **2015**, 87, 357.
- [4] J.-H. Bahk, H. Fang, K. Yazawa, A. Shakouri, *J. Mater. Chem. C* **2015**, 3, 10362.
- [5] <https://www.azocleantech.com/article.aspx?ArticleID=987>
- [6] F. Q. Wang, S. Zhang, J. Yu, Q. Wang, *Nanoscale* **2015**, 7, 15962.
- [7] E. Alleno, *Introduction course to thermoelectricity*, **2017**.
- [8] J. He, T. M. Tritt, *Science* **2017**, 357, 1369.
- [9] D. M. Rowe, *CRC Handbook of Thermoelectrics*, CRC Press, **1995**.
- [10] G. J. Snyder, E. S. Toberer, *Nat. Mater.* **2008**, 7, 105.
- [11] D. K. Aswal, R. Basu, A. Singh, *Energy Convers. Manag.* **2016**, 114, 50.
- [12] Z.-H. Ge, L.-D. Zhao, D. Wu, X. Liu, B.-P. Zhang, J.-F. Li, J. He, *Mater. Today* **2016**, 19, 227.
- [13] A. A. Olvera, N. A. Moroz, P. Sahoo, P. Ren, T. P. Bailey, A. A. Page, C. Uher, P. F. P. Poudeu, *Energy Environ. Sci.* **2017**, 10, 1668.
- [14] W. Shi, M. Gao, J. Wei, J. Gao, C. Fan, E. Ashalley, H. Li, Z. Wang, *Adv. Sci.* **2018**, 5, 1700602.
- [15] B. Subramanian, T. Mahalingam, C. Sanjeeviraja, M. Jayachandran, M. J. Chockalingam, *Thin Solid Films* **1999**, 357, 119.
- [16] L.-D. Zhao, S.-H. Lo, Y. Zhang, H. Sun, G. Tan, C. Uher, C. Wolverton, V. P. Dravid, M. G. Kanatzidis, *Nature* **2014**, 508, 373.
- [17] X.-L. Shi, W.-Y. Chen, X. Tao, J. Zou, Z.-G. Chen, *Mater. Horiz.* **2020**, 7, 3065.
- [18] X.-L. Shi, X. Tao, J. Zou, Z.-G. Chen, *Adv. Sci.* **2020**, 7, 1902923.
- [19] R. E. Abutbul, E. Segev, S. Samuha, L. Zeiri, V. Ezersky, G. Makov, Y. Golan, *CrystEngComm* **2016**, 18, 1918.
- [20] X. Guan, P. Lu, L. Wu, L. Han, G. Liu, Y. Song, S. Wang, *J. Alloys Compd.* **2015**, 643, 116.
- [21] S. Sassi, C. Candolfi, J.-B. Vaney, V. Ohorodniichuk, P. Masschelein, A. Dauscher, B. Lenoir, *Appl. Phys. Lett.* **2014**, 104, 212105.
- [22] E. Barrios-Salgado, M. T. S. Nair, P. K. Nair, *Thin Solid Films* **2016**, 598, 149.
- [23] M. Biçer, İ. Şişman, *Appl. Surf. Sci.* **2011**, 257, 2944.
- [24] R. D. Engelken, A. K. Berry, T. P. Van Doren, J. L. Boone, A. Shahnazary, *J. Electrochem. Soc.* **1986**, 133, 581.

- [25] D. T. Quan, *Phys. Status Solidi A* **1984**, 86, 421.
- [26] D. Martínez-Escobar, M. Ramachandran, A. Sánchez-Juárez, J. S. Narro Rios, *Thin Solid Films* **2013**, 535, 390.
- [27] E. M. El-Menyawy, A. A. Azab, L. M. El-Khalawany, N. Okasha, F. S. Terra, *J. Mater. Sci. Mater. Electron.* **2018**, 29, 8354.
- [28] B. Pejova, I. Grozdanov, *Thin Solid Films* **2007**, 515, 5203.
- [29] H. Y. He, *JOM* **2015**, 67, 2071.
- [30] K. Ananthi, K. Thilakavathy, N. Muthukumarasamy, S. Dhanapandian, K. R. Murali, *J. Mater. Sci. Mater. Electron.* **2012**, 23, 1338.
- [31] D. Shikha, V. Mehta, J. Sharma, R. P. Chauhan, *J. Mater. Sci. Mater. Electron.* **2017**, 28, 2487.
- [32] S. Yang, Y. Liu, M. Wu, L.-D. Zhao, Z. Lin, H. Cheng, Y. Wang, C. Jiang, S.-H. Wei, L. Huang, Y. Huang, X. Duan, *Nano Res.* **2018**, 11, 554.
- [33] G. Shi, E. Kioupakis, *Nano Lett.* **2015**, 15, 6926.
- [34] R. Fei, W. Li, J. Li, L. Yang, *Appl. Phys. Lett.* **2015**, 107, 173104.
- [35] I. Lefebvre, M. A. Szymanski, J. Olivier-Fourcade, J. C. Jumas, *Phys. Rev. B* **1998**, 58, 1896.
- [36] F. K. Butt, M. Mirza, C. Cao, F. Idrees, M. Tahir, M. Safdar, Z. Ali, M. Tanveer, I. Aslam, *CrystEngComm* **2014**, 16, 3470.
- [37] L. Li, Z. Chen, Y. Hu, X. Wang, T. Zhang, W. Chen, Q. Wang, *J. Am. Chem. Soc.* **2013**, 135, 1213.
- [38] M. A. Franzman, C. W. Schlenker, M. E. Thompson, R. L. Brutchey, *J. Am. Chem. Soc.* **2010**, 132, 4060.
- [39] G. Zhang, W. Luo, Q. Qin, Y. Liu, C. Jin, J. Hao, J. Zhang, W. Zheng, *CrystEngComm* **2018**, 20, 1141.
- [40] B. Xu, J. Zhang, G. Yu, S. Ma, Y. Wang, L. Yi, *J. Electron. Mater.* **2016**, 45, 5232.
- [41] G. Shi, E. Kioupakis, *J. Appl. Phys.* **2015**, 117, 065103.
- [42] T. Koga, *Concept and Applications of Carrier Pocket Engineering to Design Useful Thermoelectric Materials Using Superlattice Structures*, Harvard University, **2001**.
- [43] S. Lv, Z.-H. Ge, Y.-X. Chen, K. Zhao, J. Feng, J. He, *RSC Adv* **2016**, 6, 92335.
- [44] S. Sassi, C. Candolfi, J.-B. Vaney, V. Ohorodniichuk, P. Masschelein, A. Dauscher, B. Lenoir, *Mater. Today Proc.* **2015**, 2, 690.
- [45] G. Tang, Q. Wen, T. Yang, Y. Cao, W. Wei, Z. Wang, Z. Zhang, Y. Li, *RSC Adv* **2017**, 7, 8258.
- [46] L. D. Hicks, M. S. Dresselhaus, *Phys. Rev. B* **1993**, 47, 16631.
- [47] M. M. Rojo, B. Abad, C. V. Manzano, P. Torres, X. Cartoixà, F. X. Alvarez, M. M. Gonzalez, *Nanoscale* **2017**, 9, 6741.
- [48] P. Al-Alam, G. Pernot, M. Isaiev, D. Lacroix, M. De Vos, N. Stein, D. Osenberg, L. Philippe, *Phys. Rev. B* **2019**, 100, 115304.

- [49] M. R. Burton, T. Liu, J. McGettrick, S. Mehraban, J. Baker, A. Pockett, T. Watson, O. Fenwick, M. J. Carnie, *Adv. Mater.* **2018**, *30*, 1801357.
- [50] V. R. Minnam Reddy, S. Gedi, B. Pejja, C. Park, *J. Mater. Sci. Mater. Electron.* **2016**, *27*, 5491.
- [51] C. H. Suen, D. Shi, Y. Su, Z. Zhang, C. H. Chan, X. Tang, Y. Li, K. H. Lam, X. Chen, B. L. Huang, X. Y. Zhou, J.-Y. Dai, *J Materiomics* **2017**, *3*, 293.
- [52] S. Saini, P. Mele, A. Tiwari, *J. Phys. Chem. Solids* **2019**, *129*, 347.
- [53] R. Teghil, A. Giardini-Guidoni, A. Mele, S. Piccirillo, G. Pizzella, V. Marotta, *Thin Solid Films* **1994**, *241*, 126.
- [54] V. E. Drozd, I. O. Nikiforova, V. B. Bogevoznov, A. M. Yafyasov, E. O. Filatova, D. Papazoglou, *Appl Phys* **2009**, *42*, 125306.
- [55] Z. Wang, J. Wang, Y. Zang, Q. Zhang, J.-A. Shi, T. Jiang, Y. Gong, C.-L. Song, S.-H. Ji, L.-L. Wang, L. Gu, K. He, W. Duan, X. Ma, X. Chen, Q.-K. Xue, *Adv. Mater.* **2015**, *27*, 4150.
- [56] J. P. Singh, R. K. Bedi, *J Appl Phys* **1990**, *68*, 5.
- [57] X.-Z. Li, J. Xia, L. Wang, Y.-Y. Gu, H.-Q. Cheng, X.-M. Meng, *Nanoscale* **2017**, *9*, 14558.
- [58] W. Gao, Y. Li, J. Guo, M. Ni, M. Liao, H. Mo, J. Li, *Nanoscale* **2018**, *10*, 8787.
- [59] K. S. Urmila, T. A. Namitha, J. Rajani, R. R. Philip, B. Pradeep, *J. Semicond.* **2016**, *37*, 093002.
- [60] K. J. John, B. Pradeep, E. Mathai, *J. Mater. Sci.* **1994**, *29*, 1581.
- [61] G. H. Chandra, J. N. Kumar, N. M. Rao, S. Uthanna, *J. Cryst. Growth* **2007**, *306*, 68.
- [62] N. Sabli, Z. A. Talib, W. M. M. Yunus, Z. Zainal, H. S. Hilal, M. Fujii, *Electrochemistry* **2014**, *82*, 25.
- [63] P. A. Fernandes, M. G. Sousa, P. M. P. Salomé, J. P. Leitão, A. F. da Cunha, *CrystEngComm* **2013**, *15*, 10278.
- [64] C. R. Baxter, W. D. McLennan, *J. Vac. Sci. Technol.* **1975**, *12*, 110.
- [65] N. D. Boscher, C. J. Carmalt, R. G. Palgrave, I. P. Parkin, *Thin Solid Films* **2008**, *516*, 4750.
- [66] S. Luo, X. Qi, H. Yao, X. Ren, Q. Chen, J. Zhong, *J. Phys. Chem. C* **2017**, *121*, 4674.
- [67] S. Anwar, S. Gowthamaraju, B. K. Mishra, S. K. Singh, S. Anwar, *Mater. Chem. Phys.* **2015**, *153*, 236.
- [68] S. Anwar, B. K. Mishra, S. Anwar, *Mater. Chem. Phys.* **2016**, *175*, 118.
- [69] B. Subramanian, C. Sanjeeviraja, M. Jayachandran, *J. Cryst. Growth* **2002**, *234*, 421.
- [70] R. Rostek, N. Stein, C. Boulanger, *J. Mater. Res.* **2015**, *30*, 2518.
- [71] C. I. House, G. H. Kelsall, *Electrochimica Acta* **1984**, *29*, 1459.
- [72] R. Buckle, *The Recovery of Metals from Waste Solutions by Electrochemical Methods*, Newcastle University, **2017**.

- [73] K. Scott, X. Chen, J. W. Atkinson, M. Todd, R. D. Armstrong, *Resour. Conserv. Recycl.* **1997**, *20*, 43.
- [74] J. Manfred, in *Mod. Electroplat.*, **2010**, pp. 2665–284.
- [75] J. Endlé, in *Tech. Ing.*, **1974**, p. 11.
- [76] A. Sharma, S. Bhattacharya, R. Sen, B. S. B. Reddy, H.-J. Fecht, K. Das, S. Das, *Mater. Charact.* **2012**, *68*, 22.
- [77] A. Sharma, H. Seo, B. Ahn, *Coatings* **2020**, *10*, 117.
- [78] F. C. Walsh, C. T. J. Low, *Surf. Coat. Technol.* **2016**, 288, 79.
- [79] A. Collazo, R. Figueroa, X. R. Nóvoa, C. Pérez, *Surf. Coat. Technol.* **2015**, 280, 8.
- [80] G. I. Medvedev, N. A. Makrushin, *Russ. J. Appl. Chem.* **2002**, *75*, 1234.
- [81] M. Clarke, J. A. Bernie, *Electrochimica Acta* **1967**, *12*, 205.
- [82] G. S. Tzeng, S. H. Lin, Y. Y. Wang, C. C. Wan, *J. Appl. Electrochem.* **1996**, *26*, 419.
- [83] A. H. Whitehead, J. M. Elliott, J. R. Owen, G. S. Attard, *Chem Commun* **1999**, 331.
- [84] A. Gupta, C. Srivastava, *J. Electroanal. Chem.* **2020**, 861, 113964.
- [85] X. Wen, X. Pan, L. Wu, R. Li, D. Wang, J. Zhang, P. Yang, *Appl. Phys. A* **2017**, *123*, 423.
- [86] Y. Nakamura, N. Kaneko, M. Nakamura, H. Nezu, *J. Appl. Electrochem.* **1994**, *24*, 404.
- [87] S. Bakkali, R. Touir, M. Cherkaoui, M. E. Touhami, *Surf. Coat. Technol.* **2015**, 261, 337.
- [88] K. Ui, S. Kikuchi, Y. Kadoma, N. Kumagai, S. Ito, *J. Power Sources* **2009**, *189*, 224.
- [89] D. Aranzales, J. H. O. J. Wijenberg, M. T. M. Koper, *J. Electrochem. Soc.* **2019**, *166*, D283.
- [90] S. Mohan, N. Rajasekaran, *Surf. Eng.* **2009**, *25*, 634.
- [91] M. A. Ashworth, G. D. Wilcox, R. L. Higginson, R. J. Heath, C. Liu, *Trans. IMF* **2013**, *91*, 260.
- [92] E. Rudnik, *Ionics* **2013**, *19*, 1047.
- [93] E. Rudnik, G. Włoch, *Appl. Surf. Sci.* **2013**, 265, 839.
- [94] I. S. Zavarine, O. Khaselev, Y. Zhang, *J. Electrochem. Soc.* **2003**, *150*, C202.
- [95] F. Otsubo, H. Era, Y. Tsuru, S. Hirano, *Mater. Chem. Phys.* **2020**, *251*, 122985.
- [96] F. Kesri, A. M. Affoune, I. Djaghout, *J. Serbian Chem. Soc.* **2019**, *84*, 41.
- [97] C. T. J. Low, F. C. Walsh, *J. Electroanal. Chem.* **2008**, 615, 91.
- [98] C. T. J. Low, F. C. Walsh, *Electrochimica Acta* **2008**, *53*, 5280.
- [99] M. Saitou, *Int. J. Electrochem. Sci.* **2018**, *13*, 1869.
- [100] S. Ghosh, S. Roy, *Mater. Sci. Eng. B* **2014**, *190*, 104.
- [101] N. Geoffroy, G. P. Demopoulos, *J. Chem. Technol. Biotechnol.* **2012**, *87*, 983.
- [102] A. Sharma, Y. M. Park, S. Lee, B. Ahn, *Mater. Res. Express* **2019**, *6*, 116589.
- [103] M. Bouroushian, in *Electrochem. Met. Chalcogenides*, **2010**.

- [104] I. Nandhakumar, J. M. Elliott, G. S. Attard, *Chem. Mater.* **2001**, *13*, 3840.
- [105] A. A. Aal, F. Voigts, D. Chakarov, F. Endres, *Electrochimica Acta* **2012**, *59*, 228.
- [106] V. S. Saji, C.-W. Lee, *RSC Adv.* **2013**, *3*, 10058.
- [107] C. Wei, N. Myung, K. Rajeshwar, *J. Electroanal. Chem.* **1994**, *375*, 109.
- [108] M. F. Cabral, V. A. Pedrosa, S. A. S. Machado, *Electrochimica Acta* **2010**, *55*, 1184.
- [109] T. E. Lister, B. M. Huang, R. D. Herrick, J. L. Stickney, *J. Vac. Sci. Technol. B Microelectron. Nanometer Struct. Process. Meas. Phenom.* **1995**, *13*, 1268.
- [110] A. Von Hippel, W. Bloom, M. C. Bloom, N. Highlands, **1953**.
- [111] C. Guarneros-Aguilar, O. Calzadilla, J. A. Barón-Miranda, J. L. Fernandez-Muñoz, F. Caballero-Briones, *Mater. Res. Express* **2019**, *6*, 066412.
- [112] G. Jarzabek, Z. Kublik, *J. Electroanal. Chem. Interfacial Electrochem.* **1980**, *114*, 165.
- [113] M. Alanyalioglu, U. Demir, C. Shannon, *J. Electroanal. Chem.* **2004**, *561*, 21.
- [114] R. Modolo, M. Traore, O. Vittori, *Electrochimica Acta* **1986**, *31*, 859.
- [115] B. Maranowski, M. Strawski, W. Osowiecki, M. Szklarczyk, *J. Electroanal. Chem.* **2015**, *752*, 54.
- [116] M. O. Solaliendres, A. Manzoli, G. R. Salazar-Banda, K. I. B. Eguiluz, S. T. Tanimoto, S. A. S. Machado, *J. Solid State Electrochem.* **2008**, *12*, 679.
- [117] T. Ishiyama, T. Tanaka, *Anal. Chem.* **1996**, *68*, 3789.
- [118] Y. Fan, J. Yang, L. Jiang, Y. Wang, B. K. Ng, H. Sun, Y. Lai, J. Li, F. Liu, *J. Electrochem. Soc.* **2017**, *164*, H225.
- [119] R. Kowalik, *Arch. Metall. Mater.* **2014**, *59*, 871.
- [120] Y. Lai, F. Liu, J. Li, Z. Zhang, Y. Liu, *J. Electroanal. Chem.* **2010**, *639*, 187.
- [121] R. Kowalik, *Arch. Metall. Mater.* **2015**, *60*.
- [122] A. M. Patil, A. C. Lokhande, N. R. Chodankar, J. H. Kim, C. D. Lokhande, *Int. J. Hydrog. Energy* **2016**, *41*, 17453.
- [123] S. Saha, N. Tachikawa, K. Yoshii, Y. Katayama, *J. Electrochem. Soc.* **2016**, *163*, 259.
- [124] M. Bougouma, A. Van Elewyck, M. Steichen, C. Buess-Herman, Th. Doneux, *J. Solid State Electrochem.* **2013**, *17*, 527.
- [125] A. Cojocar, I. Sin, C. Agapescu, A. Cotarta, T. Visan, *Chalcogenide Lett.* **2016**, *13*, 127.
- [126] D. W. Redman, S. Murugesan, K. J. Stevenson, *Langmuir* **2014**, *30*, 418.
- [127] A. A. Aal, R. Al-Salman, M. Al-Zoubi, N. Borissenko, F. Endres, O. Höfft, A. Prowald, S. Zein El Abedin, *Electrochimica Acta* **2011**, *56*, 10295.
- [128] S. Zein El Abedin, A. Y. Saad, H. K. Farag, N. Borisenko, Q. X. Liu, F. Endres, *Electrochimica Acta* **2007**, *52*, 2746.
- [129] O. Dilmli, M. Benaicha, *Russ. J. Electrochem.* **2017**, *53*, 140.
- [130] Z. Qiao, W. Shang, C. Wang, *J. Electroanal. Chem.* **2005**, *576*, 171.
- [131] D. Coelho, G. M. Luiz, S. A. S. Machado, *J. Electroanal. Chem.* **2018**, *820*, 89.

- [132] [https://chem.libretexts.org/Bookshelves/Analytical_Chemistry/Supplemental_Modules_\(Analytical_Chemistry\)/Qualitative_Analysis/Characteristic_Reactions_of_Select_Metal_Ions/Characteristic_Reactions_of_Tin_Ions_\(Sn²⁺2C_Sn⁴⁺\)](https://chem.libretexts.org/Bookshelves/Analytical_Chemistry/Supplemental_Modules_(Analytical_Chemistry)/Qualitative_Analysis/Characteristic_Reactions_of_Select_Metal_Ions/Characteristic_Reactions_of_Tin_Ions_(Sn²⁺2C_Sn⁴⁺))
- [133] K. R. Murali, K. Ananthi, N. Muthukumarasamy, K. Thilagavathy, S. Dhanapandiyan, *Meet. Abstr.* **2011**, *MA2011-01*, 1550.
- [134] K. Ananthi, S. Dhanapandian, N. Muthukumarasamy, K. Thilagavathy, K. R. Murali, *Int. J. Intell. Electron. Syst.* **2012**, *6*, 36.
- [135] K. R. Murali, *J. Mater. Sci. Mater. Electron.* **2014**, *25*, 2374.
- [136] A. Lukinskas, V. Jasulaitienė, P. Lukinskas, I. Savickaja, P. Kalinauskas, *Electrochimica Acta* **2006**, *51*, 6171.
- [137] S.-Y. Ham, S.-U. Choi, Y.-J. Chae, W. Lee, K.-J. Paeng, W.-G. Kim, N. Myung, *Bull. Korean Chem. Soc.* **2010**, *31*, 3403.
- [138] N. R. Mathews, *Sol. Energy* **2012**, *86*, 1010.
- [139] T. Mahalingam, V. Dhanasekaran, J. P. Chu, T. Kim, Y. D. Kim, *ECS Trans.* **2011**, *35*, 61.
- [140] A. Zatirostami, *J. Alloys Compd.* **2020**, *844*, 156151.
- [141] F. Jamali-Sheini, M. Cheraghizade, R. Yousefi, *Appl. Surf. Sci.* **2018**, *443*, 345.
- [142] Z. Zainal, A. J. Ali, A. Kassim, M. Z. Hussein, *Sol. Energy Mater. Sol. Cells* **2003**, *79*, 125.
- [143] V. Dhanasekaran, J. Jung, K. Keun Lee, T. Mahalingam, *Ionics* **2014**, *21*, 1187.
- [144] D. V. Shinde, S.-K. Min, M.-M. Sung, N. K. Shrestha, R. S. Mane, S.-H. Han, *Mater. Lett.* **2014**, *115*, 244.
- [145] P. Mandal, D. Banerjee, A. Mondal, Erode, India, **2019**, p. 020006.
- [146] C. Lu, Y. Zhang, L. Zhang, Q. Yin, *Appl. Surf. Sci.* **2019**, *484*, 560.
- [147] M. R. Burton, C. A. Boyle, T. Liu, J. McGettrick, I. Nandhakumar, O. Fenwick, M. J. Carnie, *ACS Appl. Mater. Interfaces* **2020**, *12*, 28232.
- [148] R. Rostek, J. Kottmeier, M. Kratschmer, G. Blackburn, F. Goldschmidtboing, M. Kroner, P. Woias, *J. Electrochem. Soc.* **2013**, *160*, D408.
- [149] V. Dhanasekaran, K. Sundaram, J. Jung, T. Mahalingam, *J. Mater. Sci. Mater. Electron.* **2015**, *26*, 1641.
- [150] B. Jalalian-Larki, F. Jamali-Sheini, R. Yousefi, *Solid State Sci.* **2020**, *108*, 106388.
- [151] A. R. Paris, A. B. Bocarsly, *ACS Catal.* **2019**, *9*, 2324.
- [152] L. Maya, *J. Common Met.* **1983**, *90*, 137.
- [153] S. Kim, K. Seong, O. Kim, S. Kim, H. Seo, M. Lee, G. Khang, D. Lee, *Biomacromolecules* **2010**, *11*, 555.
- [154] S. K. Ghosh, G. Waghoo, A. Kalita, D. Balgude, K. R. Kumar, *Prog. Org. Coat.* **2012**, *73*, 70.
- [155] <https://fr.vwr.com/store/product/4568277/etain-ii-oxalate>
- [156] H. Ju, D. Park, J. Kim, *Sci. Rep.* **2017**, *7*, 18051.

- [157] H. Ju, D. Park, J. Kim, *J. Mater. Chem. A* **2018**, 6, 5627.
- [158] https://www.merckmillipore.com/FR/fr/product/msds/MDA_CHEM-106557?Origin=PDP
- [159] https://www.merckmillipore.com/FR/fr/product/msds/MDA_CHEM-816144?Origin=PDP
- [160] M. S. Chandrasekar, M. Pushpavanam, *Electrochimica Acta* **2008**, 53, 3313.
- [161] W. E. G. Hansal, S. Roy, *Pulse Plating: Including 25 Tables*, Leuze, Bad Saulgau, **2012**.
- [162] O. Caballero-Calero, P. Díaz-Chao, B. Abad, C. V. Manzano, M. D. Ynsa, J. J. Romero, M. M. Rojo, M. S. Martín-González, *Electrochimica Acta* **2014**, 123, 117.
- [163] F. Claudel, *Development of anticorrosive Zn-based alloy coatings for cold formed steel body parts*, Université de Lorraine, **2019**.
- [164] <https://www.ecam.fr/materiaux-structures/microscope-electronique-a-balayage/le-microscope>
- [165] https://fr.wikipedia.org/wiki/Microscopie_électronique_en_transmission
- [166] https://en.wikipedia.org/wiki/Annular_dark-field_imaging
- [167] B. J. Inkson, in *Mater. Charact. Using Nondestruct. Eval. NDE Methods* (Eds.: G. Hübschen, I. Altpeter, R. Tschuncky, H.-G. Herrmann), Woodhead Publishing, **2016**, pp. 17–43.
- [168] <https://www.orsayphysics.com/what-is-fib>
- [169] <https://www.sciencedirect-com.bases-doc.univ-lorraine.fr/topics/biochemistry-genetics-and-molecular-biology/inductively-coupled-plasma>
- [170] <https://www.labcompare.com/347303-Viewing-ICP-OES>
- [171] M. A. Rutzke, in *Encycl. Geochem. Compr. Ref. Source Chem. Earth* (Ed.: W.M. White), Springer International Publishing, Cham, **2017**, pp. 1–8.
- [172] J.-M. Greneche, A. Wattiaux, *La spectroscopie Mössbauer*, **n.d.**
- [173] J.-P. Eymery, J. Teillet, in *Tech. Ing.*, **1994**, p. 27.
- [174] P. Colomban, *Actual. Chim.* **2003**, 12.
- [175] H. Oechsner, in *Thin Film Depth Profile Anal.* (Ed.: H. Oechsner), Springer, Berlin, Heidelberg, **1984**, pp. 63–85.
- [176] K. Vad, A. Csik, G. A. Langer, **2009**, 21, 4.
- [177] https://fr.wikipedia.org/wiki/Spectrométrie_photoélectronique
- [178] <https://ywcmatsci.yale.edu/xps>,
- [179] <https://fr.wikipedia.org/wiki/Ellipsométrie>
- [180] M. Gaillet, *L'Ellipsométrie Spectroscopique et ses Applications Industrielles & Scientifiques*, **2008**.
- [181] M. De Vos, A. Danine, L. Adam, S. Diliberto, O. Caballero-Calero, M. Martín-González, L. Péter, A. Csík, V. Kálmán, L. Philippe, D. Osenberg, P. Al-Alam, G. Pernot, D. Lacroix, N. Stein, *J. Electrochem. Soc.* **2020**, 167, 162502.
- [182] S. Motoo, M. Watanabe, *J. Electroanal. Chem. Interfacial Electrochem.* **1976**, 69, 429.

- [183] N. Furuya, S. Motoo, *J. Electroanal. Chem. Interfacial Electrochem.* **1979**, 98, 195.
- [184] T. Frelink, W. Visscher, J. A. R. van Veen, *Electrochimica Acta* **1994**, 39, 1871.
- [185] Y. Du, B. Su, N. Zhang, C. Wang, *Appl. Surf. Sci.* **2008**, 255, 2641.
- [186] Q.-W. Zheng, C.-J. Fan, C.-H. Zhen, Z.-Y. Zhou, S.-G. Sun, *Electrochimica Acta* **2008**, 53, 6081.
- [187] I. Pašti, S. Mentus, *J. Alloys Compd.* **2010**, 497, 38.
- [188] Y. YAPONTSEVA, V. Kublanovsky, *Turk. J. Chem.* **2019**, 43, 73.
- [189] <https://fr.wikipedia.org/w/index.php?title=Viscosité&oldid=179005875>
- [190] L. Thouin, S. Rouquette-Sanchez, J. Vedel, *Electrochimica Acta* **1993**, 38, 2387.
- [191] J. Su, X. Lin, S. Zheng, R. Ning, W. Lou, W. Jin, *Sep. Purif. Technol.* **2017**, 182, 160.
- [192] Y. Q. Liang, Z. D. Cui, S. L. Zhu, X. J. Yang, *Electrochem. Solid-State Lett.* **2012**, 15, D4.
- [193] J. Schoenleber, N. Stein, C. Boulanger, *J. Electroanal. Chem.* **2014**, 724, 111.
- [194] M. S. Martín-González, A. L. Prieto, R. Gronsky, T. Sands, A. M. Stacy, *J. Electrochem. Soc.* **2002**, 149, C546.
- [195] A. C. Bernardes-Silva, A. F. Mesquita, E. de M. Neto, A. O. Porto, J. D. Ardisson, G. M. de Lima, F. S. Lameiras, *Mater. Res. Bull.* **2005**, 40, 1497.
- [196] H. R. Chandrasekhar, R. G. Humphreys, U. Zwick, M. Cardona, *Phys. Rev. B* **1977**, 15, 2177.
- [197] A. Anderson, A. Sanders, W. Smith, *J. Raman Spectrosc.* **2000**, 31, 403.
- [198] V. V. Poborchii, A. V. Kolobov, K. Tanaka, *Appl. Phys. Lett.* **1998**, 72, 1167.
- [199] G. Lucovsky, A. Mooradian, E. Burstein, *Solid State Commun.* **1967**, 5, 113.
- [200] S. N. Yannopoulos, K. S. Andrikopoulos, *J. Chem. Phys.* **2004**, 121, 4747.
- [201] Y. Saejeng, N. Tantavichet, *J. Appl. Electrochem.* **2009**, 39, 123.
- [202] J. P. G. Farr, *Trans. IMF* **2008**, 86, 275.
- [203] S. Roy, S. Caprodossi, *Trans. IMF* **2009**, 87, 78.
- [204] K. M. Youssef, C. C. Koch, P. S. Fedkiw, *Electrochimica Acta* **2008**, 54, 677.
- [205] P. Leisner, I. Belov, *Trans. IMF* **2009**, 87, 90.
- [206] P. N. Sayar, M. E. Bahrololoom, *Trans. IMF* **2009**, 87, 246.
- [207] A. Sharma, S. Bhattacharya, S. Das, K. Das, *Appl. Surf. Sci.* **2014**, 290, 373.
- [208] C. Larson, J. P. G. Farr, *Trans. IMF* **2010**, 88, 237.
- [209] K.-L. Lin, L.-M. Sun, *J. Mater. Res.* **2003**, 18, 2203.
- [210] B. H. An, H. M. Ji, J.-H. Wu, M. K. Cho, K.-Y. Yang, H. Lee, Y. K. Kim, *Curr. Appl. Phys.* **2009**, 9, 1338.
- [211] M. K. L. Mendoza, B. J. V. Tongol, S. Shanmugam, H. Kim, *Int. J. Hydrog. Energy* **2018**, 43, 19930.
- [212] D. Landolt, A. Marlot, *Surf. Coat. Technol.* **2003**, 169–170, 8.

- [213] D. Rafaja, C. Schimpf, T. Schucknecht, V. Klemm, L. Péter, I. Bakonyi, *Acta Mater.* **2011**, 59, 2992.
- [214] S. Mirzamohammadi, R. Kiarasi, M. K. Aliov, A. R. Sabur, A. Hassanzadeh-Tabrizi, *Trans. IMF* **2010**, 88, 93.
- [215] X. Yang, K. Eckert, S. Mühlenhoff, M. Uhlemann, S. Odenbach, *Electrochem. Commun.* **2009**, 11, 318.
- [216] L. M. Chang, H. F. Guo, M. Z. An, *Mater. Lett.* **2008**, 62, 3313.
- [217] N. Imaz, E. García-Lecina, C. Suárez, J. A. Díez, J. Rodríguez, J. Molina, V. García-Navas, *Trans. IMF* **2009**, 87, 64.
- [218] B. Djurfors, D. G. Ivey, *J. Electron. Mater.* **2001**, 30, 1249.
- [219] S. Chaudhari, S. Palli, K. P.K., S. R. Dey, *Thin Solid Films* **2016**, 600, 169.
- [220] K. Takeuchi, M. Ichimura, E. Arai, Y. Yamazaki, *Sol. Energy Mater. Sol. Cells* **2003**, 75, 427.
- [221] X. Dou, G. Li, H. Lei, X. Huang, L. Li, I. W. Boyd, *J. Electrochem. Soc.* **2009**, 156, K149.
- [222] C. V. Manzano, A. A. Rojas, M. Decepidá, B. Abad, Y. Feliz, O. Caballero-Calero, D.-A. Borca-Tasciuc, M. Martin-Gonzalez, *J. Solid State Electrochem.* **2013**, 17, 2071.
- [223] D. Del Frari, S. Diliberto, N. Stein, C. Boulanger, J.-M. Lecuire, *J. Appl. Electrochem.* **2006**, 36, 449.
- [224] M. Shenasa, S. Sainkar, D. Lichtman, *J. Electron Spectrosc. Relat. Phenom.* **1986**, 40, 329.
- [225] M. Pawar, S. Kadam, D. J. Late, *ChemistrySelect* **2017**, 2, 4068.
- [226] M. A. Stranick, A. Moskwa, *Surf. Sci. Spectra* **1998**, 2, 50.
- [227] M. Gilliot, *Appl. Opt.* **2017**, 56, 1173.
- [228] S. Logothetidis, H. M. Polatoglou, *Phys. Rev. B* **1987**, 36, 7491.
- [229] Z.-G. Chen, X. Shi, L.-D. Zhao, J. Zou, *Prog. Mater. Sci.* **2018**, 97, 283.
- [230] C. Yamamoto, X. He, T. Katase, K. Ide, Y. Goto, Y. Mizuguchi, A. Samizo, M. Minohara, S. Ueda, H. Hiramatsu, H. Hosono, T. Kamiya, *Adv. Funct. Mater.* **2021**, 31, 2008092.
- [231] İ. Şişman, H. Öz, *Electrochimica Acta* **2011**, 56, 4889.
- [232] Y. Liu, K. Cao, J. Liu, Z. Zhang, J. Ji, F. Wang, Z. Li, *J. Mater. Sci. Mater. Electron.* **2019**, 30, 15880.
- [233] K. Ui, S. Kikuchi, Y. Jimba, N. Kumagai, *J. Power Sources* **2011**, 196, 3916.
- [234] X. Dong, W. Liu, X. Chen, J. Yan, N. Li, S. Shi, S. Zhang, X. Yang, *Chem. Eng. J.* **2018**, 350, 791.
- [235] http://www.ars-chemia.net/Permanent_Files/Tables/Solubility_Product_Constants.pdf
- [236] C. T. J. Low, C. P. de Leon, F. C. Walsh, *Trans. IMF* **2015**, 93, 74.
- [237] C. P. de Leon, F. C. Walsh, *Trans. IMF* **2003**, 81, B95.
- [238] L. Trnkova, L. Zerzankova, F. Dycka, R. Mikelova, F. Jelen, *Sensors* **2008**, 8, 429.

- [239] A. Baral, C. K. Sarangi, B. C. Tripathy, I. N. Bhattacharya, T. Subbaiah, *Hydrometallurgy* **2014**, 146, 8.
- [240] D. Zheng, H. Fang, M. Long, F. Wu, P. Wang, F. Gong, X. Wu, J. C. Ho, L. Liao, W. Hu, *ACS Nano* **2018**, 12, 7239.
- [241] J. A. Hernandez, A. Ruiz, L. F. Fonseca, M. T. Pettes, M. Jose-Yacaman, A. Benitez, *Sci. Rep.* **2018**, 8, 1.
- [242] G. Shen, D. Chen, X. Jiang, K. Tang, Y. Liu, Y. Qian, *Chem. Lett.* **2003**, 32, 426.
- [243] C. R. Martin, *Chem. Mater.* **1996**, 8, 1739.
- [244] A. M. R. Elbasiony, S. Zein El Abedin, F. Endres, *J. Solid State Electrochem.* **2014**, 18, 951.
- [245] S. Al Kiey, A. El Warraky, S. Abdel Rehim, S. Zein El Abedin, *Egypt. J. Chem.* **2018**, 0, 0.
- [246] T.-I. Leong, Y.-T. Hsieh, I.-W. Sun, *Electrochimica Acta* **2011**, 56, 3941.
- [247] M.-J. Deng, J.-K. Chang, T.-I. Leong, S.-W. Fang, P.-Y. Chen, I.-W. Sun, *Electrochemistry* **2009**, 77, 588.
- [248] R. Al-Salman, H. Sommer, T. Brezesinski, J. Janek, *Electrochimica Acta* **2017**, 246, 1016.
- [249] A. W. Lodge, M. M. Hasan, P. N. Bartlett, R. Beanland, A. L. Hector, R. J. Kashtiban, W. Levason, G. Reid, J. Sloan, D. C. Smith, W. Zhang, *RSC Adv.* **2018**, 8, 24013.
- [250] G. Schmid, *J. Mater. Chem.* **2002**, 12, 1231.
- [251] B. Luo, D. Yang, M. Liang, L. Zhi, *Nanoscale* **2010**, 2, 1661.
- [252] G. S. Harlow, J. Drnec, T. Wiegmann, W. Lipé, J. Evertsson, A. R. Persson, R. Wallenberg, E. Lundgren, N. A. Vinogradov, *Nanoscale Adv.* **2019**, 1, 4764.
- [253] A. Sharma, S. Das, K. Das, *Electrodepos. Compos. Mater.* **2016**, DOI 10.5772/62036.
- [254] A. Sharma, A. K. Srivastava, Y. Jeon, B. Ahn, *Metals* **2018**, 8, 347.
- [255] T. Djenizian, I. Hanzu, Y. D. Premchand, F. Vacandio, P. Knauth, *Nanotechnology* **2008**, 19, 205601.
- [256] S. Shin, T. T. Al-Housseiny, B. S. Kim, H. H. Cho, H. A. Stone, *Nano Lett.* **2014**, 14, 4395.
- [257] M. Steichen, P. Dale, *Electrochem. Commun.* **2011**, 13, 865.
- [258] S.-Y. Zhang, J. Zhang, Y. Liu, X. Ma, H.-Y. Chen, *Electrochimica Acta* **2005**, 50, 4365.
- [259] N. Kumar, R. Kumar, S. Kumar, S. K. Chakarvarti, *J. Mater. Sci. Mater. Electron.* **2014**, 25, 3537.
- [260] S. Kumar, *J. Exp. Nanosci.* **2009**, 4, 341.
- [261] X. Y. Zhang, Y. Cai, J. Y. Miao, K. Y. Ng, Y. F. Chan, X. X. Zhang, N. Wang, *J. Cryst. Growth* **2005**, 276, 674.
- [262] C. Lin, W. Cheng, Z. Guo, G. Chai, H. Zhang, *Phys. Chem. Chem. Phys.* **2017**, 19, 23247.
- [263] Q. Han, Y. Zhu, X. Wang, W. Ding, *J. Mater. Sci.* **2004**, 39, 4643.

- [264] L. Zhao, M. Yosef, M. Steinhart, P. Göring, H. Hofmeister, U. Gösele, S. Schlecht, *Angew. Chem. Int. Ed.* **2006**, 45, 311.
- [265] S. Liu, X. Guo, M. Li, W.-H. Zhang, X. Liu, C. Li, *Angew. Chem. Int. Ed.* **2011**, 50, 12050.
- [266] J. M. Doña Rodríguez, J. A. Herrera Melián, J. Pérez Peña, *J. Chem. Educ.* **2000**, 77, 1195.
- [267] J. Schoenleber, *Électrodéposition et caractérisations de nanofils thermoélectriques Bi_{0,5}Sb_{1,5}Te₃ dans des matrices mésoporeuses en polycarbonate*, Université de Lorraine, **2014**.
- [268] M. P. Proenca, C. T. Sousa, J. Ventura, M. Vazquez, J. P. Araujo, *Nanoscale Res. Lett.* **2012**, 7, 280.

Summary

Since recent works highlighting its high figure of merit (2.6 at 923 K), SnSe is fingered as promising candidate for thermoelectric applications. Mainly synthesized by physical way and in bulk shape, few works present the elaboration of SnSe at a decreased dimensionality. However, it was shown that the thermal conductivity of thermoelectric materials is considerably reduced at low dimensionality. A synthesis method which is particularly suitable to the elaboration of low dimensionality deposits is the electrodeposition, poorly used for SnSe. In this thesis, the electrodeposition of SnSe was thus thoroughly discussed. In continuous mode, the influence of the potential on the films composition and morphology was studied from an innovative electrochemical bath, regarding the literature. The conditions providing the best films were preserved in order to study the pulse mode syntheses. The pulse conditions have also proved to be decisive on the composition and morphology of the films. As first prospect of this work, doping with copper was investigated from the best pulse conditions. As second promising prospect, this thesis work was extended to the electrodeposition of SnSe nanowires and nanotubes. These 1D nanostructures, synthesized in continuous mode, show an evolution of the crystallinity, of the composition and even of the morphology with the potential.

Résumé

Depuis des travaux récents mettant en avant son facteur de mérite élevé (2,6 à 923 K), SnSe est pointé du doigt en tant que candidat prometteur pour des applications thermoélectriques. Principalement synthétisé par voie physique et sous forme massive, peu de travaux présentent l'élaboration de SnSe à une dimensionnalité diminuée. Pourtant, il a été montré que la conductivité thermique des matériaux thermoélectriques est considérablement réduite à basse dimensionnalité. Une méthode de synthèse qui se prête particulièrement à l'élaboration de dépôts à basse dimensionnalité est l'électrodéposition, faiblement utilisée pour SnSe. Dans cette thèse, l'électrodéposition de SnSe a donc été abordée de manière approfondie. En mode continu, l'influence du potentiel sur la composition et la morphologie des films a été étudiée à partir d'un bain électrochimique innovant au regard de la littérature. Les conditions procurant les meilleurs films ont été conservées afin d'étudier les synthèses en mode impulsionnel. Les conditions d'impulsion se sont également révélées déterminantes sur la composition et la morphologie des films. Comme première perspective de ce travail, le dopage par le cuivre a été étudié, à partir des meilleures conditions impulsionnelles. Comme seconde perspective prometteuse, ce travail de thèse a été étendu à l'électrodéposition de nanofils et de nanotubes de SnSe. Ces nanostructures 1D, synthétisées en mode continu, montrent une évolution de la cristallinité, la composition et voire la morphologie avec le potentiel.